# 3D printed leaf biosensor

A thesis submitted to The University of Manchester for the degree of
Doctor of Philosophy
in the Faculty of Science and Engineering
**2022**

**Mohamed Hassan**

**Supervisors:**
*Prof. Paulo Bartolo*
*Prof. Bruce Grieve*

Department of Mechanical, Aerospace and Civil Engineering

School of Engineering

# Table of Contents

Table of Contents ..... 2
Chapter 1: Introduction .....
1.1 Background ..... 17
1.2 Research aim and objectives ..... 21
1.3 Structure ..... 22
Chapter 2: literature review .....
2.1 Recent advances in enzymatic and non-enzymatic electrochemical glucose sensors ..... 26
2.1.1 Introduction ..... 26
2.1.2 Three Generations of Enzymatic Glucose Sensors ..... 29
2.1.3 First-Generation Enzymatic Glucose Biosensors ..... 31
2.1.4 Second-Generation Enzymatic Glucose Biosensors ..... 32
2.1.5 Third-Generation Enzymatic Glucose Biosensors ..... 33
2.1.6 Recent Developments in Enzymatic Glucose Biosensors ..... 34
2.1.7 Recent Developments in Non-Enzymatic Glucose Sensors ..... 40
2.1.8 Metal-Based Glucose Sensors ..... 41
2.1.9 Pt-Based Glucose Sensors ..... 41
2.1.10 Au-Based Glucose Sensors ..... 43
2.1.11 Transition Metals-Based Sensors ..... 45
2.1.12 Metal Alloy-Based Glucose Sensors Agriculture ..... 46
2.1.13 Conclusion and future perspective ..... 47
2.2 4D printing of Shape Morphing Polymers ..... 49
2.2.1 Introduction ..... 49
2.2.2 Classification ..... 52
2.2.3 Functionality ..... 52
2.2.4 Morphology ..... 56
2.2.5 Stimuli ..... 57
2.2.6 Thermo-responsive ..... 57
2.2.7 Photo-responsive ..... 59
2.2.8 Electro-responsive ..... 60
2.2.9 Magneto-responsive ..... 62
2.2.10 Chemo-responsive ..... 63
2.2.11 Bio-responsive ..... 65
2.2.12 4D printing ..... 66
2.2.13 Conclusion ..... 67

Chapter 3: 4D printing of a bioinspired leaf sensor surface .....
3.1 Introduction .....70
3.2 Materials .....72
3.3 Leaf morphology .....72
3.4 Surface patterning .....73
3.5 Middle layer fabrication .....73
3.6 Inoculation .....73
3.7 Shape recovery .....74
3.8 Results and discussions .....74
3.8.1 Leaf morphology .....74
3.8.2 Surface Patterning .....75
3.8.3 Sensing layer design .....76
3.8.4 Inoculation .....77
3.8.5 Shape recovery .....78
3.8.6 Conclusion and Future Perspective .....79
Chapter 4: Chemical and compositional analysis of PETG for 4D printing applications .....
4.1 Introduction .....81
4.2 Materials and methods .....82
4.2.1 Materials .....82
4.2.2 Fabrication .....82
4.2.3 Maldi-ToF-MS .....83
4.2.4 Mechanical tensile test .....84
4.2.5 Shape recovery .....84
4.3 Results .....84
4.3.1 Chemical analysis .....84
4.3.2 Mechanical tensile test .....86
4.3.3 Shape recovery results .....86
4.4 Conclusion .....87
Chapter 5: The potential of Polyethylene Terephthalate Glycol (PETG) as biomaterial for tissue engineering .....
5.1 Introduction .....89
5.2 Materials and Methods .....91
5.2.1 Materials .....91
5.2.2 Scaffolds Fabrication .....92
5.2.3 Morphological analysis .....92
5.2.4 Mechanical compression test .....93

5.2.5 Biological analysis .....93
5.2.5.1 Cell culture .....93
5.2.5.2 Alamar Blue Assay .....93
5.2.5.3 Statistically analysis .....94
5.3 Results and Discussion .....94
5.3.1 Chemical analysis .....94
5.3.2 Scaffold Morphology .....95
5.3.3 Mechanical compression test .....96
5.3.4 Biological test .....98
5.4 Conclusion .....100
Chapter 6: Smart polyethylene terephthalate glycol (PETG) .....
6.1 Introduction .....103
6.2 Material and methods .....104
6.2.1 Materials .....104
6.2.2 Material fabrication .....104
6.2.3 Morphology .....105
6.2.4 Chemical composition .....106
6.2.5 Shape recovery .....106
6.3 Results and Discussion .....106
6.3.1 Morphology .....106
6.3.2 Chemical composition .....107
6.3.3 Shape Recovery .....109
6.4 Conclusion .....112
Chapter 7: Electrospinning polyethylene terephthalate glycol (PETG) meshes .....
7.1 Introduction .....114
7.2 Materials and Methods .....115
7.2.1 Materials .....115
7.2.2 Mapping Spinnability of PETG on the Teas Graph .....115
7.2.3 Fabrication of PETG Meshes .....116
7.2.4 Morphological Analysis .....116
7.2.5 Chemical compositional characterisation .....117
7.2.6 Inoculation .....117
7.3 Results and Discussion .....117
7.3.1 Solubility and Electrospinnability .....117
7.3.2 Meshes Morphology .....118
7.3.3 Mesh chemical composition .....121

7.3.4 Inoculation .....123
7.4 Conclusion .....123
Chapter 8: Multi-layer biosensor for pre-symptomatic detection of Puccinia strifformis, the causal agent of yellow rust .....
8.1 Introduction .....126
8.2 Materials and Methods .....130
8.2.1 Materials .....130
8.2.2 Sensor Fabrication .....130
8.2.3 Inoculation .....132
8.2.4 Morphology .....133
8.2.5 Electrochemical measurements .....133
8.3 Results and Discussion .....134
8.3.1 Morphological Characterisation .....134
8.3.2 Electrochemical behaviour of the Au-Ni/AC SPE .....135
8.3.3 Nanoparticles characterisation .....140
8.3.4 Sensor selectivity .....141
8.3.5 Sensor Functionality .....142
8.4 Conclusion .....143
Chapter 9: Conclusion and future work .....
9.1 Conclusions .....146
9.2 Future Work .....150
References .....152

# List of Figures:

**Figure 1.1**: (a) Yellow rust fungi (*Puccinia striiformis f. sp. tritici*) spore, (b) infected wheat leaf after 14 days .....17
**Figure 1.2:** (a) Schematic representation of early infection structures of Puccinia striiformis. The spore germ tube enters the leaf through the stomata forming a substomatal vesicle from which infection-hyphae develop. Once the hyphae contact the mesophyll cell a haustoria is formed inside the plant cell. (b) Transverse section of a plant leaf showing the different layers of the leaf .....19
**Figure 1.3**: Plant cuticle chemical representation [40] .....20
**Figure 1.4**: Proposed biosensor design .....21
**Figure 2.1**: Number of glucose sensor related articles published in the past 10 years. The search was conducted using the Web of Science (Clarivate Analytics, Philadelphia, PA, USA) database considering the following keywords: "glucose," "sensors", "electrochemical. .....27
**Figure 2.2**: Materials used in electrochemical biosensors. .....28
**Figure 2.3:** Schematic representation of enzymatic glucose oxidation mechanisms for the three different generations of biosensors. .....30
**Figure 2.4:** Preparation steps of a glucose biosensor using a micro disk array electrode. (1) single disk array electrode, (2) surface magnification, (3) cysteamine modification of the Au surface, (4) CQDs/AuNPs adhered surface, (5) $GO_x$ immobilisation to the surface *[143]*.....35
**Figure 2.5:** Schematic representation of the surface modification of Pb/Pt nanocubes using chitosan and covalent immobilisation of GOx [136]. .....38
**Figure 2.6:** (a) Schematic representation of the ETC, which performs HA penetration, glucose refiltration, and glucose outward transportation (left image), and thin, flexible, and biocompatible paper battery attached to the skin surface for ETC measurement (right image) *[161]*; (b) Representation of the glucose biosensor on the PETG mouthguard support. Pt and Ag electrodes were formed on the PETG using a sputtering process. 30 units of $GO_x$ were applied to the sensing region of the working electrode *[162]*. .....39
**Figure 2.7:** Cyclic voltammetry graph displaying three potential regions where glucose is electro-chemically oxidised at a Pt electrode [159].....42
**Figure 2.8**: Trend in Shape Morphing Polymers publications by decade.....52
**Figure 2.9:** Subclasses of shape morphing polymers: (a) shape memory polymers, (b) shape changing polymers. .....53
**Figure 2.10**: Activation energy requirements for SMEs and SCPs, where H is the energy barrier for the shape memory effect, and H' is the energy barrier for the shape changing effect. (a) Shape memory-effect: the material beginning in State A (original shape) and can go to state B (temporary shape) when the appropriate stimuli supply enough energy to overcome the energy barrier H and load. (b) Shape changing effect: the material beginning in State A' (original shape) can go to State B' (temporary shape) when the appropriate stimuli supplies enough energy to overcome the energy barrier H'. .....54
**Figure 2.11**: Orthogonal (i), and sequentially (ii) coupled functions.....55
**Figure 2.12**: Smart multi-responsive hydrogel-based drug delivery system.....55
**Figure 2.13:**Active segments and crosslinks found in different types of SMPs .....57
**Figure 2.14:** Classification of shape-memory polymers based on the stimuli they are responsive to .57
**Figure 2.15**: Different classes of thermo-responsive polymers .....58
**Figure 2.16**:Thermo-responsive SMP highlighting shape changing behaviour: (a) Cold state: at equilibrium the part is in its original shape, (b) Hot state: increase in temperature will activate the shape morphing effect into the temporary shape .....59
**Figure 2.17**: Activation scheme for light responsive polymers [311].....60
**Figure 2.18:**IEAP mechanism (Left), EEAP-Intrinsic (middle), and EEAP-Extrinsic (right). .....61

**Figure 2.19**: Different magnetic states diamagnetic, paramagnetic, ferromagnetic, (d) ferrimagnetic, and antiferromagnetic [156] .....63
**Figure 2.20**: The effect of pH changes on pH-responsive hydrogels [158] .....64
**Figure 2.21:** Shape morphing of PU nanocomposite during wetting/drying cycle [165] .....65
**Figure 2.22**: 4D printing techniques used for shape morphing polymers, (a) ME, (b) Vat photopolymerization, and (c) MJ.....66
**Figure 3.1**: Wheat rust cycle [421] .....71
**Figure 3.2**: Schematic for the reaction between invertase and sucrose .....72
**Figure 3.3**: Second layer consisting of 50/50 sucrose/agar mixture .....73
**Figure 3.4**: SEM image of a hydrated wheat leaf .....75
**Figure 3.5**: Leaf surface mould .....75
**Figure 3.6**: Solidworks model for the leaf surface mould .....76
**Figure 3.7**: SPE with drop casted Pt-Ni/MWCNT composite on the surface.....77
**Figure 3.8:** CV graph showing the response of the drop casted sensor to glucose .....77
**Figure 3.9**: Inoculation results (a) agar patterned surface with 96% germination, (b) PCL patterned surface with 80% germination.....78
**Figure 3.10:** PETG membrane shape recovery process (a) original membrane shape, (b) deformed membrane, (c) recovered membrane shape.....79
**Figure 4.1**: The 3D printing system.....82
**Figure 4.2:** Dimensions of the dog bone structures. All dimensions in mm. .....83
**Figure 4.3:** PETG MALDI-TOF MS spectrum.....85
**Figure 4.4:** Shaper recovery for PETG using different recovery cycles, (a) Original (non-deformed) shape, (b) recovered structure after 1 cycle, (c) recovered structure after 5 cycle, (d) recovered structure after 10 cycle.....87
**Figure 5.1:** The Matrix-assisted laser desorption/ionization time-of-flight mass spectrometry (MALDI: -TOF MS) TOF MS) spectrum of Polyethylene terephthalate glycol modified (PETG). Its characteristic repeated units are highlighted: 192.8 g/mol for the Terephthalic acid + Ethylene Glycol (TPA + EG) unit and 274.3 g/mol for Terephthalic acid + Cyclohexanedimethanol (TPA + CHDM). .....95
**Figure 5.2:** (a) Top view of a polycaprolactone (PCL) scaffold, (b) cross-section view of a PCL scaffold, (c) top view of a Polyethylene terephthalate glycol modified (PETG) scaffold, (d) cross-section view of a polyethylene terephthalate glycol modified (PETG) scaffold. All scaffolds were designed considering a pore size .....96
**Figure 5.3**: Stress vs. strain curves for PCL scaffolds and PETG scaffolds with different pore sizes. ....97
**Figure 5.4**: Compression modulus for the PCL scaffold and PETG scaffolds with different pore size. *** p < 0.001 compared with control (PCL), ## p < 0.01 and ### p < 0.001 compared with different pore size. The *** Statistical evidence (p < 0.001) is the one-way analysis of the mechanical compression test with the use of GraphPad Prism software, and it is used to show the difference be-tween the results. The * is small difference and while more * are added the differences between the results are higher. * compared with PCL scaffolds, # compared with different pore size of PETG scaffolds. Trabecular bone Figure 4. Compression modulus for the PCL scaffold and PETG scaffolds with different pore size. *** p < 0.001 compared with control (PCL).....97
**Figure 5.5:** Compression strength values for the PCL scaffold and PETG scaffolds with different pore size. *** p < 0.001 compared with control (PCL), ## p < 0.01 and ### p < 0.001 compared with different pore size. The *** Statistical evidence (p < 0.001) is the one-way analysis of the mechanical compression test with the use of GraphPad Prism software, and it is used to show the difference be-tween the results. The * is small difference and while more * are added the differences between the results are higher. * compared with PCL scaffolds, # compared with different pore size of PETG scaffolds. .....98

**Figure 5.6:** Alamar Blue results for both PCL and PETG scaffolds at days 1, 7 and 14 post-cell-seeding. * Statistical evidence (p < 0.05) analysed by one-way analysis of variance (ANOVA) and Tukey's post-test. The * Statistical evidence (p < 0.05), **, *** is the one-way analysis of variance (one-way ANOVA) and Tukey's post hoc test with the use of GraphPad Prism software and it is used to show the difference be-tween the results. The * is small difference and while more * are added the differences between the results are higher. .....99
**Figure 5.7**: Cells on PETG-350 scaffolds after 14 days of cell seeding. (a) Top view image of the PETG scaffold, (b) cross-section image of PETG scaffold, (c) magnified image showing cells covering the PETG filament, (d) cells bridging adjacent lay.....100
**Figure 6.1**: Preparation process for the photoactive layer .....105
**Figure 6.2**: Preparation process for the thermoresponsive PETG/PVC layer.....105
**Figure 6.3**: SEM image of PVC-PETG layer produced presenting the dual phase nature of the material .....107
**Figure 6.4**: Raman spectra (red) 60/40 split and (black) 50/50 split.....108
**Figure 6.5**: FTIR spectra (red) 60/40 split and (black) 50/50 split .....109
**Figure 6.6**: Responses of the produced photoactive layers at different time points. 10 wt% of azobenzene (a, d, g, j); 30 wt% of azobenzene (b, e, h, k); and 50 wt% of azobenzene (c, f, i, l). .....111
**Figure 6.7**: Shape recovery of (a) 50/50 PETG/PVC split, and (b) 60/40 PETG/PVC split.....111
**Figure 7.1**: Electrospinning setup .....116
**Figure 7.2**: Solubility–spinnability map of PETG based on the Teas graph. The contoured region presents the solvents that can dissolve PETG, forming a homogenous solution. .....118
**Figure 7.3:** SEM image of the electrospun PETG meshes using different solvent splits (DCM/TFA) (a) 85/15, (b) 70/30, (c) 60/40, (d) 50/50, (e) 40/60, (f) 30/70, (g) 15/85. x1000 magnification. .....120
**Figure 7.4**: FTIR spectra of electrospun PETG meshes using different solvent splits (DCM/TFA). .....122
**Figure 7.5**: Figure 4: RAMAN spectra of electrospun PETG meshes using different solvent splits (DCM/TFA). .....122
**Figure 7.6**: (a) SEM image of *P. s. f. sp. tritici* spores (X100) at 0 hours of inoculation, (b) SEM image of *P. s. f. sp. tritici* spores (X200) after 24 hours, (c) SEM image of the germinated *P. s. f. sp. tritici* spores (X500), ), (d)) SEM image of the germinated *P. s. f. sp. tritici* spores (X2000). .....123
**Figure 8.1**: (a) Schematic representation of early infection structures of Puccinia striiformis. The spore germ tube enters the leaf through the stomata forming a substomatal vesicle from which infection-hyphae develop. Once the hyphae contact the mesophyll cell a haustoria is formed inside the plant cell. (b) Transverse section of a plant leaf showing the different layers of the leaf. .....127
**Figure 8.2**: Most plant volatiles are derived from four biosynthetic classes: aromatics, fatty acid, terpenoids, and amino acids. Volatiles are produced from fatty acids via oxidative cleavage. Several of these products are modified to be more lipophilic prior to release, through masking or removing of hydrophilic functional groups through methylation, or reduction reactions. Figure modified from [34]. .....128
**Figure 8.3**: Operational rationale of proposed yellow rust biosensor. The signal can be obtained directly as a CV curve indicating the presence of glucose and therefore yellow rust. .....130
**Figure 8.4**: 3D model of the designed biomimetic leaf surface .....131
**Figure 8.5**:(a) Printed mould, (b) optical microscope image presenting the details of the printed model .....131
**Figure 8.6:** Schematic of the Screen-Printed electrode. WE: working electrode, CE: counter electrode, RE: reference electrode. .....132
**Figure 8.7:** (a) SEM image of the casted biomimetic PETG layer. The created parallel venation mimics the wheat leaf with a width of 200 µm. The detailed, zoomed SEM image shows a stomatal hole with a diameter of 50 µm with an opening of 15 µm, (b) SEM images of the Au-Ni/AC modified screen-

printed electrode, presenting two distinct regions. The zoomed SEM image clarifies the two regions where the carbon bed presents a Nano-porous structure allowing glucose to flow, and the top region, a cotton-like nanostructure consisting of Au-Ni particles (c) AFM image of the Au-Ni/AC modified screen-printed electrode exhibiting cylindrical round cap columns with channels allowing glucose to pass through. .....135
**Figure 8.8:** CV curve of the Au-Ni/AC modified screen-printed electrode using NaOH as a buffer. The red curve corresponds to NaOH without glucose. The blue curve corresponds to NaOH in the presence of glucose. From the blue curve it is possible to observe the oxidation peaks at peak A (-0.27V), peak B (0.22V), peak E (0.53V), peak D (0.66V), and a reduction peak at peak C (0.04V).....138
**Figure 8.9:** CV curves without a buffer (NaOH). The blue curve represents the response to 5 mM glucose. The red curve represents the response to 5 mM sucrose**.** .....138
**Figure 8.10:** Current–time responses at 0.66 V with an increasing glucose concentration. .....139
**Figure 8.11:** Calibration curve of the current versus different glucose concentrations (1 to 10mM)139
**Figure 8.12:** Nyquist plots for Au-Ni/AC SPE in 0.1 M NaOH solution for 0–10 mM of Glucose concentration range. .....140
**Figure 8.13:** CVs of Au-Ni/AC SPE after 1, 25 and 50 times of amperometric tests in 5 mM Glucose in 0.1 M NaOH. .....140
**Figure 8.14**: Au-Ni/AC X-ray diffraction analysis. The peaks represent the different materials present on the surface of the electrode. Au (111) at 38.6o, Au (200)-Ni (111)/AC (100)(101) at 43.7o, Ni (200) at 50.8$^{o}$, Au(311)-Ni (220) at 74.4$^{o}$, Ni (311) at 90.2$^{o}$, and Au (400)-Ni (222) at 95.4$^{o}$.....141
**Figure 8.15:** (a) Biosensor assembly, (b) top surface of biosensor inoculated with spores, (c) underneath surface of the top layer of the biosensor showing a germinated *P. s. f. sp. tritici* spore, (d) CV curve obtained at 24 hours, (e) CV curve obtained after 72 hours, (f) SEM image of *P. s. f. sp. tritici* spores and a germ tube growth on the surface of the biosensor. .....143

# List of Tables

**Table 2.1**: Common definitions of smart materials. ..... 50
**Table 2.2:** Relevant properties of shape morphing alloys and polymers [35, 36] ..... 51
**Table 4.1**: Fabrication parameters ..... 83
**Table 4.2**: PETG Chemical components ..... 85
**Table 4.3**: Mechanical properties of PETG ..... 86
**Table 5.1**: Scaffold printing parameters ..... 92
**Table 5.2**: Chemical constituents for PETG ..... 95
**Table 5.3**: Compressive Mechanical Properties ..... 98
**Table 7.1**: Average fibre diameter based on the solvent split ..... 121
**Table 8.1:** Printing parameters ..... 131
**Table 8.2**: List of common wheat diseases and their agents, indicating invertase production based on their genomic make up ..... 142

# List of Abbreviations

| | |
|---|---|
| 3D | Three Dimensional |
| 4D | Four Dimensional |
| ASTM | American Society for Testing and Materials |
| DMAB | 4-(Dimethylamino)pyridine |
| DMF | Dimethylformamide |
| DMSO | Dimethyl Sulfoxide |
| EG | Ethylene Glycol |
| FTIR | Fourier Transform Infrared Spectroscopy |
| GCRF | Global Challenges Research Fund |
| hASCs | Human Adipose-Derived Stem Cell |
| $H_2O$ | Water |
| $H_2O_2$ | Hydrogen Peroxide |
| HPLC | High Performance Liquid Chromatography |
| MALDI-TOF | Matrix-assisted Laser Desorption/Ionization Time-of-Flight |
| min | Minutes |
| Mm | Millimetre |
| MPa | Mega Pascal |
| PBS | Phosphate Buffered Saline |
| PCL | Poly-ε-caprolactone |
| PET | Polyethylene Terephthalate |
| PETG | Polyethylene Terephthalate Glycol |
| SEM | Scanning Electron Microscope |
| TPA | Terephthalic Acid |
| VoCs | Volatile compounds |
| Uv | Ultraviolet |
| XRD | Electron Dispersive X-ray Spectroscopy |
| μL | Microlitre |
| μm | Micrometre |

# Abstract

This interdisciplinary research project addresses the design and development of a multilayer and multi-material 3D printed leaf biosensor that enables the instantaneous on-site detection of Puccinia striiformis. The main challenge with the detection of this disease is that it can only be visually detected on the leaf surface after 14 days of infection, by when it's too late for the use of fungicide, resulting in a significant yield loss. The objective of this research project is to develop an innovative and compact biosensor using advanced materials and additive manufacturing (3D Printing) allowing the early detection of *Puccinia striiformis f. sp. tritici* in the field enabling fast countermeasures to be taken.

The biosensor will consist of 3 layers. The first layer will mimic the top layer of the leaf which is the cuticle layer that covers the leaf. The second layer consists of a sucrose/agar mixture to act as a substrate and growth cue. The third layer will consist of a nonenzymatic glucose sensor that produces a signal once the *Puccinia striiformis f. sp. tritici* invertase gets in contact with the second layer and produces glucose.

# Declaration

I declare that no portion of the work referred to in the thesis has been submitted in support of an application for another degree or qualification of this or any other university or other institute of learning.

# Copy right statemnt

# Acknowledgments

I would like to express my gratitude to my supervisor Professor Paulo JDS Bartolo, who has supported and helped me through my whole PhD with patience and knowledge. Without his guidance and help this thesis would be impossible.

I would like to express my gratitude to my co-supervisors Professor Bruce Grieve from the School of EEE for his help and support during my study and his valuable guidance for my research. I would also like to thank the lab members Dr. Fengyuan Liu, Dr. Cian Vyas, Dr. Boyang Huang, Dr. Evangelos Daskalaksi and Abdalla Omar for their help, and support during the PhD, who helped me to go through the trainings required for my PhD experiments.

Finally, I would like show my greatest gratitude, and thank to my parents, for their support and sacrifices during my whole period of studies, giving me the chance to pursue my dream no matter how much it burdens them.

Mohamed Hassan

University of Manchester

2022

# Chapter 1: Introduction

## 1.1. Background

Wheat Stripe rust is a disease that mainly affects *Triticum aestivum* (common wheat). The disease is caused by a fungus called *Puccinia striiformis* f. sp. *tritici*. This type of fungus can infect host plants hundreds of kilometres away from the source plant. Stripe rust is the most common type of the three Rust types (leaf, strips and stem rust) [1, 2]. The pathogen growing temperature is between 7 and 22 ºC, being particularly active in the fertile crescent of the Middle East, and Europe [3-6]. This type of rust does not affect the grain quality but causes yield loss by lowering the number of kernels and/or resulting in lighter kernels [3, 7, 8]. The disease has been increasingly occurring as an epidemic across Europe, Africa, East Asia [9-11].

Common wheat is one of the most staple foods for about 40% of the world population [7]. Wheat is used in so many food products around the world and with the world population increasing and food security becoming more critical, wheat yield potential has a very high priority in the developing world [7]. The world leading producers are European Union, China, India, Russia, and Ukraine. Global warming and the current war in Ukraine have affected and will impact the production of the global wheat production. Significant disruptions in the supply chain have been reported by the media affecting, in particular, poor countries in Africa and Asia. In the current context, the epidemic caused by *Puccinia striiformis f. sp. tritici* (*P. s. f. sp. tritici*) (Figure 1.1a), a widespread pathogen, may have more serious consequences for the world population affecting food scarcity [2]. This raises the need for a fast and efficient pathogen detection system with the objective to reduce yield loss and to mitigate the impact of the increase food demand.

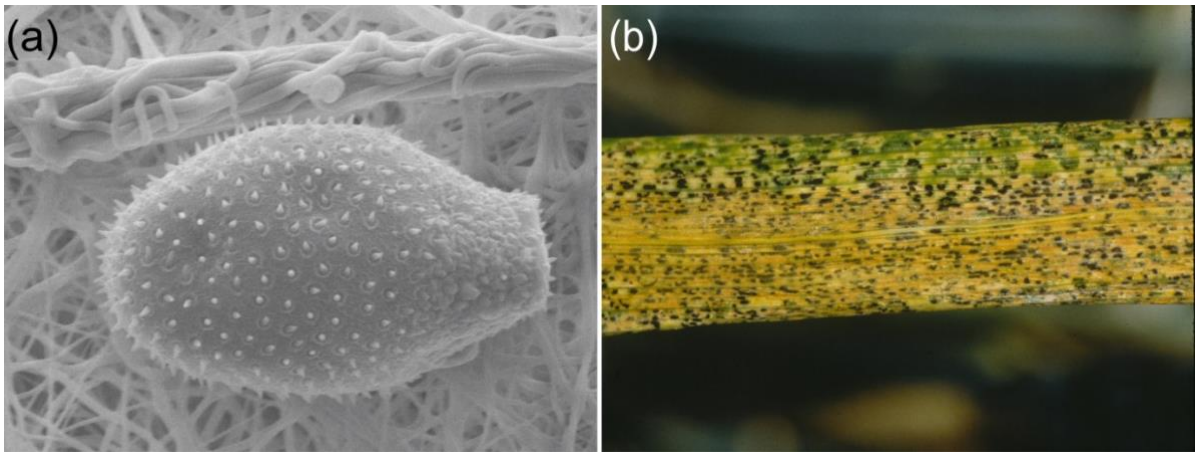


**Figure 1.1**: (a) Yellow rust fungi (*Puccinia striiformis f. sp. tritici*) spore, (b) infected wheat leaf after 14 days.

Stripe rust or yellow rust is caused by *Puccinia striiformis* (Figure 1.1b). It is a disease that infects cereal crops, barley wheat and wild grasses [12]. The disease appeared hundreds of years ago and was intensively studied in the last 120 years. The first monograph on the yellow rust was written by Hassebrauk and Röbbelen between 1965 and 1975 in German [12-15]. Part of the monograph was then revised and translated to English by Röbbelen and Sharp in 1978 [16]. In 1992, Line and Qayoum summarised the virulence, evolution, distribution and aggressiveness of stripe rust in North America [17]. Finally, in 2017 Chen and Kang published a book focusing on research and control of stripe rust [18].

Yellow rust symptoms take days to months to fully reach the diseased stage. The yellow rust life cycle is presented in Figure 1.2. First, the urediniospores of yellow rust lands on the surface of the wheat leaf. In the first 3 hours after landing, the spores absorb the moisture on the leaf's surface and germinate, growing a germ tube guided towards the stomata of the leaf. Between 6 to 8 hours post germination the germ tube grows between the guard cells of the stomata. After 8 to 12 hours a sub stomatal vesicle is formed inside the stomatal cavity. Finally, within 12 to 18 hours, a primary infection hypha develops in the sub stomatal vesicle. At this point the infection is not detectable by the naked eye but can be observed under the microscope. The yellow-coloured patches from the disease appear on the leave after 6 to 7 days depending on the environmental temperature. The udredinia or pustules appear from the patches between 11 to 14 days post infection. Uredinia are small, elongated, and yellow to orange in colour, and shortly burst after forming releasing yellow rust spores to the atmosphere. These spores are too small to be detect by naked eyes but can be seen as yellow/orange powder. A number of studies suggested that *P. s. f. sp. tritici* produces its own invertase, being required to aid nutrition uptake of the pathogen, by converting sucrose to glucose and fructose [19, 20]. Moreover, yellow rust leads to an increase in the reactive oxygen species in the infected plants, hence reducing the plant's overall photosynthetic efficiency leading to yield loss [21].

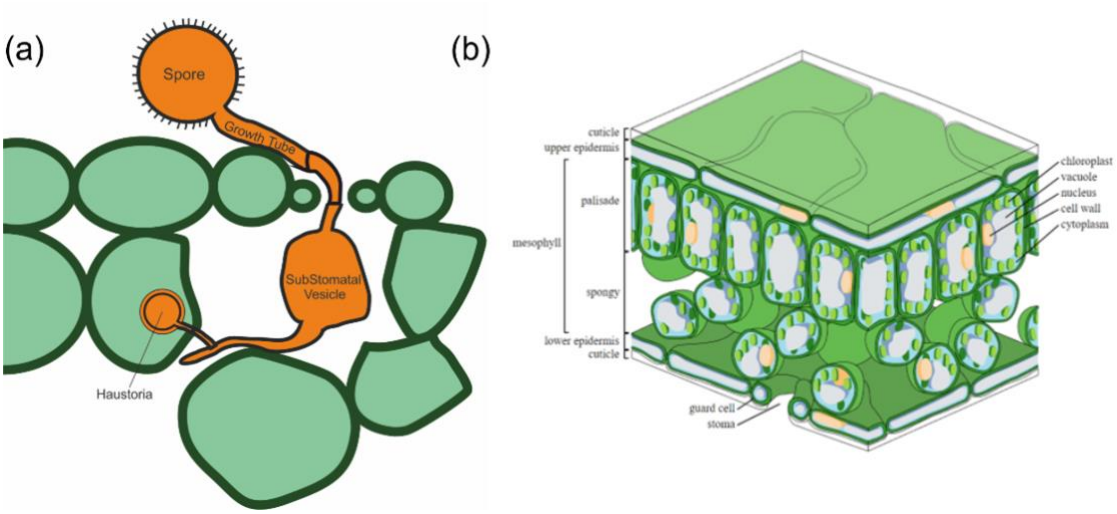


**Figure 1.2:** (a) Schematic representation of early infection structures of Puccinia striiformis. The spore germ tube enters the leaf through the stomata forming a substomatal vesicle from which infection-hyphae develop. Once the hyphae contact the mesophyll cell a haustoria is formed inside the plant cell. (b) Transverse section of a plant leaf showing the different layers of the leaf.

Stomata are pores on both sides of the leaf, and part of a stoma complex consists of a pore with guard cells on each side along with two to four subsidiary cells. The stomata main role is to control water vapour and gas exchange between the leaf interior and the outside air [22, 23]. The surface of the leaf is covered by a hydrophobic, translucent layer called cuticle. Its main role is to provide protection against dehydration and external environmental stresses [24, 25]. The cuticle (Figure 1.3), has a network structure, consisting of a covalently linked cutin macromolecular mesh containing a polyester like biopolymer made up of hydroxyl epoxy and hydroxyl fatty acids, and a range of organic solvent soluble lipids called waxes, and sometimes cutan which is made up of polyethylene chain or another polymer called lignin [23, 24].

Current strategies for yellow rust management are based on the use of genetically resistant wheat varieties and fungicide applications as part of an Integrated Pest Management scheme [26, 27]. However, a major drawback of these approaches is the potential of the pathogen to mutate, leading to the development of new races capable of overcoming the resistance [28, 29]. In addition, the timing of fungicide application is critical for treatments to be effective. Moreover, the overuse of fungicides can also lead to the appearance of new strains of the fungus with enhanced resistance to the fungicide [28, 30, 31].

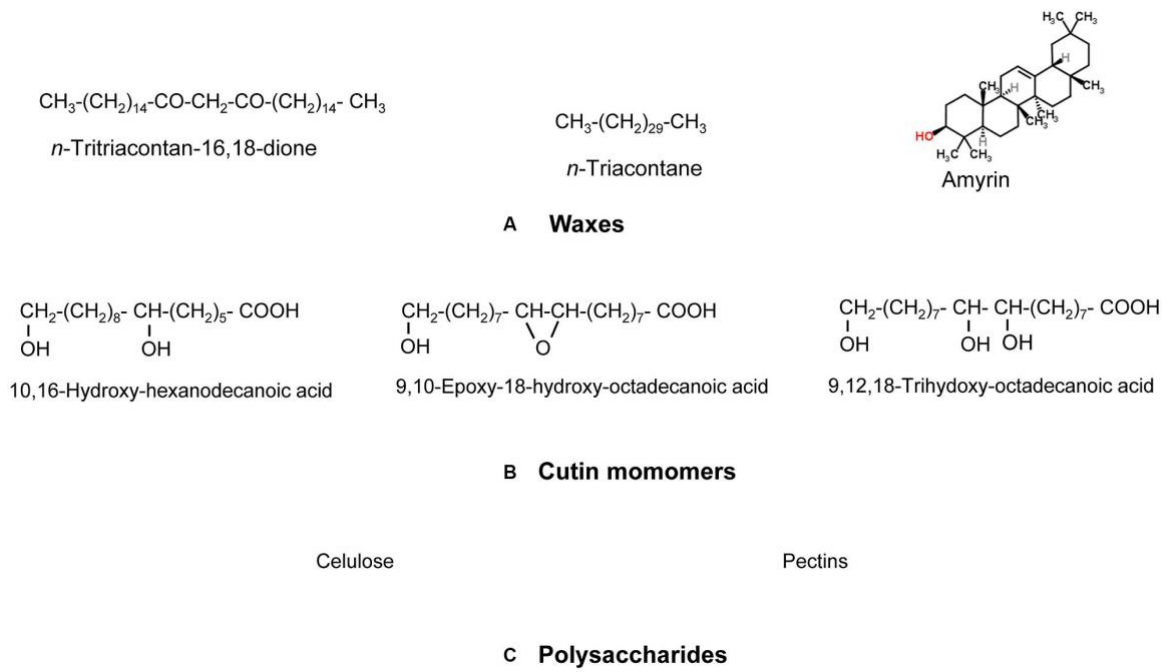


Figure 1.3: Plant cuticle chemical representation [40].

As previously mentioned, the main problem with stripe rust disease is that it can be visually detected only after 14 days of infection which is by then too late for the use of any fungicide resulting in a significant loss of yield [3, 7, 8, 32, 33]. To address this problem, this research work aims to develop a novel biosensor using advanced materials and additive manufacturing to detect the infield presence of the stripe rust pathogen, reducing detection time, as well as detecting the infection at a very early stage allowing for counter measures to be taken. The proposed design of the biosensor is shown in Figure 1.4.

To be effective, the surface the biosensor must mimic the surface of the wheat leaf including the stomata positioning as well as its opening and closing mechanism, as the stomata controls the release of volatiles (VOCs), which mainly consist of terpenoids, fatty acids, amino acids, and compounds with aromatic rings [34]. These VOCs help to protect the plant by acting as information carriers being an important cue for fungal germination [33]. This mimic behaviour can be achieved by using smart materials (see Section 2.2) able to change their shape based on an environmental cue [22, 23].

Generally, the use of biosensors for agricultural applications, such as the one proposed by this research, is a fundamental element of a novel strategy called as Agriculture 4.0, based on the use of digital tools and technologies to increase farming efficiency, reducing food waste and the effects of climate change [35]. The biosensor is aimed toward usage in low-income countries and small-scale farmers, hence, additive manufacturing provides a suitable compromise between cost and manufacturing capabilities required. Furthermore, additive

manufacturing, specifically extrusion-based manufacturing, is becoming more available with an extensive cost reduction and large range of printing material.

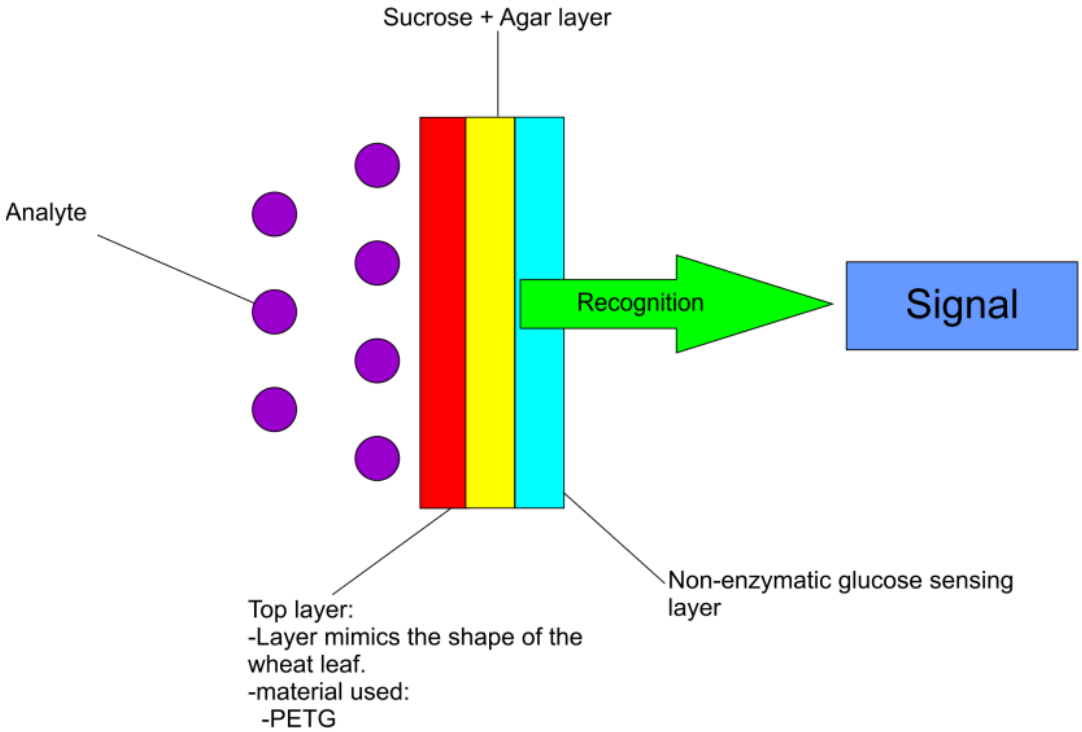


Figure 1.4: Proposed biosensor design.

### 1.2. Research Aim and Objectives

The main aim of this research is to develop a novel 3D printed "leaf biosensor" that enables the instantaneous on-site wheat stripe rust detection. To achieve this aim, the project will comprise four main stages. The first stage will focus on the identification of the most relevant factors that promote germination and the growth of wheat stripe rust infecting spores. This will be achieved through lab investigation of the germination and the growth of the germ tube of the pathogen wheat-infecting spores under different conditions, and by analysing how different factors (e.g., humidity, plant volatile) can affect these variables. The second stage will focus on the material selection. Different materials will be tested to identify the most suitable material to promote germination and germ tube growth of the pathogen, wheat-infecting spores. Moreover, the material surface must be easily imprintable allowing the mimicry of real leaf surface topology recognisable by the pathogen infecting-spores. The third stage will focus on the development of a wheat stripe rust (yellow rust) specific sensing chemistry to be used as the bio-sensing element of the biosensor. Finally, the fourth stage will correspond to the validation of the biosensor performance under lab conditions.

The proposed new biosensor comprises three layers and uses the invertase produced by the spores as an analyte. The role of the first layer is to mimic the leaf top surface providing the needed topological germination cue, the second layer will contain sucrose which is the main substrate consumed by invertase (the target analyte), and finally the third layer is a glucose sensing layer which is the by product that results from the redox reaction between sucrose and invertase.

This is a multidisciplinary research work covering a wide range of fields, such as mechanical engineering (manufacturing), polymer science and biotechnology. Key research objectives can be listed as follows:

- To develop a better understanding on plant biology, biosensors, and smart materials through an extensive literature review (**objective 1**).
- To develop a novel functional biosensor able to detect stripe rust pathogen (**objective 2**). The biosensor will be tested under lab conditions.
- To understand the key topological cues responsible for stripe rust infecting-spores germination and germ tube growth (**objective 3**). Stripe rust is an obligate parasite that is hard to grow on artificial media since it requires cues to identify and grow on the plant leaf surface.
- To identify suitable biocompatible materials that promote fungal infecting-spore germination and growth of germ tubes (**objective 4**). The fungus grows using topological cues and one of these cues seems to be the surface wetness that depends on the material type. Moreover, the material should be biodegradable avoiding any negative environmental impact.
- To identify and produce fungus specific detection mechanism capable of identifying the presence of *Puccinia striiformis* (**objective 5**). This mechanism will be designed to detect certain enzymes produced by the fungus during the growth process. These enzymes interact with a specific substrate in the sensor where the reaction will be used as a detection signal for the presence of the target pathogen.

### 1.3. Structure

This thesis comprises nine chapters, which progress in accordance with the identified research objectives, describing the work conducted. The first chapter comprises an introduction that, in addition to listing the research aim and key research objectives, also briefly describes the context of the research. The contents of the remaining chapters are summarised below.

**Chapter 2**: **Literature review -** this chapter consists of two sections. The first section introduces the concept of glucose biosensors, discussing different working principles, types, applications, trends, and research challenges. The second section introduces the concept of smart materials, specifically shape changing materials (SCP), and the concept of 4D printing.

**Chapter 3**: **4D printing of bioinspired leaf sensor surface -** this chapter discusses preliminary studies on the topological cues to promote fungal growth on the surface of the biosensor and describes the multi-material and multi-functional biosensor considered in this research. Different candidate materials for the fabrication of the biosensor are considered.

**Chapter 4: Chemical and compositional analysis of PETG for 4D printing applications -** this chapter investigates the potential use of PETG as a shape memory polymer (SMP). A full characterization analysis of PTEG is presented, including mechanical analysis, chemical analysis, printability, and shape recovery behaviour. Shape recovery behaviour is assessed using cyclic thermomechanical experiments where stress and temperature are controlled during the programming and recovery processes. A stress strain graph was obtained leading to the determination of shape fixity ratio and shape recovery rate.

**Chapter 5**: **The potential of Polyethylene Terephthalate Glycol (PETG) as a biomaterial for tissue engineering** - This chapter investigates the potential of PETG, a shape changing material as discussed in Chapter 3, to support cell attachment and proliferation assuming that PETG is used to produce bone scaffolds using a filament-based additive manufacturing. Scaffolds were produced considering different pore sizes. Scaffolds were seeded with human adipose derived stem cells (hADSCs) and the cell metabolic activity determined using the Alamar Blue assay.

**Chapter 6: Smart Polyethylene terephthalate glycol (PETG)** – This chapter investigates the incorporation of photochromic molecules such as azobenzene to produce a photoactive material that can respond to UV light by changing shape and regaining its original shape in the dark. The resultant material was designed with the intent of producing bioinspired functional surfaces. Moreover, PETG was also mixed with Polyvinyl chloride (PVC) to fabricate a thermo-responsive material that can respond to temperature changes. The produced material was designed with the intent of incorporating in pathogen detection sensors, where the material simulates the morphology and functionality of a leaf surface.

**Chapter 7: Electrospinning polyethylene terephthalate glycol (PETG) meshes** – This chapter investigate the use electrospinning to create PETG electrospinning meshes. However, PETG is a difficult to spin material and no previous papers reported the correct conditions to create PETG meshes. To address this issue, a preliminary study on the solubility and

electrospinnability of PETG using a range of solvent systems was conducted and a Teas graph was established allowing to select the ideal solvent system. Produced meshes were extensively characterised and the results demonstrate for the first time the ability of PETG electrospun meshes to support the inoculation and germination of yellow rust spores, thus confirming that PETG is an ideal material to be used in the proposed biosensor (see Chapter 1).

**Chapter 8: Novel multi-layer biosensor for pre-symptomatic detection of Puccinia strifformis, the causal agent of yellow rust** – this chapter, which consolidates the knowledge generated in the previous chapters, describes the overall biosensor design, consisting of three different layers, and the fabrication process. The first layer mimics the wheat leaf surface morphology. The second layer consists of a sucrose/agar mixture that acts as a substrate and contains a wheat-derived terpene volatile organic compound that stimulates germination and growth of the spores of the yellow rust pathogen *P. s. f. sp. tritici*. The third layer consists of a nonenzymatic glucose sensor that produces a signal once invertase, produced by P. striiformis, comes into contact with the second layer, converting sucrose to glucose. Results show for the first time that the developed biosensor enables the detection of viable yellow rust spores in 3 days.

**Chapter 9**: **Conclusion and future work** – this chapter outlines the key results and achievements of the thesis and proposes future research directions.

# Chapter 2: Literature review

*This Chapter, comprising two sections, reviews the current state-of-the-art of the research domains covered by this dissertation. The first section discusses the mechanisms of electrochemical glucose sensing with a focus on the different generations of enzymatic-based sensors, their recent advances, and provides an overview of the next generation of non-enzymatic sensors. Advancements in manufacturing techniques and materials are key in propelling the field of glucose sensing, however, significant limitations remain which are also highlighted. The second section discusses the concept of 4D printing, key additive manufacturing technologies and a classification of smart materials. The mechanism beyond the material response to different stimuli is discussed in detail.*

## 2.1 Recent advances in enzymatic and non-enzymatic electrochemical glucose sensors♣

### 2.1.1 Introduction

Glucose detection is an important factor in the food, beverage, and fermentation manufacturing sectors as well as in the medical sector. The increased sugar consumption in people's diet is related to many chronic health problems including cardiovascular diseases (including heart failure, stroke or heart attack), type 2 diabetes, sleep apnea, metabolic syndrome, and obesity [36, 37]. Diabetes mellitus is a chronic condition that results in systemic and metabolic disorders. In 2019, diabetes affected 463 million people worldwide, was responsible for 1.5 million deaths, and the number of diabetic patients is expected to increase to 700 million by 2045 [38]. Moreover, diabetes is associated with other pathologies such as the risk of blindness, kidney failure, nerve damage, and heart problems [39]. Therefore, diabetic patients need to accurately determine their glucose blood level not just at the diagnosis stage but in all stages of treatment and disease management, and the use of non-invasive and rapid glucose level testing methods is critical [40-43]. Consequently, the food, beverage and fermentation manufacturing sectors are under pressure to reduce and control the level of sugar whilst maintaining the quality and safety of ingredients. This requires monitoring and measuring all analytes such as sugars, phenols, and alcohols throughout the manufacturing process and in the final product [37, 44].

In the last decade, the demand for glucose detection and monitoring systems significantly increased. This is reflected in the increased number of publications related to glucose sensors, illustrated in Figure 2.1. Glucose sensors comprise optical and electrochemical sensors. Optical

♣ This section is based on the following publication: Mohamed Hassan, Cian Vyas, Bruce Grieve, Paulo Bartolo – "Recent advances in enzymatic and non-enzymatic electrochemical glucose sensing", Sensors, 21, 4672, 2021. Mohamed Hassan main contributions: data collection, data analysis, writing and reviewing the manuscript.

glucose biosensors, encompassing different optical methods such as fluorescence, absorptiometry, and surface plasmon resonance (SPR) [41, 45-50], use fibre optics to detect analytes using absorption, illumination, light scattering or refraction principles [51]. Optical biosensors have many advantages including remote sensing, low cost, electrical interference-free, and fast response time in comparison to normal test methods [52]. However, these sensors also present several disadvantages such as interference from surrounding light, the need for high-energy light sources, and limited concentration range, which limit their use [53].

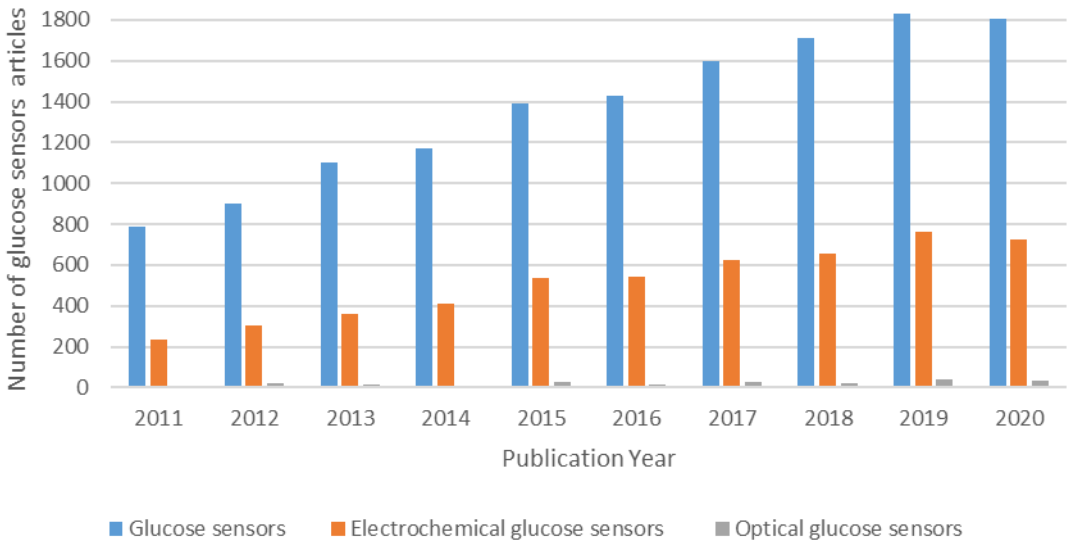


**Figure 2.1**: Number of glucose sensor related articles published in the past 10 years. The search was conducted using the Web of Science (Clarivate Analytics, Philadelphia, PA, USA) database considering the following keywords: "glucose," "sensors", "electrochemical.

Electrochemical sensors, mainly based on amperometric methods, represent the most relevant group of glucose biosensors, and comprise enzymatic and non-enzymatic sensors. Non-enzymatic amperometric glucose sensors are based on the direct electrochemical oxidation of glucose. A wide range of materials has been used in both enzymatic and non-enzymatic glucose biosensors (Figure 2.2) such as conductive polymers, enzymes, carbon nanotubes, and molecularly imprinted polymers (MIPs). MIPs mimic enzymes by creating polymeric crosslinked active sites for specific analytes, predominantly used in optical sensing they have been explored in recent years in electrochemical glucose sensing; however, they are out of the scope of this review [54-56]. Noble metals and their composites have been used specifically as the electrode materials for non-enzymatic sensors due to their high electrocatalytic activity, and high sensitivity to the electrooxidation of glucose [57-60]. The principle behind nonenzymatic glucose sensors was first reported by Walter Loeb [61] who observed a direct electro-oxidation of glucose in sulfuric acid-producing gluconic acid at a lead (Pb) anode.

Direct electro-oxidation [62] and electroreduction [63] of glucose in alkaline (pH > 11) and acidic (pH < 2) solutions have also been investigated. The major problem faced by non-enzymatic glucose sensors is the absorption of glucose oxidation intermediates (e.g., CO) or solution active species (e.g., Cl−) which can lead to blockage of electrode activity for direct glucose electro-oxidation [64]. Furthermore, non-enzymatic amperometric glucose sensors suffer from a lower selectivity compared to enzymatic amperometric glucose biosensors due to the difficulty faced by the electrocatalytic materials to specifically catalyse glucose oxidation. However, non-enzymatic amperometric glucose sensors present long-term stability, which is the main drawback of the enzymatic biosensors due to the inherent nature of enzymes.

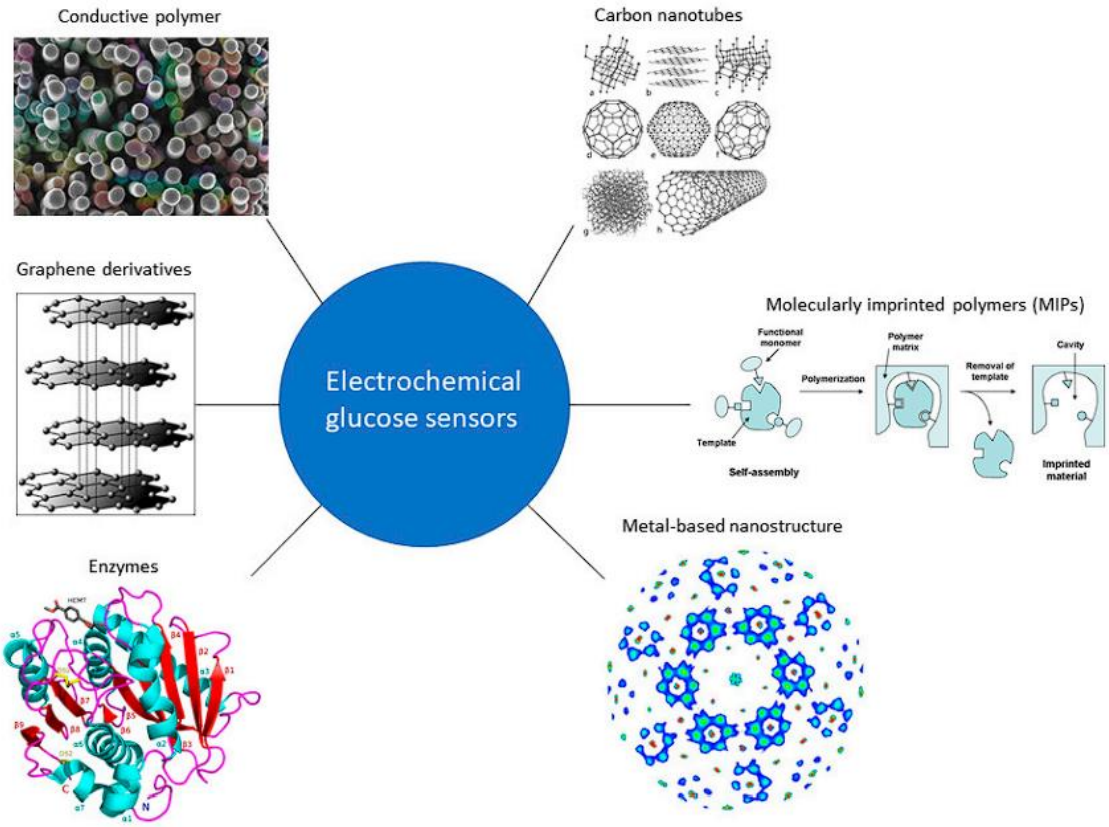


Figure 2.2: Materials used in electrochemical biosensors.

The principle behind enzymatic amperometric glucose sensors was proposed by Clark and Lyon [65] in a patent describing the use of enzymes for converting electroinactive substrates into electroactive products. Clark [66] also designed the first enzymatic amperometric glucose sensor by immobilising glucose oxidase ($GO_x$) on a platinum (Pt) electrode. Since these preliminary studies, $GO_x$ has been extensively investigated and used for glucose biosensors due to its low cost, high bioactivity, selectivity, and stability [67]. Glucose dehydrogenase (GDH) is also used for blood glucose test strips [68-71]. GDH-based biosensors have the advantage of lower detection potentials compared to the first-generation of $GO_x$-based

biosensors, and their performance is independent of the oxygen level in the analyte solution [72]. B-nicotinamide adenine dinucleotide (NAD)-dependent GDH and pyrroloquinoline quinone (PQQ)-dependent GDH (PQQGDH) are the two main types of GDH used in biosensor applications. However, GDH presents several limitations. PQQGDH suffers from low selectivity and requires suitable solubilisation detergents and purification to allow membrane binding, while water-soluble PQQGDH suffers from poor thermal stability [73]. NAD-dependent GDH biosensors require the addition of NAD cofactor which leads to complications (e.g., not always stable, contamination) in the analysis [72, 74]. Furthermore, the electrochemistry of the oxidised form (NAD+) and reduced form (NADH) of NAD cofactor is irreversible. Direct oxidation of NADH at an unmodified electrode requires high overpotential due to its slow electron-transfer kinetics [72, 73]. Moreover, for electrochemical measurements, GDH requires the use of artificial electron acceptors [75]. Alternatively, hexokinase isoenzyme II can be used for sugar sensing and glucose repression, as utilised by Saccharomyes cerevisiao, brewer's yeast [76]. However, it is more expensive and presents lower stability when compared to $GO_x$ [73, 75].

Glucose sensing has a significant scientific, clinical, and industrial relevance and significant progress has been made recently, particularly related to non-invasive methods to monitor blood [77-80]. Typically, glucose sensor reviews focus on a specific approach, enzymatic or non-enzymatic. This Section discusses and compares both techniques providing a comprehensive review on the current-state-of-the-art. This section discusses the key concepts of electrochemical glucose sensing, details the current state-of-the-art of non-enzymatic and $GO_x$ -based enzymatic glucose biosensors with a particular focus on materials and manufacturing techniques, and presents the main research challenges and opportunities.

### 2.1.2 Three Generations of Enzymatic Glucose Sensors

The concept of a glucose enzyme electrode, as proposed by Clark and Lyon [65], monitors the oxygen consumption according to the following enzyme-catalysed reaction:

$$\text{glucose} + \text{oxygen} \xrightarrow{\text{GO}_\text{X}} \text{gluconic acid} + \text{hydrogen peroxid} \tag{2.1}$$

The main problem faced by this sensor was the interference from background oxygen during the reaction. To solve this problem, Updike and Hicks [81] developed a system based on two oxygen working electrodes, measuring the current differential, hence, removing the noise created by the background oxygen. Similarly, Guilbault and Lubrano [82] developed an

enzymatic amperometric glucose biosensor by monitoring the released hydrogen peroxide ($H_2O_2$) as follows:

$$H_2O_2 \rightarrow O_2 + 2H^+ + 2e^- \quad (2.2)$$

The catalytic reaction of $GO_x$-based glucose biosensors involved the reduction of the enzyme's flavin group ($GO_x(FAD)$) to the reduced form ($GO_x(FADH_2)$) [83]:

$$\mathrm{GO_x}(FAD) + \mathrm{glucose} \rightarrow \mathrm{GO_x}(FADH_2) + \mathrm{gluconic\ acid} \quad (2.3)$$

The reduction is then counteracted using an electron acceptor and oxidation mediator, (Medox) to reoxidise the enzyme and regenerate the oxidised form ($GO_x(FAD)$) [83]:

$$\mathrm{GO_x(FADH_2) + Med_{ox} \rightarrow GO_x(FAD) + Med_{red}} \quad (2.4)$$

The regeneration of the enzyme is important to guarantee the enzymatic cycle, otherwise the enzyme will be reduced and cannot be reused, ending the sensing process.

According to the type of oxidation mediator, it is possible to identify three generations of glucose biosensors as shown in Figure 2.3. The first-generation of sensors use $O_2$ as a physiological mediator, the second-generation uses an artificial (synthetic) electron acceptor, while the third-generation uses an electrode for direct electrical communication without requiring any mediators.

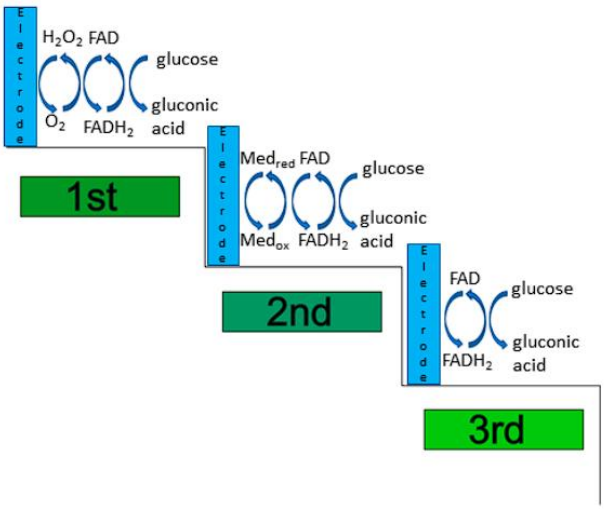


**Figure 2.3:** Schematic representation of enzymatic glucose oxidation mechanisms for the three different generations of biosensors.

### 2.1.3 First-Generation Enzymatic Glucose Biosensors

The first generation of enzymatic glucose biosensors relied on oxygen as the oxidation mediator to regenerate $GO_x$(FAD), thus detecting glucose by monitoring the oxygen consumption, or the generation of $H_2O_2$ during the enzymatic reaction [84]. The anodic oxidation and cathodic reduction of $H_2O_2$ were used to monitor the enzymatic generation process [85]. Moreover, the anodic oxidation of $H_2O_2$ enhances the ability to regenerate/replenish the oxygen, improving the enzymatic cycle [85]. The first-generation of enzymatic glucose biosensors were stable, simple, and easily used in miniaturised applications [86].

However, a major problem of the first-generation of glucose sensors was the electroactive interference as $H_2O_2$ requires a relatively high potential [86]. At a high potential level, some coexisting species such as ascorbic acid and uric acids are electroactive, reducing the selectivity and accuracy of the biosensor [87, 88]. This problem was minimised by using a permselective membrane, reducing the access of the interferent to the surface of the biosensor transducer [89-91]. Different membrane materials such as Nafion (Nf), polycarbonate, cellulose acetate, poly(1,3-diaminobenzene), and polypyrrole (PPy) osmium (Os) complexes were used based on their transport properties, pore size, charge, or polarity [92-95]. Other approaches to minimise interference were based on the use of metallised carbon [96, 97] and metal-hexacyanoferrate [84, 98] transducers, to reduce the operational potential to the optimal potential region (0 - 0.2 V vs. Ag/AgCl) used for $H_2O_2$ detection thus avoiding the electroactivity of the interferents. Similarly, Wang and Wu [99], developed a glucose biosensor with high selectivity by dispersing rhodium particles in an Nf film.

An alternative approach is the use of Prussian blue (PB) to minimise interference, for example, Kafi *et al.* [100] fabricated a $GO_x$/multiporous tin oxide nanofiber film on a PB-modified gold (Au) electrode for biosensing [100]. The aim was to develop a highly selective and low potential glucose biosensing, due to the PB having high catalytic activity and selectivity for the reduction of $H_2O_2$. Similarly, Li *et al.* [101] produced a highly sensitive imprinted electrochemical sensor based on double amplification using an inorganic PB catalytic polymer and $GO_x$ [101]. Cinti *et al*. synthesised PB nanoparticles on a filter paper, using it to immobilise $GO_x$ allowing the sensing of glucose in blood samples [102]. Moreover, a wide range of nanomaterials including carbon nanotubes (CNTs) [103], Pt nanoparticles [104], and composite nanomaterials [105, 106] were successfully used to improve selectivity due to their high catalytic effect.

Another important limitation of the first generation of glucose biosensors, based on the use of oxygen as $Med_{ox}$, was related to oxygen dependence [81, 107]. These sensors were prone to errors, due to oxygen tension fluctuation and the stoichiometric limitation of oxygen, usually referred to "oxygen deficit" (the normal oxygen concentration is an order of magnitude lower than the physiological level of glucose) [108]. To overcome this problem, Gough *et al.* [109] developed a two-dimensional cylindrical electrode using a mass transport-limiting film to increase the $O_2$/glucose permeability ratio. Other approaches included the use of an oxygen-rich carbon paste enzyme electrode [56,75,76] or an air diffusion biocathode that used oxygen directly from the air [110].

### 2.1.4 Second-Generation Enzymatic Glucose Biosensors

The second generation of enzymatic glucose biosensors relied on the use of an artificial Medox to mediate the $GO_x$ cycle instead of depending on oxygen as a mediator to transport electrons to and from the enzyme active site [111]. The artificial $Med_{ox}$ can be an immobilised mediator directly attached to the enzyme or entrapped in an enzyme film [112, 113], a solution-state mediator able to diffuse in and out of the enzyme active site [108], or a redox-conducting polymer able to transport its electrons to and from the enzyme active site [34,81,82]. Suitable mediators for $GO_x$ include conducting organic salts (particularly tetrathiafulvalene-tetracyanoquinodimethane, TTF-TCNQ), ferrocene, quinone compounds, ferricyanide, transition-metal complexes, phenothiazine, and phenoxazine compounds [86, 114-118].

The catalytic process consists of three steps: (1) the reduction of the $GO_x$(FAD) to $GO_x$ ($FADH_2$) due to the electron transfer from the glucose to the FAD reaction centres of GOx; (2) electrons transfer from the $FADH_2$ centres to the artificial mediator ($Med_{ox}$), hence reducing it from $Med_{ox}$ to $Med_{red}$; and (3) the transport of electrons through the artificial mediator to the electrode [108]. A current signal is produced due to the oxidation of $Med_{red}$ and used for glucose measurement, which requires an efficient interaction between the enzymes and the mediators to guarantee the effective transportation of the electrons between the redox active centres and the electrode [112].

Several approaches have been proposed to tailor the mediators in the electrode-supported enzyme films, including using Os complex as a mediator, non-covalent functionalisation of multiwalled carbon nanotubes (MWCNTs), $GO_x$ and binding proteins, and stabilising artificial mediators [119-121]. Heller [121] was a pioneer in the field of directly connecting an enzyme redox centre to an electrode and the results of his work was a glucose biosensor with a sensitivity up to 1 A $M^{-1}$ $cm^{-2}$. Marquitan *et al.* [119] designed a redox polymer by crosslinking

poly(4-styrene sulfonate-co-glycidyl methacrylate-co-butyl acrylate) (P(SS-GMA-BA)), and Os complex as a mediator producing a P(SS-GMA-BA)-Os matrix. $GO_x$ was then entrapped in the matrix forming a polymer/enzyme film used to modify the surface of a sub-micrometre scale carbon electrode [119]. Gallay *et al.* [122], designed a bienzymatic glucose biosensor based on the non-covalent functionalisation of MWCNTs with $GO_x$ and avidin (to allow the specific anchoring of biotinylated horseradish peroxidase (b-HRP)). Al-Sagur *et al.* [123] synthesised a multifunctional conducting polyacrylic acid (PAA) hydrogel (MFH) integrated with reduced graphene oxide (rGO), vinyl substituted polyaniline (VS-PANI), and lutetium phthalocyanine ($LuPc_2$) to create a three dimensional (3D) robust matrix for $GO_x$ immobilisation (PAA-rGO/VS-PANI/$LuPc_2$/GOx-MFH) and glucose measurement [123]. Schuhmann *et al.* [112] proposed the use of ferrocene amines directly attached to the surface of the enzyme through flexible linkages. Seketaryova *et al.* [108] designed a reagentless biosensor with free diffusing mediators by covalently bonding the $GO_x$ to the surface of the biosensor followed by exposing it to a water-organic mixture containing a high content of organic solvent [108]. In the case of immobilised mediator-based biosensors, it is important to immobilise the artificial mediator near both the enzyme's redox centre and the electrode surface to ensure high electron-exchange efficiency. Contrary to solution-based mediator biosensors, the immobilised mediators suffer from limited range of motion.

### 2.1.5 Third-Generation Enzymatic Glucose Biosensors

The third generation of enzymatic glucose biosensors relies on direct energy transmission (DET), which depends on the distance between the enzyme's redox centre and the electrode surface [124, 125]. Several approaches were investigated to overcome the long electron tunnelling distance to achieve the direct electrochemistry of enzymes [126-128]. The reassembling of apo-proteins on cofactor modified enzymes and the reassembling of apo-enzymes on cofactor Au nanoparticles (AuNPs) are widely used strategies to align redox enzymes on the electrodes [126, 127, 129-131]. These methods are effective in the process of electrically wiring the redox enzyme to the electrode surface but are complex processes which limit their usage. The fundamental concept of DET was proposed by Heller and Degani [131] which demonstrated the possibility of connecting the enzyme active site covalently to the surface of the electrode using a redox polymer. Yehzekeli *et al.* [132] described a technique to electrically wire the enzyme, and the ability to transform the enzyme from an oxidase to hydrogenase by implanting Pt nanoclusters into $GO_x$, which can be achieved by thermodynamically reducing Pt salts into Pt nanoclusters using the reduced factor $FADH_2$.

Several nanomaterials were described to directly achieve $GO_x$ electrochemistry [133-136]. Jose *et al.* [136] covalently immobilised $GO_x$ directly on the surface of MWCNT-coated electrospun Au fibre electrode. Tasviri *et al.* [134] produced an amine ($NH_2$) functionalised tin-oxide ($TiO_2$) coated carbon fibre nanotube ($NH_2$–$TiO_2$–CNT) layer used for the adsorption of $GO_x$. The $GO_x$ containing matrix was then used to modify the surface of a glass carbon electrode (GCE) [134]. Zhang *et al.* [133] developed a glucose biosensor using bio-mediated AuNPs dispersed in a CNT–polyvinyl alcohol solution. After the dispersion, the $GO_x$ was added to the solution, which was then dried to produce a film. The obtained film was used to modify a GCE thus producing a mediator-free glucose biosensor. Holland *et al.* [137] achieved direct energy transfer between $GO_x$ and electrode via a site-specific modification of $GO_x$ to display a free thiol group near the active site, hence facilitating site-specific attachment of maleimide modified AuNPs to the enzyme. Tasca *et al.* [138] developed a cellobiose dehydrogenase (CDH) based glucose biosensor by directly adsorbing CDH to single-walled carbon nanotubes (SWCNTs). The CDH was extracted from Corynascus thermophilus (Ct) fungi and the results showed that the CtCDH can catalyse glucose oxidation in neutral ph. The biosensor was successfully used to detect glucose in both normal and diabetic patients under physiological conditions.

This third generation of glucose sensors produced better results than both the first and second generation, but still present restrictions stemming from their dependency on the enzyme's activity which can be influenced by external environmental factors such as temperature, pH, and humidity [92,107,108]. Moreover, the biosensor performance also depends on the enzymatic layer thickness with high layer thickness resulting in signal dampening or loss [139, 140].

Despite all these developments, the different generations of biosensors present several limitations not yet fully addressed, which has led to the development of non-enzymatic glucose detection systems. These non-enzymatic glucose sensors, sometimes referred to as the fourth generation of glucose sensors, rely on the concept of oxidising glucose directly on the electrode surface.

### 2.1.6 Recent Developments in Enzymatic Glucose Biosensors

Advances in the field of nanomaterials have led to the development of enzymatic biosensors incorporating nanomaterials (e.g., noble and transition metal nanoparticles, CNTs, graphene, and nanostructured metal oxides) to amplify the electron transfer rate, improving the biosensor performance in terms of selectivity and sensitivity [141]. Kumar-Krishnan *et al.* [142]

developed a $GO_x$ immobilisation matrix by using AuNPs supported on a functionalised nano-silica ($SiO_2$) surface using a deep eutectic solvent (DES). The $SiO_2$ was first functionalised using a DES-mediated amine functionalisation to incorporate NH2 groups, and then the AuNPs were added to the solution to produce Au-$SiO_2$NP. $GO_x$ was then covalently immobilised to the Au-$SiO_2$NP followed by drop casting of the $SiO_2$NP/ $GO_x$ solution on the surface of a glass electrode. The obtained biosensor exhibited a sensitivity of 9.69 $\mu AmM^{-1}cm^{-2}$, and a wide linear range from 0.2 to 7 mM [142]. Buk and Pemble [143] prepared a glucose biosensor using a micro disk array electrode, modified with carbon quantum dots (CQDs)-AuNPs as a matrix for $GO_x$ (Figure 2.4). The microfabricated Au electrode was dipped in cysteamine to be functionalised by the $NH_2$ groups, and then a solution containing CQDs mixed with AuNPs was drop casted on the surface of the electrode. Finally, glutaraldehyde was used to immobilise $GO_x$, producing a micro disk array with a sensitivity of 626.06 $\mu AmM^{-1}cm^{-2}$ and a wide linear range from 0.16 to 4.32 mM [143].

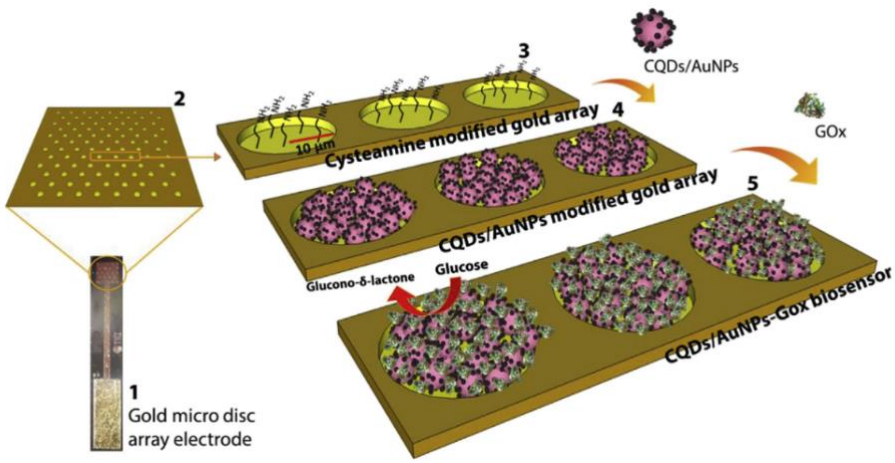


**Figure 2.4:** Preparation steps of a glucose biosensor using a micro disk array electrode. (1) single disk array electrode, (2) surface magnification, (3) cysteamine modification of the Au surface, (4) CQDs/AuNPs adhered surface, (5) $GO_x$ immobilisation to the surface *[143]*.

MWCNTs were recently investigated to produce immobilisation matrices for $GO_x$ due to their high stability and ability for direct electron transfer [144-146]. Shrestha *et al.* [144] developed a bio-nanohybrid material by dispersing functionalised MWCNTs (fMWCNTs) in a Nf film dopped with PPy. $GO_x$ was then covalently immobilised in the material, producing Nf- $GO_x$ -fMWCNTs-PPy using electrochemical polymerisation on a surface of a Pt electrode [144]. The obtained Nf- $GO_x$ -fMWCNTs-PPy/Pt electrode detected glucose with a high sensitivity, 54.2 $\mu A\ mM^{-1}cm^{-2}$, in a linear range of up to 4.1 mM. Li *et al.* [145] used cobalt (II) sulphide nanoparticles (CoSNPs) to coat MWCNTs through an in situ hydrothermal method, obtaining a CoS-MWCNTs composite used as a matrix for $GO_x$ immobilisation. The CoS-MWCNTs was

dispersed in water, $GO_x$ was added to the solution, and the mixture stirred gently to produce CoS-MWCNTS/ $GO_x$, which was drop casted to modify a GCE. Finally, to increase selectivity and sensitivity, Nf solution was added to the electrode surface resulting in the fabrication of a CoS-MWCNTs/ $GO_x$ /GCE/Nf electrode with a sensitivity of 15 mA $M^{-1}cm^{-2}$ and a wide linear range from 8 µM to 1.5 mM [145]. Hao *et al.* [146] developed a functional nanocomposite by depositing manganese dioxide ($MnO_2$) on the surface of MWCNTs via an in situ hydrothermal method. The nanocomposite ($MnO_2$/MWCNTs) was used for the direct detection of $H_2O_2$, or as a matrix to immobilise $GO_x$ [146]. $GO_x$ was adsorbed by the $MnO_2$/MWCNTs nanocomposite producing $GO_x$ /$MnO_2$/MWCNTs, which was then used to modify the surface of a GCE producing an electrode with two distinct linear ranges from 5 -200 µM and 0.2 - 1 mM [146].

Similarly, graphene has been used to produce enzymatic glucose biosensors. A disposable glucose biosensor was developed by Vukojevic *et al.* [147] using $MnO_2$ nanoparticles to decorate graphene nanoribbons (GNR) followed by surface modification using a drop coating method with $GO_x$ and Nf. The $MnO_2$-GNR composite solution was created using a simple hydrothermal mixing process. The composite solution was then drop cast on the screen printed carbon electrode (SPCE) producing a $MnO_2$-GNR/SPCE electrode, followed by the addition of $GO_x$ and Nf, which resulted in an enzymatic glucose biosensor with a sensitivity of 56.32 µA $mM^{-1}cm^{-2}$ and a linear range from 0.1 to 1.4 mM [147]. Mao *et al.* [148] investigated the use of reduced graphene oxide (rGO) to increase the sensitivity and selectivity of a zinc oxide (ZnO) nanorod based biosensor. In this case, a polyethylene terephthalate (PET) substrate was used to hydrothermally synthetise the ZnO nanorods. Then, electrodeposited rGO was used to coat the ZnO/PET working electrode and AuNPs were dispersed on the surface leading to the production of ZnO/rGO/Au/PET. Finally, the $GO_x$ was physically adsorbed on the surface of the electrode leading to the fabrication of a $GO_x$/rGO/ZnO/Au/PET glucose biosensor with a sensitivity of 56.32 µA $mM^{-1}cm^{-2}$ and a linear range from 0.1 to 12 mM [148].

Recently, Hossain and Slaughter [149] proposed a hybrid glucose biosensor with high sensitivity and selectivity using both MWCNTs and graphene. Chemically derived graphene and MWCNTs functionalised with carboxylic groups were synthesised using a one-step solvothermal technique to produce a suspension containing both materials. This suspension was then drop casted on an Au electrode forming a thin film onto which PtNPs were electrochemically deposited. Finally, $GO_x$ was immobilised on the nanostructured electrode and coated with Nf. The fabricated hybrid biosensor exhibited sensitivity of 26.5 µA $mM^{-1}cm^{-2}$ and linear detection range from 0.5 to 13.5 mM [149].

High selectivity is a key requirement for glucose sensing applications. One approach to improve selectivity consists of using a red blood cell membrane (RBCM) as a diffusion barrier on the surface of the enzymatic glucose biosensor to eliminate any interfering molecules from reaching the surface [150]. The cell membrane's main role is to block ions and small molecules to access the cell. However, the cell membrane contains glucose transporter-1 (GLUT1) proteins that promotes the exchange of glucose in and out of the cell [151, 152]. As the RBCM is rich in GLUT1, if isolated from the cells, it can be used as a diffusion barrier on the surface of the enzymatic biosensor [153, 154]. This approach was explored by Kim *et al.* [150] by coating a screen-printed Au electrode (SPGE) with glucose dehydrogenase (GDH), pyrroloquinoline (PQQ), mediator, and a buffer medium (0.1 M phosphate buffer solution). RBCM collected from red blood cells was used to coat the outer surface of the coated SPGE. The RBCM coated enzymatic glucose biosensor was then tested, showing lower limit of detection than the uncoated biosensor demonstrating that the RBCM increases the biosensor selectivity and its performance [150].

Conductive polymers (CP), prepared mostly by incorporating conductive nanoparticles within a polymer matrix, can be used for enzyme immobilisation due to their unique properties such as high electron affinity, electrical conductivity, redox activity, stability, and low cost [155, 156]. Soylemez *et al.* [157] fabricated an enzymatic glucose biosensor using a novel electrochromic conductive polymer, poly(2,5-di(furan-2-yl)thiazolo[5,4-d]thiazole) (PTTzFr), to immobilise $GO_x$. PTTzFr, obtained using cyclic voltammetry (C-V), was drop coated by $GO_x$ using glutaraldehyde as a crosslinking agent. The biosensor exhibited a wide linear range from 5 μM to 0.7 mM. The biosensor readings were compared to readings from real sample analysis showing minor deviation [157]. Wang *et al.* [158] developed a ratiometric enzymatic glucose biosensor using Schiff base polymers (SBPs) due to their stability, biocompatibility, and good mechanical and catalytic properties. Thionine, which carries two primary amine groups and p-benzaldehyde carrying aldehyde functional groups on the two sides of the ring, were the two monomers used to synthesise the SBPs. The SBPs nanosheets were used to immobilise $GO_x$ and the $GO_x$ /SBP matrix was used to modify a GCE via drop coating [158]. The biosensor showed two wide linear ranges from 1.97 μM to 4.0 mM at -0.2 V reference peak signal and from 0.82 μM to 4.0 mM at -0.05 V reference peak signal [158]. Krishnan *et al.* [159] designed Pb/Pt core/shell nano cubes electrode (Figure 2.5). The electrodes were coated with chitosan as an immobilisation matrix for $GO_x$ allowing the covalent bonding of the $GO_x$ to its surface via the active amine (NH) side group, improving stability and preserving the

biocatalytic functions of the enzyme. The sensor showed a sensitivity of 6.82 μA $mM^{-1}cm^{-2}$ and a wide linear range from 1 to 6 mM [159].

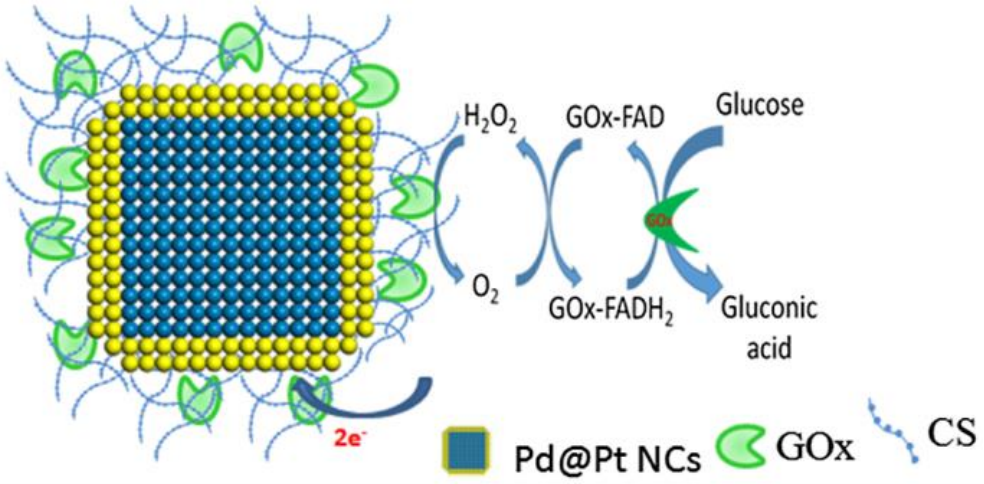


**Figure 2.5:** Schematic representation of the surface modification of Pb/Pt nanocubes using chitosan and covalent immobilisation of GOx [136].

Enzymatic glucose biosensors for blood glucose monitoring led to the development of patient friendly devices, enabling continuous and real-time glucose monitoring. Csoregi *et al.* [160] developed one of the earliest subcutaneous biosensors which led to the development of skin-like biosensors. This was a three-layered sensor based on a glucose sensing layer, a glucose mass transport restricting layer, and an outer biocompatible layer. The glucose sensing layer was prepared by cross-linking (poly [(l-vinyl imidazolyl) osmium (4,4′-dimethylbipyridine)2Cl]$^{+/2+}$(PVI13-dme-Os) and $GO_x$ with poly(ethylene glycol) diglycidylether (PEG). The glucose mass transport restricting layer consisted of a poly (ester sulfonic acid) film (Eastman AQ 29D) and a copolymer of polyaziridine and poly(vinyl pyridine) partially quatemized with methylene carboxylate. Finally, the outer biocompatible layer was prepared by photo cross-linking tetraacylated poly(ethylene oxide). Below the glucose sensing layer, a flexible gold wire electrode was used. This layer was formed by sequentially depositing gold in a 0.09 mm deep shielded recess at the tip of a polyimide. The insulated 0.25 mm gold wire formed a “wired” glucose oxidase sensing layer. The produced 5 × $10^{-4}$ $cm^{-2}$ sensor had a sensitivity range from 1 to 2.5 nA $mM^{-1}$. An interesting example is the skin-like biosensor developed by Chen *et al.* [161] for non-invasive intravascular blood glucose monitoring (Figure 2.6a). The system compromises an ultra-thin (~3 μM) skin-like layer and a battery-powered paper. When the biosensor is attached to the skin it creates a subcutaneous electrochemical channel (ETC). Before implantation, the biosensor was sprayed with hyaluronic acid (HA). The ETC depends on the HA penetration into the interstitial fluid

(ISF) (anode channel), intravascular blood glucose refiltration from vessels, and glucose reverse iontophoresis to the skin surface (cathode channel). The HA is repelled at the anode increasing the ISF osmotic pressure, forcing intervascular blood glucose to move out of the vessels towards the skin surface [161]. Arakawa *et al.* [162] developed a detachable mouth sensor to detect the level of glucose using saliva (Figure 2.6b). The biosensor is made of Pt and a silver/silver chloride (Ag/AgCl) electrode on a polyethylene terephthalate glycol (PETG) mouthguard, fitted with a wireless transmitter to enable direct readings. $GO_x$ is entrapped using a poly (2-methacryloyloxyethyl phosphorylcholine-co-2-ethylhexyl methacrylate (PMEH) film coating the Pt electrode, while the Ag/AgCl electrode is used as a reference electrode. Another relevant biosensor based on the detection of glucose in bodily fluid was proposed by Orzari *et al.* [163] which allowed the detection of glucose in sweat. In this case, a disposable biosensor was produced using graphite and a conductive ink. The conductive ink was printed on an adhesive sheet creating the electrode, followed by drop casting of $GO_x$ and dihexadecyl phosphate on the electrode surface. The biosensor could detect glucose in the sweat on the skin with a linear detection range of 1 - 10 µM.

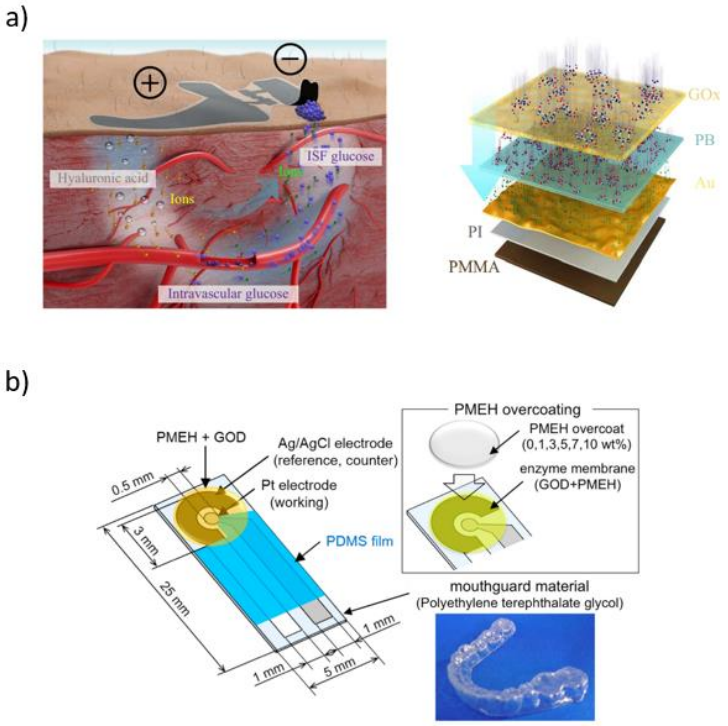


**Figure 2.6:** (a) Schematic representation of the ETC, which performs HA penetration, glucose refiltration, and glucose outward transportation (left image), and thin, flexible, and biocompatible paper battery attached to the skin surface for ETC measurement (right image) [161]. (b) Representation of the glucose biosensor on the PETG mouthguard support. Pt and Ag electrodes were formed on the PETG using a sputtering process. 30 units of $GO_x$ were applied to the sensing region of the working electrode [162].

### 2.1.7 Recent Developments in Non-Enzymatic Glucose Sensors

Non-enzymatic glucose sensing is a cheap and rapid technique that relies on the direct electrochemistry of glucose (oxidation or reduction) [63]. However, direct glucose oxidation on noble metal electrodes suffer from three major limitations [164-168]: (1) restricted glucose sensitivity which can be attributed to the slow glucose electro oxidative kinetics on conventional electrodes; (2) low selectivity as several sugars can be oxidised in the same potential range as glucose; and (3) reduced electrode activity due to ion contamination, mainly chloride ions ($Cl^-$). The sensitivity and selectivity limitation can be countered by increasing the surface area of the electrode allowing more glucose to be in direct contact with the electrode's surface. In order to achieve this, several nanomaterials are being investigated [169, 170]. Particularly relevant are noble metals such as Pt, nickel (Ni), Ag, zinc, and Au, which are highly utilised to develop novel non-enzymatic glucose sensors [59, 171-173]. The ion contamination limitation can be eliminated using alkaline conditions on the electrode surface, as the hydroxyl groups (OH) eliminates the chloride adsorption to the surface [64, 174].

The non-enzymatic glucose oxidation catalytic process involves the hemiacetalic hydrogen atom abstraction that occurs in parallel with the adsorption of the organic species [175]. This process is regarded as the rate-determining step in the glucose electro-oxidation catalytic process. Bruke *et al.* [175] proposed the ''incipient hydrous oxide adatom mediator'' (IHOAM) model describing the complex electrocatalytic process of glucose. The IHOAM model describes the significance of the "active" hydroxide anions in the domain of the electrode surface produced by the separation of water to the electro-oxidation of glucose and other organic compounds [167, 168]:

$$H_2O \rightarrow H^+ + OH^- \tag{2.5}$$

Moreover, the chemisorption of hydroxide anions to the reductive metal adsorption site (M), results in the production of oxidative adsorbed hydroxide radical ($MOH_{ads}$) according to the following equation [176]:

$$M + OH^- \rightarrow MOH_{ads} \tag{2.6}$$

From Equations (2.5) and (2.6) it is possible to observe that the $MOH_{ads}$ formation increases by increasing the concentration of OH-. Therefore, non-enzymatic glucose sensing is a pH dependent process, and an highly alkaline environment improves its sensitivity [174].

### 2.1.8 Metal-Based Glucose Sensors

Several metals, especially noble metals, have been studied as a base material for the electrodes of non-enzymatic glucose biosensors [63, 177]. As a result, a deeper understanding of the glucose direct oxidation mechanism was achieved, showing that the mechanism depends directly on the metallic catalyst used in the electrode [110,137,138]. Moreover, advances in material science led to the development of several metal alloys and hybrid materials, allowing for improved properties when compared to noble metals and metal oxides alone [60, 178-180].

### 2.1.9 Pt-Based Glucose Sensors

Pt is widely used as an electrocatalytic electrode material due to its high catalytic activity and stability [175]. The glucose oxidation mechanism on the Pt electrode can be described using C-V, with the corresponding plots presenting three distinct peaks (Figure 2.7). The first peak (potential region 0.15 V - 0.3 V vs. RHE (reversible hydrogen electrode) corresponds to the hydrogen region and it is characterised by glucose dehydrogenisation leading to glucose adsorption to the electrode surface [175]. The second peak (potential region 0.4 V - 0.8 V vs. RHE) represents the double layer region and it is associated to the water dissociation process (Equation (2.5)) followed by glucose oxidation that occurs at a lower potential than the required glucose thermodynamic oxidation potential as predicted by the IHOAM model [167, 175]. The third region (potential region higher than 0.8 V vs. RHE), corresponds to the oxide region. In this region, the Pt electrode surface is oxidised changing to PtO. As a result, the glucose oxidation becomes diffusion-controlled, leading to direct bulk glucose oxidation on the oxide layer instead of a surface-bound reaction [167, 181].

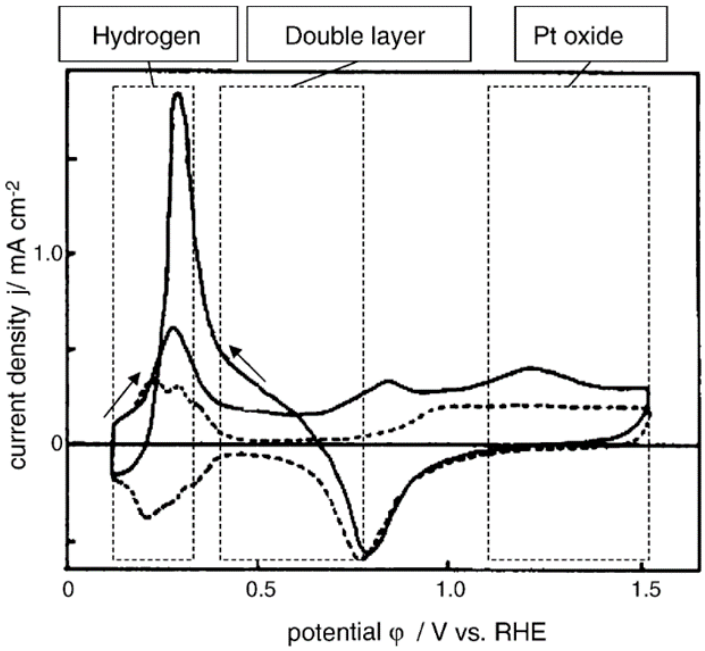


**Figure 2.7:** Cyclic voltammetry graph displaying three potential regions where glucose is electro-chemically oxidised at a Pt electrode [159].

Noble metals such as Pt and Au, experience a large oxidative current in the double layer region during cathodic scan. Identical anodic currents appear during the cathodic scan for many other organic species, specifically alcohols [182]. Investigations of the produced oxidative currents have demonstrated the current dependence on the glucose concentration [183], pH [184], upper limit potential [174], surface morphology [185], and electrode ion contamination [62].

Strategies to overcome the Pt limitations comprise nanoengineering the Pt surface, fabricating nanocomposite structures, adjusting surface morphology, roughness, and increasing porosity [177, 186-189]. Additionally, the fabrication of nanocomposite Pt-based structures is a widely used approach to improve the catalytic efficiency of noble metals [22,134,144]. This approach reduces production costs and the required amount of Pt and augments the surface catalytic activity by increasing the electrode surface area, evenly dispersing Pt on different substrates such as graphene [190], CNTs [164], and mesoporous carbon [191].

Xiao *et al.* [190] developed a flexible electrochemical glucose sensor using free-standing graphene paper carrying a nanocomposite PtAu alloy and $MnO_2$. Electrodeposition was used to grow the PtAu-$MnO_2$ nanocomposite on the graphene paper resulting in close contact between the PtAu alloy and $MnO_2$. The glucose sensor exhibited high sensitivity of 58.54 μA $mM^{-1}cm^{-2}$ and a wide linear range from 0.1 mM to 30 mM [156,161,163]. Similarly, Hu *et al.* [185] developed a graphene-supported hollow Pt-Ni nanostructure electrode. The electrode was fabricated using a galvanic replacement approach at ambient temperature. The sensor presented high sensitivity of 30.3 μA $mM^{-1}cm^{-2}$ and a wide linear range from 0.5 mM to 20

mM. Chang *et al.* [192] used a hydrothermal synthesis approach to produce 22 nm Pt nanoclusters on GO using polyvinylpyrrolidone as a surfactant. The produced sensor showed high sensitivity of 1.21 μA $mM^{-1}cm^{-2}$ and a wide linear range from 1 mM to 25 mM [192]. Nguyen *et al.* [164] developed a non-enzymatic biosensor by electrodepositing Au and Ruthenium (Ru) on the surface of a CNT-based Pt-nanoparticle hybrid composite in a poly(3,4-ethylenedioxythiophene) polystyrene sulfonate (PEDOT:PSS) conductive polymer. The sensor presented sensitivity of 0.234 μA $mM^{-1}cm^{-2}$ and a linear range of 10 mM [164].

A nano-porous Pt electrode is a 2D or a 3D porous film with nanosized pores usually produced using surface templated electrodeposition [193] and selective dealloying [194]. The pioneering work of Park *et al.* [195] demonstrated the potential of using nano porous Pt for non-enzymatic glucose sensing applications and this was followed by several other studies on Pt film electrodes [147,158,159]. Lee *et al.* [177], developed a prototype of a disposable non-enzymatic blood glucose sensing strip, using nano porous Pt as an electrode material mixed with poly(vinyl acetate) acting as a binding material. The mixture was then dispensed on the surface of a conducting circuit screen printed on a polyimide film. The sensor was able to detect glucose in whole human blood with acceptable stability for 30 days and a sensitivity of 0.0054 $\mu Acm^{-2}mgdL^{-1}$ [177]. Kim *et al.* [194] selectively dealloyed Si from Pt-Si alloy to create a nano porous Pt electrode with an increase in roughness due to the higher porosity which led to higher glucose sensitivity and lower sensitivity to interfering species such as ascorbic acid.

### 2.1.10 Au-Based Glucose Sensors

Au is an extensively investigated electrode material, characterised by providing a high glucose oxidation current in both neutral and alkaline environments [193]. However, contrary to Pt its glucose oxidation mechanism is still vague, requiring further studies. In this case, the cyclic voltammetry graph only presents two regions, corresponding to the double layer and Au oxide region [26,29,105,155,168]. Previous studies seem to indicate a dependence between the oxidation mechanism and the presence of surface oxides such as Au(OH) [184]. Moreover, the glucose oxidation is not as dominant in the Au oxide region compared to Pt and mainly occurs in the double layer region where the surface $OH_{ads}$ layers are formed [184]. Results also suggest that high pH levels result in higher faradic current, while at low pH the oxidative current is only detected at potentials higher than the oxide region [136,155,169].

Different methods such as electrochemical etching and dissolution [148,170,171], electrochemical deposition [196-198], and thermal annealing [199] have been used to produce nano porous Au samples aiming to reduce ion contamination and interference with the sensor

surface. Verma [178], used Oryza sativa (Asian rice) extract as a reducing agent for the bio-reduction of Au ($Au^{3+}$) and Ag ($Ag^{+}$) ions, producing nano precursors leading to the formation of 0D monodispersed tuneable nano porous AuNPs. The obtained nano porous AuNPs were then used to modify the surface of a GCE and tested for non-enzymatic glucose sensing using C-V. The electrode had a linear range from 1 to 50 μM and sensitivity of 6.67 μA $\mu M^{-1} cm^{-2}$ [178]. $H_2O_2$ detection can be also used as an indicator for the glucose presence in a sample. Xue *et al.* [200] used magnetron sputtering to fabricate nano porous Au thin films by chemically dealloying the nano porous Au to obtain a 3D bicontinuous ligament nanopore film. The film was then used to detect $H_2O_2$ with a linear relationship from 0.1 mM to 10 mM [200]. Sanzó *et al.* [198] used bubble electrodeposition to grow Au nanocorals on an Au screen-printed electrode. The modified electrode was used to directly detect glucose and was assessed using C-V, showing a linear range from 0.1 to 13 mM, and sensitivity of 0.5 μA $mM^{-1} cm^{-2}$ [198]. Han *et al.* [199] developed a new facile, environmentally friendly, cost-effective, and bottom-up approach to obtain a hierarchically porous Au cluster film for direct electrochemical non-enzymatic glucose sensing. The Au-cluster film consisted of a network structure interconnected with Au particles and disordered 3D hierarchical pores. The produced film showed a large surface area, high electrocatalysis, and electroconductivity towards glucose oxidation. The resulting film had a linear range from 0.01 to 10 mM and sensitivity of 10.76 μA $\mu M^{-1} cm^{-2}$ [199]. Scandurra *et al.* [201] used the dewetting technique to prepare a graphene paper-based electrode. In this case, an 8 nm thick Au layer was sputter deposited on a graphene paper and then a laser was used to dewet the Au layer. The laser-based dewetting resulted in smaller AuNPs on the electrode surface. The sensor had a sensitivity of 1240 μA $mM^{-1}$ $cm^{-2}$. The major advantage of using Au-based electrodes for glucose sensing is the higher current response when compared to Pt-based electrodes, allowing for higher sensitivity and the ability to detect glucose in a neutral pH [184]. However, the main limitation of Au-based electrodes is related to the low glucose oxidation efficiency on the Au electrode surface, especially in the presence of surface $OH_{ads}$ [168], which can be reduced by using arrays of nanoelectrodes spaced by non-electroactive materials. Additionally, as these electrodes are better activated in alkaline solutions they cannot be used for *in-vivo* studies, they suffer from surface contamination from anions such as phosphates and chlorides, and the selectivity is lower than Pt-based electrodes.

### 2.1.11 Transition Metals-Based Sensors

Pt and Au are suitable electrode materials for glucose detection but are expensive. Therefore, other non-precious transition metals [202] including Nickel (Ni) [27,141,178,179], and Copper (Cu) [203-205] and their oxides have been investigated. The redox reaction of transition metals does not follow IHOAM and chemisorption models. Under an anodic bias, transition metal's oxide layer oxidizes into a higher oxidation number (i.e., Ni (II) to Ni (III)) [137,178,179]. The oxidative power of the higher oxide later has enough strength to create surface bound $OH_{ads}$ radicals, which oxidises organic compounds such as glucose on the electrode surface.

Previous studies highlighted that Cu (II) and Cu (III) couple on the anodic surface of the Cu electrode during glucose electro-oxidation in an alkaline environment [206, 207]. Initially the $Cu(OH)_2$ is oxidised to CuOOH, followed by hydrogen abstraction at the electrode surface, forming a radical intermediate and reforming the $Cu(OH)_2$. Finally, the hydroxyl anions rapidly oxidise the radical intermediate producing gluconolactone [208]. The main disadvantage of a Cu electrode is its lack of ability to work in low or neutral pH as the CuOOH catalysis requires the presence of hydroxyl anions. Another important disadvantage is related to the competitive ethanol interference which negatively impacts the ability to detect blood glucose level.

The disadvantages associated with Cu were countered by using Cu nanostructured materials that enable an increase in the surface area. Recently Chen *et al.* [209], developed a portable micro glucose sensor using Cu oxide (CuO) nano-coral arrays (NCA) grown on a nano porous Cu (NPC) electrode. This non-enzymatic sensor showed high catalytic activity of glucose due to the CuO nano-coral arrays and high conductivity due to the NPC. The sensor had a sensitivity of 1621 $\mu A\ mM^{-1}\ cm^{-2}$ and a linear range from 0.0005 to 5 mM. Zhang *et al.* [210] used a simple substrate-assisted electroless deposition technique to anchor Cu nanoparticles (CuNPs) on the surface of laser-induced graphene (LIG) producing a CuNPs-LIG composite sensor. The sensitivity of the sensor was 495 $\mu A\ mM^{-1}\ cm^{-2}$, and the detection limit was 39 μM. Liu *et al.* [211] used a wet chemical technique combined with an annealing procedure to produce 3D copper oxide nanowire arrays (CuONWA) on a copper foam (CF) skeleton. The resulting CuONWA/CF platform was used as a glucose sensor, exhibiting a sensitivity of 32,330 $\mu A\ mM^{-1}\ cm^{-2}$, and a linear range from 0.10 to 0.50 μM. The increased sensitivity of this sensor can be attributed to the increase in surface area due to the nanowire arrays as well as the porous copper foam.

In the case of Ni, which exhibits a similar glucose electro-oxidation mechanism to Cu, Ni (II) and Ni (III) couple mediate the glucose redox on the electrode surface. Gao *et al.* [212] used a femtosecond laser direct writing technique to prepare an Ni foam (NiF). The obtained NiF exhibited a controlled micro and nano superhydrophilicity structure leading to an increased detection area and higher sensitivity (13.822 mA $mM^{-1}$ $cm^{-2}$) and a detection limit of 0.0019 mM. Wang *et al.* [213] used a combination of solvothermal and ultrasonic techniques to synthesise a hierarchical 3D flower-like nickel (II)-terephthalic acid (Ni(TPA)) metal-organic framework (MOF), which was used to dope SWCNTs. The nanocomposite was then used to modify the surface of the GCE to detect glucose. The sensor had a linear range from 20 μM to 4.4 mM and a detection limit of 4.6 μM. Zhang *et al.* [214] developed a glucose-sensing composite through in situ self-assembly of Ni-based MOF in the presence of functional CNTs. The sensor had a sensitivity of 13.85 mA $mM^{-1}$ $cm^{-2}$, and linear detection range from 1 μM to 1.6 mM.

### 2.1.12 Metal Alloy-Based Glucose Sensors Agriculture

Metal alloys are highly relevant electrode materials due to their high electrocatalysis. The different atoms inside an alloy create a new binding site or reaction pathway that can greatly impact the activation or binding energy of the reagent or intermediate, resulting in a possibly new reaction pathway and reduced overpotential [215]. Novel multi-metallic Pt and Au-based alloys and advances in computational chemistry have allowed development of electrodes with improved catalytic efficiency, stability, and anti-interference [25,149,150].

Several noble metal-based catalysts such as Pt-Ag [189], Pt-Ni [216], Pt-Pb [217], Pt-iridium (Pt-Ir) [218], and Au-Pt [179] were investigated for the development of novel electrodes using electrodeposition or selective dealloying techniques [150,185,196,197]. Lin *et al.* [189] prepared a PtAg/MWCNT modified GCE using drop casting. The sensor was used to determine the glucose level in bovine serum albumin samples and showed a linear detection range from 1 to 25 mM and sensitivity of 115.5 μA $mM^{-1}cm^{-2}$ [189]. The combined use of Pt and Ag resulted in a low overpotential, high sensitivity, and good stability when compared to monometallic-based non-enzymatic glucose sensors. Pt and Ag were also drop casted on the surface of a boron-doped diamond electrode (BDD) resulting in a modified electrode with high stability and selectivity [219]. Different percentages of Pt and Ag were investigated, and the best results were obtained for a 50/50 Pt to Ag ratio. The obtained non-enzymatic sensor had a linear detection range from 0.01 to 7.5 mM and a limit of detection of 0.007 mM [219].

Bimetallic systems were also investigated using one noble metal and one transition metal. Guascito *et al.* [220] modified the surface of a Pt electrode using tellurium microtubes through a drop casting method. The produced non-enzymatic glucose sensor was compared to a non-modified Pt electrode and showed higher sensitivity, stability, and reproducibility. The sensor exhibited two linear ranges with different sensitivity for each range - first range between 0.1 and 1 mM and sensitivity of 522.61 μA $Mm^{-1}cm^{-2}$ and second linear range from 1 to 29 mM with a sensitivity of 62.45 μA $Mm^{-1}cm^{-2}$ [220]. Guo *et al.* [221] fabricated Pt-Cu nano strands (70/30 Pt to Cu ration) using wet chemistry and the nano strands to modify the surface of a GCE. The produced sensor had a linear oxidation current of glucose ranging from 0.1 to 19 mM, sensitivity of 23 μA $mM^{-1}cm^{-2}$, and the interference from ascorbic acid, uric acid, and fructose was avoided [221].

Metal alloy-based non-enzymatic glucose sensors have great potential in facilitating glucose electro-oxidation with several studies [168] showing its higher sensing performance compared to monometallic-based sensors [222]. The alloy-based sensors typically based on Pt or Au are usually more expensive but present better current response and anti-interference, whilst operating in a neutral pH environment.

### 2.1.13 Conclusion and future perspective

Due to health and regulatory pressures, the demand for low-cost, efficient, and accurate glucose sensors is significant, and the glucose market size is expected to be worth $36.7 billion by 2026 [223]. This section reviews the current state-of-the-art of glucose sensors considering two major groups of sensors: enzymatic and non-enzymatic.

As discussed in detail, enzymatic-based glucose biosensors seem to correspond to the ideal model for glucose biosensing. However, many challenges such as short operational lifetime, temperature, and pH range, are limiting their performance requiring the use of more advanced materials and fabrication techniques. Currently, the most used materials are noble and transition metal nanoparticles, CNTs, graphene, and nanostructured metal oxides and different techniques were explored including using semi-permeable films, conductive polymers, and metal-based mediators. Further studies are also required to improve the selectivity and stability of these sensors and novel fabrication techniques should be considered to allow miniaturisation. Besides glucose oxidase, other enzymes such as pyranose oxidase ($PO_x$) [224], which is a promising enzyme belonging to the glucose-methanol-choline (GMC) superfamily, have been investigated. $PO_x$ has a higher thermal stability compared to $GO_x$ and it is not glycosylated thus presenting a shorter distance between the enzyme active site and the electrode, leading to better

electron transfer and thus higher sensitivity. The main drawback of $PO_x$ is its lower oxygen turnover compared to $GO_x$ which can interfere with its sensitivity. This drawback could be improved by tailoring the enzyme (e.g., genetic modification or selective breeding) [225, 226]. Additive manufacturing (3D/4D printing) (see Section 2.2) is developing at a fast rate with increasing choice of material selection [227]. Materials such as conductive polymers can be used in additive manufacturing to fabricate the enzymatic immobilisation matrix. Additive manufacturing builds products layer by layer which enables the fabrication of not only the surface of the biosensor but also a full biosensor with interchangeable materials to vary and control the biosensor properties. The combined use of additive manufacturing and smart materials (materials that respond to an external environmental stimulus), usually named as 4D printing [228, 229], seems to offer significant potential to produce interactive systems that allow the biosensor to detect glucose only in specific scenarios.

Other potentially relevant manufacturing strategies, not fully explored, including screen-printed electrodes [230], ink jet sputtering [231], and nanolithography [232], all of them presenting advantages and drawbacks. Screen-printed electrodes are portable, disposable, low cost, and easy to use, but suffer from stability problems as the enzyme is immobilised in the ink which can leak with repetitive use, as well as ink dissolution [233]. Ink jet sputtering can be used to print any computer-generated pattern on the printing surface allowing the deposition of multilayers of enzymes, and the automatisation of the manufacturing process. However, this technique presents some limitations such as the lack of control on the layer homogeneity due to nozzle clogging and irregular droplet sizes, adverse effects on the enzymes due to printing stresses, and the potential contamination of the ink due to the refilling step [234]. Nanolithography allows for high fabrication resolution, being able to pattern biomolecular materials on many substrates, but the thermal force due to the increase in temperature can result in enzymatic denaturation and it is an expensive technique [235]. Moreover, the relationship between the enzyme's conformation and the enzyme's catalytic activity requires further research, which will potentially lead to significant innovations in the enzymatic biosensor field.

Contrary to enzymatic sensors, non-enzymatic glucose sensing presents higher stability, selectivity, less complex manufacturing procedures, and clinical uses [236]. The most used materials are Pt and Au composites and alloys, and popular techniques are electrodeposition, dewetting, and selective dealloying. Non-enzymatic sensors have been demonstrated to be functional for more than 30 days in undiluted whole blood after sterilisation, which is not possible with enzymatic sensors [236]. However, they still face several key challenges such as

using alkaline operating conditions in testing, the high cost of materials, and the need for a protective layer on the surface to enhance selectivity.

Typically, glucose biosensor investigations focus on materials and manufacturing techniques, neglecting aspects related to the testing conditions. However, these testing conditions are usually impractical for usage in the human body which is the goal for clinical glucose sensors. A major limitation, which must be addressed in the future, is the lack of standards for testing and evaluation of different sensors against a specific criterion.

Further research is also required to fully understand the sensing mechanism of different materials and to explore techniques such as 3D/4D printing to produce glucose sensors, especially with the maturation and cost reduction in metal-based printing strategies such as electron beam melting [237]. Using different materials and combinations also hinders the commercialisation of non-enzymatic sensors which is a very important aspect to be considered. Disposable printed electrodes for direct electrochemical sensing would also help in reducing cost while increasing usage simplicity. The development of conducting polymeric nanowires, embedded metal nanoparticles in polymeric films, and polymeric ionic liquids are all important trends with high potential to expand the usage of biosensors in other fields such as point of care testing, agriculture, explosive and biological warfare agents detection [238].

Biosensors are a fast-growing field attracting researchers from different disciplines. Due to significant progress in areas related to advanced materials, manufacturing technologies, Internet of Things and artificial intelligence, it is foreseeable that the next generation (fifth generation) of biosensors will be able not only to monitor glucose levels but also able to respond to changing cues, predicting trends, and helping in managing glucose levels [239].

## 2.2 4D printing of Shape Morphing Polymers♣

### 2.2.1 Introduction

Smart materials are a special class of materials that demonstrate an intelligent behaviour, being able to respond to external stimuli [240]. This response depends on the type of material, additives, and/or material morphology [241, 242]. The material response can be programmed by one or several cycles of activation that tune the state/microstructure of the material. Smart materials exhibit these functions on their own, as well presenting intelligence in the form of

♣ This section is partially based on the following submitted publication: Abdalla Omar, Mohamed Hassan, Wajira Mirihanage, Paulo Bartolo – "4D printing of Shape Morphing Polymers", International journal of Bioprintring. Mohamed Hassan main contributions: data collection, data analysis, writing and reviewing the manuscript

self-sensing and control *[243]*. This is an emerging field and different definitions for smart materials have been proposed as summarised in Table 2.1. In the scope of this Section, smart materials are considered as functional, active, or intelligent materials with special behaviour due to their molecular structures, morphologies, and/or compositions, which can respond to a stimulus and in exchange produce a response. Smart materials exhibit highly relevant properties such as self-healing, self-reinforcing, self-sensing, colour-changing, viscosity-changing, light/matter-emitting, optically changing, and shape-morphing, making them relevant to a variety of fields such as agricultural, structural, aerospace, robotics, electronics and biomedical *[244-249]*.

Table 2.1: Common definitions of smart materials.

| Definitions | References |
|---|---|
| **Smart materials consist of materials which respond to changes in their environment, thus rendering them stimuli responsive.** | [250] |
| **Smart materials are materials and structures with built-in sensing and/or actuation functions** | [251] |
| **Smart materials are materials whose properties (mechanical, optical, electrical, thermal, chemical, electromagnetic) are changeable in response to a change in one of the surrounding properties of its environment.** | [3] |
| **Smart materials are materials which can show noticeable changes in their properties with environmental stimulation** | [252] |
| **Smart materials are a special class of materials of which the material properties can be influenced in a significant or novel way by changing the environmental conditions in which they operate.** | [253] |
| **Smart materials are common name for a wide group of different substances. The general feature of all of them is the fact that one or more properties might be significantly altered under controlled condition** | [254] |

Shape morphing materials, which can change shape in the presence of an appropriate stimulus, are a promising subclass of stimuli-responsive materials. These materials were firstly reported by Greninger and Mooradian in 1938 [255] which used the term “shape-memory” to describe the behaviour of cooper-zinc (Cu-Zn) and cooper-tin alloys (Cu-Sn) and by Chang and Read [256] on gold-cadmium (Au-Cd) alloys. Similar effects have been reported for other copper-based (Cu-Zn-Al, Cu-Al-Ni, and Cu-Mn), iron-based (Fe–Pt and Fe Mn—Si), and nickel-based (Ni–Ti and Ni Mn—Ga) alloys [257-259]. Nitinol (Ni-Ti alloy) was first patented in 1965 by Buehler *et al.* [260, 261]. Similarly, Vernon [262] used the term “shape-memory” in a US patent to describe the behaviour of methacrylic ester-based dental materials. In the 1960s, covalently crosslinked polyethylene (PE) was used to fabricate heat-shrinkable tubing [263]. Later, CDF Chimie (France) and Mitsubishi (Japan) developed polynorbornene and polyurethane (PU) shape memory polymers, respectively [264, 265]. Since these pioneering

studies, a wide range of smart materials have been investigated including multiple thermoplastics, thermosets, elastomers, hydrogels, liquid crystals, and composites [266-268]. Smart alloys present very interesting properties such as excellent mechanical properties, high actuation stresses (> 400 MPa) and high energy density (~1200 J/kg) [269]. However, they have limitations in terms of actuation strain (max of 8%), actuation frequency due to the slow recovery, energy efficiency (< 15%) and transformation induced plasticity [269]. Moreover, they are difficult to process and expensive [270]. On the other hand, shape morphing polymers easily respond to the same stimulus, present lower density, large shape deformability, high recoverable strain, being less expensive and easy to process [271-273]. A brief comparison between shape morphing alloys and polymers is presented in Table 2.2. Due to these advantages shape morphing polymers are gaining increasing relevance as shown in Figure 2.8, which presents the number of papers published since 1961, based on a search using the Scopus database and the following keywords: “shape morphing polymers”, “shape memory polymers”, “shape changing polymers”, “shape morphing materials”, “shape memory materials” and “shape changing materials”. As observed the number of published papers focusing on smart polymers accounts for almost 25%.

**Table 2.2:** Relevant properties of shape morphing alloys and polymers [35, 36]

| | **Alloys** | **Polymers** |
|---|---|---|
| Density range | 6-8 (g/cm$^3$) | 0.9–1.1 (g/cm$^3$) |
| Shape recovery percentage | < 8% | <800% |
| Processing conditions | >1000 ºC; high pressure | < 200 ºC; low pressure |
| Stiffness (GPa) | ~80 | 0.01-0.03 |
| Deformation stress (MPa) | 50-200 | 1-3 |
| Recovery stress (MPa) | 150-300 | 1-3 |
| Response time | < 1 s | > 1 s to 1 min |
| Number of cycles | High | Very high |

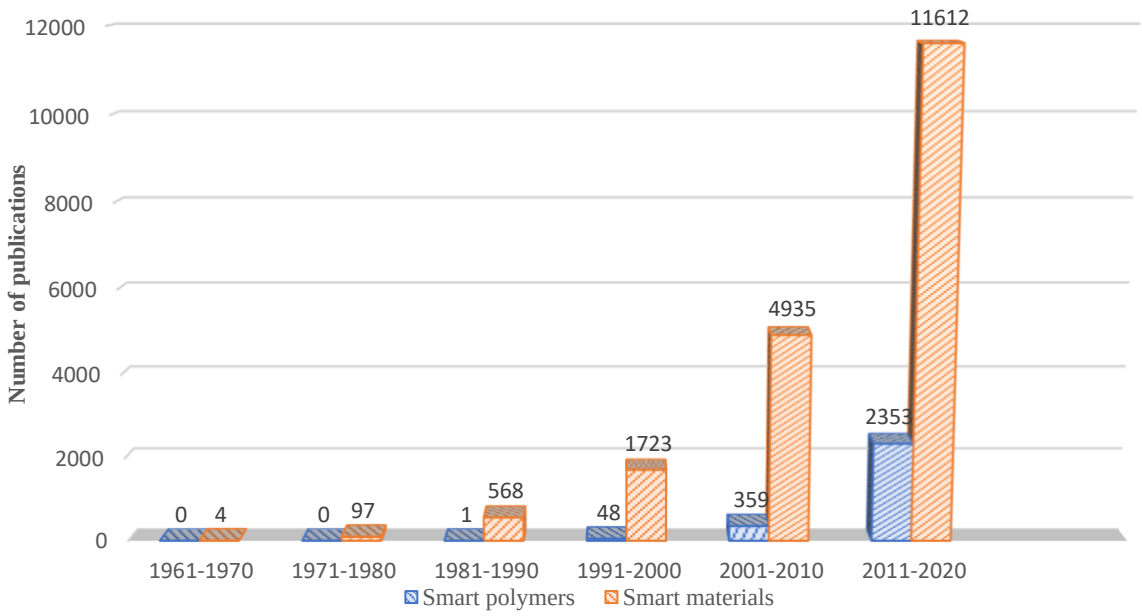


**Figure 2.8**: Trend in Shape Morphing Polymers publications by decade.

Up-to-date research and review papers discuss shape memory polymers extensively presenting different responses, morphologies, and applications. With the increase in reversible shape-effect polymers, there is a need for a classification of different functional mechanisms including reversible and non-reversible shape-effect polymers, morphologies, and applicable characterization techniques. Based on this knowledge, we propose a general classification of shape-effect polymers combining reversible and non-reversible shape-effect polymers into shape-morphing polymers.

### 2.2.2 Classification

Shape-morphing polymers are broadly classified based on their functionalities, morphologies, and stimuli.

### 2.2.3 Functionality

Shape-morphing polymers exhibit a deformation response when a stimulus is applied, and can be classified as follows (Figure 2.9) [274, 275]:

- *Shape memory polymers (SMPs)* present a non-reversible deformation to a temporary programmed shape when a stimulus and a force are applied, and then recover to their original shape either instantly or gradually when the stimulus is applied (Figure 4a). Examples include polylactic acid (PLA), thermoplastic polyurethane (TPU), and polyethylene terephthalate glycol (PETG) [276-278].

- *Shape changing polymers (SCPs)* present a reversible deformation behaviour either instantly or gradually when the stimulus is applied or removed without the need for an external force (Figure 4b). Examples include Polyvinylidene Fluoride (PVDF), Azobenzene, and Polyvinyl Chloride (PVC) [279-281].
- *Hybrid shape polymers (HSPs)* exhibit the behaviour of both SMPs and SCPs [282-284].

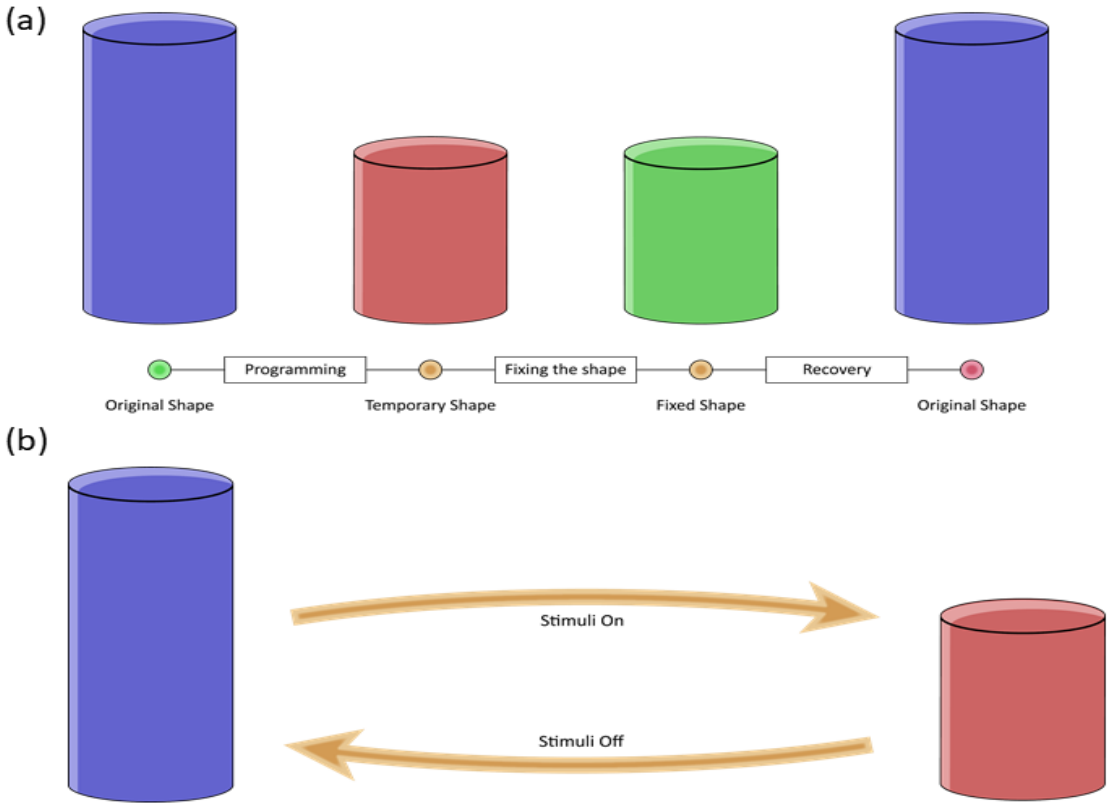


**Figure 2.9:** Subclasses of shape morphing polymers: (a) shape memory polymers, (b) shape changing polymers.

Design the functionality can be achieved by controlling the activation energy (Figure 2.10). The non-reversible and slow-shape-morphing effect, known as the shape memory effect, is characterised by a high-energy barrier. However, the reversible and fast shape-morphing-effect is characterised by low energy [285, 286].

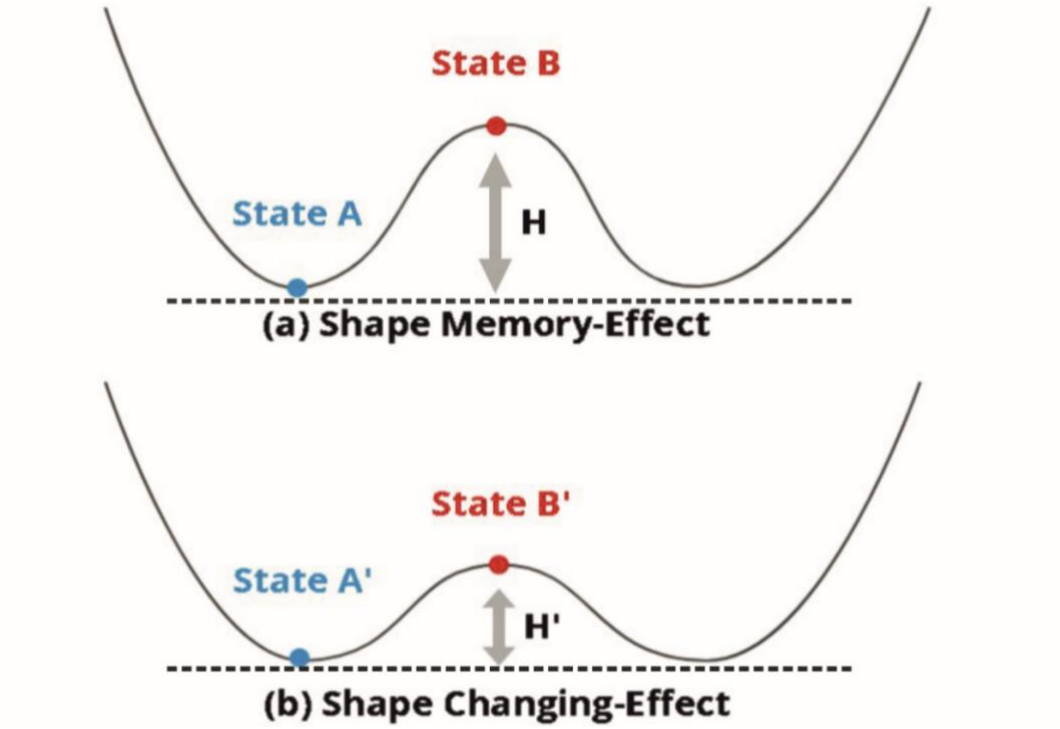


**Figure 2.10**: Activation energy requirements for SMEs and SCPs, where H is the energy barrier for the shape memory effect, and H' is the energy barrier for the shape changing effect. (a) Shape memory-effect: the material beginning in State A (original shape) and can go to state B (temporary shape) when the appropriate stimuli supply enough energy to overcome the energy barrier H and load. (b) Shape changing effect: the material beginning in State A' (original shape) can go to State B' (temporary shape) when the appropriate stimuli supplies enough energy to overcome the energy barrier H'.

Multi-responsive polymers can follow non-sequential and sequential pathways as shown in Figure 2.11. Orthogonal or non-sequential multi-response materials (Figure 2.11a) are the ones that exhibit multi-responses each one independent from each other. An example is a smart tissue engineering scaffold that presents a shape-memory effect to self-adjust to a specific defect (Output 1), triggered by body temperature, and a degradation response (Output 2) due to hydrolysis and/or enzymatic activity. Sequentially multi-responsive materials (Figure 2.11b) exhibits coupled multi-responses. An example is a hydrogel-based drug release system that changes its shape (Output 1), due to pH or temperature changes, releasing the encapsulated drugs (Output 2) (Figure 2.12).

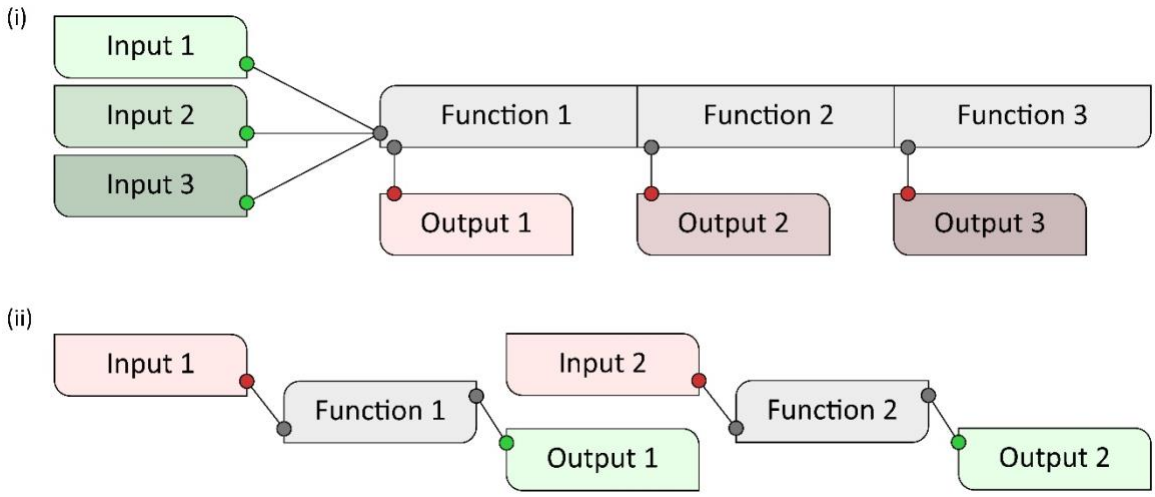


Figure 2.11: Orthogonal (i), and sequentially (ii) coupled functions.

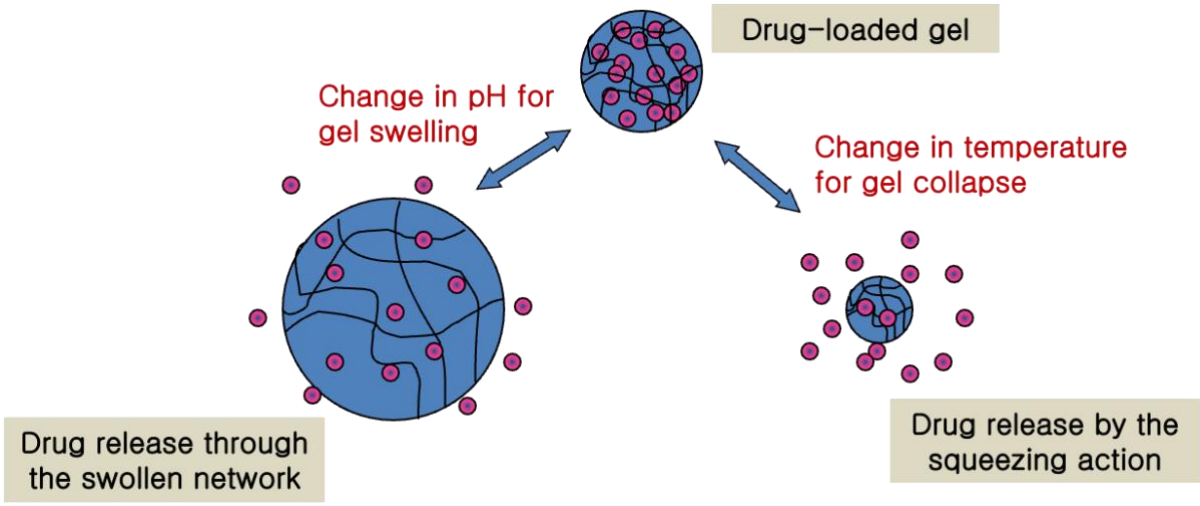


**Figure 2.12**: Smart multi-responsive hydrogel-based drug delivery system.

SMPs and SCPs can be engineered to exhibit one, two, or multiple responses based on programmed inputs [38]. At the macroscopic level, few properties (e.g., shape fixity, recovery, and recovery time) can be evaluated to assess the responses and extent of shape-morphing polymers. The ability to switch segments to fix a mechanical deformation, known as shape fixity ratio ($R_f$), describes the ability of the material to maintain the programmed shape after the stimuli is removed, and can be described as follows [287, 288]:

$$R_f(N) = \frac{\varepsilon_u(N) - \varepsilon_p(N-1)}{\varepsilon_m(N) - \varepsilon_p(N-1)} \tag{2.7}$$

where N is the number of cycles, $\varepsilon_u(N)$ is the strain after removing the stimuli, $\varepsilon_p(N)$ is the strain in the temporary state, and $\varepsilon_m(N)$ is the maximum strain [289].

Shape recovery (Rr), describes the ability of the material to recover to its original shape and can be evaluated on a per-cycle basis after N cycles to that of the permanent shape [287, 288]:

$$R_r(N) = \frac{\varepsilon_u - \varepsilon_p(N)}{\varepsilon_m(N) - \varepsilon_p(N-1)} \tag{2.8}$$

The shape recovery time ($R_{r,tot}(N)$), or the time required for the material to reach a recoverable strain is given by the following equation [290-293]:

$$R_{r,tot}(N) = \frac{\varepsilon_m - \varepsilon_p(N)}{\varepsilon_m} \tag{2.9}$$

### 2.2.4 Morphology

The morphology of shape-morphing polymers comprises (a) net points that behave as connecting points being responsible for the permanent shape, and (b) active segments responsible for the shape-morphing effect [294, 295]. Net points can be chemical crosslinks (covalent bonds) or physical crosslinks (physical interactions, chain entanglement, interpenetrated polymer networks, and crystalline and glassy polymer segments) (Figure 2.1) [296, 297]. Physical crosslinks are reprocess able, allowing the material to be reprogrammed to change its temporary shape if desired [296-298], but they can degrade throughout their lifetime, which might compromise their long-term performance [296, 297]. Chemical crosslinks cannot be reprocessed, thus improving both the performance over shape-morphing cycles and recovery [299, 300]. Active segments are polymer chains between net points and usually involve supramolecular interactions (e.g. hydrogen bonding, metal coordination, ionic interactions, and π–π or arene–arene interactions) in which non-covalent forces hold the structure together, reversible interactions/bonds, isotropic-anisotropic phase transition, vitrification-glass transitions, and crystallization-melting transitions [300, 301].

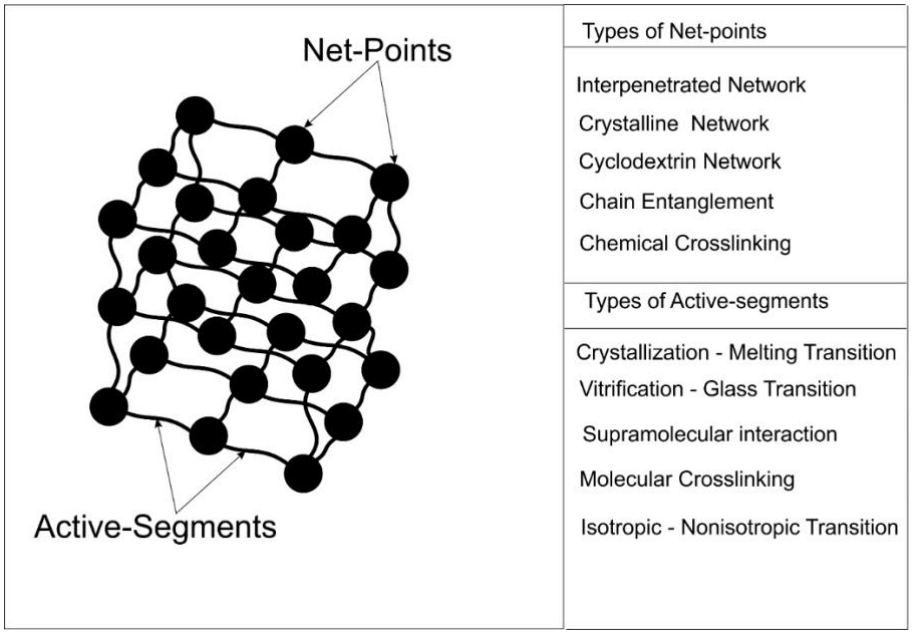


**Figure 2.13:**Active segments and crosslinks found in different types of SMPs.

### 2.2.5 Stimuli

Shape-morphing polymers can also be classified based on the stimuli they respond to as shown in Figure 2.14 and discussed in detail in this sub-section.

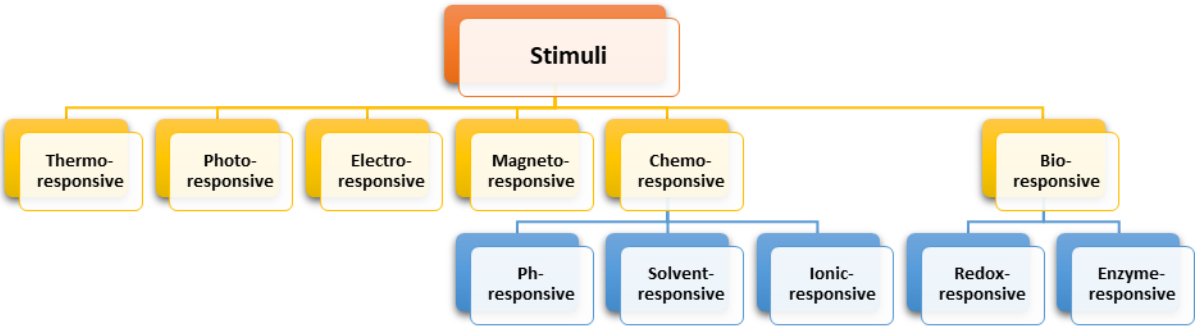


**Figure 2.14:** Classification of shape-memory polymers based on the stimuli they respond to.

### 2.2.6 Thermo-responsive

Thermo-responsive polymers comprise thermoset SMPs (TS-SMPs) and thermoplastic SMPs (TP-SMPs) materials [302-304]. TS-SMPs are based on chemical crosslinks (e.g. covalent bonds) formed by the reaction between two functional groups, while TP-SMPs are based on physical crosslinks (e.g. dipole interactions, London dispersion forces, and hydrogen bonds) [305]. Moreover, physically, and chemically crosslinked polymers can exhibit both crystalline and glassy networks. Therefore, the responsive mechanisms of TS and TP-SMPs differ because of the nature of the crosslinks that determines if the shape is permanent or not, and the network

type that determines the transition temperatures ($T_{trans}$) for each class of materials [306]. Multiple material composite networks exhibit multiple $T_{trans}$ as shown in Figure 2.15. These different polymers can be summarised as follows:

- Physically crosslinked crystalline networks (Type I, $T_{trans} = T_m$),
- Physically crosslinked glassy networks (Type I, $T_{trans} = T_g$),
- Covalently crosslinked crystalline networks (Type II, $T_{trans} = T_m$),
- Covalently crosslinked glassy networks (Type II, $T_{trans} = T_g$),
- Multiple composite networks (Type III, $T_{trans} = T_g$ and $T_{trans} = T_m$)

Figure 2.16 highlights the thermo-response of a shape morphing polymer going from cold state (blue) to hot state (red) [307].

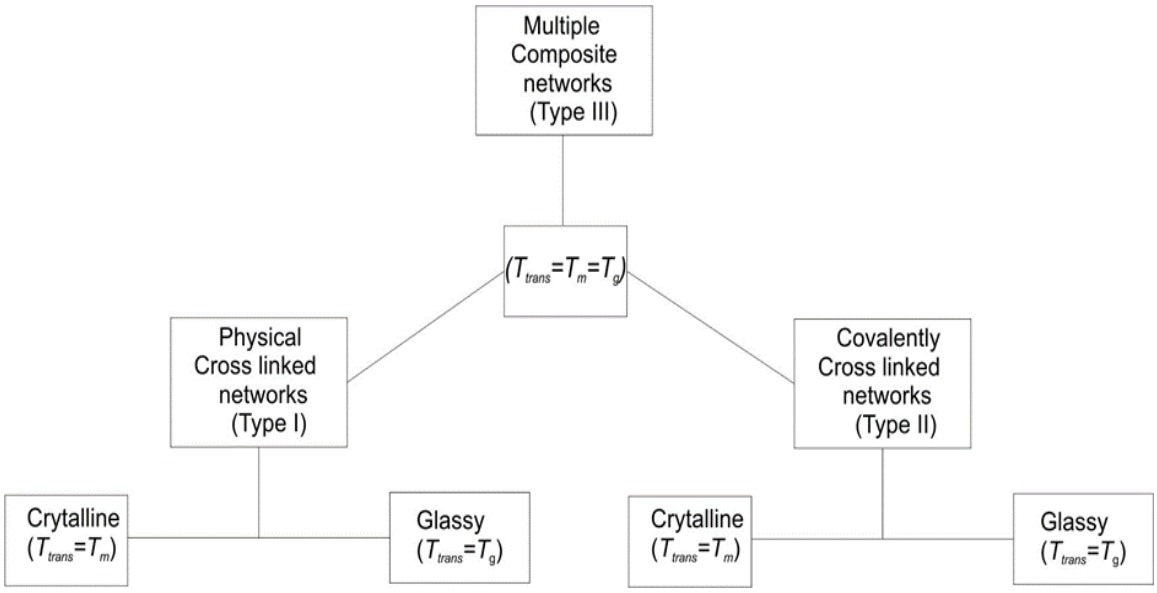


Figure 2.15: Different classes of thermo-responsive polymers.

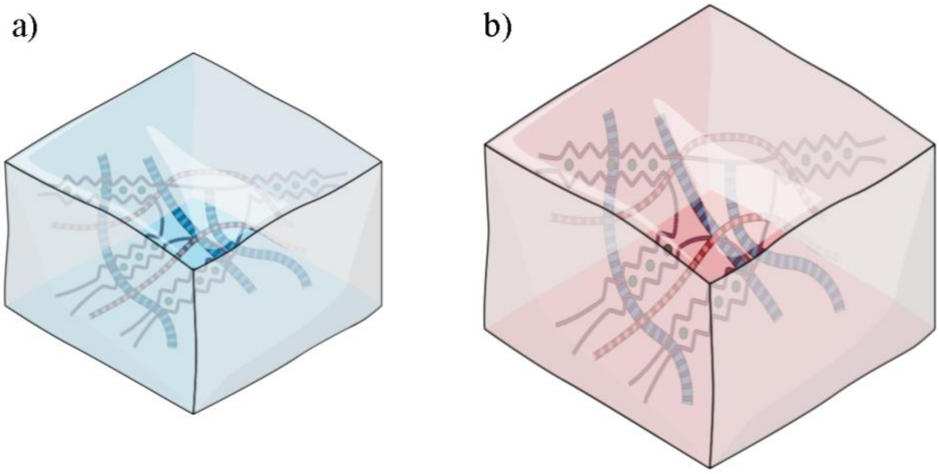


**Figure 2.16**:Thermo-responsive SMP highlighting shape changing behaviour: (a) Cold state: at equilibrium the part is in its original shape, (b) Hot state: increase in temperature will activate the shape morphing effect into the temporary shape.

Liquid crystal elastomers (LCEs) are thermoplastic materials with the unique ability to undergo a phase change when heated above the transition temperature ($T_{trans}$). This phase change occurs from the ordered nematic phase to the disordered isotropic phase, and as a result, the LCE begins to contract along the direction of alignment and expands in the orthogonal directions. This phase change is reversible upon cooling the LCE [308, 309].

### 2.2.7 Photo-responsive

Photo-responsive polymers are obtained by adding a proper chromophore or nanofiller to the polymer. Therefore, two different mechanisms can be obtained. The addition of nanofillers induces a photothermal mechanism, where the activation mechanism is due to the fillers absorbing the irradiated light and transforming it into heat, which triggers shape-morphing effects. In contrast, photochemical molecules absorb light and transfer it to chemical energy, causing isomerisation, scission, or the formation of extra crosslinks [310-313].

An example of a photo-thermal-responsive polymer is LCE, demonstrating this functionality, where heat is dissipated to trigger a phase transition from an ordered nematic phase to a random phase presenting a large reversible volume contraction [314]. Another example is the use of polymers with different coefficients of thermal expansion (CTE) as a bilayer structure, resulting in a bending motion [315]. Polymers with photothermal fillers such as graphene oxide (GO), carbon nanotubes (CNT), carbon black (CB), gold, cellulose, and dyes can exhibit this functionality and large reversible reactions [314-318].

Photochemical fillers can act as crosslinks if the reaction is irreversible, or as active segments and reversible crosslinks if the reaction is reversible [319]. Upon activation each chromophore undergoes different reactions. Common crosslinkers, such as azobenzene, undergo reversible trans-cis isomerisation when subjected to UV-visible light, mechanical stresses, or electrostatic simulation [320-322]. Other chromophores, such as cinnamic esters, coumarins, and diarylethenes, undergo a [2+2] cycloaddition, while fulgides undergo ring-opening/closing isomerisation reactions [323, 324]. Spiropyran and spirooxazine undergo photocleavage under UV irradiation [325], salicylideneanilines undergo enol–keto tautomerization [326], and anthracene undergoes a 4+4 photocycloaddition reaction under UV irradiation [327]. The same molecules can also undergo other reactions, depending on the synthesis route and whether they are substituted or a derivative [328, 329]. Examples of photothermal and photochemical processes are shown in Figure 2.17.

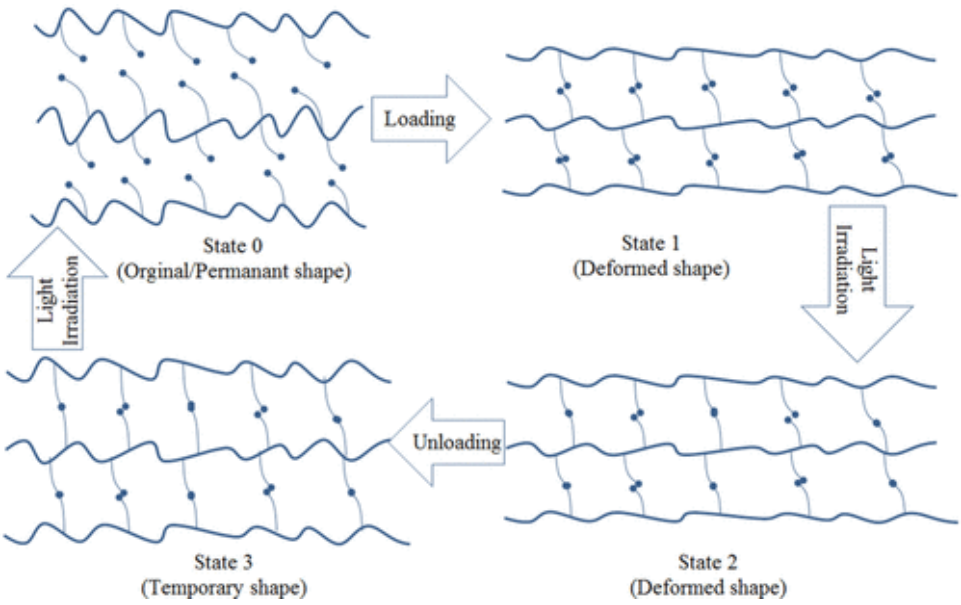


Figure 2.17: Activation scheme for light responsive polymers [311].

### 2.2.8 Electro-responsive

Electro-responsive polymers can be classified as Ionic electroactive polymers (IEAPs) and Intrinsic- or Extrinsic-Electronic electroactive polymers (EEAPs) [330-333]**.** IEAPs react to the movement of ions or molecules, causing dimensional changes in the intermolecular or intramolecular interactions (Figure 2.18) [334, 335]. The advantages of IEAPs include significant displacements, low operating voltages, and bidirectional actuation based on the voltage polarity. However, IEAPs cannot hold strain under DC voltage, except for conductive polymers (CPs) and carbon nanotubes (CNT). These materials also present a slow response,

and bending induces low actuating forces (REF). Moreover, they suffer electrolysis at higher voltages (aqueous systems), and have low electromechanical coupling efficiencies [336-338].

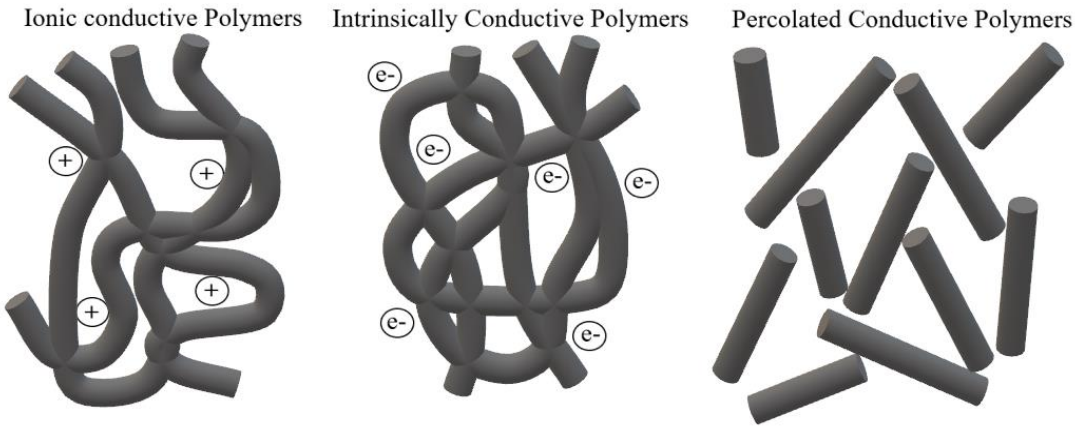


**Figure 2.18:**IEAP mechanism (Left), EEAP-Intrinsic (middle), and EEAP-Extrinsic (right).

IEAPs function is based on ion migration. However, the mechanism of each material varies only marginally. Ion-exchange polymer-metal composites (IPMC), an important sub-class of IEAPs, present a polyelectrolyte membrane plated with a noble metal and neutralised with a counter ion to balance the charge of the positive ions covalently bonded to the backbone. Bending arises from the negative ion movement under an applied voltage [339]. On the other hand, ionic gels consist of a simple structure where the gel embedded with ionic liquid is sandwiched between flexible electrodes, and as the voltage is applied electromechanical motion takes place because of ions travelling towards the opposing electrode [340]. Carbon-based materials, such as carbon nanotubes (CNTs) suspended in an electrolyte, form a double layer with the nanotubes, allowing the injection of charges which in turn changes the charge balance. In addition, the number of charges affects dimensional changes. Electrons leaving will result in an overall positive charge that will create repulsion and increasing bond length, and the addition of electrons will also cause the opposite [341].

EEAPs react to electric fields and Coulomb forces [342], and the activation is caused by intrinsic or extrinsic conduction mechanisms (Figure 2.18) [337]. The advantages of EEAPs are their ability to function under room conditions for a long time, quick response (millisecond), ability to hold strain, and to produce large actuating forces [343]. However, they require very high field strengths and voltages (20 – 150 V/µm), and the actuation is independent of voltage polarity [338, 344].

EEAP-Intrinsic are regarded as synthetic metals as they have similar electrical, magnetic, and optical properties to metals and semiconductors [345]. This is because of the conjugated nature

of the polymer, where there is an alternating single- and double-bond sequence in the polymer backbone [346]. This configuration leads to the creation of high-energy orbitals with delocalised polarisable π-electrons. However, the real use is only realised after doping to improve charge carrier movement and conductivity [345, 346]. The advantages include ease of processing, soft/compliance, conductivity, biocompatibility, and tunability [347].

EEAP-Extrinsic are prepared by adding conductive fillers to the polymer matrix. When fillers exceed a minimum concentration value, known as the percolation threshold, one or more continuous networks form throughout the polymer [348]. Therefore, conductive paths are created for the charges to flow through, due to the proximity of the fillers [349]. This percolation limit depends on the polymer matrix, filler conductivity, filler shape, mixing method (preventing agglomeration), and polymer-filler interaction [350-352]. A major advantage is their tunability using different additives, which improves their mechanical properties [349].

### 2.2.9 Magneto-responsive

Magnetic-responsive SMPs and SCPs are obtained by adding magnetic nanoparticles (MNPs) such as Ni, $Fe_3O_4$, $Fe_2O_3$, niquel-manganese-gallium (Ni-Mn-Ga), NiZn and neodymium-iron-boron (NdFeB). Fillers such as magnetite nanoparticles ($Fe_3O_4$) also exhibit low cytotoxicity and excellent magnetic properties.

Magnetically induced recovery is caused by inductive heating (eddy currents, hysteresis, and rotational losses) of the magnetic particles under an alternating magnetic field. The application of a magnetic field induces two mechanisms. The first mechanism takes place when the magnetic field affects the average interaction between moments in the system [353]. Therefore, upon the application of the magnetic field, the moments co-align, and the average interaction becomes direction-dependent, resulting in an elongation parallel to the field and a shrinkage in the perpendicular direction. Adequate interactions between the particles are critical to achieve this. In the second mechanism, a homogenous field is applied to a material, with particles acting as crosslinkers. The applied field causes the particles to rotate, and the strain is transferred to the polymer, resulting in an overall shape change.

There are five possible magnetic states: (a) paramagnetic, (b) diamagnetic, (c) ferromagnetic, (d) antiferromagnetic, and (e) ferrimagnetic, as shown in Figure 2.19 [354]. Depending on the magnetic state, the application of an external magnetic field can highlight the different pole alignments of these states, where each state represents a particular texture. The degree of alignment describes the magnitude of the magnetic moment and susceptibility of the magnetic

material. Ferromagnetic materials exhibit the highest alignment, followed by ferrimagnetic, antiferromagnetic, paramagnetic, and diamagnetic materials [355]. The approach of using magnetic nanoparticles below a critical size reduces the domains to a single domain that exhibits uniform magnetisation and no hysteresis loop. This behaviour is labelled as superparamagnetic. Therefore, MNPs have large magnetic moments and behave like large paramagnetic atoms with fast responses [353].

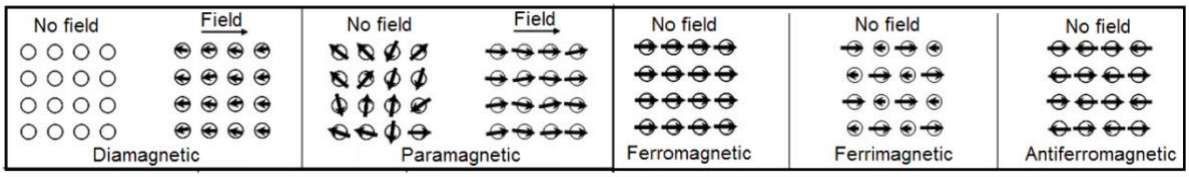


**Figure 2.19**: Different magnetic states diamagnetic, paramagnetic, ferromagnetic, (d) ferrimagnetic, and antiferromagnetic [156].

### 2.2.10 Chemo-responsive

Several materials fall under the chemically responsive group of polymers including pH-responsive materials, which can swell or shrink because of the pronation or ionization of chemical groups [356]. pH-responsive materials exhibit a polyelectrolyte functionality due to the pronation of polymers. This occurs when a proton is accepted or donated based on changes in pH causing a globule-coil transition (polymer chain coiling) due to electrostatic repulsion of charged functional groups or globule structure if the charge is neutralized [357]. Weak poly bases accept protons under acidic conditions, or weak polyacids that donate protons under neutral and basic conditions and still accept protons under acidic conditions, as shown in Figure 2.20 [358]. Examples of weakly acidic polymers include those containing carboxylic groups, sulfonic acids, phosphonic acids, and boronic acids, while weakly basic polymers include amine groups, morpholino and pyrrolidine, piperazine and pyridine, or dendrimers [359]. Natural polymers such as collagen, gelatine, and keratin, commonly used for tissue engineering applications are pH-responsive [359].

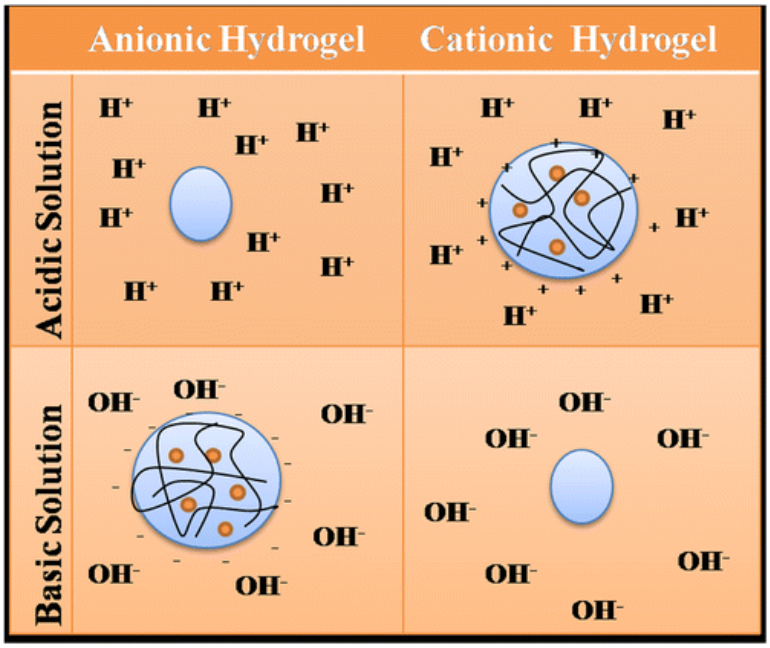


**Figure 2.20**: The effect of pH changes on pH-responsive hydrogels [158].

Another type of chemically responsive materials are solvent-responsive polymers, whose response depends on the type of solvent and polymer being used. For example, water-responsive polymer functions are based on the chemical reaction with water that acts as a plasticiser to reduce the transition temperature or by interacting with hydrogen bonds [360, 361]. It also occurs through physical interactions, such as water migration in the structure, inducing shape changes and recovery [360]. ]. Relevant polymers include polyurethane with pyridine moieties, cross-linked poly(vinyl alcohol) (PVA), cross-linked poly(ethylene glycol) (PEG), and polycaprolactone (PCL) [361, 362]. A common feature of these materials is the presence of hydrophilic or hydrophobic segments.

The effects of different solvents (e.g., water, dimethyl sulfoxide (DMSO), methanol, acetic acid, and tetrahydrofuran) were assessed on some materials, such as cross-linked PVA. Solvent-induced swelling reduces the glass transition temperature and flexibility of the polymer chain segments, thereby triggering shape recovery. The type of solvent strongly determines the absorption, diffusion, and interaction with the functional groups in the polymer (e.g. hydroxyl) [363]. Other examples of PVA embedded with graphene oxide (GO) also indicate that water immersion can result in hydrogen bond formation with the hydroxyl group, which can affect the hydrogen bond between PVA and GO [364]. Competitive hydrogen bonding reduces the internal energy and has a similar effect on increasing temperature [364]. It was also reported that polyurethane with cellulose nano whiskers (CNW) when exposed to water, exhibits a phenomenon like PVA-GO with competitive hydrogen bonding between water and CNW. This

leads to reduced hydrogen bonding and weakens the CNW network, and the change in stiffness allows shape change and recovery of the composite, as shown in Figure 2.21 [365].

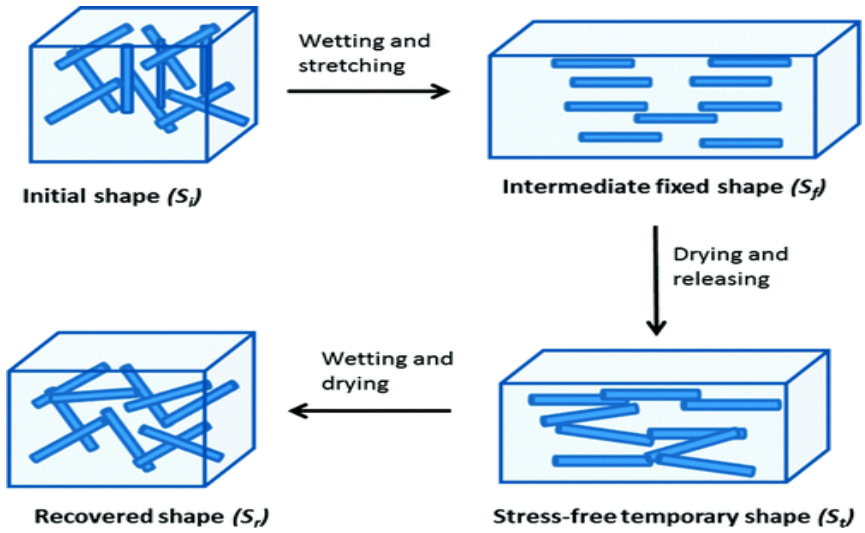


**Figure 2.21:** Shape morphing of PU nanocomposite during wetting/drying cycle [165].

### 2.2.11 Bio-responsive

Redox/glucose-responsive polymers can mimic the response of the human body to glucose fluctuations and insulin secretions [366-368]. This response is typically produced through the enzymatic oxidation of glucose-by-glucose oxidase ($GO_x$), binding of glucose with lectin, or phenylboronic acid moieties [369]. The polymer does not directly detect glucose, but by-products such as gluconic acid produced through the enzymatic oxidation of glucose. The response mechanism can be explained by the conjugation of $GO_x$ with poly (acrylic acid) (PAA), leading to the conversion of glucose into gluconic acid, pronating the PAA carboxylate, and reducing the pH. A reduction in pH leads to the release of insulin, which mimics the endogenous secretion of insulin by the pancreas.

Molecules such as diglucosylhecadiamine have also been used [370]. In this case, the material responds to an increase in the glucose concentration by decreasing the crosslinking density of the gel, thus secreting insulin. A reversible mechanism can be achieve through the crosslink between diglucosylhecadiamine and borate polyol l [357]. A similar strategy was used to produce shape memory effects through the oxidation of glucose by $GO_x$ to produce hydrogen peroxide, an oxidant that interacts with a cyclodextrin modified chitosan and ferrocene modified branched ethylene imine polymer (B-CD-CS/Fc-PEO). This structure has both reversible redox phases and covalent crosslinks [371].

Enzyme-responsive polymers can catalyse the conversion of molecules (substrates), and the design of such polymers can produce structures with enhanced triggering specificity and

selectivity [372]. Shape recovery is triggered when enzymatic-catalysed degradation occurs. This mechanism depends on the dose of the enzyme supplied, time, sensitivity and active segments [373].

### 2.2.12 4D printing

The combined used of additive manufacturing (3D Printing) and smart materials has been termed as 4D printing. The fourth dimension is functionality or time [374]. 4D printing results in dynamic structures in contrast to static structures produced by conventional additive manufacturing [375]. These dynamic structures can be utilised for several applications, including sensing, actuating, electronics, and biomedicine [376-378].

The most common AM systems for 4D printing of SMPs are Extrusion based printing including fused deposition modelling (FDM), Vat Polymerisation (VP), and Material Jetting (MJ) (Figure 2.22) [356, 379]. Printing parameters can control the performance of SMPs printed parts, as they affect their morphology [380-383]. Moreover, various factors must be considered prior to the selection of the printing method: (1) material rheological properties, (2) material thermal stability, and (3) form of the material (e.g., pellets, filaments, ink, gel) [384-386].

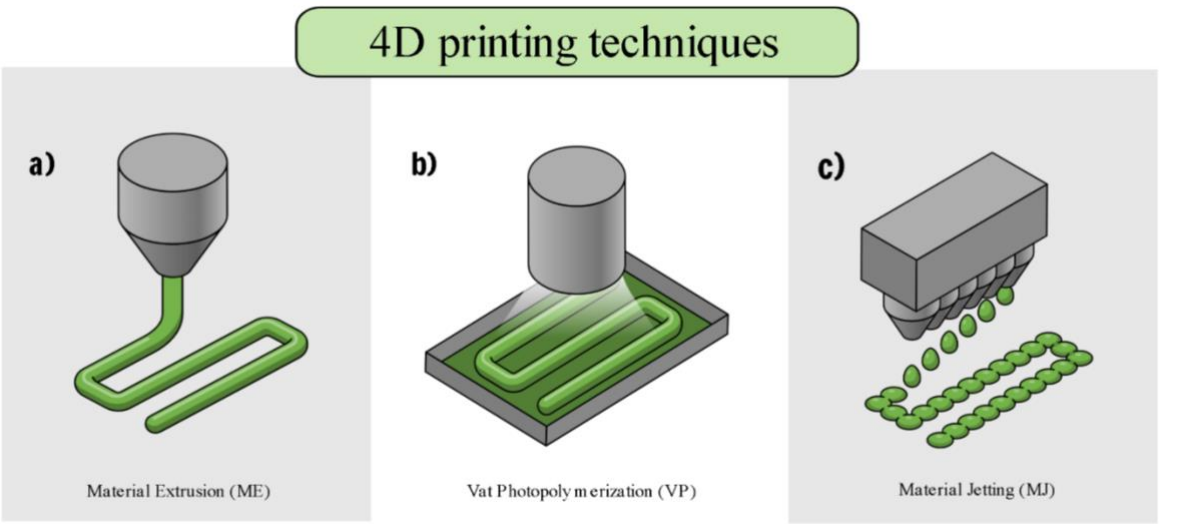


**Figure 2.22**: 4D printing techniques used for shape morphing polymers, (a) ME, (b) Vat photopolymerization, and (c) MJ.

Fused-deposition modelling (FDM) uses filaments for printing, such as thermos-responsive shape memory polymers (e.g., Polylactic Acid (PLA), Polyethylene terephthalate glycol (PETG), Thermoplastic Polyurethane (TPU), and Polyamide (Nylon)) [387-389]. The challenge of using FDM is the availability of filament materials. It is possible to address this issue by using screw-assisted 3D printing, which allows the use of granular materials such as

pellets [390]. In addition, the screw presents improved mixing, homogeneity, and orientation of polymer chains and crystals. This allows to control the physical properties through the screw rotation and printing temperature [391, 392]. Challenges faced by extrusion-based AM processes included the limited printing resolution due to the dependence of the viscosity on the highest temperature achievable, and limited nozzle sizes. Moreover, the use of temperature can degrade some temperature-sensitive polymers, therefore, limiting their functionality [393].

Vat photopolymerization uses light to activate photo-initiators which trigger a chemical curing reaction [394]. The advantage of such technique is the high resolution and ability to control monomer and crosslinker content. However, vat photopolymerization systems are expensive, and there is a strong dependency between resolution and material viscosity tat as also an impact on the overall printing time [395].

Material jetting is based on ejection of liquid droplets. Inks used must be very fluid to address problems related to nozzle clogging, and that can also limit the concentration of added material [396].Direct ink writing (DIW) it a strategy which combines elements of material extrusion and the use of inks with a wider range of viscosities without relying on temperature [396]. The extrusion of the material is through pneumatic, mechanical pistons, or screw rotation. Ink structure and composition can affect the resolution, viscosity, and properties of the material, thus, ability to design an ink allows the use of a wide range of shape morphing polymers as shear thinning behaviour is observed in polymer, hydrogel, and soft matter inks [397, 398]. Limitations of printed components include limited mechanical properties, and may need to be post processed [399]. Developing of multi-material inks can extend the capabilities of DIW by presenting improved physical and chemical properties for single- or multi-functional structure designs [400-404]. Printed components using DIW allows a range of polymers, solvents, and fillers can allow high polymer and filler content in the inks, thus, improving their properties and functionalities [405-408]. These advantages highlight the promising potential of DIW strategy and the use of printable inks for 4D printing of shape morphing polymers.

### 2.2.13 Conclusion

Enormous progress has been made in terms of the performance and functionality of SMPs since they were first introduced in the 1960s. Commercial and advanced applications have led to rapid improvements in our understanding of shape-memory behaviour. This section discusses state-of-the-art developments in shape-morphing polymers. First, the concept of smart materials is introduced and defined. Different classifications of shape morphing polymers are presented and discussed in detail. The concept of 4D printing, the combined use of smart

materials and additive manufacturing, is also introduced. This is a rapidly growing field. However, the response of the most commonly used smart materials to external stimuli is highly dependent on the printing technique and printing strategies (e.g., lay-down pattern, layer thickness) and the combination of multiple materials can have a significant impact on such response. Few systems were reported to be sensitive to a range of different stimuli and this represents an important topic of research. The development of standards is another important challenge. The development of correlations between processing conditions, morphological behaviour and short-, medium- and long-term behaviour of printed parts is fundamental. This will allow to better tune the performance of the parts. In the case of composite/multi-material printing it will be important to have a better understanding on the interaction between materials during the printing and post-printing stages.

The development of mathematical models to predict and design the behaviour of responsive shape morphing polymers is also critical. Moreover, additive manufacturing systems must include extra elements (e.g., sensors, machine learning controls, etc.) to address 4D printing technological challenges such as triggering or activation mechanism and structural stability [409-411]. Finally, it will be important to further investigate direct and indirect activation methods for shape morphing polymers, as well as improving shape morphing capabilities to achieve more cycles before degradation, higher forces, and speeds during shape transformation, and improve shape fixity are also critical [412-414].

Section 2.1 investigated thoroughly the use of non-enzymatic sensors for glucose detection which is a very important part of the proposed biosensor. Non-enzymatic sensors present with a very high electrocatalytic activity, and high sensitivity to the electrooxidation of glucose, while not using any biological sensing molecules hence having long shelf life. This makes non-enzymatic glucose sensor the perfect candidate for infield usage. Section 2.2 studies and introduces smart) shape morphing) materials which are materials that can respond to a change in environment by changing shape. To replicate the structure and function of stomata the use of smart material with a response to light and temperature is the most suitable. Finally, based on the extensive investigation could not find any publication (application) use of these materials in non-enzymatic biosensors. The combination of non-enzymatic glucose sensing and smart material achieves the required yellow rust germination cues (i.e., replicating the plant morphology and stomatal behaviour, detecting produced glucose from the invertase enzyme secreted by the spores).

# Chapter 3: 4D printing of a bioinspired leaf sensor surface

*A plant leaf is a highly hierarchical and complex structure essential for plants to perform photosynthesis and to develop. It is also through the leaf and through their stomata, openings used by the plant for gas exchange, that pathogenic fungus after germination penetrate the leaf and infect the plant. It is challenging to germinate yellow rust on artificial surfaces as it requires specific germination ques. These ques require the surface to have the same morphology as the target crop (wheat), suitable volatiles, as well as a non-enzymatic layer which can detect glucose however needs to be stable in field environment. The following research questions are addressed in this chapter. What is the required surface morphology? How to obtain a biomimetic replica of the target crop? What volatile would enhance germination? How is glucose detected? This Chapter presents the preliminary results on the study of topological cues to promote fungal growth on the surface of a biosensor and describes the multi-material and multi-functional biosensor, with biological detecting elements, mimicking the structure of a plant leaf in terms of structure and topography being able to detect the presence of specific pathogens (e.g., yellow rust, brown rust).*

## 3. 4D printing of bioinspired leaf sensor surface♣

### 3.1 Introduction

Rusts are the most relevant fungal diseases affecting wheat. Among the three rusts types (leaf, strips and stem) the leaf rust is the most common type [1, 2]. The pathogen growing temperature is between 7 and 22 ºC and, being particularly active in the fertile crescent of the Middle East. This type of rust has a significant spread capacity, traveling long distances, being able create new resistant races and to rapidly develop under optimal climate conditions. Climate changes are also significantly contributing to its wide distribution across the planet. Strip rust, also known as yellow rust, is particularly damaged when the upper leaves of the plant become highly rusted before flowering, causing early loss of leaves, reducing grain size, which results in smaller kernels [3, 7, 8]. The wheat rust cycle is briefly summarised in Figure 3.1.

Strip rust is caused by *Puccinia striiformis* an heteroecious fungus that requires a host (usually common wheat, *Triticum aestivum*) and an alternative host (*thalctrum speciosissimun* or *isoprysum fumaroides*) to complete the cycle. *Puccinia striiformis* is characterised by highly variable virulence but extremely difficult to detect on time to prevent its dissemination in the field. The current strategy for wheat leaf rust management is the use of genetically resistant varieties, but the main drawback of this approach is that the pathogen has high capacity to mutate generating new strains that can break down this resistance rendering genetic resistance less effective [7, 8].

♣ This section is based on the following publication: Mohamed Hassan, Abdalla Omar, Bruce Grieve, Paulo Bartolo – "4D printing of bioinspired leaf sensor surface", MACE PGR Conference 2020. Mohamed Hassan main contributions: the design of the biosensor, design of the experimental work, conducted all the experimental and validation tests, analysed the obtained data.

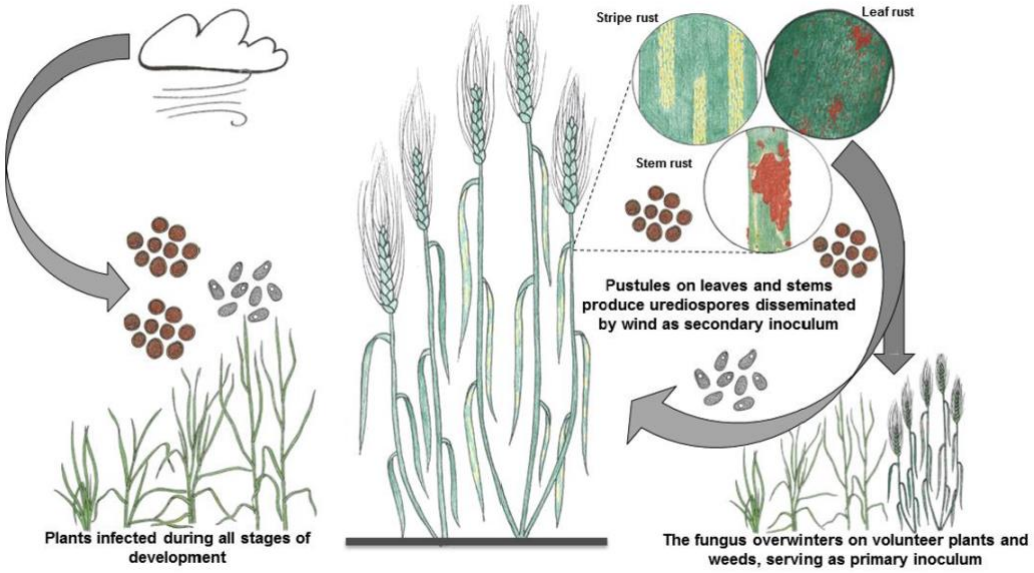


Figure 3.1: Wheat rust cycle [421].

The development of a system able to early detect the presence *Puccinia triticina* is critical, but not available, as it will allow the implementation of proper countermeasures to treat the infection and to reduce the spread of the disease. Typically, leaf rust disease can be visually detected only after 14 days of infection which is by then too late for the use of any fungicide resulting in a significant loss of yield [3, 7, 8, 32, 33].

A three-layer biosensor is proposed in this Chapter and potential candidate materials for its development discussed. The first layer mimics the wheat leaf morphology and the topological cues required to promote fungal growth on the biosensor surface. The second layer is made up of invertase and agar. The agar is used as the hydrogel media creating the solid-like part of the feeding layer. The sucrose is the main substrate and is broken down by the invertase produced by the yellow rust (Figure 3.2), thus enabling its detection. The third and final layer is a Pt/Ni/MWCNT based non-enzymatic glucose sensor fabricated to detect the glucose produced by the yellow rust fungi.

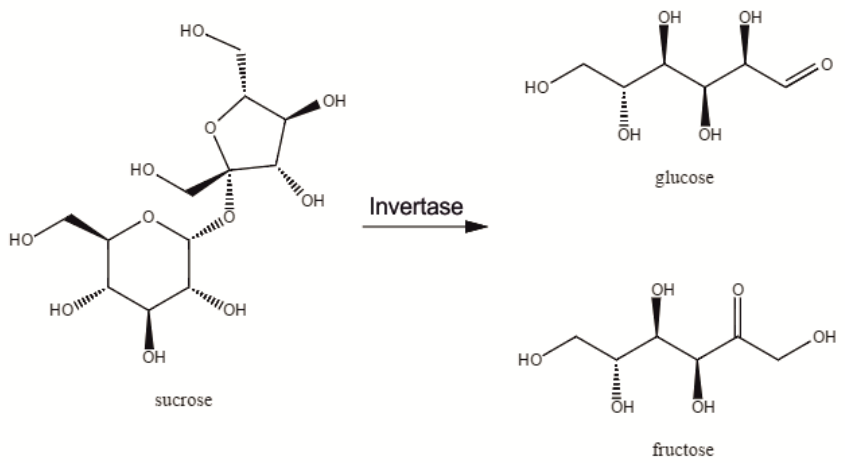


**Figure 3.2**: Schematic for the reaction between invertase and sucrose.

## 3.2 Materials

Different natural and synthetic materials (agar, polycaprolactone and mylar) were used to investigate the yellow rust germination, allowing to study materials with different surface stiffness and wettability. Despite the lack of published information on the yellow rust germination cues, it can be assumed that surface patterning, wettability and volatiles have a major role. Agar 4450 (Sigma-Aldrich, UK) is a natural polymer commonly used for growing different bacteria and microbes. Polycaprolactone (PCL) (CAPA, UK), is a synthetic biodegradable polymer commonly used for tissue engineering applications. It presents high surface stiffness, it is a hydrophobic material, and can be easily printed. Mylar (RS components, UK), a polyethylene terephthalate (PET) based material was used due its easy patterning.

Moreover, polyethylene terephthalate glycol (PETG) (RS components, UK), a glycol modified polyethylene (PET), was also considered as a potential alternative material due to its shape changing behaviour. The ability of PETG to sustain the yellow rust germination is demonstrated in Chapters 7 and 9. Polydimethylsiloxane (PDMS) (Sigma-Aldrich, UK) was used to create the negative moulds used to pattern the different materials, sucrose (Sigma Aldrich, UK) was used as a substrate for the feeding media, and N, N-dimethylformamide (DMF) (Sigma Aldrich, UK) was used to drop cast glucose sensing particles on the screen printed electrodes (SPE).

## 3.3 Leaf Morphology

The wheat leaf surface morphology was characterised using the TESCAN VEGA3 FESEM (Tescan, Czech Republic), scanning electron microscope (SEM). The leaf was not coated, and

it was imaged at its hydrated state. The imaging was conducted at 20KV acceleration voltage and 50Pa chamber pressure.

### 3.4 Surface Patterning

The biosensor surface was initially designed by imprinting the leaf shape using PDMS, creating a negative mould used to pattern PCL, Mylar, and Agar. The leaf was washed using deionised water to remove any surface contamination, dried and secured on a flat surface. PDMS was prepared by mixing an elastomer (Poly (acrylamide-co-acrylic acid), and a curing agent (Poly (glycidyl methacrylate acid)) at a 10:1 ratio. The mix was then poured on the leaf surface and left to cure 48 to 72 hours at room temperature.

### 3.5 Middle Layer Fabrication

The middle layer of the biosensor consists of a mixture of sucrose and agar 4450 with a 50/50 ratio (Figure 3.3). The layer was designed to have dual functionality where the sucrose acts as a substrate for the yellow rust invertase to break down, and the agar 4450 act as a topological cue.

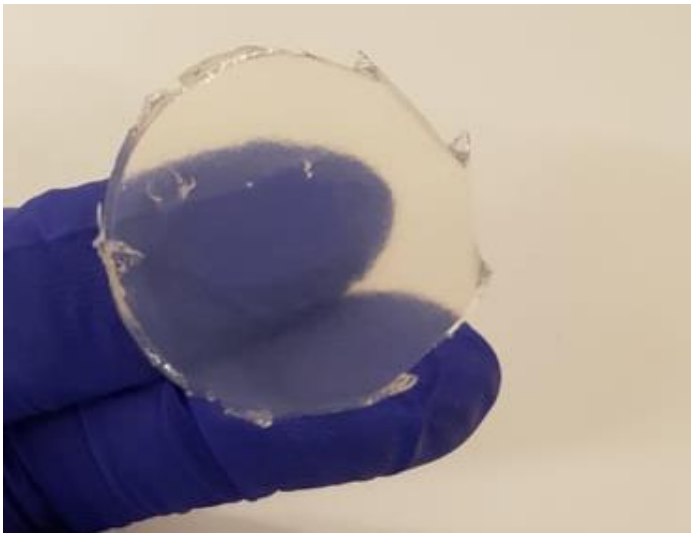

Figure 3.3: Second layer consisting of 50/50 sucrose/agar mixture.

### 3.6 Inoculation

The growth capability of *Puccinia triticina* on the artificial surface was tested to identify the most suitable material characteristics for the upper layer of the biosensor (see Chapter 1). The fungal spores were seeded on the artificial surface (first layer of the sensor), below which we have the volatiles (3-hexen-1-ol), 1ml of volatiles injected in the agar (second layer), acting as growth cues. The spores were left for 24 hours under a sunlight lamp and 90-100% humidity,

and then observed using a light microscope (Carl ZEISS Axio Imager, Zeiss, Jena, Germany). ImageJ ((Laboratory for Optical and Computational Instrumentation, University of Wisconsin, WI, USA) was used to count the germinated spores on the produced surfaces.

### 3.7 Shape Recovery

A PETG porous membrane was printed using an extrusion-based additive manufacturing (3D Discovery, RegenHU, Switzerland), considering a printing temperature of $190^0$C, screw rotational speed of 12mm/s and a travel speed of 20mm/s. Shape Recovery was evaluated by heating the printed membrane above the glass transition temperature (Tg), applying a load to deform the membrane, cooling down the membrane below Tg keeping its deformed shape, removing the load, and finally reheating the membrane above Tg allowing the membrane to regain its original shape. The time for recovery was recorded to investigate shape recovery. Deforming the membrane and keeping its deformed shape is considered as the programming stage, reheating the membrane to regain its original shape is considered as the recovery stage. PETG glass transition temperature is 75 ºC, and the programming and recovery stages were carried out at 80 ºC.

### 3.8 Results and Discussions

#### 3.8.1 Leaf Morphology

Figure 3.4 shows a detailed SEM image of a hydrated wheat leaf, being possible to observe its detailed structure including the stomata, grooves, and leaf hair. From this Figure it is possible to observe that the stomata are randomly scattered on the surface of the leaf, surrounded by two epidermal cells, and parallel to the leaf venation. The grooves on the leaf surface are unidirectional, running parallel in the longitudinal direction across the leaf. Leaf hairs are also randomly scattered across the leaf surface helping in entrapping contaminants and harmful particles preventing them from damaging the leaf surface.

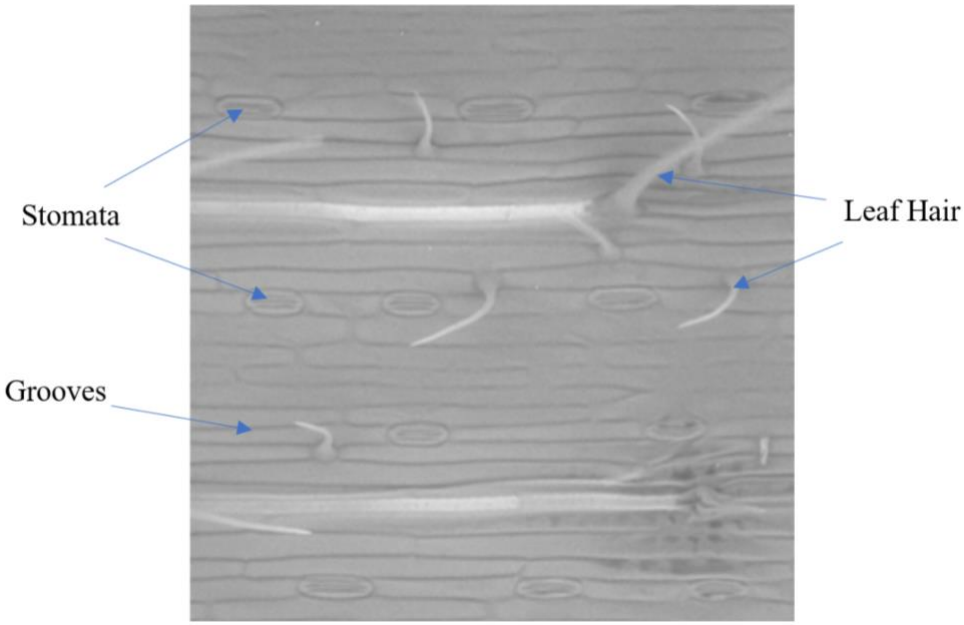

Figure 3.4: SEM image of a hydrated wheat leaf.

### 3.8.2 Surface Patterning

The surface of the PDMS mould is shown in Figure 3.5. As observed, the PDMS mould was able to capture the microstructure of the leaf morphology, but nanostructures (e.g., hair like structures) were not able to be replicated properly due to the PDMS low mechanical properties. This process of moulding allowed to produce an identical morphology on the PCL, mylar and agar surfaces. The biosensor surface was designed using Solidworks (Dassault Systems, USA) to produce the 3D model for the mould (Figure 3.6). The mould pattern was built based on the SEM images (Figure 3.5). The ProJet 1200 (3D systems, USA) vat photopolymerisation system was used to print the designed mould, using the Visijet FTX green resin. This additive manufacturing system was used due to its high resolution (56μm).

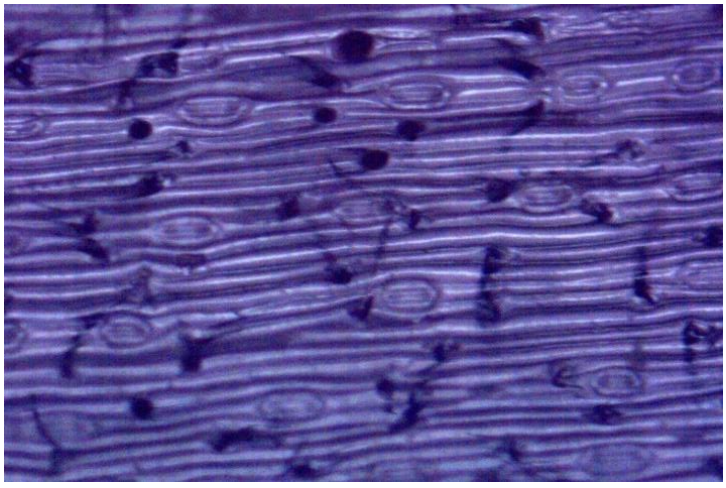
Figure 3.5: Leaf surface mould.

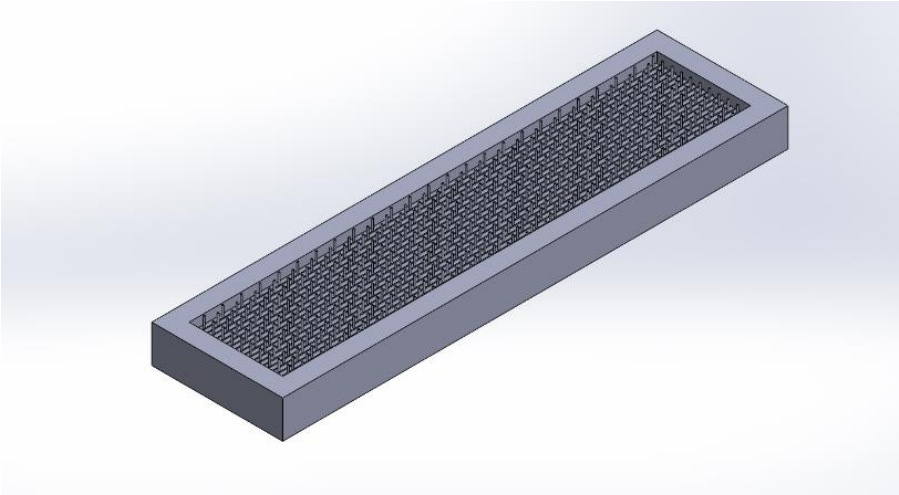

Figure 3.6: Solidworks model for the leaf surface mould.

### 3.8.3 Sensing Layer Design

The third layer of the biosensor was redesigned to be a non-enzymatic electrochemical glucose sensor instead of an optical sensor to gain more stability and longer working life. The sensing layer consists of platinum, nickel/multiwalled carbon nanotube (Pt Ni/MWCNT) nanocomposite drop casted on the surface of a screen-printed electrode (Figure 3.7). The nanocomposite was prepared using the following procedure. First, equal amounts (0.25 mmol) of Ni $(CO_2CH_3)2$ 4H2O and $PtCl_2$ were dissolved in ethanol. MWCNTs were added to the solution (2.5 mmol), and the mixture was continuously stirred to provide a homogeneous solution. Then the resulting mixture was refluxed for 2 h at 90 °C. Finally, DMAB was added to the resultant and refluxed for 1 h. The solution colour change from light brown to black indicated that Pt-Ni/MWCNT nanocomposites were formed.

The produced nanocomposite was then dispersed in 10 mL of DMF in an ultrasonic bath. 20 µL of this solution was casted on the active area of the SPE (Figure 3.7). After the casting step, the solvent was evaporated at 50 °C to prepare the Pt Ni/MWCNT modified electrode. The produced sensor was tested to detect glucose with a concentration as low as 5mM. This detection behaviour was investigated using cyclic voltammetry (CV) and the results shown in Figure 3.8. The oxidation peak A (1.4V) is a common oxidation peak for Pt based glucose sensors [415]. However, this voltage is very high for the intended application of the biosensor. Therefore, further investigation is required to decide a more suitable material.

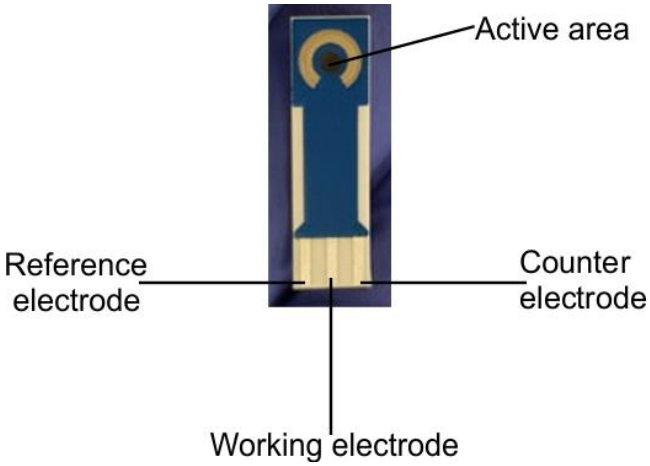


**Figure 3.7**: SPE with drop casted Pt-Ni/MWCNT composite on the surface.

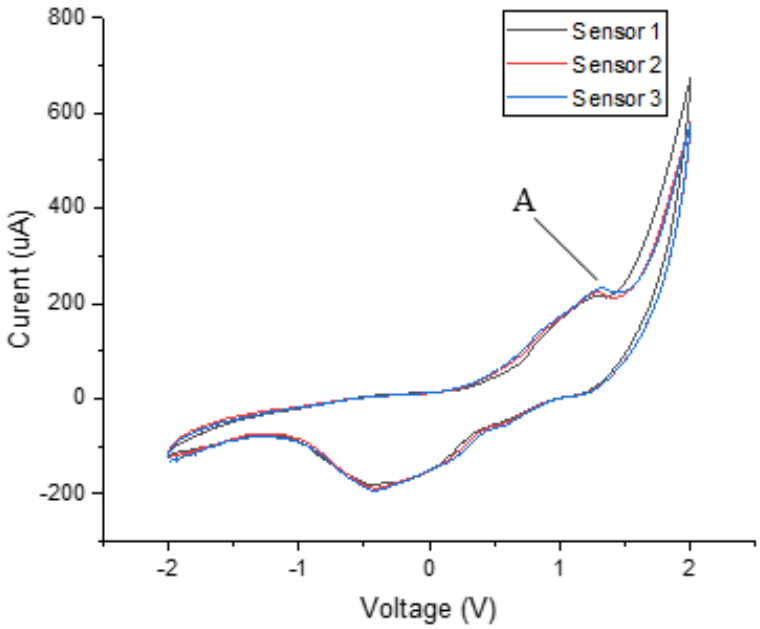


**Figure 3.8: CV** graph showing the response of the drop casted sensor to glucose.

### 3.8.4 Inoculation

The fungal germination was evaluated by inoculating the printed surface using fungal spores. After 24 hours the surface was observed using a light microscope to detect whether germination occurred or not. Results presented in Figure 3.9 show that the agar substrate allowed for the highest germination (96%), followed by the PCL (80%) and finally the mylar which was not able to sustain any germination. Agar layer presents the best germination but, as it is a hydrogel, it is not suitable for long shelf time, while PCL is able to sustain germination but presents low permeability and consequently volatiles cannot pass through [416].

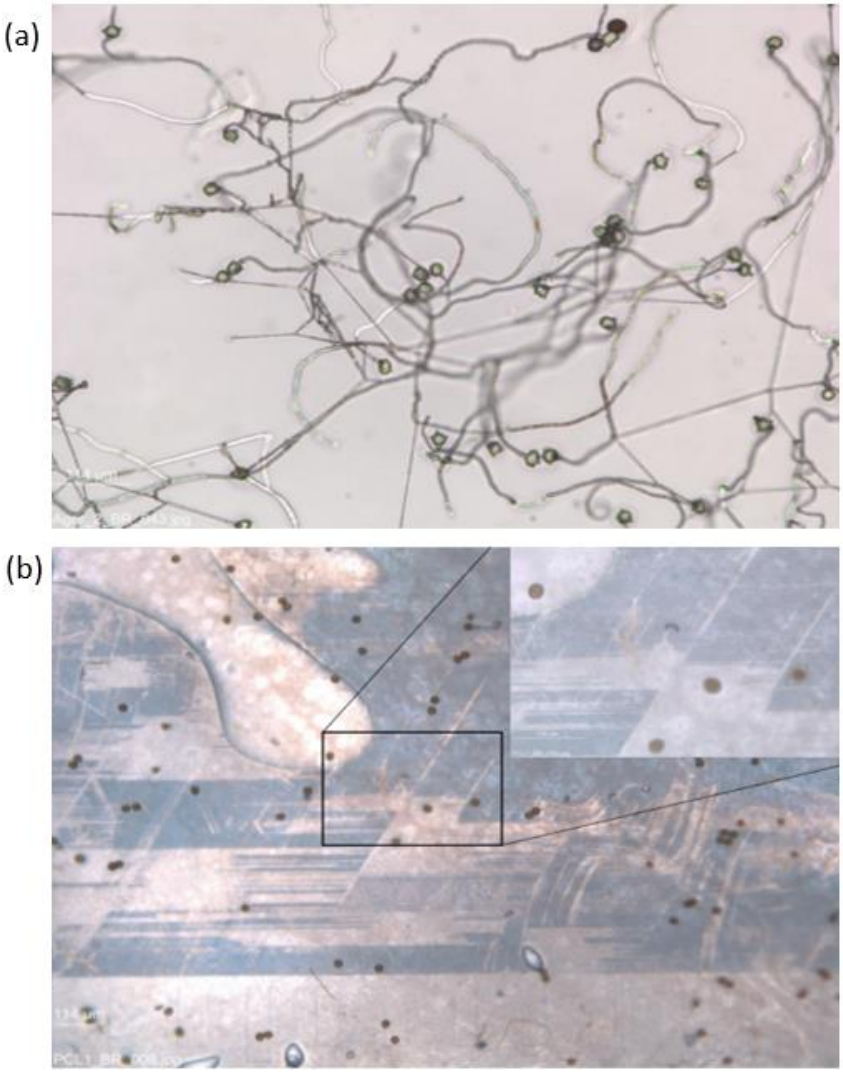


**Figure 3.9**: Inoculation results (a) agar patterned surface with 96% germination, (b) PCL patterned surface with 80% germination.

### 3.8.5 Shape Recovery

Shape recovery in response to heat is shown in Figure 3.10. The heat was selected as the main stimuli in the field are heat and light. Results demonstrate the ability of PETG to sense environmental temperature variations, altering its shape in response. Figure 3.10 (a) shows the original printed PETG structure before any programming to recovery occurs, Figure 3.10 (b) shows the deformed structured after the programming stage, and Figure 3.10 (c) shows the recovered structure shape after the recovery stage. The structure recovered in 35.71 seconds.

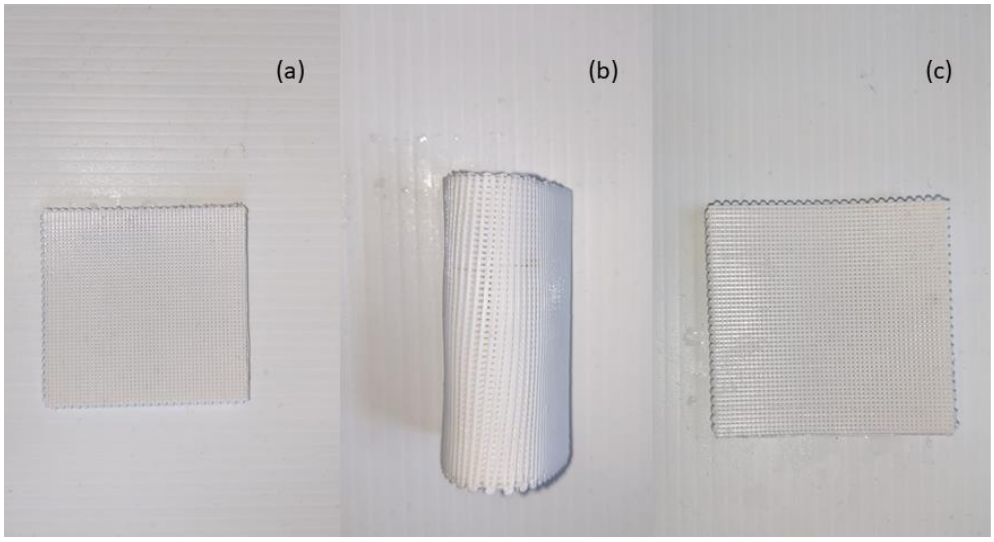


**Figure 3.10:** PETG membrane shape recovery process (a) original membrane shape, (b) deformed membrane, (c) recovered membrane shape.

### 3.8.6 Conclusion and Future Perspective

This Chapter presents the preliminary results of a novel concept for a biosensor, for agriculture applications, consisting of three layers. The PDMS casting strategy presented in this Chapter allowed to create an exact replica of the wheat leaf surface and can be used to replicate any plant surface. The proposed method does not require the use of heat hence minimising the number of bubbles in the produced mould. Multiple materials were investigated for the upper layer of the biosensor. Results show that the agar layer presents the best germination, but it cannot be used as the biosensor material as it requires permanent hydration; PCL is also able to sustain germination but presents low permeability and consequently volatiles cannot pass through and mylar was not able to sustain any germination. Finally, the shape changing capabilities of PETG, a potential alternative material for the upper layer, were demonstrated and the results seem to indicate that this is a potential material to replicate the aperture and closure mechanisms of stomata. This control would help in the release of VOC, which is a crucial germination cue for the spores, that could help in increasing the efficiency of the proposed sensor.

Based on the results from this Chapter the shape-memory behaviour of PETG is further investigated in the next Chapter, while its biological characteristics and the ability to sustain yellow rust are investigated in Chapters 4 and 5.

# Chapter 4: Chemical and compositional analysis of PETG for 4D printing applications

*Based on the results from Chapter 3, that suggests the potential use of PETG as a shape memory polymer (SMP), this Chapter fully investigates its stimuli-responsive characteristics to temperature changes. A full characterization analysis is carried out, including tensile mechanical analysis, chemical analysis and shape recovery. The shape recovery behaviour is assessed using cyclic thermomechanical experiments where stress and temperature are controlled during the programming and recovery processes. A stress strain graph is obtained leading to the determination of the shape fixity ratio and shape recovery rate.*

## 4. Chemical and compositional analysis of PETG for 4D printing applications♠

### 4.1 Introduction

Smart materials also known as intelligent materials, are a special class of materials due to their thermodynamic nature (see Section 2.2 for detailed information). They are active materials producing a response when a stimulus is present (e.g. pressure, temperature, electric and magnetic fields). Shape memory polymers represent a special sub-class of smart materials that undergo shape changing due to the presence of a stimulus [417, 418]. The special property of a shape memory material is its ability to memorise its original shape. Therefore, when programmed, these materials deformed, and then they can regain to their original shape when a suitable stimulus is present. The degree of smartness can be measured based on their responsiveness to a stimulus and degree of shape recovery. As suggested in Chapter 3, PETG is a thermo-responsive material able to change its shape at different temperatures. It can also be deformed and return to its original shape by heating. Throughout this process an actuating force is produced. Smart materials are the core of creating a smart and responsive structure and based on the preliminary results presented in Chapter 3, it seems that PETG can be considered a potential material for the fabrication of the upper layer of the proposed biosensor (see Chapter 1).

This Chapter investigates in more detail the shape changing characteristics of PETG samples under different heating/cooling cycles, which allows to determine the number of programming/recovering cycles. PETG samples were produced using filament-based extrusion additive manufacturing. Pre-processed PETG was chemically characterised to understand its chemical composition and the printed samples were mechanically and shape recovery

♠ This Chapter is based on the following publication: Hassan, M., Abdalla, O., Daskalakis, E, Liu, F., Bartolo, P.," Chemical and compositional analysis of PETG for 4D printing applications", ICMMEN, MATEC Web of Conferences 318, 01010, 2020. Mohamed main contribution is material selection, material fabrication, experiment design, experimental and validation tests, analysed the obtained data.

investigated. Matrix assisted laser desorption-ionisation time of flight mass spectroscopy (Maldi-ToF-Ms) was used to investigate the chemical characteristics and key components of PETG. Tensile tests were performed to determine the tensile modulus and tensile strength of the material.

## 4.2 Materials and methods

### 4.2.1 Materials

PETG was purchased from RS components (Northants, UK) in a filament form (diameter of 1.75 mm). Its printing temperature ranges between 195 and 220ºC and its molecular weight is 300 g/mol. The materials used in the Maldi-TOF MS sample preparation were chloroform (HPLC grade), phenol, and 2, 5 Dihydroxybenzoic acid (DHB), all purchased from Sigma Aldrich (Dorset, UK).

### 4.2.2 Fabrication

PETG dog bone structures were produced using a filament-based extrusion 3D printer (Flashforge Creator pro, China) (Figure 4.1). The structures were designed according to the ASTM D638-14 standard, which is a specific standard to determine the tensile properties of plastics. Dog bone structures were designed based on Type I specimen dimensions (Figure 4.2), and printed layer by layer with 100% infill. The printing parameters are presented in Table 4.1.


Figure 4.1: The 3D printing system.

Table 4.1: Fabrication parameters

| Parameters | Values |
|---|---|
| Layer thickness (mm) | 0.15 |
| Nozzle diameter (mm) | 0.40 ± 0.05 |
| Nozzle Temperature (℃) | 230 |
| Bed temperature (℃) | 60 |
| Printing speed (mm/s) | 60 |
| Fan cooling | Yes |
| Retraction length (mm) | 3.0 |
| Retraction speed (mm/s) | 25 |

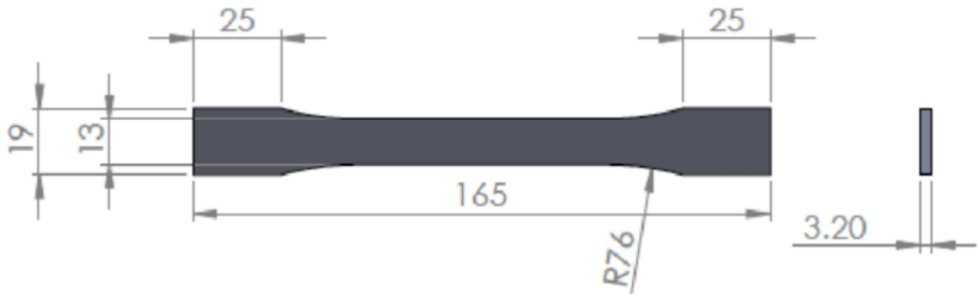


**Figure 4.2:** Dimensions of the dog bone structures. All dimensions in mm.

### 4.2.3 Maldi-ToF-MS

MALDI-TOF MS is based on the use of short, high intensity laser pulses to produce gas ions from a matrix. Investigated samples are composed of the analyte (PETG) and solvent (chloroform and phenol) and the matrix formed by small organic compounds (DHB). The matrix, which must experience a strong absorption of the laser wavelength, should present high electronic absorption for the used laser wavelength, stable under vacuum, low vapour pressure, good solubility in solvents that dissolve the analyte, and good miscibility with the analyte in a solid state. Commonly used matrices for synthetic polymers are DHB, dithranol (1,8,9-trihydroxyanthracene), IAA (3-β-indoleacrylc acid), and HABA (2, (-4-hydroxyphenylazo)benzoicacid).

Briefly, PETG samples were dissolved in phenol/chloroform, 1/1 (v/v). DHB was used as the matrix. Dried droplet samples were prepared by putting 1µL of polymer in phenol/chloroform, 1/1 (v/v), and 1µL of a mixture of 1ml of DHB in phenol/chloroform, 1/1 (v/v), as a matrix on the target plate. To determine the chemical composition of PETG, the mass spectrometer Plus MALDI-TOF/TOFMS analyser (Axima Confidence, Shimadzu Biotech, Japan) equipped with a nitrogen laser emitting at 337.1 nm was used to achieve data acquisition in positive ion mode. Data acquisition and processing were carried out using the Kratos analyser software (Kratos, United Kingdom). The acceleration voltage was 20KV and the extraction delay time was 15000

in reflector MS mode. All mass spectra were collected by averaging the signal of 1620 laser shots [419, 420].

### 4.2.4 Mechanical Tensile Test

The mechanical properties of PETG were evaluated using the uniaxial tensile tests. The tests were carried out using an SAUTER TVL [Manual Crank Handle Test Stand] (Sauter GmbH, UK). The machine is fitted with a 500N load cell and two AC 01R fine point clamps that are fitted to the platform and the loadcell. Tests were repeated 5 times and conducted in a dry state to ~2% strain which is the yield point. The acquired data is presented in the form of a table alongside the respective average values.

### 4.2.5 Shape Recovery

The shape recovery of PETG was evaluated by printing a structure and heating the structure above the glass transition temperature (Tg), applying a force to deform it, cooling down the structure below Tg to keep its temporary shape, removing the force, and finally heating up the structure over Tg allowing it to regain its permanent shape [421]. This procedure was repeated using 5 and 10 cycles to investigate the effect of the number of cycles on the shape recovery process. The steps followed to deform the structure and keeping its temporary shape are considered the programming step and the following step of reheating the structure to regain its permanent shape is considered as the recovery step. The PETG has a glass transition temperature of 75 $^{o}$C.

Firstly, the force was applied to the structure while the temperature was held at 80$^{o}$C. Secondly, the structure was cooled down below the Tg. Thirdly, the applied force was removed after cooling. Finally, the structure was reheated to 80 $^{o}$C under no force.

## 4.3 Results

### 4.3.1 Chemical Analysis

The spectrum obtained from the MALDI-TOF MS is presented in Figure 4.3 showing a broad peak in the high mass range for polymers, thus structural information cannot be obtained. The repeating units is the only possible method to identify different polymers in MALDI MS analysis [422]. Therefore, oligomers with low mass, are excited in the sample and had the same repeated unit as high mass segments, are studied to identify the structural information such as possible end groups and repeated units [419, 420].

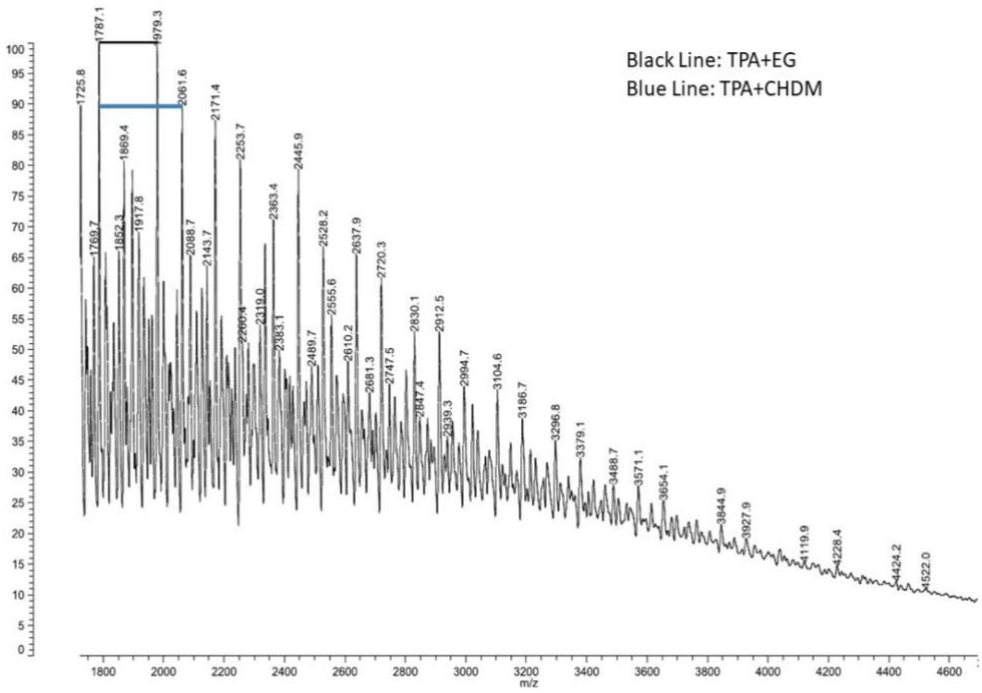


Figure 4.3: PETG MALDI-TOF MS spectrum.

PETG is composed of terephthalic acid (TPA), ethylene glycol (EG) and cyclohexanedimethanol (CHDM) as shown in Table 4.2. To identify the presence of these components, two lines were considered in Figure 4.3, a black line (TPA + EG) and a blue line (TPA + CHDM). Briefly, based on the molecular weight values of the key components of PETG shown in Table 4.2, the sum of the molecular weights of TPA and EG, and TPA and CHDM were calculated. Then, from the results presented in Figure 4.3, the value of a peak was subtracted from the subsequent peak. Once the value reaches the one corresponding to either TPA+EG or TPA+CHDM these peaks indicate the presence of these components. This procedure confirmed the presence of the key chemical constituents of PETG. However, the results of MALDI contain some peaks which do not correspond to the molecular weights of TPA, EG or CHDM. These peaks can be attributed to fragment ions.

Table 4.2: PETG Chemical components

| Compound | Molecular Formula | Molecular weight |
|---|---|---|
| Terephthalic acid (TPA) | $C_8H_6O_4$ | 166.13 |
| Ethylene Glycol (EG) | $(CH_2OH_2)$ | 62.07 |
| Cyclohexanedimethanol (CHDM) | $C_8H_{16}O_2$ | 144.21 |

### 4.3.2 Mechanical Tensile Test

The obtained mechanical tensile test results are presented in Table 4.3. Polyethylene terephthalate (PET) is the most used plastic material, but due to its high melting point it is not suitable for extrusion-based additive manufacturing. A common approach to address this issue is to reduce its crystallinity by adding CHDM. These results show that PETG presented reduced mechanical properties when compared to PET. As observed, PETG tensile stress is 23.5% lower than PET (54 MPa) and the young's modulus is 25.1% lower than PETG (2950 MPa) [423] . However, as the biosensor is a non-load bearing device the mechanical properties are still totally acceptable.

Table 4.3: Mechanical properties of PETG

| Test | Force (N) | Displacement (mm) | Stress (MPa) | Strain | Modulus (MPa) |
|---|---|---|---|---|---|
| Test 1 | 399.7 | 1.53 | 49.941 | 0.024 | 1749.408 |
| Test 2 | 404.3 | 1.56 | 42.423 | 0.024 | 1726.871 |
| Test 3 | 397.5 | 1.58 | 41.710 | 0.024 | 1676.335 |
| Test 4 | 404.9 | 1.46 | 42.486 | 0.022 | 1847.888 |
| Test 5 | 400.1 | 1.49 | 41.983 | 0.023 | 1789.217 |
| Average | 401.3 | 1.52 | 42.109 | 0.024 | 1756.202 |

### 4.3.3 Shape Recovery Results

The results of the shape recovery of the samples in response to heat are shown in Figure 4.4. The permanent printed structure (Figure 4.4 a) was bent to a temporary shape for 1 recovery cycle (55 s) (Figure 4.4 b), for 5 recovery cycles (Figure 4.4 c), and 10 recovery cycles (Figure 4.4 d). Experimental results showed that the shape recovery performance deteriorated over time, but the shape fixity did not change. After 1 cycle the sample fully recover its original shape, while after 5 cycles the recovery was 80% and after 10 cycles was 60%.

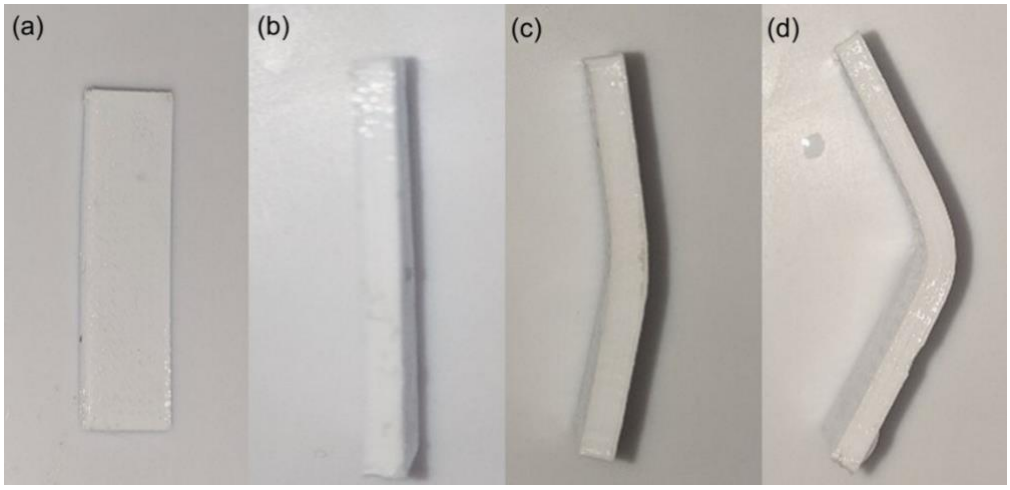


**Figure 4.4:** Shaper recovery for PETG using different recovery cycles, (a) Original (non-deformed) shape, (b) recovered structure after 1 cycle, (c) recovered structure after 5 cycle, (d) recovered structure after 10 cycle.

## 4.4 Conclusion

The results presented in this Chapter show that PETG is a relevant material for smart applications, exhibiting promising shape recovery properties. The chemical analysis demonstrated that the considered material, used as purchased, is a modified PET (PETG), with reduced mechanical properties than PET but that did not compromise its use for the proposed biosensor. The potential of PETG to sustain the adhesion a proliferation of biological elements is investigated in Chapter 5, which investigates the biocompatibility of PETG considering human cells assuming that the obtained results can be translated to spores, which was validated in Chapter 7. Wheat field temperature usually ranges from 7 to 20 $^{o}$C in Europe and from 20 to 40 $^{o}$C in Africa which requires the PETG glass transition temperature to be lower than it currently is (85 $^{o}$C), hence requiring further modification to the material before being field ready. The material has a reduced shape fixity and recovery after 10 cycles and is completely lost after 20 cycles. Further investigation and work need to be carried out to improve the number of shapes changing cycles.

# Chapter 5: The potential of Polyethylene Terephthalate Glycol (PETG) as biomaterial for tissue engineering

*In the previous Chapter, polyethylene terephthalate glycol (PETG) was investigated as a potential shape changing material. This behaviour is highly important to create a layer of the biosensor mimicking the opening and closing mechanism of stomata. Due to the lockdown of the University facilities, it was not possible to immediately investigate the ability of PETG to sustain inoculation and germination. However, the potential use of PETG for tissue engineering and the potential of PETG scaffolds to support human cells attachment and proliferation was investigated and our assumption is that similar results will be achieved with the yellow rust. Therefore, this Chapter investigates the use of PETG to produce bone scaffolds using a filament-based additive manufacturing. Scaffolds were produced considering different pore sizes. Matrix assisted laser desorption-ionisation time of flight mass spectroscopy (Maldi-ToF-Ms) was used to chemically characterise the PETG material, confirming the presence of terephthalic acid (TPA), ethylene glycol (EG) and cyclohexanedimethanol (CHDM) in the polymer structure. Compressive tests were performed to investigate the effect of pore size on both compressive modulus and compressive strength and values were compared to PCL scaffolds used as a reference. Scaffolds were seeded with human adipose derived stem cells (hADSCs) and the cell metabolic activity determined using the Alamar Blue assy. PCL scaffolds were also considered as a reference.*

## 5. The potential of Polyethylene Terephthalate Glycol (PETG) as biomaterial for tissue engineering♣

### 5.1 Introduction

Tissue engineering is an interdisciplinary field that applies the concepts of engineering and life sciences for the development of biological substitutes that maintain, restore or improve tissue or organ functions, and comprises two main strategies: scaffold-based and cell-laden approaches [424-429]. The scaffold-based approach, the most common strategy for bone tissue engineering applications, is based on the use of three-dimensional (3D) biocompatible and biodegradable porous structures that provide the substrate and the biomechanical environment for cells to attach, differentiate and proliferate [101, 430-434]. Bone scaffolds must be produced using non-toxic materials (the materials must also degrade into non-toxic products),

♣ This Chapter is based on the following publication: Mohamed Hassan, Abdalla Omar, Evangelos Daskalakis, Yanhao Hou, Boyang Huang, Ilya Strashnov, Bruce Grieve, Paulo Bartolo – "The potential of polyethylene terephthalate glycol as biomaterial for bone tissue engineering", Polymer, 12, 12, 2020. Mohamed Hassan contribution: conceptualisation, methodology, formal analysis, material preparation, scaffold fabrication, characterisation, and validation.

the degradation rate of the scaffold must be adjustable in order to match the rate of tissue regeneration, must present appropriate porosity, pore interconnectivity and pore structure (large number of pores may be able to enhance vascularization, while small pore sizes are preferable to provide large surface per volume ratio), should encourage the formation of the extra cellular matrix (ECM) by promoting cellular functions, should present sufficient strength and stiffness to withstand stresses in the host tissue environment and present adequate surface finish, guaranteeing that a good biomechanical coupling is achieved between the scaffold and the tissue [435-439].

Cell seeding on printed scaffolds depends on fast attachment of cell to scaffolds, high cell survival and uniform cell distribution, and these are strongly dependent on the scaffold material, architecture, surface stiffness and surface energy [425, 440].

A variety of biodegradable materials have been used to produce the scaffolds, including a wide range of organic, inorganic, and composite materials [437, 441-443]. Among these materials, polycaprolactone (PCL), an aliphatic polyester, was extensively used by our group for bone tissue engineering applications. PCL scaffolds with different porosities and pore sizes were successfully used to support the attachment and proliferation of osteoblasts and mesenchymal stem cells and osteogenic differentiation [444-447]. In vivo studies, using PCL scaffolds to treat critical size calvaria defects in rats, also showed the ability to support new tissue formation [448]. However, PCL presents limited bioactivity, long degradation times and low mechanical properties not suitable for load-bearing applications [431]. In order to improve the bioactivity nature of the scaffolds, new surface modification strategies such as selective plasma modification, acetone vapor annealing surface treatment and dopamine grafting, and silica nanoparticles coating, were explored [444]. Bioactivity was also improved by mixing PCL with ceramic materials such as hydroxyapatite (HA) and tricalcium phosphate (TCP), which also allowed to increase mechanical properties and to accelerate the degradation process. PCL/HA/multi-wall carbon nanotubes, mimicking the structure of bone, were successfully produced using extrusion-based additive manufacturing [449]. Carbon nanomaterials such as graphene and carbon nanotubes were also used to improve mechanical properties and to allow the fabrication of electro-active scaffolds. In vivo studies showed that these scaffolds together with electrical stimulation significantly accelerate the formation of new bone and the production of more organized new bone [443]. However, in all these cases, as PCL is the main material, the overall biological and mechanical properties of the scaffolds were constrained by the individual PCL properties. Therefore, the rationale of this research is to identify a biocompatible and biodegradable synthetic polymer that can be used as an alternative to PCL,

allowing to produce scaffolds with significantly better mechanical and biological properties. Polyethylene Terephthalate (PET) has been used in the medical field, for example for prosthetic vascular grafts, due to its good mechanical properties and biocompatibility [450]. Moreover, PET is also biodegradable, making it an interesting material for tissue engineering, but due to its high crystallinity, it presents significant printability limitations [451]. One route to overcome this printability limitation is through a glycol modification process, which allows to reduce the crystallinity level by disrupting the order of the polymer chain without compromising the biological characteristics of the initial polymer [446]. This strategy allows to obtain Polyethylene Terephthalate Glycol (PETG), investigated for the first time in this paper, as a potential material for tissue engineering applications. Thus, this research work addresses the following research questions: (1) is it possible to create PETG scaffolds, with significantly improved mechanical properties compared to PCL scaffolds, presenting compressive modulus in the range of trabecular bone (2) Is it possible to create PETG scaffolds with superior biological performance compared to PCL scaffolds without any surface modification.

## 5.2 Materials and Methods

### 5.2.1 Materials

PETG, with a printing temperature between 195 and 220$^{o}$C, was purchased from RS components (Northants, UK). PCL pellets (Mw 50,000 Da, CAPA 6500) were supplied by Perstorp Caprolactones (Malmo, Sweden). Matrix-assisted laser desorption/ionization time-of-flight mass spectrometry (MALDI-TOF MS) matrix was prepared using 2,5 Dihydroxybenzoic acid (DHB), Phenol and Chloroform (HPLC (High Performance Liquid Chromatography) grade), which were purchased from Sigma Aldrich (Dorset, UK). Biological analysis was conducted using Human adipose-derived stem cells (hADSCs), MesenPRO RSTM basal media, 2% (v/v) growth supplement, 1% (v/v) glutamine and 1% (v/v) penicillin/streptomycin, purchased from STEMPRO Invitroge, Thermo Fisher (Glasgow, UK) 2.2. Chemicals Analysis (MALDI-TOF MS). PET is a common polymer used in many applications due to its high melting point, but it presents low printability. To overcome these problems, manufacturers such as RS components modified PET by adding Cyclohexanedimethanol (CHDM), producing PETG. MALDI-TOF MS was used to confirm the CHDM presence. This technique is based on the use of short, high-intensity laser pulses to form gas ions. In this case, the analyte molecules are not exposed to the laser but are added to a matrix of small organic molecules.

The matrix shows strong absorption of the laser wavelength, improving efficiency and energy transfer [452]. Therefore, the matrix must have high electronic absorption for the used wavelength, stable under vacuum, low vapor pressure, good solubility in solvents that dissolve the analyte and good miscibility with the analyte in solid state. The PETG sample was dissolved in phenol/chloroform 1/1 (v/v). 2,5 Dihydroxybenzoic acid (DHB) was used as a matrix. A dried droplet sample was prepared by putting 1 µL of a mixture of 1 mL of 2,5 DHB in Phenol/chloroform, 1/1 (v/v), as a matrix and 1 µL of polymer in phenol/chloroform, 1/1 (v/v), on the target plate [452, 453]. To assess the chemical composition of PETG, the mass spectrometer Plus MALDI-TOF/TOFMS analyser Axima Confidence (Shimadzu Biotech, Kiyamachi-Nijo, Japan) equipped with a Nitrogen laser emitting at 337.1 nm was used to achieve data acquisition in positive ion mode. Data acquisition and processing were conducted using the Kratos analyser software (Kratos, Manchester, UK). The acceleration voltage was set to 20 KV and the extraction delay time used was 15,000 in reflector MS mode. All mass spectra were collected by averaging the signal of 1620 laser shots.

### 5.2.2 Scaffolds Fabrication

PETG and PCL scaffolds were produced using a filament-based additive manufacturing system (Flashforge Creator pro, Jinhua, China), considering a 0/90◦ lay-down pattern. PCL scaffolds were designed considering a pore size of 300 µm, and PETG scaffolds were designed considering three different pore sizes (PETG-300: 300 µm of pore size; PETG-350: 350 µm of pore size; PETG-450: 450 µm of pore size). Each scaffold was printed considering a total of 12 layers. The printing conditions are listed in Table 5.1.

Table 5.1: Scaffold printing parameters

| Parameters | Values |
|---|---|
| Layer Thickness (mm) | 0.33 |
| Filament diameter (mm) | 0.35 |
| Nozzle Temperature ($^0$C) | 230 |
| Bed temperature ($^0$C) | 60 |
| Printing speed (mm/s) | 20 |

### 5.2.3 Morphological Analysis

The scaffolds' morphology was characterised using the Scanning Electron Microscopy (SEM) FEI ESEM Quanta 200 system (FEI Company, Hillsboro, USA). The EMITECH K550X sputter coater (Quorum Technologies, Lewes, UK) was used for gold-coating the scaffolds prior to imaging. Imaging was conducted using 15 KV acceleration voltage. The obtained

images were analysed using the ImageJ software (Laboratory for Optical and Computational Instrumentation, University of Wisconsin, WI, USA), allowing to determine pore size, filament diameter and layer thickness. For each scaffold type, a total of nine measurements were considered.

### 5.2.4 Mechanical Compression Test

Uniaxial compression tests were performed using an INSTRON X testing system (High Wycombe, UK) equipped with a 100 N load cell according to the ASTM D695-1. The scaffold samples were cut into 3 × 3 mm2 blocks. Samples (n = 6) were tested in a dry state at the displacement rate of 0.5 mm/min until the strain reached 0.3 mm/mm. The obtained strain-stress data were further processed and plotted using the software Origin (Origin Lab, Northampton, MA, USA).

### 5.2.5 Biological Analysis

#### 5.2.5.1 Cell Culture

Human adipose-derived stem cells (hADSCs) were used to investigate the cytotoxicity of the scaffolds. MesenPRO RSTM, Thermo Fisher (Glasgow, UK),1 basal media, 2% (v/v) growth supplement, 1% (v/v) glutamine and 1% (v/v) penicillin/streptomycin were used for cell culture. hADSCs (passage = 5) were cultured in an incubator (37 ◦C, 5% CO2 and 95% humidity) until an appropriate cell density (90%) was achieved before cell seeding. Scaffolds were sterilized in an 80% Ethanol solution for 4 h, followed by washing with Phosphate Buffered Saline (PBS) solution twice. The scaffolds were left to dry overnight in a sterile lamina flow cabinet. The sterilized scaffolds were transferred into 24-well plates and kept inside the incubator before the cell seeding. An 89 µL cell suspension containing 50,000 cells was added into each scaffold at day 0. The samples were then transferred to the incubator for 2 h, allowing hADSCs to attach to the scaffolds followed by adding 900 µL of cell culture media to cover the scaffold. The scaffolds were transferred into new 24-well plates on the following day and the cell culture media was replaced.

#### 5.2.5.2 Alamar Blue Assay

Cell metabolic activity was investigated using the Alamar Blue assay, Sigma Aldrich (Dorset, UK), which can be used as an indicator of cell proliferation as it quantifies the metabolic activity of cells. Tests were performed at days 1, 7 and 14 after cell seeding. At each time point,

90 µL of Alamar Blue solution was added to each scaffold and the scaffolds were incubated for 4 h. Then, 200 µL solution from each sample was transferred into a 96-well plate and assessed using a microplate reader at 530 nm excitation and 590 nm emission. After the measurements, the scaffolds were washed three times with sterilized PBS to remove the residual Alamar Blue solution and new media was added. Cell culture media was changed every two days.

#### 5.2.5.3 Statistically analysis

Statistical analysis was performed using one-way analysis of variance (ANOVA) with Tukey's test. Differences were considered statistically significant at * $p < 0.05$, ** $p < 0.01$, *** $p < 0.001$ and **** $p < 0.0001$. GraphPad Prism software (GraphPad Software Inc., San Diego, CA, USA) was used in this research.

## 5.3 Results and Discussion

### 5.3.1 Chemical Analysis

The MALDI-TOF MS spectrum presented in Figure 5.1 shows a wide peak in the high mass range, and consequently, cannot provide structural information. Therefore, to identify the polymeric material under analysis, the repeating units is the only possible method [454, 455]. In this case, the oligomers with low mass are considered to obtain the relevant structural information, such as repeated units and possible end groups [452, 453]. In Figure 5.1, two lines were drawn to highlight the terephthalic acid (TPA) + ethylene glycol (EG) (black line), and TPA + CHDM (blue line). Besides the TPA + EG and TPA + CHDM peaks, the MALDI spectrum contains other peaks that correspond to fragment ions. The main constituent compounds and corresponding molecular weight values before the condensation reaction are presented in Table 5.2 [456].

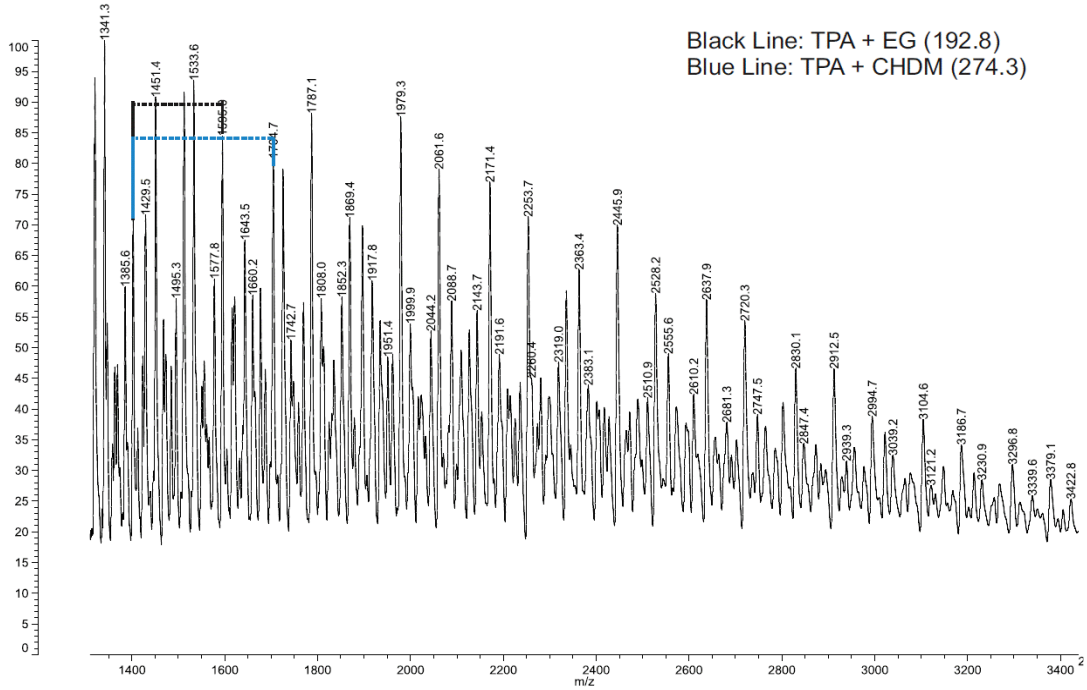


**Figure 5.1:** The Matrix-assisted laser desorption/ionization time-of-flight mass spectrometry (MALDI: -TOF MS) TOF MS) spectrum of Polyethylene terephthalate glycol modified (PETG). Its characteristic repeated units are highlighted: 192.8 g/mol for the Terephthalic acid + Ethylene Glycol (TPA + EG) unit and 274.3 g/mol for Terephthalic acid + Cyclohexanedimethanol (TPA + CHDM).

Table 5.2: Chemical constituents for PETG

| Parameters | Molecular Formula | Molecular weight |
|---|---|---|
| Terephthalic acid (TPA) | $C_8H_6O_4$ | 166.13 |
| Ethylene Glycol (EG) | $(CH_2OH_2)$ | 62.07 |
| Cyclohexanedimethanol (CHDM) | $C_8H_{16}O_2$ | 144.21 |

It is also important to notice that the addition of CHDM to PET disturbs the structure of the polymer, thus reducing the crystallinity, melting temperature and mechanical properties, therefore increasing printability [457].

### 5.3.2 Scaffold Morphology

Figure 5.2 show the SEM micrographs of the printed scaffolds. As observed, scaffolds present well-defined geometries with regular distributed squared pores. The cross-section images (Figures 5.2b and d) show a uniform distribution of adjacent layers. Moreover, the presence of micro-pores on the surface of the PCL filaments can be observed from Figures 5.2 a and c, which can be attributed to the material rheological characteristics and to the presence of brittle crystalline zones on the filament surface that collapse during the printing process [431]. This can also explain the better surface quality of PETG scaffolds as it is known that PETG is less crystalline than PCL [457]. However, further studies must be conducted to confirm this.

Contrary to PETG scaffolds, which present pore size (350 µm) and filament diameter (370 µm) values like the designed ones, a deviation was observed for PCL scaffolds (filament diameter of 340 ± 20, and pore size of 360 ± 10).

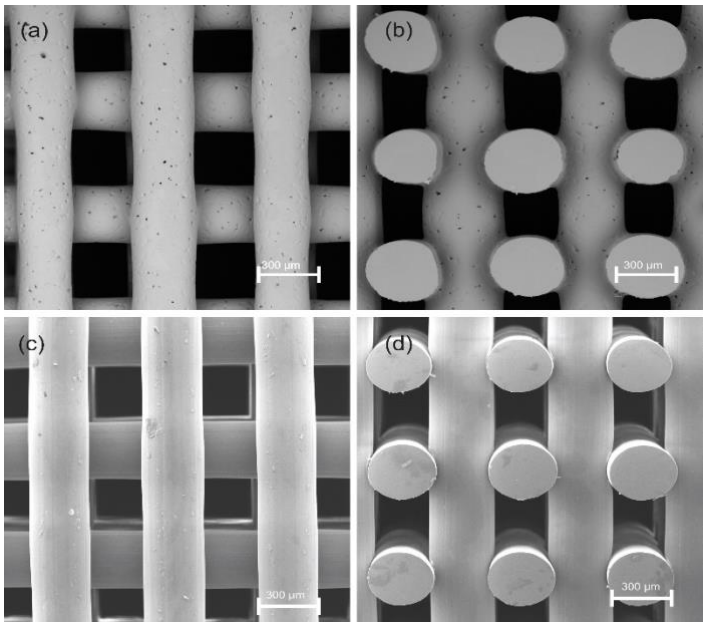


**Figure 5.2:** (a) Top view of a polycaprolactone (PCL) scaffold, (b) cross-section view of a PCL scaffold, (c) top view of a Polyethylene terephthalate glycol modified (PETG) scaffold, (d) cross-section view of a polyethylene terephthalate glycol modified (PETG) scaffold. All scaffolds were designed considering a pore size.

### 5.3.3 Mechanical Compression Test

Mechanical compression test results are presented in Figures 5.3–5.5. Figure 5.3 presents the stress versus strain curves for all considered scaffolds, showing that, even for large pore sizes, PETG scaffolds exhibit higher mechanical properties. These curves were also used to calculate both compressive modulus and compressive strength. From Figures 5.4 and 5.5, it is possible to observe that compared to PCL scaffolds, PETG scaffolds with the same pore size (350 µm) exhibit significantly higher compressive modulus and compressive strength, indicating that, from a mechanical perspective, and considering the same scaffold architecture, PETG scaffolds are more suitable for bone tissue engineering than PCL scaffolds. For PETG scaffolds, the results also show that by increasing the pore size from 300 to 450 µm, the compressive modulus of the PETG scaffolds decreases from 213 ± 12.2 to 141 ± 8.20 MPa. Results also show that by increasing the pore size, compressive strength decreases from 5.44 ± 0.19 to 3.55 ± 0.17 MPa. The average compressive modulus and strengths are presented in Table 5.3. Results also show that the PETG-300 and PETG-350 scaffolds have the same order of magnitude of

mechanical properties as human trabecular bone (compressive modulus mean value of 194 MPa [458-461].

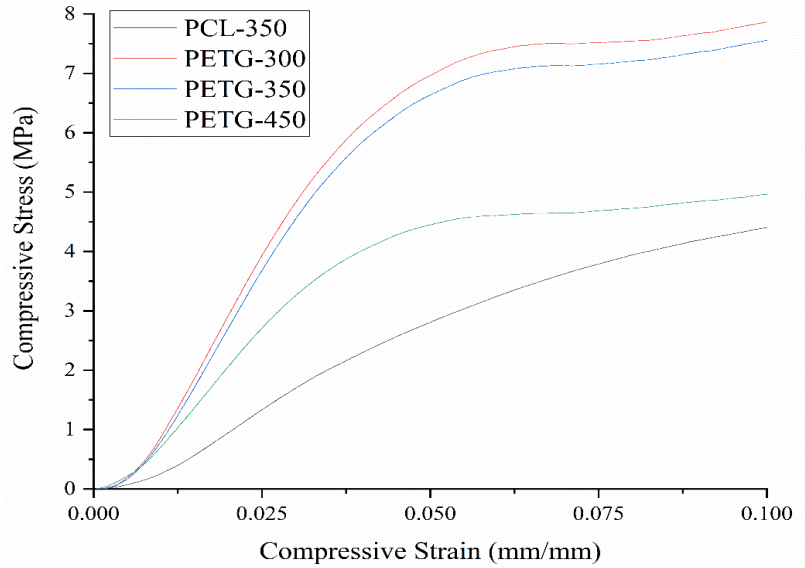


**Figure 5.3**: Stress vs. strain curves for PCL scaffolds and PETG scaffolds with different pore sizes.

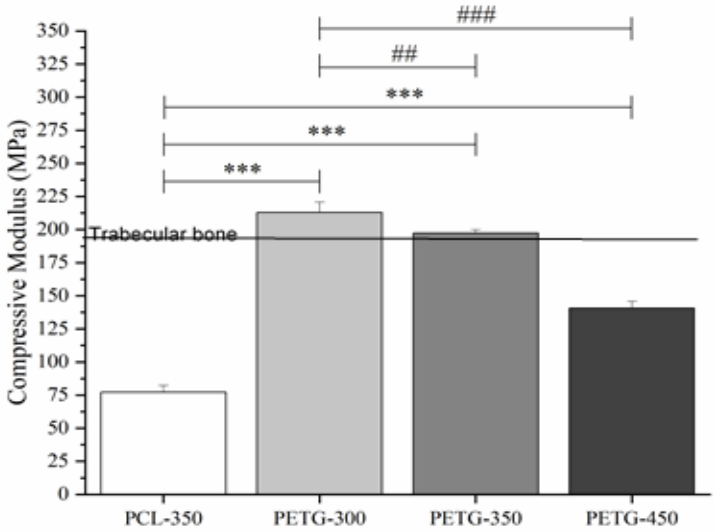


**Figure 5.4**: Compression modulus for the PCL scaffold and PETG scaffolds with different pore size. *** $p < 0.001$ compared with control (PCL), ## $p < 0.01$ and ### $p < 0.001$ compared with different pore size. The *** Statistical evidence ($p < 0.001$) is the one-way analysis of the mechanical compression test with the use of GraphPad Prism software, and it is used to show the difference be-tween the results. The * is small difference and while more * are added the differences between the results are higher. * compared with PCL scaffolds, # compared with different pore size of PETG scaffolds. Trabecular bone Figure 4. Compression modulus for the PCL scaffold and PETG scaffolds with different pore size. *** $p < 0.001$ compared with control (PCL).

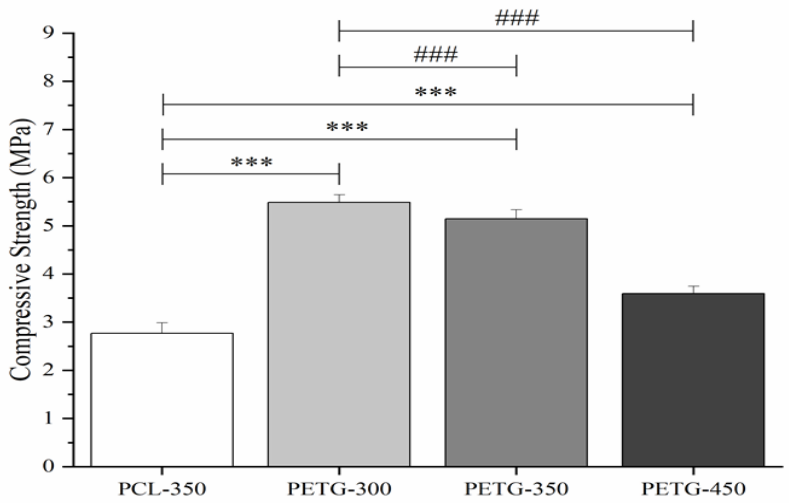


**Figure 5.5:** Compression strength values for the PCL scaffold and PETG scaffolds with different pore size. *** $p < 0.001$ compared with control (PCL), ## $p < 0.01$ and ### $p < 0.001$ compared with different pore size. The *** Statistical evidence ($p < 0.001$) is the one-way analysis of the mechanical compression test with the use of GraphPad Prism software, and it is used to show the difference be-tween the results. The * is small difference and while more * are added the differences between the results are higher. * compared with PCL scaffolds, # compared with different pore size of PETG scaffolds.

Table 5.3: Compressive Mechanical Properties

| | PCL | PETG-300 | PETG-350 | PETG450 |
|---|---|---|---|---|
| Modulus (MPa) | 76.12 ± 7.53 | 213.14 ± 12.23 | 195.99 ± 6.53 | 141.00 ± 8.20 |
| Strength (MPa) | 2.56 ± 0.26 | 5.44 ± 0.19 | 5.09 ±0.21 | 3.55 ±0.17 |

### 5.3.4 Biological test

Alamar Blue Assay was used to assess the metabolic activities of hADSCs seeded on PETG and PCL scaffolds at days 1, 7 and 14 of cell culture (Figure 5.6). Results show that the fluorescence intensities for all scaffolds increase by increasing the cell culture time, indicating that all scaffolds are cytocompatible and able to support cell attachment and spreading. At day 1, the fluorescence intensity of the PCL scaffold is statistically higher than PETG scaffolds. However, the fluorescence intensities of PETG-300 and PETG-350 scaffolds significantly increase and are statistically higher than those of PCL scaffolds at day 7 of cell culture. Moreover, the differences of the fluorescence intensities for all PETG scaffolds from day 1 to day 7 of cell culture are significantly higher than those of PCL scaffolds, suggesting a rapid colonization of hADSCs on PETG scaffolds. At day 14, all PETG scaffolds present statistically higher fluorescence intensities than PCL scaffolds. Although the differences of the fluorescence intensities from day 7 to day 14 decrease for all scaffolds, all PETG scaffolds present higher values than PCL scaffolds. These results show that PETG scaffolds present

better cell affinity than PCL scaffolds. In terms of pore size, PETG-350 scaffolds show overall higher fluorescence intensities than other PETG scaffolds at days 1 and 7. However, PETG-450 scaffolds exhibit a fast increase on the cellular metabolic activity from day 7 to day 14 compared to other scaffolds. This might be attributed to low cell seeding efficiency at day 0. At day 14, both PETG-350 and PETG-450 scaffolds present similar fluorescence intensity results. are metabolic activity from day 7 to day 14 compared to other scaffolds. This might be attributed to low cell seeding efficiency at day 0. At day 14, both PETG-350 and PETG-450 scaffolds present similar fluorescence intensity results [462].

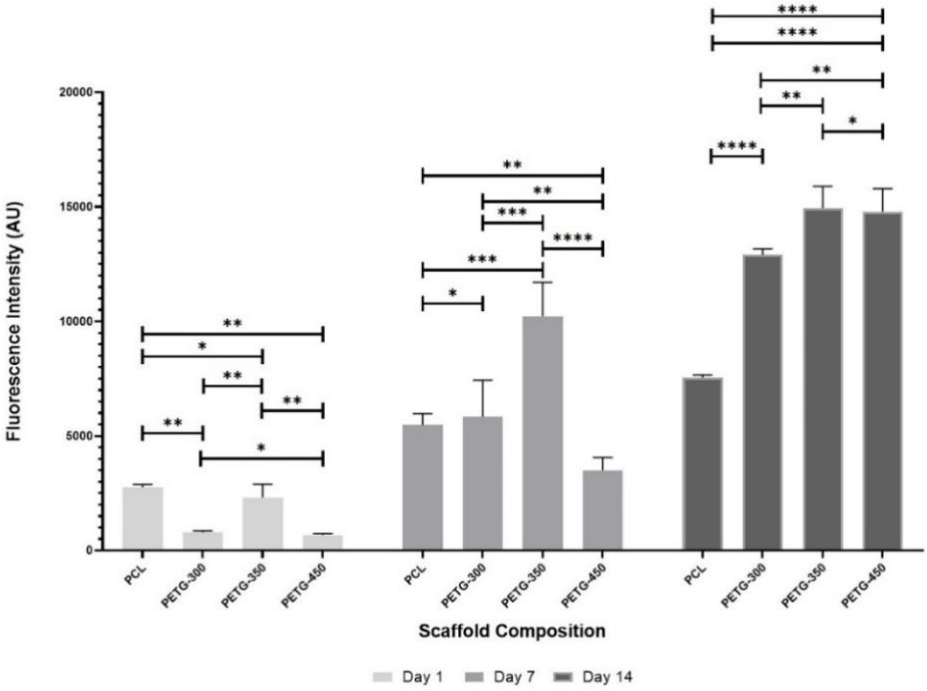


**Figure 5.6:** Alamar Blue results for both PCL and PETG scaffolds at days 1, 7 and 14 post-cell-seeding. * Statistical evidence ($p < 0.05$) analysed by one-way analysis of variance (ANOVA) and Tukey's post-test. The * Statistical evidence ($p < 0.05$), **, *** is the one-way analysis of variance (one-way ANOVA) and Tukey's post hoc test with the use of GraphPad Prism software and it is used to show the difference be-tween the results. The * is small difference and while more * are added the differences between the results are higher.

SEM images of cells attached and spreading on PETG-350 scaffolds are shown in Figure 5.7. From this figure, it is possible to observe that cells are homogeneously distributed on the filaments, establishing cell–cell networks and bridging adjacent layers.

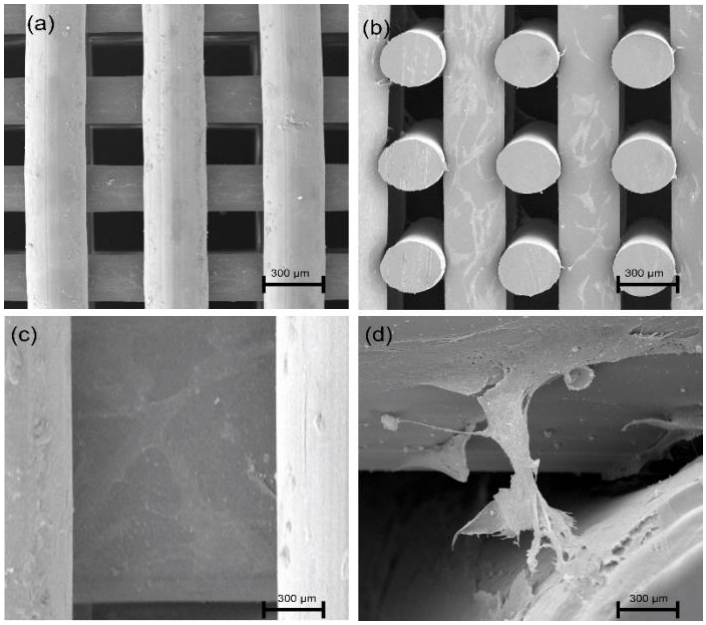


**Figure 5.7**: Cells on PETG-350 scaffolds after 14 days of cell seeding. (a) Top view image of the PETG scaffold, (b) cross-section image of PETG scaffold, (c) magnified image showing cells covering the PETG filament, (d) cells bridging adjacent lay.

## 5.4 Conclusion

Scaffolds for bone tissue engineering should present appropriate mechanical properties and promote the right environment for cells to attach and proliferate. Among the different biocompatible materials being investigated for bone applications, PCL is the most common one. However, PCL scaffolds do not present suitable mechanical properties and these properties significantly decrease by increasing porosity or pore size, important parameters to allow vascularization, supplying oxygen and nutrients to cells inside the scaffold. This paper investigated, for the first time, the potential use of PETG as an alternative material to PCL. This material, obtained by adding CHDM to PET (as confirmed by MALDI analysis), was successfully printed, and the produced scaffolds exhibited a well-defined geometry. Results also showed that PETG scaffolds present higher compressive modulus and compressive strength than PCL scaffolds, not only for the reference case (350 µm of pore size) but also when we considered PETG scaffolds with larger pore sizes (450 µm). Moreover, PETG scaffolds also showed better biological behaviour, as observed from the Alamar Blue assay. In this case, it was also possible to observe high cellular activity in scaffolds presenting large pore sizes. Considering both mechanical and biological performances, results seem to suggest that the PETG scaffold with pore size of 350 µm is, among the different scaffolds considered in this study, the most appropriate one.

The results shown in this Chapter demonstrated the ability of PETG to sustain cell growth. PETG was identified as a new biomaterial. The bioactivity of the material was investigated using human cells as they are the standard tests followed in research. The bioactivity could be extrapolated and assumed towards plant cells as both cells essentially use a similar growth behaviour. The PETG scaffolds were designed with a 0/90 pattern that emulates the parallel venation on the surface of the wheat leaf. Based on these results it was decided to further investigate PETG as a photo- and thermal-responsive material, which, as discussed in Chapter 1, represents another important requirement for the proposed biosensor.

# Chapter 6: Smart polyethylene terephthalate glycol (PETG)

*In Chapter 4 it was discussed the potential of PETG to be used as a smart material considering temperature as a stimulus. This Chapter investigates the incorporation of photochromic molecules such as azobenzene. Therefore, PETG was mixed with azobenzene (chromophore) to produce a photoactive material that can respond to UV light by changing shape and regaining its original shape in the dark. The resultant material was designed with the intent of producing bioinspired functional surfaces. PETG was also mixed with Polyvinyl chloride (PVC) to fabricate a thermo-responsive material able to respond to temperature change by changing shape. The produced material was designed with the intent of incorporating in pathogen detection sensors, where the material simulates the morphology and functionality of a leaf surface.*

## 6. Smart polyethylene terephthalate glycol (PETG)♠

### 6.1 Introduction

Smart polymers, are polymers that have the ability to respond to an external stimulus, such as pH, electrical and magnetic fields, temperature, pressure and light (see Chapter 2, section 2.2) by changing some of their properties [463]. Smart materials present sensing, actuation, self-healing, self-cleaning, and shock absorber properties, making them a promising group of materials for a wide range of applications including biotechnology, robotics, construction, and aerospace [464-466].

Polyethylene terephthalate glycol (PETG) is a common 3D printing material, obtained from polyethylene terephthalate by adding glycol [467]. The main reason behind the modification is to reduce the material crystallinity allowing for better printability. Moreover, PETG also shows a shape memory behaviour, where it can be programmed by heating above its glass transition temperature, deformed into a new shape and then cooled down below glass transition temperature. After this programming step, the deformed PETG can be heated above the glass transition temperature regaining its original (undeformed) shape [456]. This was demonstrated in Chapter 4 (see Figure 4.2). However, the PETG glass transition temperature is 75$^{o}$C, which is very high for the infield application of the biosensor. This is due to its crystalline structure, as PETG has a 70/30 ratio of amorphous to crystalline phase [468, 469]. To address this issue a proper strategy is to blend PETG with another polymeric material exhibiting lower crystallinity. In this research this was achieved by blending polyvinyl chloride (10%

♠ This chapter is based on two following publications: Mohamed Hassan, Abdalla Omar, Evangelos Daskalakis, Bruce Grieve, Paulo Bartolo "Photoactive PETG", IUPESM conference, 2022, and , Mohamed Hassan, Abdalla Omar, Evangelos Daskalakis, Bruce Grieve, Paulo Bartolo "Design of thermos-responsive PETG for 4D printing of Biosensors" International Conference on 3D Printing, 2022. Mohamed Hassan contribution for this work is conceptualisation, methodology, formal analysis, material preparation, scaffold fabrication, characterisation, and validation.

crystallinity) and PETG [470]. Polyvinyl chloride (PVC) is one of the most used thermoplastic [471]. However, PVC thermal stability and processability is limited in comparison to other common polymers such as polystyrene and polyethylene, but can be enhanced through the incorporation of additives including heat stabilizers, plasticizers, and fillers [471].

Moreover, as PETG is aimed to be used as the top layer of an in-field biosensor, it was decided to add a chromophore to change the PETG into a photoactive polymer, which corresponds to a subclass of smart materials that respond to changes in light conditions by changing its shape [472]. Typically, these materials are produced by incorporating photochromic molecules such as azobenzene [473, 474]. Azobenzene, a diazene (HN=NH) derivative, where phenyl groups replaces both hydrogens [473, 475], can exist in trans or cis forms. The trans → cis transformation occurs upon irradiation with UV or visible light [473, 475-478], through electrostatic stimulation [474] or by applying mechanical stresses [479]. The cis → tans transformation occurs spontaneously in the dark due to the thermodynamic stability of the trans isomer [473, 477, 478].

This Chapter describes the main steps to produce a photoactive PETG material using a solvent mixing approach to mix PETG and azobenzene chromophores, as well as a thermoresponive PETG/PVC mix with a lower activation temperature, Results shows that the new photoactive material exhibit a change in shape under UV light and regain its original shape in the dark, being a suitable material for the upper layer of the biomimetic sensor considered in this research.

## 6.2 Material and Methods

### 6.2.1 Materials

PETG with molecular weight of 300 g/mol and printing temperature ranging between 195 $^{o}$C and 220$^{o}$C was purchased from RS components (Northants, UK). Azobenzene, dichloromethane (DCM), PVC powder (molecular weight 30,000 g/mol), sodium hydroxide, tetrahydrofuran (THF), and Triton X 100 required for sample preparation were purchased from Sigma Aldrich (Dorset, UK).

### 6.2.2 Material Fabrication

Briefly, 10 % w/v of PETG was added to 5 ml DCM and mixed for 20 minutes until the PETG is fully dissolved, producing a homogenous solution. 20% (w/w) triton X 100 to PETG was added to the solution. Triton X100, a non-ionic surfactant, was used to decrease the viscosity

of the solution by increasing the dispersion of the azobenzene and reducing the rigidity of the matrix. This approach reduces the resistance to deformation when the material is photo-chemically or photo-thermally activated, as the stiffness of the matrix dictates the speed of the deformation and chain movement. The solution was mixed for 10 minutes at room temperature. Different concentrations of azobenzene (10, 30 and 50 % (w/w)), were added to the solution and mixed for 10 minutes. Then, the obtained solution was casted into a thin layer with a thickness of 5mm and left to dry for 1 hour. The preparation process is presented in Figure 6.1 Moreover, the PETG solution was prepared by dissolving PETG in DCM 1:10 ratio (w/v). PVC solution was prepared by dissolving PVC in THF considering a 1:10 ratio (w/v). Solutions with a ratio of 50/50 and 60/40 (v/v) (PETG/PVC) were mixed using a magnetic stirrer for 1 hour, and then poured in a glass dish and left to dry in a fume cupboard for 24 hours. The preparation method is presented in Figure 6. 2.

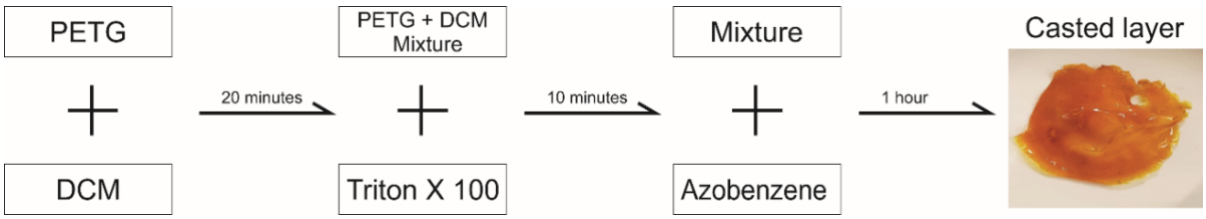


Figure 6.1: Preparation process for the photoactive layer.

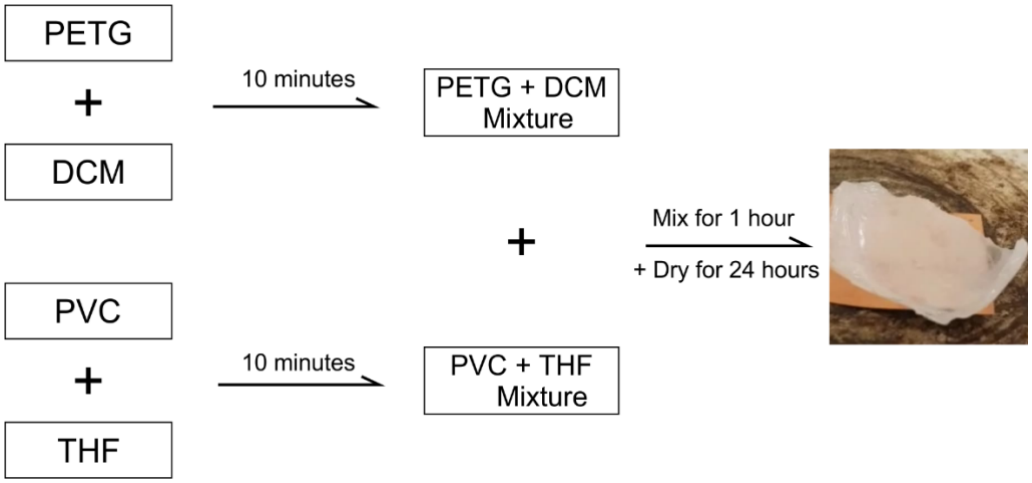


**Figure 6.2**: Preparation process for the thermosresponsive PETG/PVC layer.

### 6.2.3 Morphology

The material morphology was assessed using the scanning electron microscope (SEM) Quanta 200 SEM (FEI company, Hillsboro, Oregon, USA). The samples were sputter coated using gold/palladium (Au/Pd (80/20)) using the Quorum sputter coater (Quorum tech, UK). Imaging was collected at a 15 KV acceleration voltage. SEM was used to assess the morphology of the

PETG/PVC samples. However, it was not possible to use SEM to assess the morphology of the PETG/azobenzene layers due to the destructive impact of the electron beam on the material.

### 6.2.4 Chemical Composition

The chemical composition of prepared samples was investigated using Raman spectroscopy and Fourier-transform infrared spectroscopy (FTIR). Raman spectroscopy was carried out using the Renishaw inVia confocal Raman microscope (Renishaw Plc, UK) using a laser wavelength of 432 nm and 1200 g/mm grating in a regular mode and a magnification of x50 microscope. FTIR was carried out using the Varian 670-IR spectrometer (Agilent Technologies, CA, USA). Each sample was scanned 20 times at the resolution of 1cm, over a wavelength scanning ranging from 800 to 3100 $cm^{-1}$. RAMAN and FTIR were used to assess the chemical composition of the PETG/PVC samples. However, it was not possible to use both RAMAN and FTIR to assess the morphology of the PETG/azobenzene layers due to the destructive impact of the electron beam on the material.

### 6.2.5 Shape Recovery

The material shape recovery was assessed by heating the produced structure over the activation temperature (Ta ~ 40$^{o}$C), applying a force to create a new temporary shape, cooling down the structure below Ta to keep its temporary shape, removing the force, and finally reheating the structure again over Ta allowing it to regain its original shape. The shape recovery of the produced PETG/azobenzene layer was tested under ultraviolet (UV) light at a wavelength of 350 nm using the Hamamatsu UV-LED light source (Hamamatsu, UK). The samples were placed under the UV light at a 400 mm distance and checked for response (motion) every 10 minutes. The experiments were conducted for 30 minutes. The samples were imaged using a Canon camera and compared for response.

## 6.3 Results and Discussion

### 6.3.1 Morphology

Due to the significant differences in the molecular weight between PETG (300 g/mol) and PVC (30,000 g/mol), these polymers are considered as incompatible for mixing hence resulting in a dual phase material. The dispersion morphology of the produced dual-phase material was analysed using SEM. Figure 6.3, presents the dual-phase nature of the material. PETG granules

are dispersed in the PVC gel hence explaining the soft morphology presented by the materials as well as the lower activation temperature.

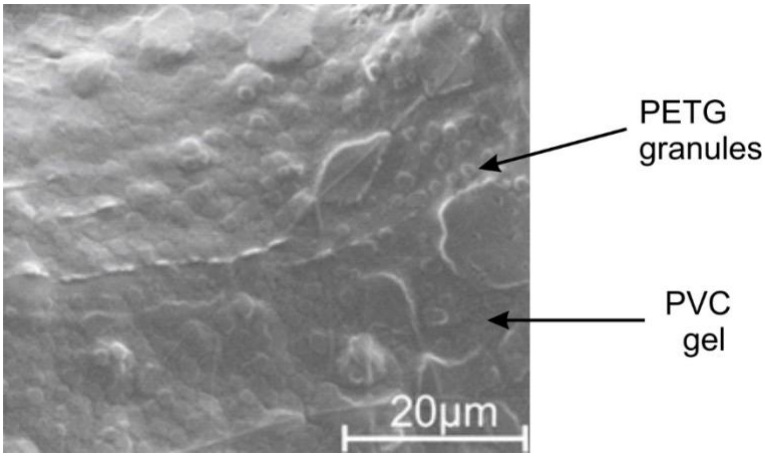


**Figure 6.3**: SEM image of PVC-PETG layer produced presenting the dual phase nature of the material.

### 6.3.2 Chemical Composition

Raman spectroscopy was used to qualitatively evaluate the difference between two samples with different split of PETG and PVC. Figure 6.4 presents the Raman spectra for the different samples. All the obtained spectra baseline was postprocessed through the subtraction of a polynomial fit of the baseline from the raw spectra. This was conducted to remove any variations due to noises.

Common PETG characteristic peaks were obtained at 800 $cm^{-1}$ (C-H ring out-of-plane bending + C=O bending) [480], 840 $cm^{-1}$ (C-H ring out-of-plane-bending) [480] , 943 $cm^{-1}$ (C–H stretching peak of the cyclohexene ring) [480]. 1038 $cm^{-1}$ (C-H ring in-plane bending) [480], 1119$cm^{-1}$ (C-O stretching) [480], 1287 $cm^{-1}$ (C-O stretching of ester group) [480], 1387 $cm^{-1}$ (gauche $CH_2$ wagging) [480], 1448 $cm^{-1}$ (-$CH_2$ bending peak of the PETG macromolecular chain backbone) [480], 1600 $cm^{-1}$ (symmetric stretching of the 1,4 para di-substituted benzene ring) [481], and 1725 $cm^{-1}$ (C=O stretching of ester group) [480].

Common PVC peaks were identified at 633 and 696 $cm^{-1}$ (stretching vibrations of C-Cl bonds.) [482], and 2915 $cm^{-1}$( stretching vibrations of C-H bonds in the $CH_2$ structural fragment) [482]. The Raman spectroscopy graph confirms the presence of PETG and PVC in the produced samples. The peak intensities for each sample are correlated to the difference in the percentages of both materials used in each sample.

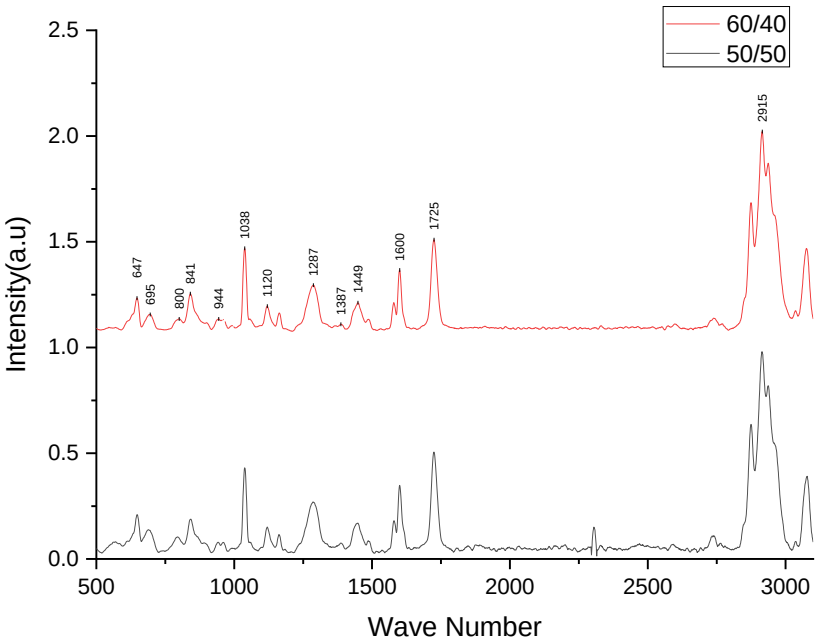


Figure 6.4: Raman spectra (red) 60/40 split and (black) 50/50 split.

FTIR was used as a non-destructive analytical technique to qualitatively assess the difference between samples with different PETG and PVC splits. Figure 6.5 presents the FTIR spectra for the different materials. Common PETG peaks are observed at 732 $cm^{-1}$ (C–H out-of-plane deformation of two carbonyl substituents on the aromatic ring), [483], 1243 $cm^{-1}$ (C(O)–O stretching of ester groups) [483], 1432 $cm^{-1}$ ($CH_2$ deformation band) [483], 1712 $cm^{-1}$ (C=O ester groups) [483], 2854 $cm^{-1}$ and 2944 $cm^{-1}$ (methyl groups) [483]. Common PVC peaks are observed at 618 - 650 $cm^{-1}$ C−Cl gauche bond) [484], 921 - 1113 $cm^{-1}$ (C−C stretching bond of the PVC backbone chain) [484], 1243 $cm^{-1}$ (bending bond of C−H near Cl) [484], 1414 $cm^{-1}$ (C−H aliphatic bending bond) [484], 2914 $cm^{-1}$ (symmetrical stretching bond of C−H), [484] and 2975 $cm^{-1}$ (asymmetric stretching bond of C−Hs) [484].The FTIR graph confirms the presence of PETG and PVC in the produced samples. The peak intensities for each sample are correlated to the difference in the percentages of both materials used in each sample.

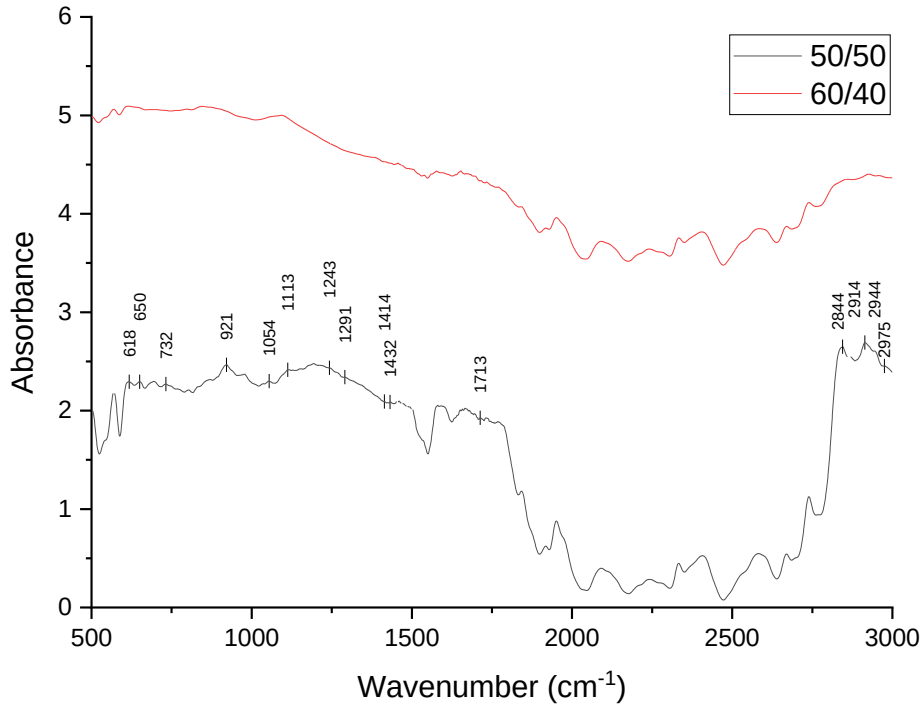


Figure 6.5: FTIR spectra (red) 60/40 split and (black) 50/50 split.

### 6.3.3 Shape Recovery

Figure 6.6 presents the activation results at different time points for samples containing different levels of azobenzene. As observed, samples containing 30 wt% of azobenzene (Figures 6.6 b, e, h, and k) show a faster and more significant response than the samples containing 10 wt% of azobenzene (Figures 6.6 a, d, g, and j), and 50 wt% azobenzene the slowest responsive samples (Figures 6.6 c, f, i, and l). As observed, there is a very clear correlation between the azobenzene concentration and the activation time up to a specific percentage (threshold value) then the response is reduced. This trend can be attributed to the overall reduction of PETG content, which is much stiffer than azobenzene thus requiring less energy to change shape. The surfactant Tritonx100 contains hydrophilic and hydrophobic groups making it very efficient for the dispersion and wetting as an emulsifier. The benefit of such approach counteracts the noticeable drying of polymer with increasing content of azobenzene that limits the shape changing effect and recovery. At 50% the sample dries and becomes stiffer due to the competitive interaction between the PETG and azobenzene, resulting in the observed slower response.

The increase in azobenzene content increases the light absorption promoting shape changing. However as light absorption follows the Beer-Lambert model, it decreases across the sample

thickness [485]. High concentration of azobenzene will absorb most of the light at the top surface of the material significantly blocking light penetration and making the process less effective. Moreover, azobenzene is thermally reversible, which means that the photo generated isomer can revert to its initial form. This is known as a reversible isomerisation process between the trans and cis isomers, where the activation is a trans-to-cis reaction, and the reserve reaction is a cis-to-trans reaction happening in the dark [473, 486]. Figure 6.6 shows the overall process of activation and shape change for the produced layer, which exhibits a curving shape change motion due to the UV light irradiation.

The addition of solvents (DCM and THF) which plasticize the polymer matrix controls the stiffness and the elasticity, and consequently the overall shape changing process [487]. The use of surfactants enhances the ability of the macro-deformation of the photo-responsive PETG-azobenzene. This is a result of the improved dispersion of the photoactive chromophore and reducing the force required to deform the polymer chains of the matrix. Moreover, the high thermal conductivity of polyethylene oxide (PEO), a Tritonx100 component, better distributes the heat in the matrix, possibly activating the shape memory effect presented by the PETG [488]. Relaxation is also improved due to the faster heat dissipation.

Figure 6.7 shows the shape change process of the PETG/PVC samples. As shown in Figure 6.7a the 50/50 split requires 80 s to completely recover its original shape while Figure 6.7 b shows that the 60/40 split recovers its shape after 50 s. These differences can be attributed to the morphological characteristics of the material, as the crystalline (decreases shape recovery) and amorphous (increases shape recovery) phases determine the shape memory behaviour. Therefore, the fast recovery of the 60/40 split can be attributed to a decrease in the overall crystallinity due to the presence of PVC.

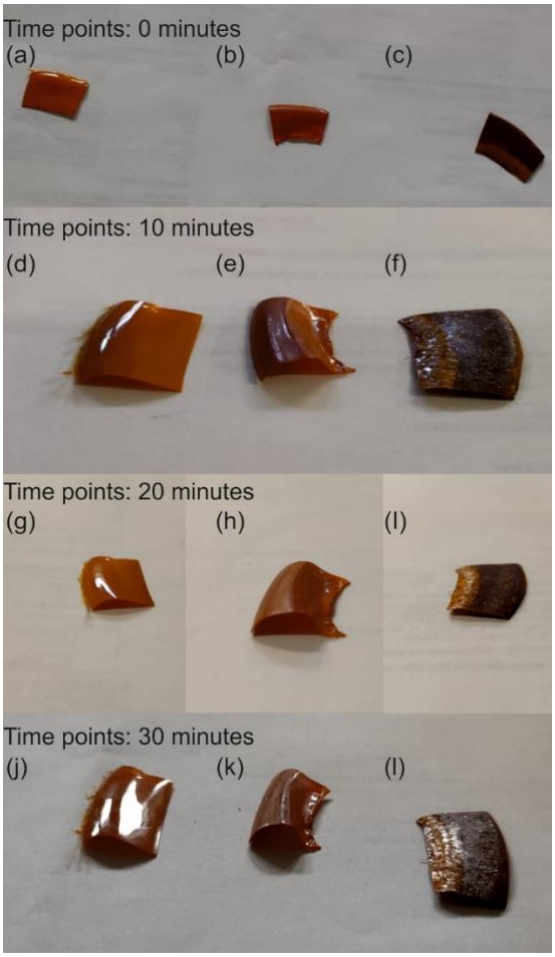


**Figure 6.6**: Responses of the produced photoactive layers at different time points. 10 wt% of azobenzene (a, d, g, j); 30 wt% of azobenzene (b, e, h, k); and 50 wt% of azobenzene (c, f, i, l).

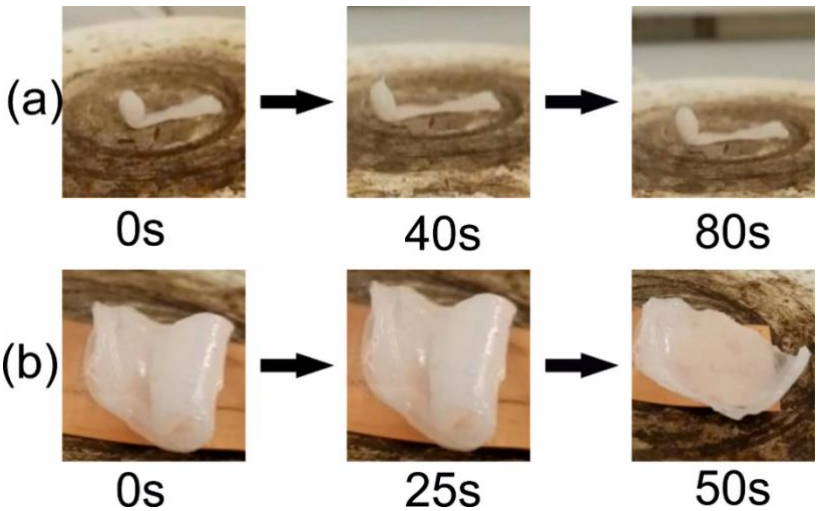


**Figure 6.7**: Shape recovery of (a) 50/50 PETG/PVC split, and (b) 60/40 PETG/PVC split.

## 6.4 Conclusion

This Chapter investigated the use of azobenzene, a photoactive chromophore, to prepare photoactive PETG samples, and the ability to reduce the time response of PETG by mixing it with PVC, which can be attributed to the decrease in the crystallinity. Composite materials, containing different concentrations of azobenzene, were produced using a solvent casting method. A tri-solvent system incorporating a plasticiser, used to increase the intrachain spacing, and a surfactant, to prevent the azobenzene agglomeration, was used, and the mixture was dried to produce the photoactive films. These films exhibit a reversible shape changing behaviour as a response to UV light. The shape changing and recovery was tested, and the results indicate curling and relaxation in the direction of the incident light. The photo-responsive material is characterised by higher shape changing response in comparison to other polymer matrix composites [489-491]. The tri-solvent system led to a more elastic polymer matrix, resulting in less activation energy required to obtain the shape changing effect. However, further work is required to optimise the azobenzene loading percentage in order to obtain a more stable and faster response material. The curved motion of the layers can be used to produce a layer mimicking the motion of the top and bottom surface of the leave with opening and closing stomata. However, the resultant reduction of the activation temperature of the composite effect on reversibility of the shape change requires further investigation. Moreover, SEM images confirm that the material is a dual phase material, showing both PETG and PVC phases, which can be attributed to the significant differences in their molecular weights. The Raman and FTIR spectra also confirm the presence of both PETG and PVC in the produced materials. Further investigation needs to be carried out on the produced material considering different factors such as morphological changes with time, potential shape changes upon other external stimuli (e.g. light, humidity) as well as degradability and biological behaviour. Agricultural fields could have drastic changes in light, temperature, and humidity. The photoactive PETG works under UV light however it needs 8 hours of darkness to recover its original shape which is not ideal for field application. The PETG/PVC is thermoresponsive at 40 $^{o}$C which is suitable for warmer environments, however it requires further investigation before being field ready.

# Chapter 7: Electrospinning polyethylene terephthalate glycol (PETG) meshes

*In Chapter 5, it was demonstrated the suitability of PETG scaffolds for tissue engineering applications. Results using hADSCs showed that PETG scaffolds do not present any cytotoxicity effects being able to support cell attachment and proliferation. These results suggest that PETG can be a good candidate to support the inoculation and germination of yellow rust spores. This is confirmed in this Chapter. Moreover, it is also known that cell attachment and cell spreading increase by increasing the surface area of the scaffolds. FDM was investigated to produce PETG meshes however due to limitations in resolution and accuracy, meshes produced did not achieve the required morphology. Electrospinning ability to produce nano-fibres resulted in meshes with acceptable morphology. Therefore, it was decided to investigate the use electrospinning to create PETG electrospinning meshes. However, PETG is a difficult to spin material and no previous papers reported the correct conditions to create PETG meshes. To address this issue, a preliminary study on the solubility and electrospinnability of PETG using a range of solvent systems was conducted and a Teas graph was established allowing to select the ideal solvent system. Based on these results electrospun PETG fibres were produced using a highly volatile binary solvent system consisting of dichloromethane (DCM) and Trifluoroacetic acid (TFA). Produced meshes were extensively characterised and the results demonstrate for the first time the ability of PETG electrospun meshes to support the inoculation and germination of yellow rust spores, thus confirming that PETG is an ideal material to be used in the proposed biosensor (see Chapter 1).*

## 7. Electrospinning polyethylene terephthalate glycol (PETG) meshes♣

### 7.1 Introduction

Solution electrospinning is a simple electrostatic and versatile technique to produce micro to nanoscale fibre meshes exhibiting large surface area to volume ratio [492-495]. In this process, a polymeric solution is ejected from a needle tip, positioned at a specific height over a grounded collector, by applying a high electrical field [496]. Typically, an electrospinning system consists of a high voltage power supply, a capillary that includes the material container and a spinneret, and a grounded metal collector. The process starts by applying an electrical field between the needle tip and the metallic collector. A material droplet is formed at the end of the needle tip because of surface tension and viscoelastic stresses [106]. When the electrostatic forces overcome the surface tension of the material, the material droplet approaches a cone shape (Taylor cone) and a charged jet is ejected [497]. Then, the jet follows a path that is usually characterised by an initial stable region, where the fibre is parallel to the direction of the jet and its diameter decreases monotonically by increasing the distance from the tip [106].

♣ This Chapter is based on the following publication: Mohamed Hassan, Abdalla Omar, Evangelos Daskalakis, Bruce Grieve, Paulo Bartolo – "Electrospinning polyethylene terephthalate glycol (PETG) meshes", Materials Today, *Submitted.* Mohamed Hassan contribution: material preparation, solubility and electrospinnability tests, mesh production, characterisation, and data analysis.

Afterwards, the jet starts to coil and undergo bending instabilities that further reduces the fibre diameter. Electrospinning has been used for a range of applications such as support structures for cell attachment, proliferation, and differentiation [106, 445, 496, 498], wound dressings [499, 500], and sensing membranes [501, 502]. In this Chapter, electrospinning is investigated as a potential technology to produce the upper layer of the proposed biosensor. As electrospinning allows to produce meshes with high surface area, this will increase the capability to support pathogen inoculation and germination.

In previous Chapters, it was also shown that polyethylene terephthalate glycol (PETG) is an ideal material for the fabrication of the upper layer due to its shape changing properties, biodegradability, and the ability to support cell attachment and proliferation, suggesting a similar behaviour regarding the yellow rust. However, PETG has low solubility in most solvents, which are also usually highly volatile, making it difficult to electrospinning.

This paper investigates for the first-time the fabrication of electrospun PETG meshes. A preliminary study on the solubility and electrospinnability of PETG using a range of solvent systems was conducted and a Teas graph was established allowing to select the ideal solvent system. Based on these preliminary results electrospun PETG fibres were produced and extensively characterised. The results demonstrate for the first time, the ability of PETG electrospun meshes to support the inoculation and germination of yellow rust spores, thus confirming that PETG is an ideal material to be used in the proposed biosensor.

## 7.2 Materials and Methods

### 7.2.1 Materials

Polymeric electrospun meshes were produced using PETG purchased from RS components (Northants, UK). Solutions were prepared using acetic acid (AA), acetone (ACE), ethanol (ETH), dimethyl sulfoxide (DMSO), dimethylformamide (DMF), tetrahydrofuran (THF), dichloromethane (DCM), and trifluoroacetic acid (TFA), all purchased from Sigma Aldrich (Dorset, UK).

### 7.2.2 Mapping Spinnability of PETG on the Teas Graph

The solubility of PETG on the different solvents was investigated using the Teas graph that allows to identify the solvents fractional cohesion parameters (hydrogen bonding, polar force, and dispersion force) [503-506]. Solubility was assessed at 20% w/v polymer concentration, atmospheric pressure, and room temperature (20$^{o}$C). Briefly, 2 g of PETG were added to 10 ml of single solvents (AA, ACE, ETH, DMSO, DMF, THF, DCM, or TFA), and binary solvent

systems DCM/DMF, DCM/AA, DCM/THF, DCM/TFA. The mixture was stirred with a magnetic stirring bar at room temperature. The process was visually assessed after 1 h, 2 h, and 4 h. Then, solubilities were categorized as insoluble (no dissolution), partially soluble (dissolution achieved but at lower rate or lower capacity), soluble (quick and complete dissolution), based on the time to form a homogeneous solution. The binary solvent systems were also identified and calculated using the lever rule assuming 1:1 ratio [507]. Finally, the solubility results of the binary solvent systems were compared to the single solvent systems on the Teas graph, and then the solubility region was constructed

### 7.2.3 Fabrication of PETG Meshes

Based on the solubility results (Section 7.2.2), PETG (20% (w/v)) was dissolved in different splits of DCM/TFA (85/15, 70/30, 60/40 ,50/50, 40/60, 30/70, 15/85(v/v)), and electrospun using a solution electrospinning (Spraybase, Ireland) (Figure 7.1). Meshes were produce at room temperature with a voltage of 16 kV, feed flow rate of 4 ml/h, humidity of 45% (±5%), and 150 mm distance between the needle tip and the collector, which was covered with aluminium foil. Finally, the obtained meshes were dried in vacuum for 48 hours to ensure the complete removal of solvents. These were considered the optimised parameters. Voltage values lower than 16 kV were not enabling the formation of a stable jet but only a dropping effect, while values higher than 16 KV induces electrospraying. Moreover, flow rate values lower than 4 ml/h induces a fast evaporation of the solvent blocking the needle, while above 4ml/h a dropping effect was observed.

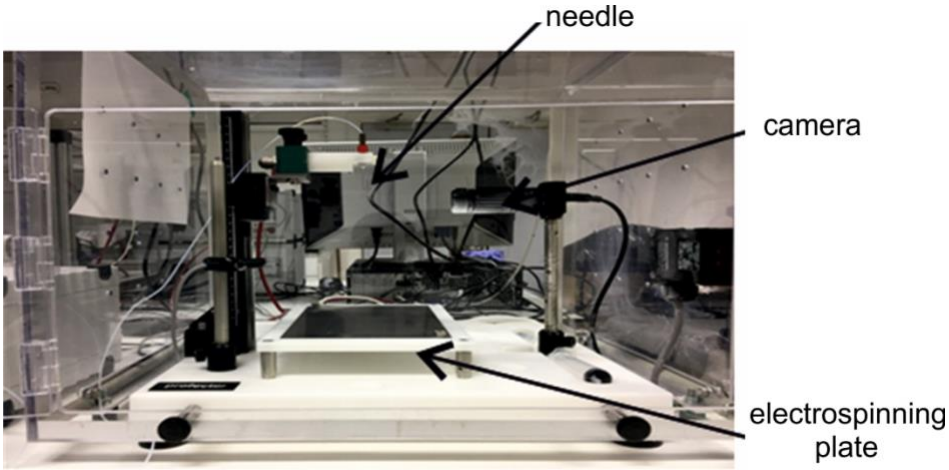


Figure 7.1: Electrospinning setup.

### 7.2.4 Morphological Analysis

The Quanta 650 (FEI company, Hillsboro, Oregon, USA) scanning electron microscopy (SEM) was used to characterise the mesh morphology. All meshes were sputter coated with

gold/palladium (Au/Pd (80/20)) using the Quorum sputter coater (Quorum tech, UK) and imaged at an acceleration voltage of 15 kV. The obtained images were analysed using the ImageJ software (Laboratory for Optical and Computational Instrumentation, University of Wisconsin, WI, USA), allowing to determine fibre diameter. For each mesh a total of 9 measurements were considered.

### 7.2.5 Chemical compositional characterisation

The chemical composition of produced meshes was analysed using Fourier-transform infrared spectroscopy (FTIR), and Raman spectroscopy. FTIR tests were conducted using the Varian 670-IR spectrometer system (Agilent Technologies, CA, USA). Each sample was scanned 20 times at the resolution of 1cm$^{-1}$, over a frequency scanning range from 800 to 3100 cm$^{-1}$. Raman spectroscopy tests were carried out on the Renishaw inVia confocal Raman microscope (Renishaw Plc., Gloucestershire, U.K.) using a laser (432 nm) with a grating of 1200 g/mm in a regular mode and considering a x50 magnification on the microscope.

### 7.2.6 Inoculation

The ability of the electrospun meshes to sustain pathogen attachment and germination was assessed using the yellow rust spores' inoculation process. The meshes were placed in a tray in a stainless-steel pipe, simulating a wind tunnel. The spores were released in the pipe, landing on the meshes at the bottom of the pipe. The meshes were kept in the pipe for 15 to 30 minutes ensuring that all spores have settled on the surfaces. Then, the inoculated surfaces were imaged under a light microscope to make sure spores were attached. Finally, the meshes were placed in the Innova 44 incubator (Eppendorf, Hamburg, Germany) set at 7 $^{o}$C for 24 hours.

## 7.3 Results and Discussion

### 7.3.1 Solubility and Electrospinnability

Solubility, which describes how easy is to dissolve the polymer in a solvent, and electrospinnability, which describes the ability of a polymeric solution to be stretched under a specific current, were investigated for different solvents and the results are presented in Figure 7.2. The lower right quadrant in Figure 7.2 presents the best solutions for the dissolution of PETG in TFA or DCM. These solvents can produce nanofibers as single and binary solvent systems. As DCM exhibits the highest solubility it was decided to investigate its use in combination with other solvents (binary solvent systems) such as DCM/DMF, DCM/AA, DCM/THF, DCM/TFA. Results showed that the DCM/TFA binary solvent system allowed the

best spinnability. Therefore, different splits of DCM/TFA were investigated to produce the meshes (see Sections 7.2.3 and 7.3.2).

However, there were some challenges regarding the reproducibility of the meshes and stability of the Taylor cone due to the high evaporation rate of the solvents. Two parameters were investigated to address this issue. Firstly, a high flow rate was used to stabilize the Taylor cone and counteract the rapid evaporation rate of the binary solvent system. Secondly, based on a preliminary investigation on the effect of the relative humidity (RH) on the spinnability, RH was fixed around 45% (±5%) allowing the best spinnability condition as the evaporation rate of the solvent would be limited.

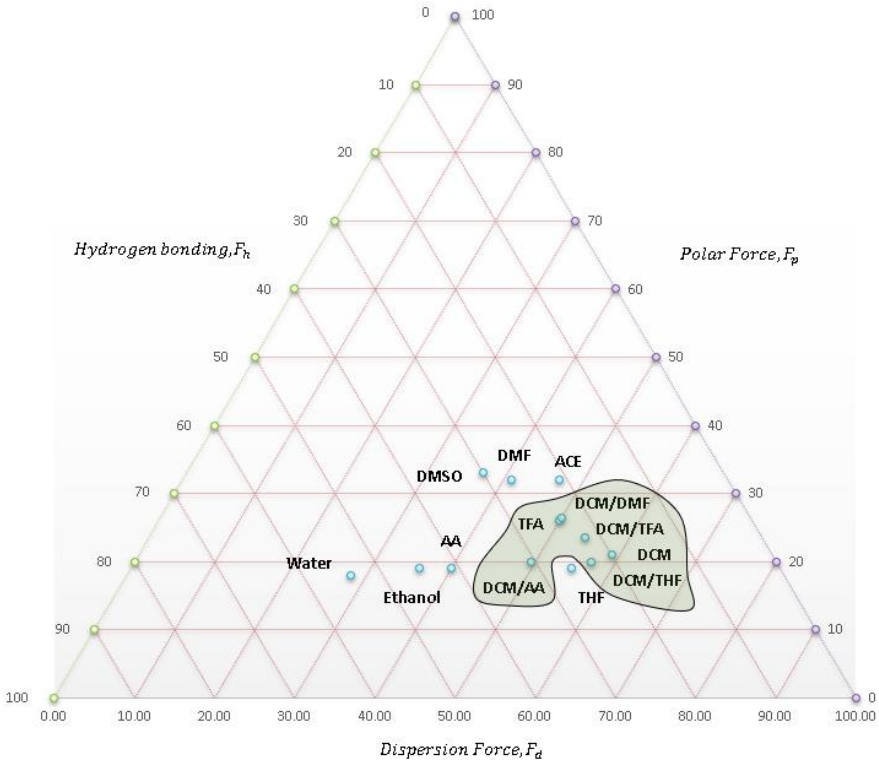


**Figure 7.2**: Solubility–spinnability map of PETG based on the Teas graph. The contoured region presents the solvents that can dissolve PETG, forming a homogenous solution.

### 7.3.2 Meshes Morphology

Figure 7.3 presents SEM images of the produced meshes at x1000 magnification. As observed from Figures 7.3 (a) to 7.3 (g), the fibre thickness and porosity decreases by increasing the content of TFA (more viscous than DCM), while fibre roughness and bead content increases. Moreover, as DCM is a stronger solvent (higher polar force) but presenting slower evaporation rate, it contributes to the formation of fibres with higher diameter. Therefore, by controlling the ratio between DCM and TFA it is possible to control the thickness of the fibres, roughness, and porosity, thus allowing to create meshes with different fibre densities. In this study, the

optimal mesh density is shown in Figure 7.3 (d) and corresponds to the 50/50 (v/v) DCM/TFA system. This mesh exhibits optimal morphology by presenting thin fibres, lower porosities, and absence of beads. Moreover, meshes produced from 85/15, 70/30, 60/40, 50/50 (v/v) solutions were bead free, while meshes produced from 40/60, 30/70, 15/85(v/v) solutions present beads.

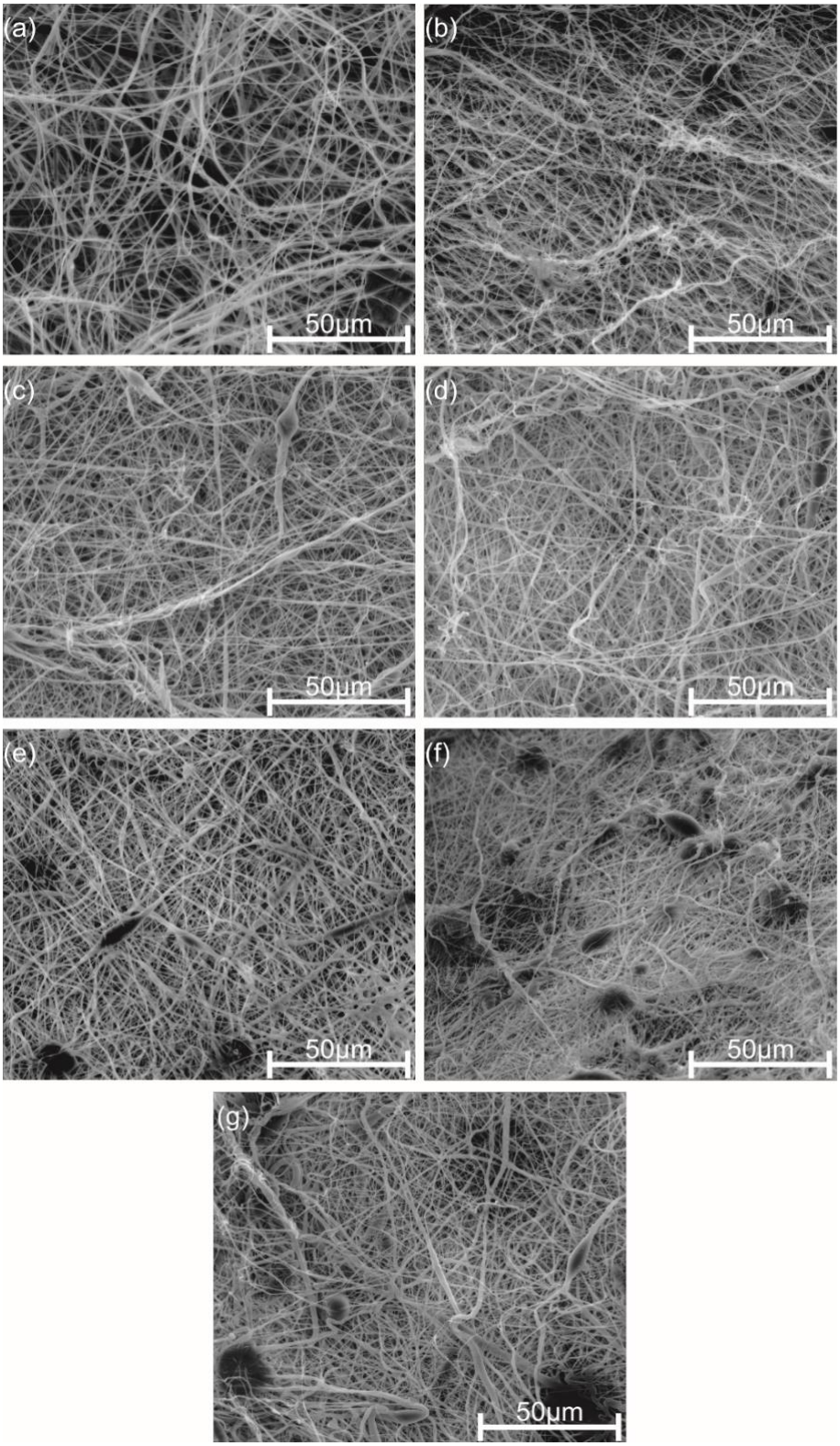


**Figure 7.3:** SEM image of the electrospun PETG meshes using different solvent splits (DCM/TFA) (a) 85/15, (b) 70/30, (c) 60/40, (d) 50/50, (e) 40/60, (f) 30/70, (g) 15/85. x1000 magnification.

Table 7.1 presents the average fibre diameter per mesh, which decreases by decreasing the DCM content. This can be attributed to the volatility of the solvents, as TFA is more volatile than DCM, thus presenting a fast evaporation that leads to thinner fibres.

Table 7.1: Average fibre diameter based on the solvent split

| Solution (DCM/TFA) (v/v) | Fibre Diameter (µm) |
|---|---|
| 85/15 | 1.108 |
| 70/30 | 0.800 |
| 60/40 | 0.677 |
| 50/50 | 0.559 |
| 40/60 | 0.428 |
| 30/70 | 0.289 |
| 15/85 | 0.243 |

### 7.3.3 Mesh Chemical Composition

The chemical composition of the electrospun PETG meshes was investigated using FTIR, a non-destructive analytical technique that allows to qualitatively assess the crystallinity of the electrospun meshes. Figure 7.4 shows the FTIR spectra for the different electrospun meshes. Common PETG characteristic peaks were recorded at 965 $cm^{-1}$ (C–H stretching peak of cyclohexene ring) [483], 1106 $cm^{-1}$(in-plane vibrations of the CH bonds) [483], 1260 $cm^{-1}$ (ester groups) [483], 1717 $cm^{-1}$ (C=O ester group) [483], 2861 and 2939 $cm^{-1}$ (C-H symmetrical and asymmetrical stretching vibration in the aliphatic polymeric chains) [483].

As the C-H stretching of cyclohexene ring increases it can be concluded that the CHDM (amorphous material) content also increases, and crystallinity decreases (see Chapter 4). Moreover, from the different solvent splits, it can be noted that the TFA dominant splits have a slightly higher crystallinity compared to DCM dominant splits.

Raman spectroscopy was used as a non-destructive, robust, and rapid analytical technique to qualitatively assess the chemical difference between different electrospun meshes. Results are presented in Figure 7.5. All obtained spectra were treated with baseline correction by subtracting a polynomial fit of the baseline from the raw spectra. This was done to remove the tilted baseline variation occurring due to different noises.

Common PETG characteristic peaks were obtained at 793 $cm^{-1}$ (C-H ring out-of-plane bending + C=O bending) [480], 900 $cm^{-1}$ (C-H ring out-of-plane-bending) [480], 1021 $cm^{-1}$ (C-H ring in-plane bending) [480], 1116 $cm^{-1}$ (C-O stretching) [480], 1273 $cm^{-1}$ (C-O stretching of ester group) [480], 1377 $cm^{-1}$ (gauche $CH_2$ wagging) [480], 1502 $cm^{-1}$ (-$CH_2$ bending peak of the PETG macromolecular chain backbone) [480], 1613 $cm^{-1}$ (symmetric stretching of the 1,4 para di-substituted benzene ring) [481], and 1727 $cm^{-1}$ (C=O stretching of ester group) [480].

The crystallinity of PETG can be observed from the 1116 $cm^{-1}$ (C-O stretching) as it is slightly shifted to the right and exhibits shoulder at ~1190 $cm^{-1}$ [508]. In addition, the peak at 1727 $cm^{-}$

[1] appears wider for lower crystalline materials. Both phenomena are observed in the DCM dominated solvent splits, indicating lower in crystallinity [508].

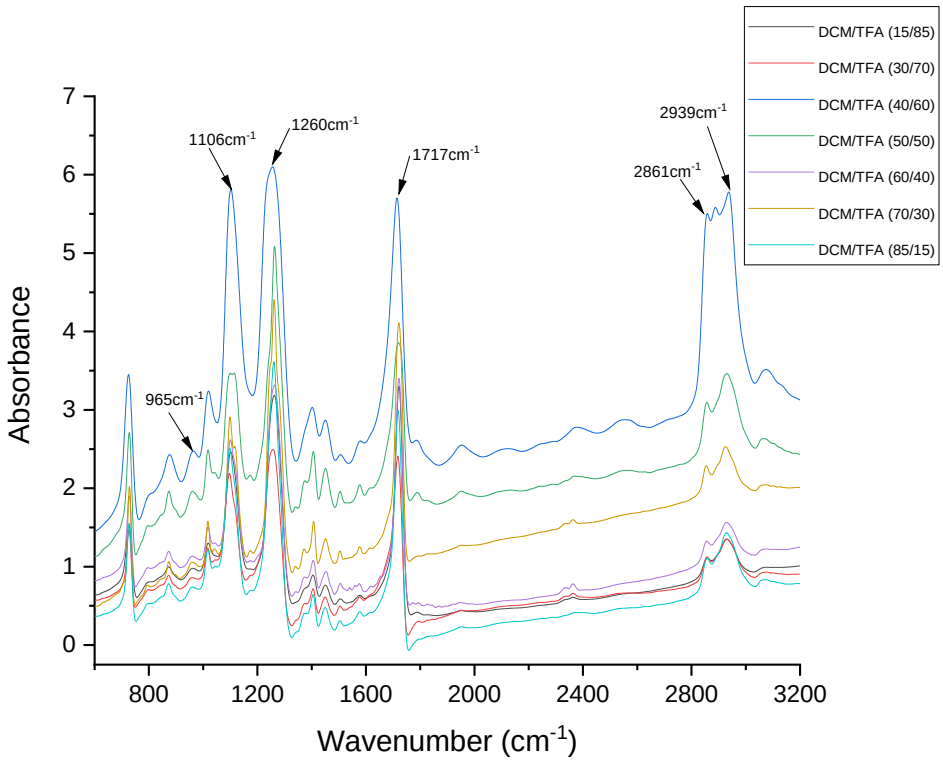


**Figure 7.4**: FTIR spectra of electrospun PETG meshes using different solvent splits (DCM/TFA).

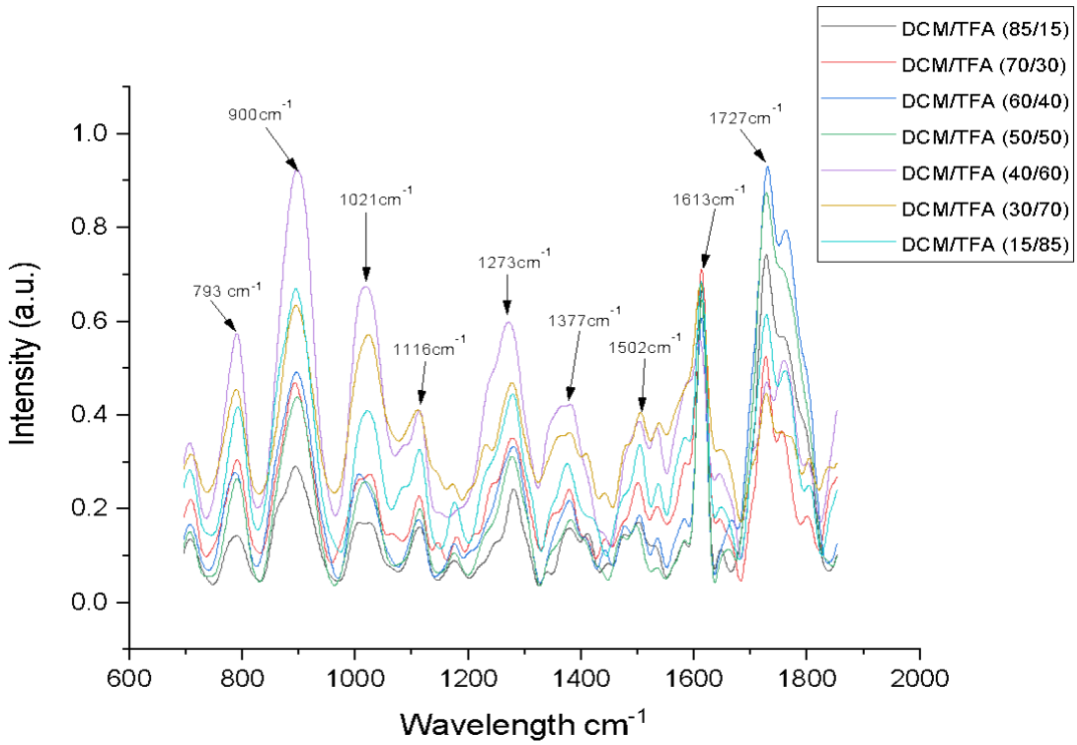


**Figure 7.5**: Figure 4: RAMAN spectra of electrospun PETG meshes using different solvent splits (DCM/TFA).

### 7.3.4 Inoculation

Inoculation tests were conducted to investigate the ability of the different meshes to sustain pathogen attachment and germination, and the results are presented in Figure 7.6. From Figure 7.6 (a) it possible to observe that, immediately after inoculation, the spore are dispersed on the meshes. Figure 7.6 (b) shows the clusters growth of the fungal spores after 24 hours, while Figures 7.6 (c) and 7.6 (d), presents a magnified image of the germinated germ tubes. These results demonstrate that the produced meshes enable the growth of the fungal spores.

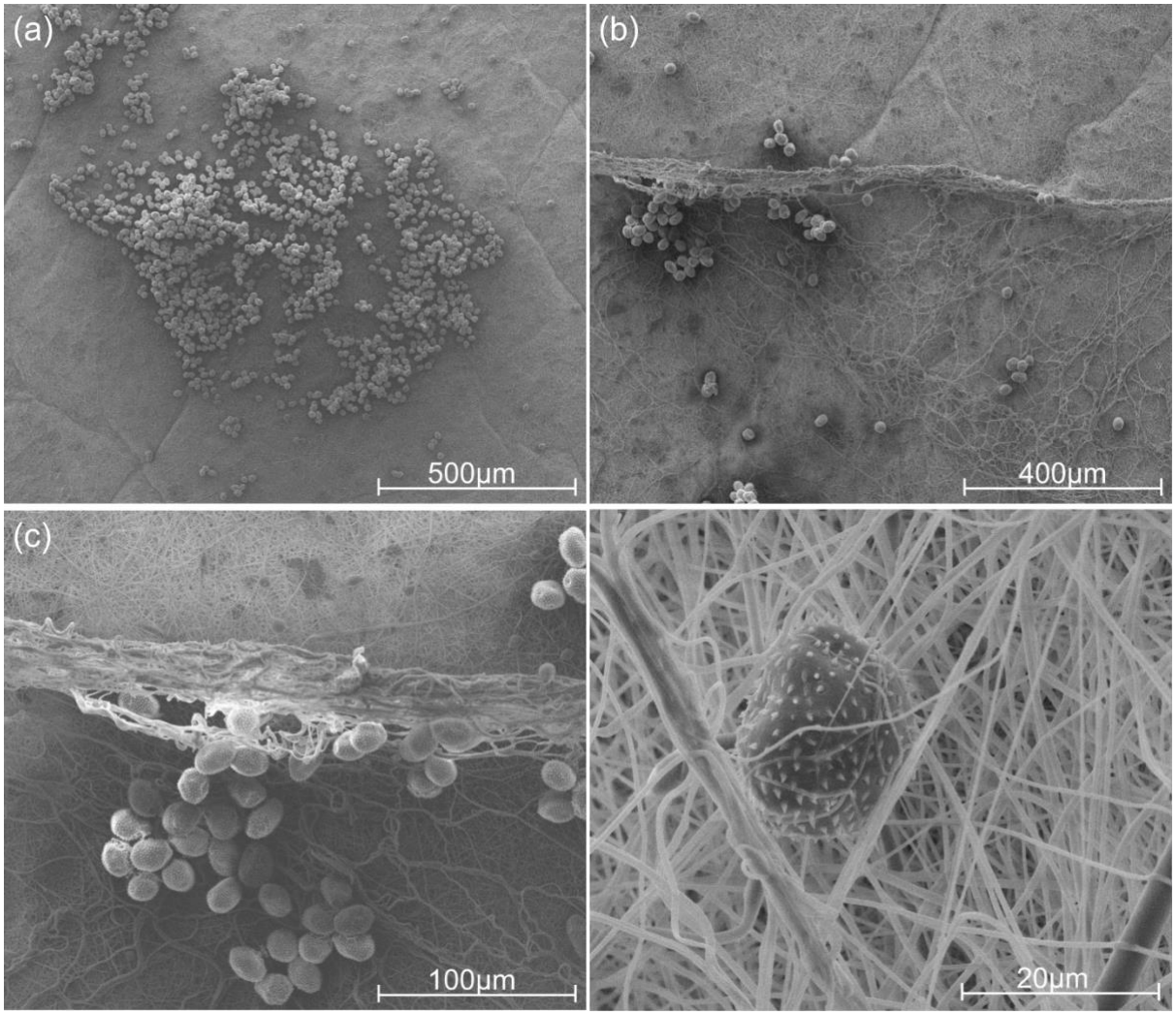


**Figure 7.6**: (a) SEM image of *P. s. f. sp. tritici* spores (X100) at 0 hours of inoculation, (b) SEM image of *P. s. f. sp. tritici* spores (X200) after 24 hours, (c) SEM image of the germinated *P. s. f. sp. tritici* spores (X500), ), (d)) SEM image of the germinated *P. s. f. sp. tritici* spores (X2000).

## 7.4 Conclusion

This Chapter investigates strategies to create PETG electrospinning meshes, a polymeric material considered difficult to spin. According to our best knowledge this was the first attempt

to create PETG meshes using solution electrospinning. Multiple single and binary-solvent systems were used to investigate the solubility of PETG, and it was found that DCM/TFA presented the best solubility-spinnability results among the different solvents. Optimal processing conditions were determined, and final meshes were produced at flow rate of 4 mm/h, voltage of 16 kV, and humidity of 40-50 %. Meshes obtained under optimal processing conditions were chemically characterised using both FTIR and Raman, and the results show that meshes produced using DCM dominant splits have lower crystallinity, while meshes produced using TFA dominated splits seem to exhibit higher crystallinity. This can be attributed to the difference in volatility and evaporation rate of DCM and TFA.

Morphological characterization was performed using SEM and the results showed the presence of beads in TFA dominant splits, whereas DCM dominant splits were bead-free. Moreover, meshes produced using DCM/TFA (1:1) present the best trade-off between fibre thickness and surface roughness. Moreover, inoculation on the optimal mesh was carried to investigate the bioactivity, and the results demonstrated fungal germination and proliferation of the yellow rust spores. Results presented in this Chapter suggest that the produced electrospun PETG meshes have high potential to be use in sensing applications. However, it was decided to use casted PETG as electrospun PETG did not offer the morphology required to optimise the spore germination.

# Chapter 8: Multi-layer biosensor for pre-symptomatic detection of Puccinia strifformis, the causal agent of yellow rust

*As discussed in Chapter 1, yellow rust of wheat caused by Puccinia striiformis f. sp. tritici is a devastating fungal infection responsible for significant wheat yield losses. The main challenge with the detection of this disease is that it can only be visually detected on the leaf surface between 7 and 10 days after infection, and by then counter measures such as fungicides are generally less effective. Based on the results obtained from previous Chapters, this Chapter discusses a novel compact electrochemical-based biosensor for the early detection of P. striiformis, enabling fast countermeasures to be taken. This is a major innovation as the proposed biosensor allows the detection of yellow rust spores in 72 hours. The biosensor developed consists of 3 layers. The first layer should mimic the wheat leaf surface morphology. Despite the successful results presented in Chapter 7, it is not possible to create a biomimetic layer using electrospinning. However, the results presented in Chapter 7 demonstrated the ability of PETG to sustain pathogen inoculation and germination. In this Chapter a casting method is considered using a mould that replicates the leaf surface. The second layer consists of a sucrose/agar mixture that acts as a substrate and contains a wheat-derived terpene volatile organic compound that stimulates germination and growth of the spores of the yellow rust pathogen P. s. f. sp. tritici. The third layer consists of a nonenzymatic glucose sensor that produces a signal once invertase, produced by P. striiformis, encounters the second layer, converting sucrose to glucose.*

## 8. Multi-layer biosensor for pre-symptomatic detection of Puccinia strifformis, the causal agent of yellow rust♠

### 8.1 Introduction

To accommodate for the rapidly increasing global population, it is estimated that global food production would need an increase of 70% to avoid a food crisis [509-513]. Wheat (*Triticum aestivum* L.) is an important cereal crop and a staple source of food for approximately 40% of the world's population [514]. In 2021 the world production of wheat was 778.6 million metric tons, with the European Union, China and India being the three largest producers [515]. Due to the importance of this crop wheat yield losses present a major problem for global food security [516, 517].

♠ This Chapter is based on the following publication: Mohamed Hassan, Abdalla Omar, Evangelos Daskalakis, Abubaker Mohamed, Lesley Boyd, Christopher Blanford, Bruce Grieve, Paulo Bartolo – "Multi-layer biosensor for pre-symptomatic detection of Puccinia strifformis, the causal agent of yellow rust", Biosensors, 12, 829, 2022.. Mohamed Hassan contribution: material preparation, solubility and electrospinnability tests, mesh production, characterisation, and data analysis.

Wheat yellow rust fungi (*P. s.* f. sp. *tritici)* is a fungal, biotrophic pathogen that affects grain quality, reducing protein content, as well as reducing yield [8, 518]. As an air-borne pathogen, spores can be transported considerable distances via wind, and can also be carried on animals and human clothing [1, 519]. Yellow rust is found predominantly in temperate and maritime environments, and its optimal temperature for infection and growth ranges between 7 d 22°C [4, 5].

Current strategies for yellow rust management are based on the use of genetically resistant wheat varieties and fungicide applications as part of an Integrated Pest Management scheme [26, 27]. However, this contributes to the presence of pesticide-resistant fungal strains [28, 29]. In addition, the timing of fungicide application is critical for treatments to be effective.

*P. s.* f. sp. *tritici* spore germination can be seen within three hours of being deposited on the leaf surface (Figure 8.1). The spore absorbs the free moisture on the leaf surface, producing a germ tube. The cytoplasm within the spore moves into the growing germ tube as it orientates perpendicular to the epidermal cells of the leaf surface until it reaches a stoma [520-523]. Between 6-8 hours post inoculation the germ tube grows between the guard cells of a stomata and by 8-12 hours a substomatal vesicle is formed inside the stomatal cavity. Primary infection hyphae develop on the substomatal vesicle between 12-18 hours [523, 524]. A number of studies have suggested that *P. s.* f. sp. *tritici* produces its own invertase, being required to aid nutrition uptake of the pathogen, by converting sucrose to glucose and fructose [19, 20]. Yellow rust leads to an increase in the reactive oxygen species in the infected plants, hence reducing the plant's overall photosynthetic efficiency leading to yield loss [21].

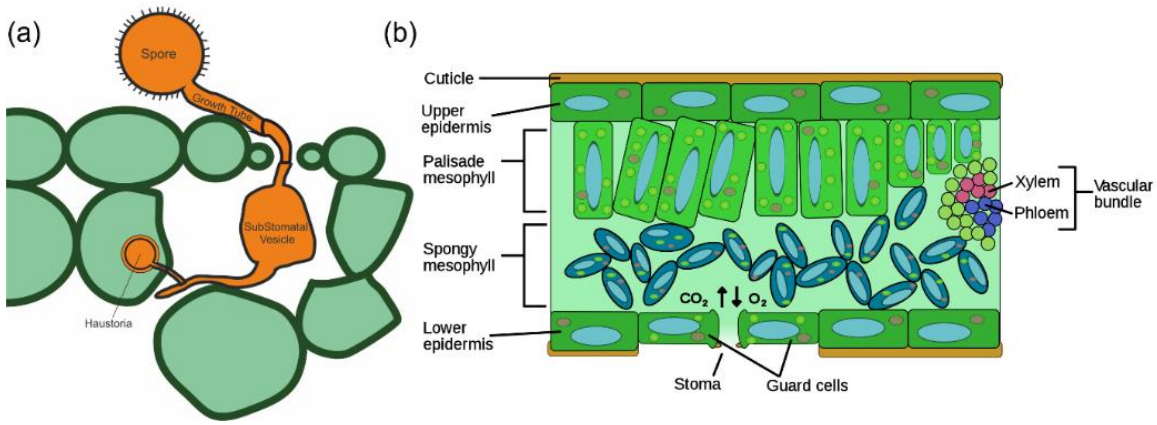


**Figure 8.1**: (a) Schematic representation of early infection structures of Puccinia striiformis. The spore germ tube enters the leaf through the stomata forming a substomatal vesicle from which infection-hyphae develop. Once the hyphae contact the mesophyll cell a haustoria is formed inside the plant cell. (b) Transverse section of a plant leaf showing the different layers of the leaf.

Volatile organic compounds (VOC) are metabolites produced by plants that are released into the air. Plants use volatiles to protect themselves from abiotic and biotic stresses, and supply information (or disinformation) to mutualists (ex: pollen carriers) and competitors [34, 525]. VOC acts as information transferors, resolving many problems faced by the plant's lack of mobility. VOC blends are dominated by four biosynthetic classes, terpenoids, fatty acids, amino acids, and compounds with aromatic rings (Fig. 8.2). Several lipophilic volatiles are released from the membranes of the plant's epidermal tissues. However, in leaves and stems VOC are released through the stomata, and as a consequence the opening and closing of the stomata influences the volatiles release [34, 525].

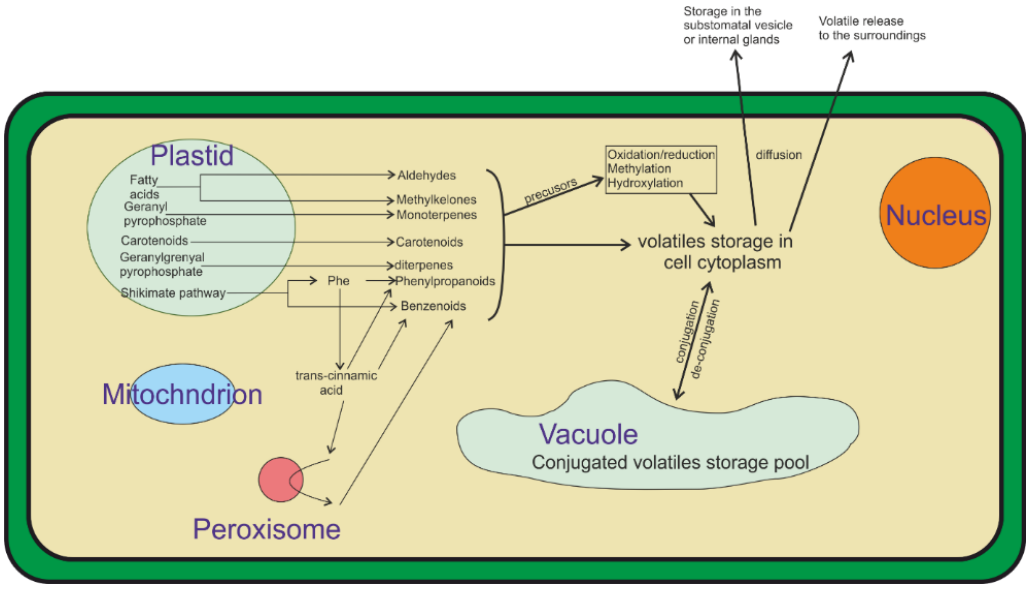


**Figure 8.2**: Most plant volatiles are derived from four biosynthetic classes: aromatics, fatty acid, terpenoids, and amino acids. Volatiles are produced from fatty acids via oxidative cleavage. Several of these products are modified to be more lipophilic prior to release, through masking or removing of hydrophilic functional groups through methylation, or reduction reactions. Figure modified from [34].

A major challenge related to yellow rust is that disease symptoms can only be visually detected 7 to 10 days after infection. However, at this stage the use of preventative fungicides is redundant, as the production of large numbers of spores being seen by 14 days already spread the disease through the field. This raises the need for an early pathogen detection system that would enable farmers to apply preventative fungicide treatments well in advance of infection and disease establishment.

Hyperspectral imaging technologies are used for plant disease detection and recently have been increasingly investigated for yellow rust detection [526-528]. Spectral sensors measure the light reflected from the plant surface [529]. As the disease develops the light spectrum shifts enabling disease detection [530-532]. These systems use machine learning and, to operate

properly, require the crop to be monitored for a few seasons to collect enough data to enable subsequent accurate detection, as well as detecting the symptomatic responses of plants. Thus, immediate deployment and use is not possible. Moreover, these systems are prone to errors due to different angles of sunlight reflected from the plant surface.

Biosensors are used for agricultural and environmental monitoring applications to detect various pathogens and other environmental contaminants [533, 534]. Due to their relatively high detection rate and short response time, the use of biosensors is increasing [535, 536]. However, the main challenges faced by current biosensors lie in the sensor performance, sampling, scaling up and detection in open areas [533, 534]. Roy *et al.* [537] fabricated an array of whole cell biosensors to detect aromatic pollutants such as benzene, phenols and toluene, which are carcinogenic compounds found in polluted water sources. The sensor was able to detect inert pollutants without any functional groups. However, this biosensor was temperature-sensitive, which limited its operation in the field. Moreover, authors did not provide any details regarding the detection time. Shi *et al.* [538] designed a colorimetric nano biosensor to detect acetamiprid in soil. The sensor exhibited high stability, sensitivity, and selectivity. However, it requires the soil samples to be air-dried, and ground to pass through a 1 mm sieve, then oven dried at 35$^{o}$C for 48h. Then, dichloromethane (DCM) is added to the sample and filtered, and finally mixed with the sensing solution [538].

Advances in the field of nanomaterials have produced promising nanoparticle-based biosensors. Nanoparticles (e.g., noble and transition metal nanoparticles, CNTs, graphene, and nanostructured metal oxides) have been used for both enzymatic and non-enzymatic glucose biosensors, aiming to amplify the electron transfer rate, improving the biosensor performance in terms of selectivity and sensitivity [415, 539].

This Chapter presents an innovative, pre-symptomatic yellow rust detection system consisting of a three-layered biosensor and representing the first biosensor for yellow rust detection. The proposed biosensor is a low cost, and accessible detection in-field device for yellow rust. The material and fabrication cost has been kept below £5 per unit. The production of the sensor is a simple and direct method that used commonly found apparatus and has an average lead time of 15 minutes. The operational rationale of the proposed modular sensor is shown in Figure 8.3. The target analyte (spores of *P. s.* f. sp. *tritici*) lands on the artificial surface of the sensor (first layer). This layer mimics the wheat leaf morphology with parallel venation and artificial stomatal openings. Following the spores landing, germination takes place. The spores produce germ tubes that grow through the artificial stomatal opening towards the second layer, which consists of a sucrose/agar mixture acting as a feeding media, and a plant VOC that acts as a

growth enhancing stimulant [525]. Invertase is produced by the germinated spores breaking down the sucrose into glucose. The third layer is a nonenzymatic glucose sensor that detects the glucose [20], generating an electrochemical response which can be detected using cyclic voltammetry (CV), thereby signalling the presence of the target pathogen.

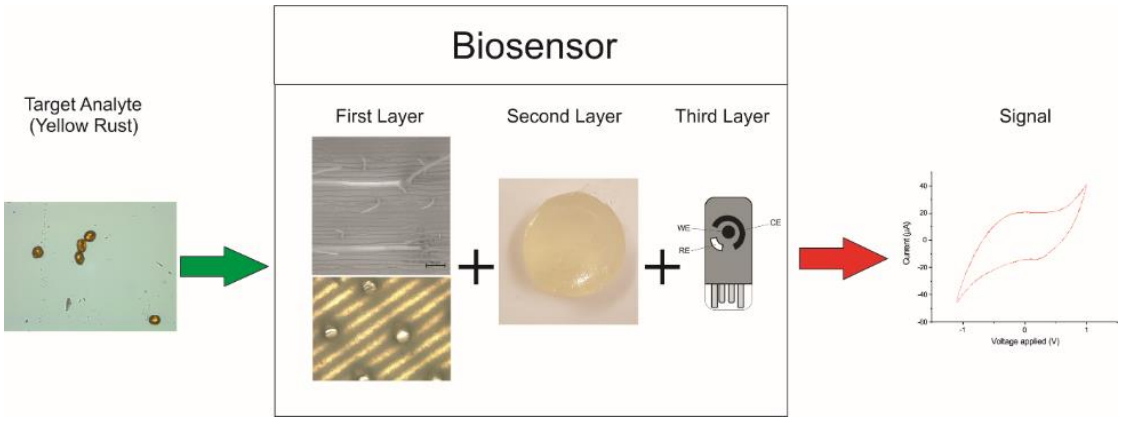


**Figure 8.3**: Operational rationale of proposed yellow rust biosensor. The signal can be obtained directly as a CV curve indicating the presence of glucose and therefore yellow rust.

## 8.2 Materials and Methods

### 8.2.1 Materials

Polyethylene terephthalate glycol (PETG) was purchased from RS components (Northants, UK). MicruX single thick screen-printed electrodes (working electrode (WE): Carbon; reference electrode (RE): Silver; counter electrode (CE): Carbon) were purchased from Alvatek (Hampshire, UK). Gold (III) chloride (AuCl3), nickel acetate tetrahydrate (Ni (OCOCH3)2 · 4H2O), N, N-dimethylformamide (DMF), activated carbon (AC), dichloromethane (DCM), ethanol, agar A4550, dimethylamine borane (DMAB), terpene and sucrose were purchased from Merck (Dorset, UK).

### 8.2.2 Sensor Fabrication

The sensor biomimetic surface was fabricated through a casting process. A mould was previously designed using Solidworks (Dassault systems, Massachusetts, USA) mimicking the wheat leaf surface (Figure 8.4). Formlabs Form3 (Formlabs, Somerville, Massachusetts, USA) was used to produce the mould with a resolution of 100 µm (Table 8.1). After printing the mould (Figure 8.5), a PETG solution was prepared by dissolving PETG in DCM 1:10 ratio (w/v). The PETG solution (viscosity of 0.005 Pas) was then poured into the mould and left to dry for two hours. The produced layer was then peeled off.

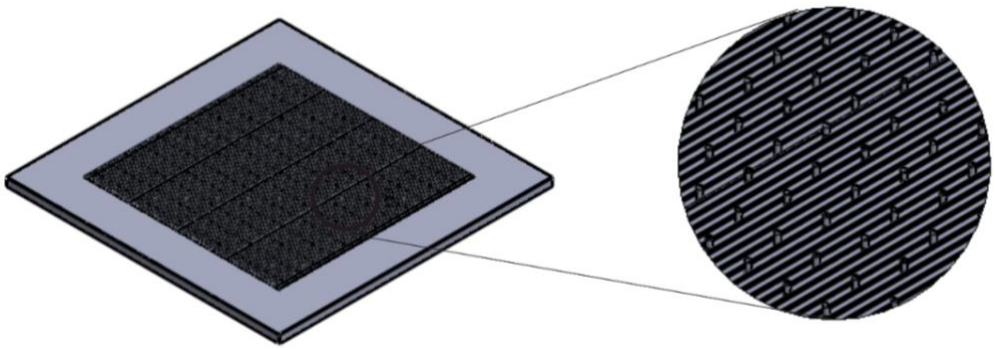

Figure 8.4: 3D model of the designed biomimetic leaf surface

**Table 8.1:** Printing parameters

| Parameter | Value |
|---|---|
| **Material** | **Formlabs Clear resin** |
| **Exposure time** | **1.7 s** |
| **Material Volume** | **3 ml** |
| **Number of layers** | **782** |
| **Layer thickness** | **1.7 µm** |

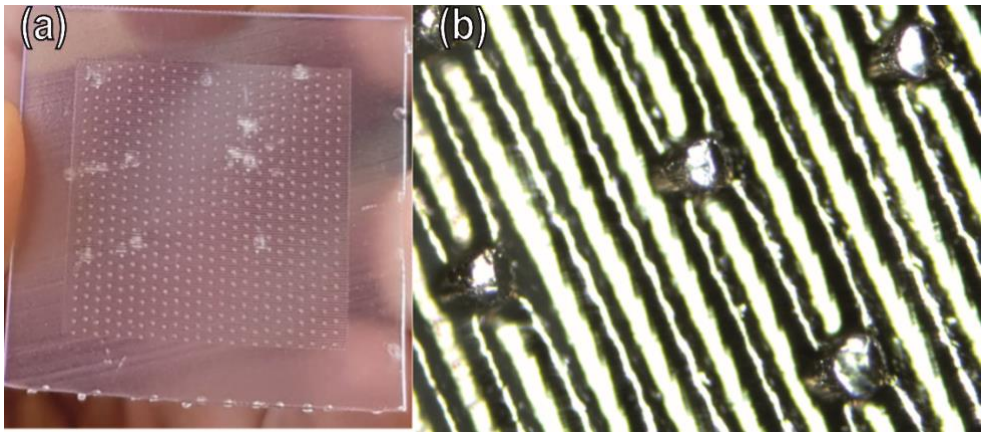


**Figure 8.5**:(a) Printed mould, (b) optical microscope image presenting the details of the printed model

The second layer was fabricated by mixing Agar A4550 and sucrose with a 1:4 (w/w) ratio. Briefly, 0.1g of agar and 0.4 g of sucrose were added to 20 ml of de-ionised water and stirred until a homogenous solution was obtained. The solution was heated up to 100 $^{o}$C using a hot plate, cooled down to 35 $^{o}$C allowing for gelation, and left to cool down to room temperature. Finally, a terpene VOC was injected into the produced agar gel.

The third layer consists of an Au-Ni/AC modified screen-printed electrode. An equal amount of Gold (III) chloride and Nickel (II) acetate (0.25 mmol) was dissolved in 15 ml of ethanol, followed by the addition of 2.5 mmol of activated Carbon. Activated carbon was used to increase the surface area, amplifying the sensing response by providing a larger area for the

interaction between the glucose and the nanoparticles. The solution was stirred until a homogenous mixture was obtained and refluxed for two hours at 90 $^{o}$C. Then, dimethylamine borane (DMAB) was added (1 mg) and the mixture was refluxed again for an additional hour. DMAB was used for the reflux, and this is used for activation of the Gold-Nickel-Activated carbon nanocomposite. Finally, the obtained mixture was dried to obtain the sensing Gold-Nickel-Activated carbon nanocomposite (Au-Ni/AC). The screen-printed electrode was modified using drop casting. Briefly, 1:10 (w/v) of Au-Ni/AC was added to DMF. The solution was sonicated for 30 minutes ensuring that the material was completely dispersed. Finally, 10 µl of the solution was drop casted on the SPE working electrode (WE) (Figure 8.6). The SPE was left to dry for 24 hours in the fume cupboard.

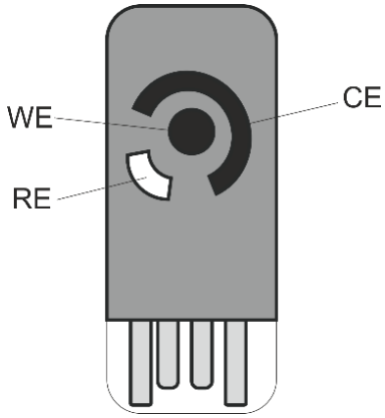


**Figure 8.6:** Schematic of the Screen-Printed electrode. WE: working electrode, CE: counter electrode, RE: reference electrode.

The casing of the sensor was designed considering a layering approach. The casing was designed with an insert slot to accommodate the screen-printed electrode (SPE), the top of the casing had an inclination to accommodate the agar/sucrose layer with a hole over the active area of the SPE allowing for the produced glucose to directly flow on the active area. Finally, the top of the casing was designed to be open to accommodate the casted top surface.

The sensor production can be scaled up by breaking down the production process. The casing can be produced using injection moulding, the top casted layer can be produced using vacuum forming, and the middle (feeding layer) can be produced using large scale polymerisation.

### 8.2.3 Inoculation

The bioactivity of the top layer was tested by inoculating *P. s. f. sp. tritici* spores onto the surface. Briefly, the surface was placed in the middle of a stainless-steel pipe covered by an aluminium sheet at the top and bottom (spore inoculation tower). A small hole at the side of the steel pipe was used to blow the spores into the pipe, with the spores settling onto the

biosensor surface by gravity. The surfaces were left in the steel pipe for 15 to 30 minutes to ensure that all spores had settled to the bottom of the pipe. The inoculated surfaces were then inspected under a light microscope to confirm that the spores had landed on the surface. The inoculated biosensors were placed in an incubator at 7$^{o}$C, in total darkness, for 24 hours.

### 8.2.4 Morphology

*P. s. f. sp. tritici* spore growth was investigated using optical microscopy (Keyence VHX-5000; Keyence, Milton Keynes, UK). The images were obtained using top light at two magnifications (x5 and x10). The light exposure was 100%.

The morphology of both first and third layers of the biosensor was characterised using the scanning electron microscopy (SEM) Tescan Mira3 system (Tescan, Kohoutovice, Czech Republic). The first layer was platinum coated prior to imaging using the 108-auto sputter coater (Cressington scientific instruments, Watford, UK). Imaging was performed using 20 KV acceleration voltage. Images were analysed using ImageJ (Laboratory for Optical and Computational Instrumentation, University of Wisconsin, WI, USA), to determine the pore size of the first layer and the gold-nickel dispersion on the surface of the third layer. The morphology of the third layer was further studied using atomic force microscopy (AFM) nanosurf FlexAFM system (Nanosurf AG, Liestal, Switzerland). The structure was assessed using X-ray diffraction (XRD) carried out on the X'Pert Pro X'celerator (Malvern Panalytical, Malvern, UK). Spectra were collected in the range of 2θ between 20$^{o}$ and 100$^{o}$.

### 8.2.5 Electrochemical measurements

The electrochemical behaviour of the sensor was assessed through cyclic voltammetry and chronoamperometry using the µAUTOLABIII/FRA2 potentiostat (Metrohm Autolab, Netherland). Measurements were conducted at room temperature using a lab-made electrochemical cell. Cyclic voltammetry was performed using a potential ranging between -1.0 V to 1.0 V with a scan rate of 100mVs$^{-1}$, to monitor the onset-potential of the prepared sensors towards the glucose catalytic oxidation from glucose to gluconolactone. Chronoamperometry was performed using a potential of 0.66 V over 600 s.

Electrochemical Impedance Spectroscopy (EIS) was used to evaluate the performance of the sensor using the µAUTOLABIII/FRA2 potentiostat (Metrohm Autolab, Netherland). This technique applied an alternate current (AC) rather than a continuous one (DC). To obtain the optimal frequency, a frequency range between 100 kHz and 0.1 Hz was used for impedance spectroscopic measurements. The amplitude of oscillation (AC) was set to 10 mVRMS. The optimal working potential was set to 0.66 V for measurements of glucose respectively.

## 8.3 Results and Discussion

### 8.3.1 Morphological Characterisation

Read *et al.* [540] investigated the growth of *Puccinia graminis f. sp. tritici* (wheat stem rust) and *Puccinia hordei* (barley brown rust) on artificial surfaces that mimic the leaf morphology using polyesters. As *P. striiformis* is related to *P.g. f. sp. tritici* and *P. hordei* it was assumed that *P. striiformis* would be able to grow on similar materials. Therefore, it was decided to use a material with the same backbone, PETG, to fabricate the biosensor by 3D printing. PETG is a bioactive and biocompatible material (see Chapters 5 and 7). The moulded PETG layer (first layer of the biosensor) was designed to mimic the wheat leaf surface morphology, presenting parallel grooves and stomatal holes (Figure 8.7a). The parallel grooves had a size of 200 µm and the stomatal holes an average size of 50 µm, with openings with an average size of 15 µm. The SEM images of the Au-Ni/AC modified screen-printed electrode identified two distinct regions (Figure 8.7b). The upper region exhibited a cotton-like nanostructure, while the bottom region showed a brain-like nano porous structure with small grains and channels. From the SEM images it was also possible to observe the presence of gold and nickel (light white) and activated carbon (black). Atomic force microscopy (AFM) results of the third layer (Figure 8.7c) showed the presence of round cap columns composed of several grains ranging between 40 nm to 1 µm. Channels with an average width of 5µm were formed around the columns allowing the glucose to pass through them.

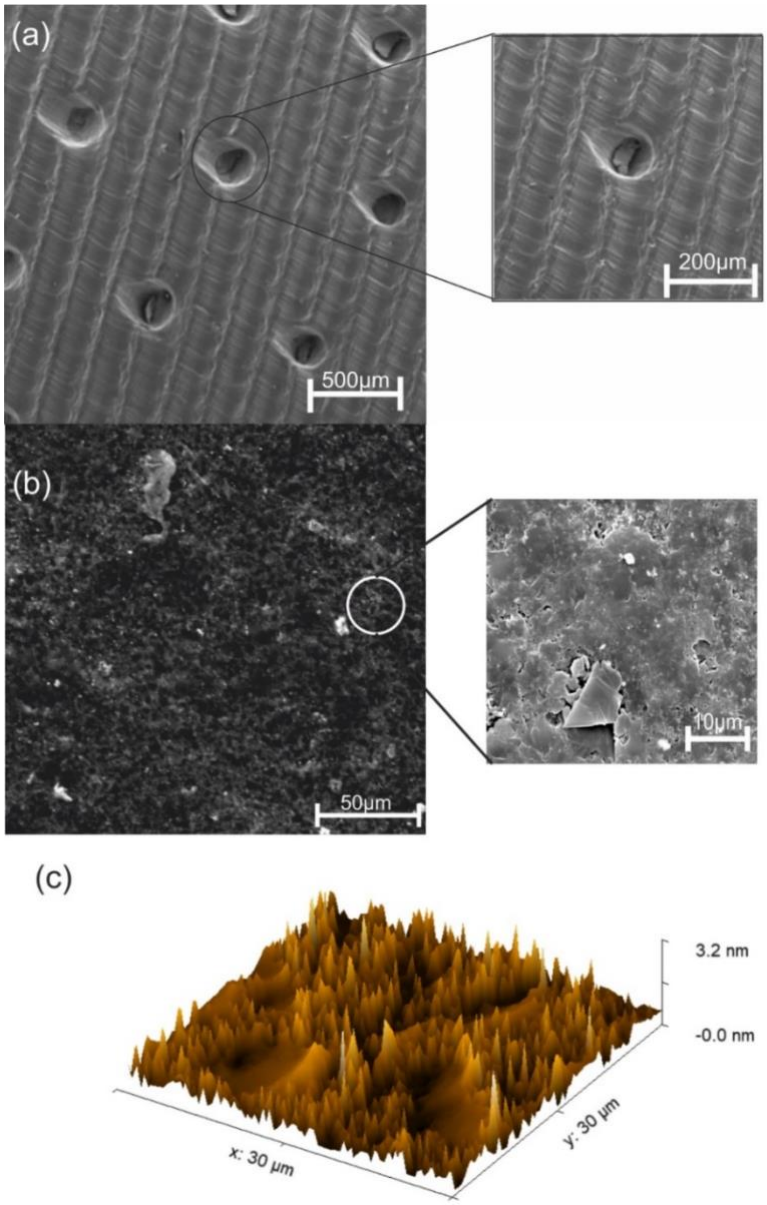


**Figure 8.7:** (a) SEM image of the casted biomimetic PETG layer. The created parallel venation mimics the wheat leaf with a width of 200 µm. The detailed, zoomed SEM image shows a stomatal hole with a diameter of 50 µm with an opening of 15 µm, (b) SEM images of the Au-Ni/AC modified screen-printed electrode, presenting two distinct regions. The zoomed SEM image clarifies the two regions where the carbon bed presents a Nano-porous structure allowing glucose to flow, and the top region, a cotton-like nanostructure consisting of Au-Ni particles (c) AFM image of the Au-Ni/AC modified screen-printed electrode exhibiting cylindrical round cap columns with channels allowing glucose to pass through.

### 8.3.2 Electrochemical Behaviour of the Au-Ni/AC SPE

The electrochemical behaviour of the Au-Ni/AC SPE toward glucose oxidation was assessed to evaluate its potential for glucose sensing. Figure 8.8 presents the CV curve of the Au-Ni/AC SPE in the absence (blue) and presence (red) of 10mmol of glucose in 0.1 mol NaOH. The CV curves obtained from the sensor exhibit four oxidation peaks at -0.27 V (peak A), 0.22 V (peak

B), 0.53V (peak E), 0.66 V (peak D), and one reduction peak at -0.04V (peak C). Peaks A, B, and C correspond to the typical two-step Au-glucose oxidation process, where peak C represents the reduction step to regenerate the sensor active sites, despite the presence of Ni. The electrocatalytic mechanism of Au-Ni/AC for glucose is a multistep process [541]. The process is initiated when the glucose molecules are dehydrogenated and adsorbed onto the surface of the Au-Ni/AC particles, followed by an increase in the metal-$OH_{ads}$ that increases the potential, hence mediating the catalytic oxidation of the intermediaries towards gluconolactone.

Similar to glucose oxidation on pure gold surfaces [542, 543], the glucose oxidation on the surface of Au-Ni/AC SPE mainly depends on the quantity of metal-$OH_{ads}$ as well as on the premonolayer oxidation of the metal producing metal-$OH_{ads}$. Peak A (Figure 8.8) can be linked to the glucose dehydrogenation forming adsorbed intermediate products. The intermediates accumulation, due to the limited number of metal-$OH_{ads}$ sites, is produced at a lower potential (-0.27 V) blocking the Au-Ni/AC SPE surface active sites, hence decreasing the current. Peak B at 0.22 V is attributed to the consecutive catalytic oxidation of the adsorbed intermediates due to the increased metal-$OH_{ads}$ sites, while peak D corresponds to the formation of metal oxides. In the negative potential scan, there is a current increase at 0.04 V due to the reduction of surface metal oxides occurring at a more negative potential than 0.23 V, and the presence of enough metal-$OH_{ads}$ sites for the glucose catalytic oxidation. A similar behaviour was observed by Gao's group, using a different setup, where Au-Ni was used as a core and shell, showing an increase in the anodic current at a potential of 0.26 V [544].

Peaks D and E are also associated with the conversion between Ni(II) and Ni(III), as they share a CV behaviour similar to Ni-based electrodes [545]. The Ni reaction mechanism in the alkaline medium for glucose oxidation can be explained as follows:

$$Ni + 2OH^- \rightarrow Ni(OH)_2 + 2e^- \quad (8.1)$$

$$Ni(OH)_2 + OH- \rightarrow NiO(OH) + H_2O + e- \quad (8.2)$$

$$NiO(OH) + glucose \rightarrow glucolactone + Ni(OH)_2 \quad (8.3)$$

The sensor was then tested for glucose detection without a buffer to simplify it. As observed from the CV profiles (Figure 8.9) it is possible to differentiate between the different electrochemical responses of glucose and sucrose.

The amperometric response of the Au-Ni/AC SPE (Figure 8.10) was investigated at 0.66 V which corresponds to the oxidation peak observed on the CV. The glucose was successively

added into the 0.1 mM of NaOH at 24s intervals for 20 steps. The sensor presented an extremely fast and stable response.

The Au-Ni/AC SPE was tested for its specific response by successive addition of glucose onto the sensor dipped in NaOH. The chosen range was 1-10 mM, as the target concentration for the detection of yellow rust is 5 mM based on the designed second layer. The calibration curve (Figure 8.11) shows an exponential increase in the peak generated current with the addition of glucose which agrees with the trends found in literature [546, 547].

As observed, there are two linear ranges between 1-8 mM and another between 8-10 mM. Based on these ranges, two sensitivities were calculated using a linear fit, being 0.25 μA $cm_2$ $mM^{-1}$ and 2.75 μA $cm^2$ $mM^{-1}$, respectively. The limit of detection (LOD) was also experimentally tested to find the lowest concentration the sensor can detect which was found to be 0.05 μM. The performance of the biosensor is in line with other non-enzymatic nanoparticle-based glucose biosensors in terms of sensitivity, linear ranges, and LOD. Reported sensitivities are between $1x10^{-2}$ – 1.04 μA $cm^2$ $mM^{-1}$, linear ranges between $7x10^{-5}$ - 20, and LOD of 0.1-15 μM [167, 548, 549].

Electrochemical impedance spectroscopy was conducted to analyze the impedance changes on the modified electrode surfaces. In EIS, an observing a straight line represents the diffusion limited electrochemical process which is the hypothesis of this research [550]. Pletcher [551] suggests that the electrocatalytic process implies a key role for adsorbed intermediates. Suggesting the initial oxidation of glucose limited to the surface would result in bulk oxidation as observed by the linear behaviour presented in Figure 8.12.

The stability of the Au-Ni/AC SPE was tested by cyclic voltammetry measurements before and after fifty times of amperometric analysis as shown in Figure 8.13. The results reveal that after a long period of electrolysis using the electrode the current kept almost 100% of its initial amount, whilst the peak potential has slightly moved positively by 0.6 V. The reproducibility and repeatability of the electrode were also determined by repeated testing for 1, 25, and 50 cycles in 5 mM Glucose in 0.1 M NaOH. These results imply that the proposed electrode has reproducible current as it is not contaminated by oxidation products and the shift remained constant between 1, 25, and 50 cycles.

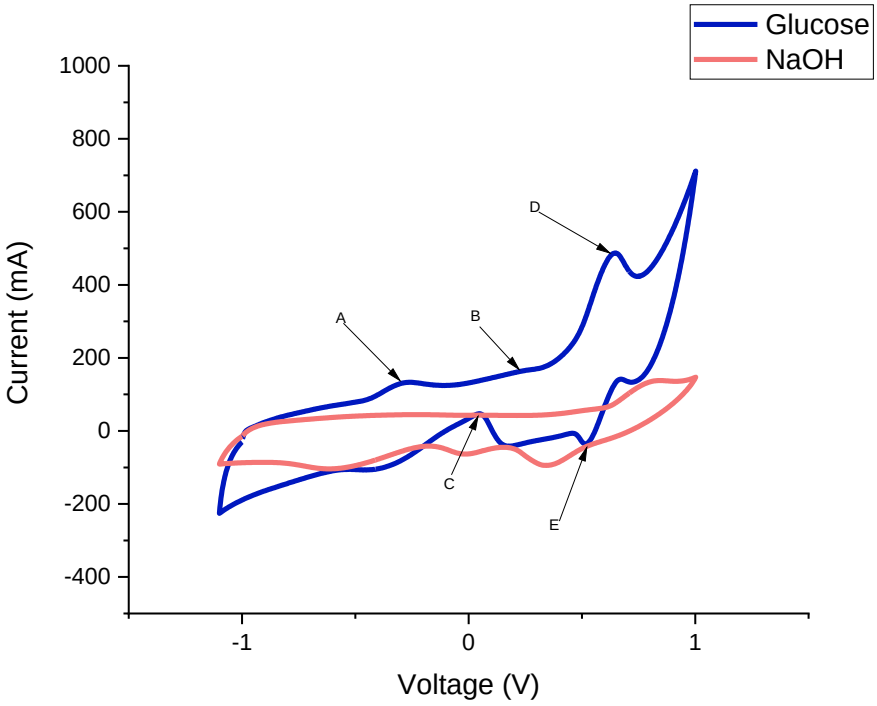


**Figure 8.8:** CV curve of the Au-Ni/AC modified screen-printed electrode using NaOH as a buffer. The red curve corresponds to NaOH without glucose. The blue curve corresponds to NaOH in the presence of glucose. From the blue curve it is possible to observe the oxidation peaks at peak A (-0.27V), peak B (0.22V), peak E (0.53V), peak D (0.66V), and a reduction peak at peak C (0.04V).

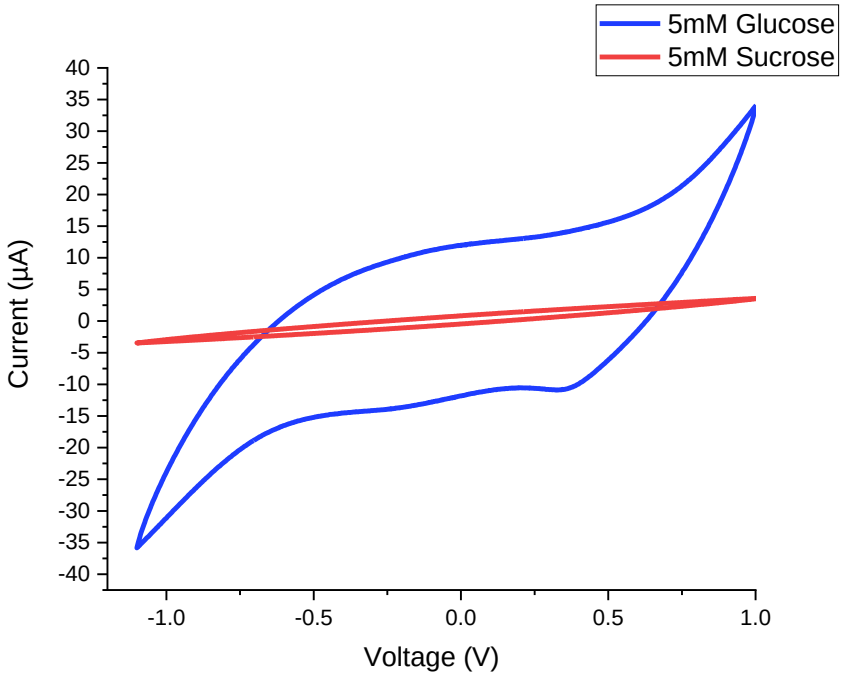


**Figure 8.9:** CV curves without a buffer (NaOH). The blue curve represents the response to 5 mM glucose. The red curve represents the response to 5 mM sucrose**.**

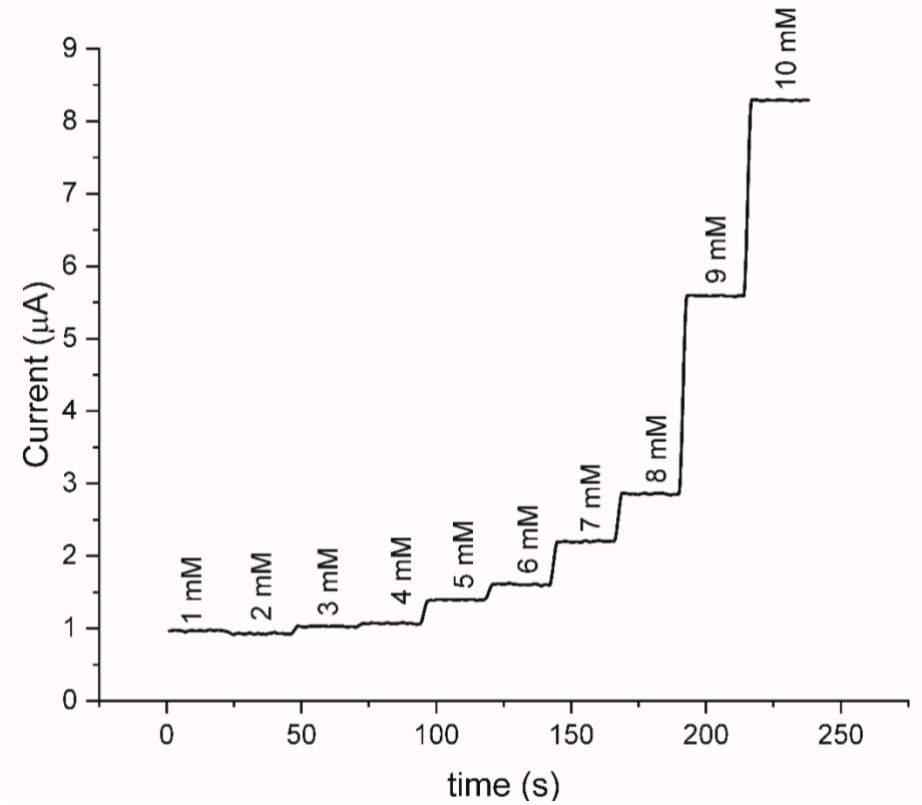


**Figure 8.10:** Current–time responses at 0.66 V with an increasing glucose concentration.

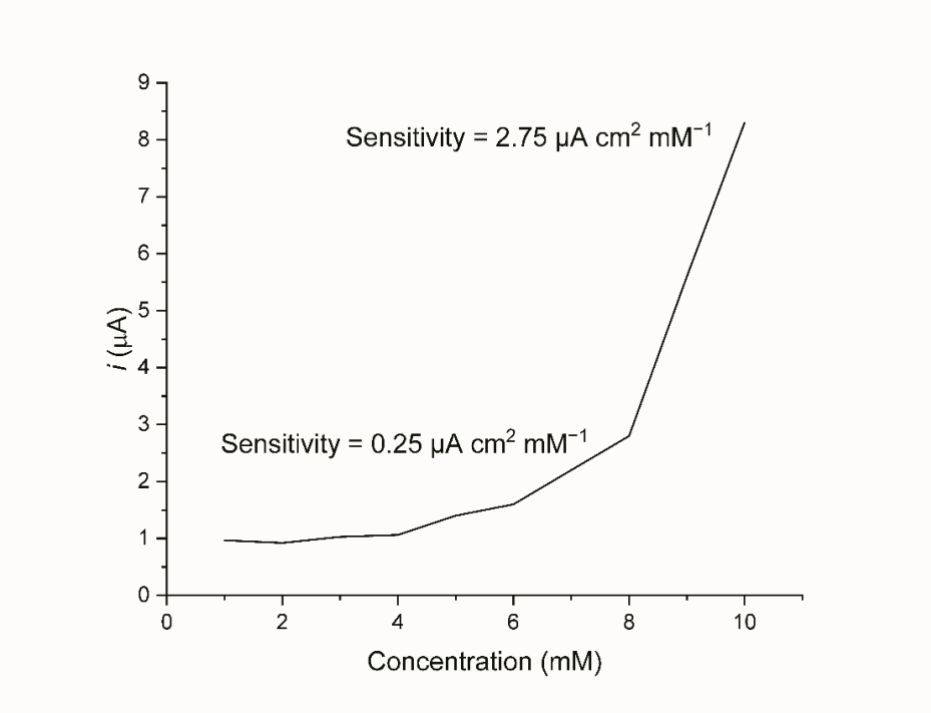


**Figure 8.11:** Calibration curve of the current versus different glucose concentrations (1 to 10mM)

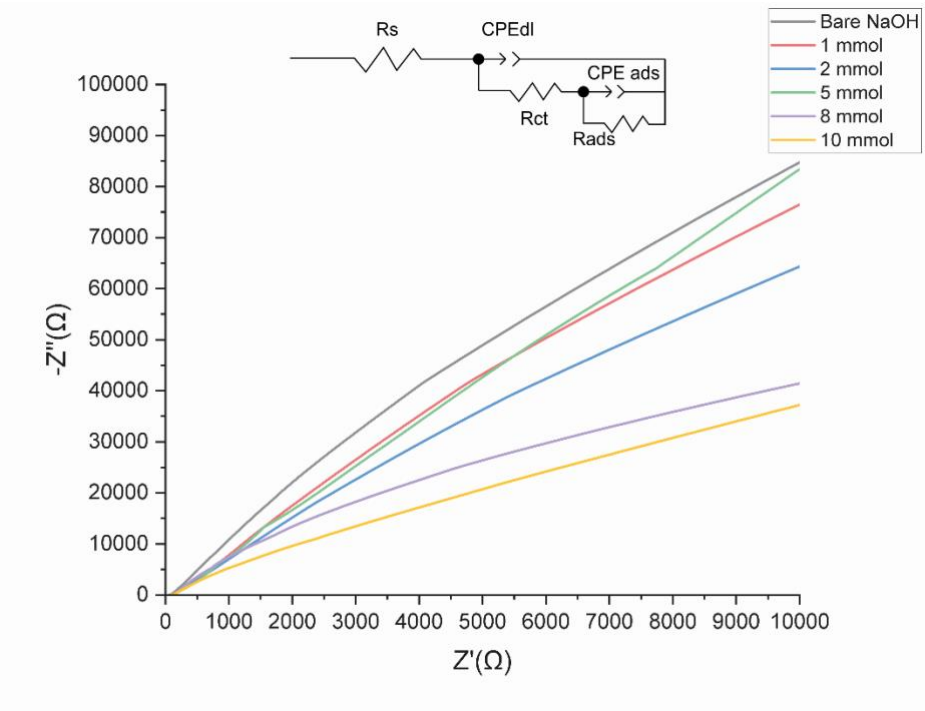


**Figure 8.12:** Nyquist plots for Au-Ni/AC SPE in 0.1 M NaOH solution for 0–10 mM of Glucose concentration range.

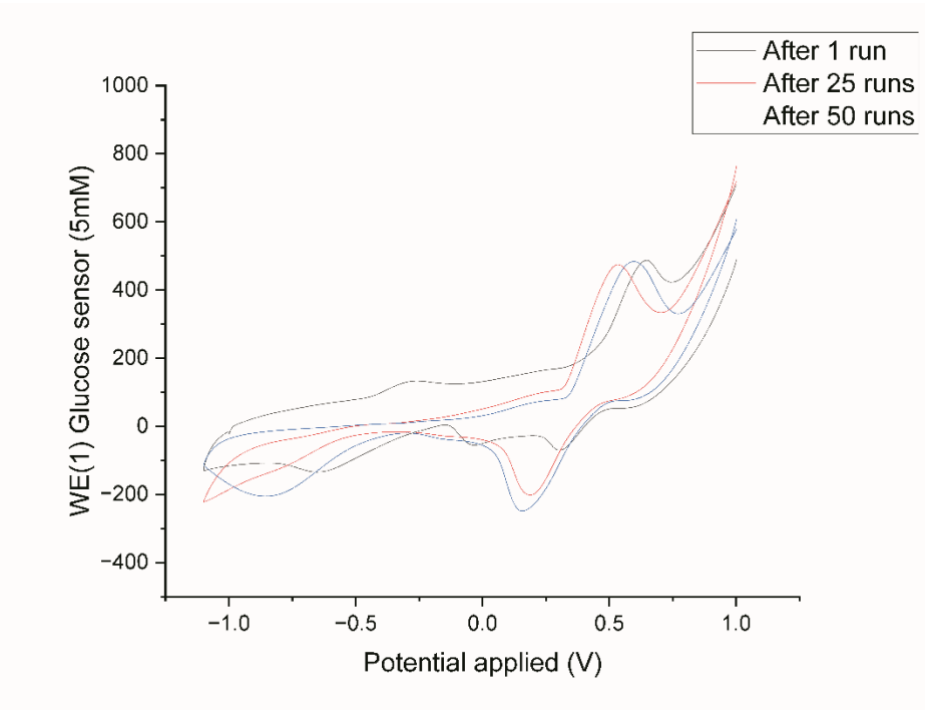


**Figure 8.13:** CVs of Au-Ni/AC SPE after 1, 25 and 50 times of amperometric tests in 5 mM Glucose in 0.1 M NaOH.

### 8.3.3 Nanoparticles characterisation

The XRD patterns of Au-Ni/AC nanoparticles are presented in Figure 8.14, showing characteristic diffraction peaks at 2θ = 38.6°, 43.7°, 50.8°, 64.9°, 74.4°, 90.2° and 95.4°. As

previously reported, the peaks confirm the presence of the elements Au and Ni: 38.7° Au (111), 43.7° Au(200)-Ni(111)/AC(100)(101), 50.8° Ni(200), 64.9° Au(220), 74.4° Au(311)-Ni(220), 90.2° Ni(311), and 95.4° Au(400)-Ni(222). Furthermore, the shift in peaks indicates that the Au-Ni/AC alloy is present on the sensor surface [552, 553]. Furthermore, the average crystallite diameter (d) values calculated using Scherrer's equation (8.4) are ~ and ~41.8 nm for Au-Ni/AC nanoparticles, using full width at half maximum (FWHM) of the most intense peak at 43.7°. β is the FWHM value (radians), 'λ' is 1.5406 Å, which is the CuKα wavelength, and θ is the Bragg diffraction [554, 555].

$$D = 0.9\lambda/(\beta \cos\theta) \quad (8.4)$$

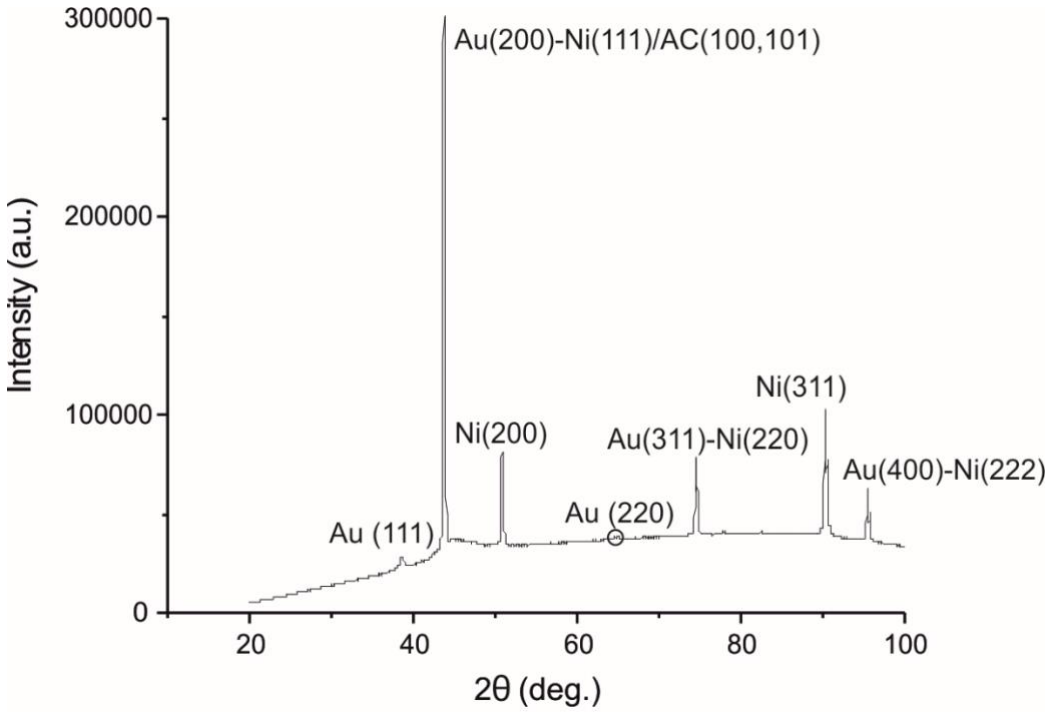


**Figure 8.14**: Au-Ni/AC X-ray diffraction analysis. The peaks represent the different materials present on the surface of the electrode. Au (111) at 38.6o, Au (200)-Ni (111)/AC (100)(101) at 43.7o, Ni (200) at 50.8°, Au(311)-Ni (220) at 74.4°, Ni (311) at 90.2°, and Au (400)-Ni (222) at 95.4°.

### 8.3.4 Sensor Selectivity

The sensor was designed to operate at a temperature ranging between 7 to 22 °C. A commercial screen-printed electrode was used to enable the connection to any CV machine, allowing for further integration in any system. Currently common wheat diseases include blotches, rusts and head blight/scab [556]. Based on the genome analysis of all the agents causing these diseases

it can be deduced that invertase production is a unique characteristic of *P. s. f. sp. tritici* spores as shown in Table 8.2 [20]. Hence the sensor was designed to selectively detect yellow rust.

**Table 8.2**: List of common wheat diseases and their agents, indicating invertase production based on their genomic make-up.

| Disease (agent) | Invertase production | Reference |
|---|---|---|
| Black rust (*Puccinia graminis*) | No | [557] |
| Yellow rust *(Puccinia striiformis*) | Yes | [20] |
| Leaf rust (*Puccinia triticina*) | No | [558] |
| Septoria blotch (*Zymoseptoria tritici*) | No | [559] |
| Septoria nodorum blotch (*Parastagonospora nodorum*) | No | [560] |
| Tan spot (*Pyrenophora tritici*) | No | [561] |
| Head blight/scab (*Fusarium graminearum*) | No | [562] |

### 8.3.5 Sensor Functionality

After printing the PETG sensor body, the agar/sucrose layer was placed inside the sensor body and covered with the casted mimetic layer. The assembled sensor (Figure 8.15a) was inoculated with spores of the yellow rust pathogen *P. s. f. sp. tritici* and placed in a temperature-controlled incubator at 7 $^{o}$C and humidity 60 %, in total darkness, for 24 hours [563]. *P. s. f. sp. tritici* spore germination on the surface of the biosensor was assessed using light microscopy (Figures 8.15b and 8.15c). The sensor was connected to the CV system to test for the presence of glucose, which was negative 24 hours after inoculation (Figure 8.15d). The sensor was placed back in the incubator at a cycle of 16 $^{o}$C/16 hours and 7 $^{o}$C/8 hours and tested for the presence of glucose again at 48 and 72 hours after inoculation. At 48 hours the response was negative, but at 72 hours a positive glucose response was obtained as shown in Figure 8.15e. The biosensor was tested three times, confirming the results. The growth of *P. s. f. sp. tritici* on the surface of the biosensor was further investigated using SEM (Figure 8.15f).

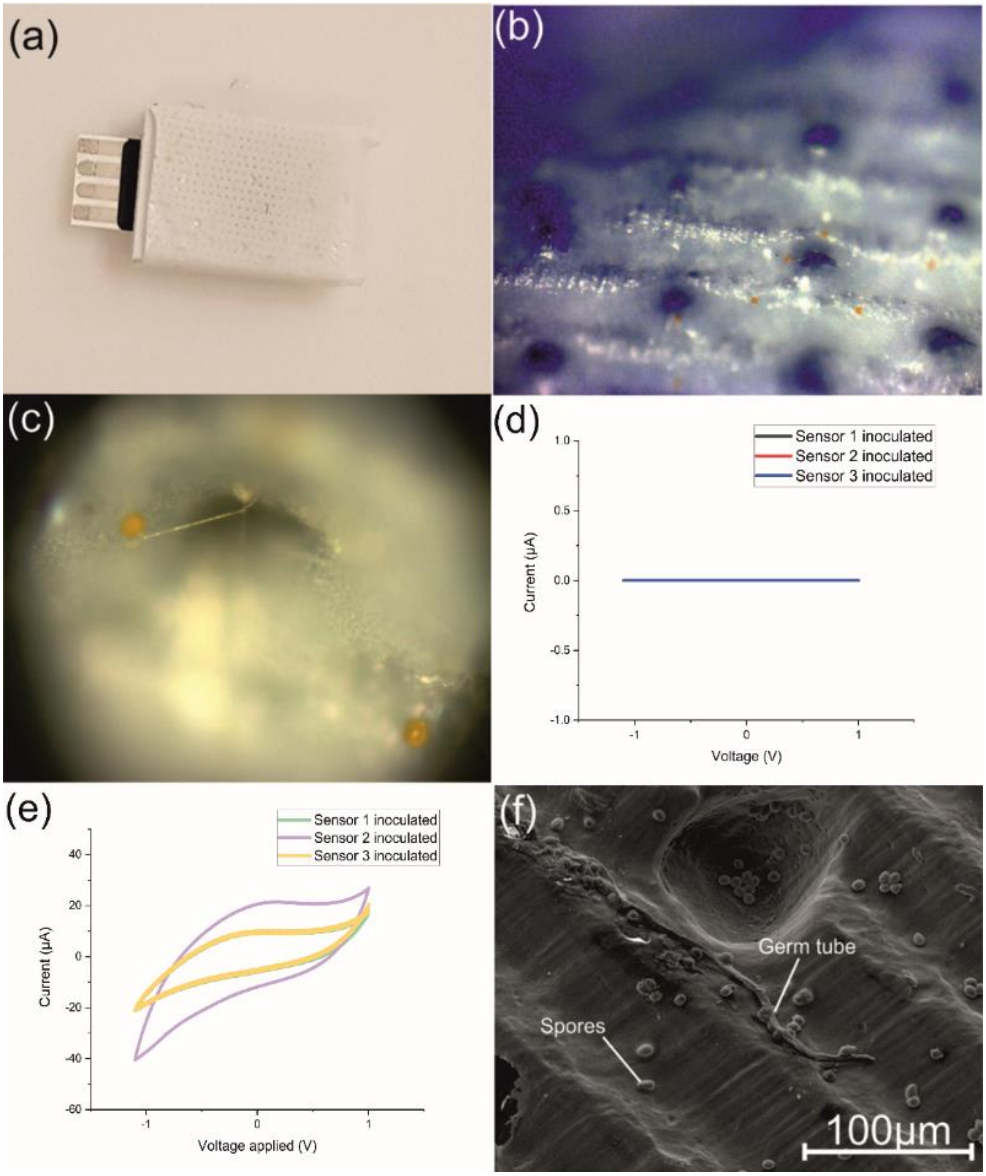


**Figure 8.15:** (a) Biosensor assembly, (b) top surface of biosensor inoculated with spores, (c) underneath surface of the top layer of the biosensor showing a germinated *P. s. f. sp. tritici* spore, (d) CV curve obtained at 24 hours, (e) CV curve obtained after 72 hours, (f) SEM image of *P. s. f. sp. tritici* spores and a germ tube growth on the surface of the biosensor.

## 8.4 Conclusion

A novel, multi-layer electrochemical biosensor was proposed for the detection of the fungal pathogen that causes the plant disease yellow rust of wheat. The first layer mimics the wheat leaf surface morphology and contains artificial stomata. The second layer consists of a sucrose/VOC/agar mixture that acts as a substrate, while a wheat terpenoid VOC provides a stimulus for *P. s.* f. sp. *tritici* germination and germ tube growth. The third layer is fabricated by casting affordable nanomaterials; the formed structure on the surface presents an innovative nonenzymatic sensor that detects glucose that is released from sucrose due to fungal invertase activity.

Inoculation of the biosensor with spores of *P. s.* f. sp. *tritici* resulted in a positive reaction 72 hours after spore inoculation. This biosensor would therefore enable pre-symptomatic yellow rust detection using an electrochemical approach. This proof of concept provides a substantial improvement to the current state-of-art biosensors, reducing the detection cost and time. Therefore, this is a promising solution for food security, and can prevent substantial annual crop yield losses due to *P. s.* f. sp. *Tritici*.

The proposed multilayer biosensor consists of three modular layers that can be easily changed allowing the detection of different pathogens. The modularity can be achieved by changing the morphology of the first layer to mimic the target crop, changing the feeding media (second layer) tailored towards the target pathogen and the third layer to be changed to detect the target analyte to signal the presence of the targeted pathogen.

# Chapter 9: Conclusion and future work

*The aim of this chapter is to provide an overview of the thesis. It starts with a summary and conclusions that can be drawn from the conducted research work as well as key contributions to the current state-of-the-art knowledge in the field of Electrochemical Agri-Biosensors. Possible future directions for research following on from this thesis are also presented.*

## 9.1 Conclusions

The agricultural sector is a major source of employment and income for the global population, with an estimate of 2.5 billion people engaged in agricultural [564]. The development of different agricultural techniques, including chemical herbicides and pesticides resulted in an enhanced crop yields by controlling weeds and pests' infestation. The toxic residues from pesticides enters the food chain and water cycles, leading to several diseases among the populations, and sometimes leading to death [565].

Detecting such chemicals at the appropriate levels is a challenge despite the use of various laboratory techniques such as high-performance liquid chromatography (HPLC), gas chromatography (GC), flow immunoanalysis, FTIR (Fourier-transform infrared spectroscopy) and NMR (Nuclear magnetic resonance spectroscopy), which are highly sensitive, reliable and efficient. However, they are time consuming, expensive, complex, and bulky requiring skilled technicians [566].

Agri-biosensors are an emerging and novel trend used to detect specific plant disease, and environmental contaminations which extends to agricultural products. Moreover, agri-biosensors are a fundamental element of a novel strategy called as Agriculture 4.0, based on the use of digital tools and technologies to increase farming efficiency, reducing food waste and the effects of climate change.

Overtime, biosensors have evolved through different stages. Initially the sensing elements and transducers were separated. Later, the two components were integrated and connected. Finally, in modern biosensors the sensing elements are directly immobilised on the surface of the electrode, which was further developed by replacing the biological sensing elements with non-biological sensing elements (mainly nanoparticles).

The development process of biosensors includes the synthesis of the sensing materials, selection of the sensing mechanism, signal processing unit and a sensing unit. Biosensors offer a user-friendly technology, which can be easily adopted by the farming sector, opening the door for the agricultural community to get into a smart and precision agriculture.

**This research work significantly contributes to improve the current state-of-the-art by proposing and validating a novel multi-material and multi-layer biomimetic biosensor to allow the early detection of *Puccinia striiformis*.**

From a material point of view, this was achieved by combining non-enzymatic glucose sensors (**Chapter 2, Section 2.1**) and a range of materials, including shape changing polymers **(Chapter 2, Section 2.2).** This was achieved by using biodegradable and biocompatible synthetic polymers (mainly PETG) acting as a growing layer for the *Puccinia striiformis*, and gold/nickel/activated carbon nanoparticles as the glucose sensing material detecting glucose produced the *Puccinia striiformis invertase enzymes*.

From a technological point of view, this was achieved by using additive manufacturing (3D/4D printing) **(Chapter 2, Section 2.2).** Key characteristics of plant biology (pathogen growth route, plant volatiles and leaf morphology) relevant to this research were discussed in **Chapter 1** (see **Section 1.1)**, while key characteristics of nonenzymatic glucose biosensors and shape morphing polymers are presented in **Chapter 2** (**Sections 2.1** and **2.2**).

The biosensor's literature review considered different classifications of biosensors. As discussed in **Section 2.1**, the best classification criteria seem to be the transducers criteria, as it provides a complete insight on the expected performance and results when using a specific type of biosensors. The concept of non-enzymatic electrochemical biosensor was found to be the most suitable to be used in this project due to its high accuracy and quick response when compared to other types of biosensors. Moreover, it allows to create a relatively simple sensing chemistry, reducing any complications that could occur due to the immobilisation techniques that are used in other types of biosensors.

It was noticed that the spore only grows on surfaces with the same morphology as the leaf which is characterised by its parallel venations and stomate. In **Section 2.2**, smart materials were investigated as potential materials to reproduce the stomata behaviour in the biosensor. They are a class of materials that rely on their thermodynamic behaviour, which enables the material to respond to external stimuli. This response depends on the material, additives, and/or molecular architecture. The materials response can be programmed by one or multiple cycles of activation that tune the state/microstructure of the material. Based on the literature review, the initial focus of the project was to use shape memory polymer (SMP), which corresponds to a sub-class of smart materials that changes shape in response to a stimulus. The scope was later extended to produce a shape changing polymer (SCP), which corresponds to a sub-class of smart materials. SCPs deform when the appropriate stimulus is applied, returning to their original shape either instantly or gradually when the stimulus is removed. In this research, the

materials used were photoactive materials (see **Section 2.2** and **Chapter 6),** which means the main stimulus used for its control was light. The material was used to create the artificial top surface of the biosensor to enable exact replication of the leaf surface functionality and not just the structure.

The wheat leaf morphology was assessed and used to build a biomimetic replica to be used as the morphology of the top layer of the proposed sensor. The most suitable mechanism to detect *Puccinia striiformis f. sp. Tritici* was identified as the detection invertase enzyme, as its production is a unique ability of the spores. The second layer, consisted of agar, sucrose and α-pinene, provided the feeding media and growth cues for the spores to germinate and break down to glucose. Finally, different glucose sensing mechanisms were investigated (see **Chapters 2,3**, and **8**), demonstrating the suitability of the use of Au-based non-enzymatic glucose sensors due to their sturdiness, durability, and sensitivity. All these factors were combined to assemble the proposed biosensor. The assembled biosensor functionality was confirmed in laboratory environment, leading to the worlds' first electrochemical biosensor for the pre-symptomatic detection of *Puccinia striiformis f. sp. tritici*, the causal agent of yellow rust.

Yellow rust (*Puccinia striiformis*) is a widespread pathogen that affects wheat in many countries across the globe. The growth capability of *Puccinia striiformis f. sp. tritici* on an artificial surface was tested to identify the most suitable material characteristics for the upper layer of the biosensor (**Chapters 1 and 3**). Materials with different stiffness and hydrophobic properties (agar, PCL and Mylar) were investigated. The fungal germination was evaluated by inoculating the printed surface using fungal spores. After 24 hours, the surface was observed using a light microscope to detect whether germination occurred or not. Results showed that the agar substrate (less stiff and presenting high content of water) allowed for the highest germination (96%), followed by PCL (80%) and finally Mylar without any observed germination. A Pt-Ni/MWCNT composite was produced and drop casted on the surface of a screen-printed electrode (SPE) aimed to detect the glucose produced due to the fungal invertase breaking down the sucrose. The SPE was tested for several cycles to identify its sensitivity, detection limit as well as its stability. As suggested by *Read et al.* [540], spores grew on substrate with a polyester backbone, hence it was decided to investigate PETG as a possible shape changing material, to be used as the top layer of the biosensor. PETG chemical composition, mechanical properties, and shape recovery were investigated in **Chapter 4.** PETG, showed promising results as a shape memory material. The bioactivity and

biocompatibility of PETG scaffolds were assessed and discussed in **Chapter 5,** which investigates the cell metabolic activity using the Alamar Blue assay, and the results compared to commonly used PCL scaffolds. These results provided a good indication to proceed with testing PETG as a germination media for the fungal spores (**Chapter 7**). PETG was incorporated with azobenzene, a photochrompohore, to produce a photoactive material. The resultant material responds to UV light by changing shape and regaining its original shape in the dark. The photoactive PETG took 30 minutes to change shape but took eight hours to recover its original shape, making it unsuitable for field usage and requiring further development and optimisation. PETG was also mixed with Polyvinyl Chloride (PVC) to fabricate a thermo-responsive material able to respond to temperature changes by changing shape. The new thermo-responsive material responded to change in temperature at 40 $^{0}$C, which is not low enough for field implementation, making it unsuitable for field usage and requiring further development and optimisation (**Chapter 6**). Therefore, it was decided to use virgin PETG as the main material for the top layer of the proposed biosensor.

Gold (Au) is a thoroughly investigated electrode material, characterised by providing a high glucose oxidation current in both neutral and alkaline environments. The main advantage of using Au-based electrodes for glucose sensing is the higher current response when compared to Pt-based electrodes, allowing for higher sensitivity and the ability to detect glucose in a neutral pH. Therefore, Au-Ni/AC was then used to replace Pt-Ni/MWCNT due to its stability and better detection response to glucose (**Chapter 8**).

All three layers of the sensor were assembled forming one detection unit as discussed in **Chapter 8**. The assembly was tested using invertase directly on the surface of the sensor, waiting for it to go through the top layer, reaching the sucrose layer, breaking it down into glucose, flowing to the working area of the SPE, inducing a current signalling the presence of the enzyme which in the field would mean the presence of the fungal spore. The sensor functionality for sensing yellow rust presence was tested in the laboratory. Yellow rust spores were inoculated on the surface of the sensor, and then the sensor was placed in an incubator simulating the infield germination conditions. The sensor was connected to a cyclic voltammetry (CV) machine at 24 hours intervals to test for the presence of glucose. After 72 hours, the sensor showed a positive result on the CV machine showing the detection of glucose hence signalling the presence of germinated yellow rust spores on the surface of the sensor. Based on these results the sensor showed the ability of detection in 72 hours which is less than the current visual detection time of 7 to 10 days. This would allow for earlier counter measures to be used hence less crop loss and more yield.

In summary, the key contributions to the current state-of-art emerging from this dissertation are:

- Defined and coined a novel non-enzymatic glucose sensor as the fourth generation of glucose sensors (objective 1)
- Leaf morphology is usually investigated in a dry state under SEM. In this research a hydrated leaf was scanned and used as a reference for the CAD design used to replicate the morphology using 3D printing. PDMS moulds and 3D scanners where also used to confirm the obtained layer similarity to the SEM image obtained. This represents a new and cost-effective approach (objective 1)
- It was demonstrated that PETG is a suitable material to sustain spores germination and to create a proper shape changing surface layer of a biosensor; and that alpha pinene is the most suitable volatile (objective 3 & 4).
- Designing and fabricating the world's first biosensor capable of detecting yellow rust in 72 hours (objectives 2 & 5)
- The produced sensor is considered as a state of art product as it is the first and only available infield sensor allowing for the detection and sensing of yellow rust in 72 hours, allowing for pre-infection measurements to be taken to counter it, hence increasing the wheat yield crop yield without increasing agricultural land space required.

## 9.2 Future Work

Several research questions have been answered through this thesis, but several other research questions were also opened and must be addressed in the future by further research studies. Possible future directions for research following on from this thesis can be undertaken in the following areas:

1) The multi-layered design of the sensor allows for modularity, hence can be easily adapted to detect different pathogens. Based on the target pathogen, the morphology of the first layer can be changed to mimic the surface of the corresponding plant leaf. This mimicry allows the layer to provide the required morphological cues required for pathogen growth. The second layer (feeding layer) can be changed based on the target pathogen to provide the appropriate nutrition, acting as a substrate that can be broken down into the analyte detected by the third layer. Volatiles can be also added as an

additional growth cue helping the target pathogen to grow. Finally, the third layer (sensing layer) can be tailored to detect target analyte indicating the presence of the pathogen.

2) Investigate the addition of additives to the PETG to transform it from a shape memory material into a shape changing one, allowing to develop a smart functional membrane. The membrane uses biopolymers to create 3D structures on a planar substrate that will imitate biological tissues, notably plant leaves and stems. The produced surface will comprise of additively printed smart biopolymer composites suitably doped patterned to mimic the necessary topological cues within the target plant, to cause a pathogenic spore to first germinate, grow and develop to infiltrate the host. These bioinspired engineered features may be optical, surface-topology, volatile-emission, nutrients, or any other combination of plant characteristics necessary to promote the growth of the pathogen.
3) Investigate other materials rather than agar for the second layer (feeding media) aiming to increase the shelf life of the sensor. Currently, agar dries after two weeks, which means that every two weeks the second layer of the sensor needs to be replaced. Other hydrogels with longer stability must be investigated. This will also require the investigation of the incorporation of the same nutrition and volatiles, and the optimisation of the release rates.
4) Field testing for the biosensor needs to be carried out to proof functionality. Moreover, the biosensor will be integrated as part of a wider sensing network using the internet of things (IOT), leading to the development of an early disease detection and warning system. The infield number of sensors should be around 3 per 100 $m^2$ based on the yellow rust spore density in the field [568]. A spore capture kit will be developed and used to increase the number of yellow rust landing on the biosensor.

# References


1. Wan, A.M., X.M. Chen, and Z. He, *Wheat stripe rust in China.* Australian journal of agricultural research, 2007. **58**(6): 605-619.
2. Carretero, R., M.O. Bancal, and D.J. Miralles, *Effect of leaf rust (Puccinia triticina) on photosynthesis and related processes of leaves in wheat crops grown at two contrasting sites and with different nitrogen levels.* European Journal of Agronomy, 2011. **35**(4): 237-246.
3. Bolton, M.D., J.A. Kolmer, and D.F. Garvin, *Wheat leaf rust caused by Puccinia triticina.* Molecular plant pathology, 2008. **9**(5): 563-575.
4. Ali, S., P. Gladieux, M. Leconte, A. Gautier, A.F. Justesen, M.S. Hovmøller, J. Enjalbert, and C. de Vallavieille-Pope, *Origin, migration routes and worldwide population genetic structure of the wheat yellow rust pathogen Puccinia striiformis f. sp. tritici.* PLoS pathogens, 2014. **10**(1): e1003903.
5. de Vallavieille-Pope, C., B. Bahri, M. Leconte, O. Zurfluh, Y. Belaid, E. Maghrebi, F. Huard, L. Huber, M. Launay, and M.-O. Bancal, *Thermal generalist behaviour of invasive Puccinia striiformis f. sp. tritici strains under current and future climate conditions.* Plant Pathology, 2018. **67**(6): 1307-1320.
6. Bai, Q., A. Wan, M. Wang, D.R. See, and X. Chen, *Molecular characterization of wheat stripe rust pathogen (Puccinia striiformis f. sp. tritici) collections from nine countries.* International journal of molecular sciences, 2021. **22**(17): 9457.
7. Ali, S., J. Rodriguez-Algaba, T. Thach, C.K. Sørensen, J.G. Hansen, P. Lassen, K. Nazari, D.P. Hodson, A.F. Justesen, and M.S. Hovmøller, *Yellow rust epidemics worldwide were caused by pathogen races from divergent genetic lineages.* Frontiers in Plant Science, 2017. **8**: 1057.
8. Wang, M. and X. Chen, *Stripe rust resistance*, in *Stripe rust*. 2017, Springer. 353-558.
9. Chen, X., *Pathogens which threaten food security: Puccinia striiformis, the wheat stripe rust pathogen.* Food Security, 2020. **12**(2): 239-251.
10. Hovmøller, M., S. Walter, R. Bayles, A. Hubbard, K. Flath, N. Sommerfeldt, M. Leconte, P. Czembor, J. Rodriguez-Algaba, and T. Thach, *Replacement of the European wheat yellow rust population by new races from the centre of diversity in the near-Himalayan region.* Plant Pathology, 2016. **65**(3): 402-411.
11. Vidal, T., A.L. Boixel, E. Maghrebi, R. Perronne, P. du Cheyron, J. Enjalbert, M. Leconte, and C. de Vallavieille-Pope, *Success and failure of invasive races of plant*

*pathogens: The case of Puccinia striiformis f. sp. tritici in France.* Plant Pathology, 2022.

12. Krauss, A., *Hassebrauk, K.: Nomenklatur, geographische Verbreitung und Wirtsbereich des Gelbrostes, Puccinia striiformis West. Mitteilungen aus der Biologischen Bundesanstalt für Land-und Forstwirtschaft Berlin-Dahlem, Heft 116. Verlag Parey Berlin u. Hamburg 1965. 75 Seiten, kart. 17, 50 DM*, Wiley Online Library 1966.
13. Hassebrauk, K., *Der Gelbrost, Puccinia striiformis West: Befallsbild, Morphologie und Biologie der Sporen; Infektion und weitere Entwicklung; Wirkungen auf die Wirtspflanze*. 1970: Parey.
14. Hassebrauk, K. and G. Robbelen, *Gelbrost, Puccinia striiformis West. III. Die Spezialisierung.* Mitt Biol Bundesanst Land Forstwirtsch Berlin Dahlem, 1974.
15. Plate, H.P., *Hassebrauk, K. u. Röbbelen, G.: Der Gelbrost, Puccinia striiformis West. IV. Epidemiologie.–Bekämpfungsmaßnahmen. Mitt. Biol. Bundesanstalt f. Land-und Forstwirtschaft, Berlin-Dahlem, Heft 164, Berlin 1975. Kommissionsverlag Paul Parey, Berlin u. Hamburg, D–1 Berlin 61 (W.-Germany), Lindenstraße 44–47, DM 21,–o. MWSt*, Wiley Online Library 1977.
16. Röbbelen, G. and E.L. Sharp, *Mode of inheritance, interaction and application of genes conditioning resistance to yellow rust [in wheat].* Fortschritte der Pflanzenzuechtung, 1978.
17. Line, R.F. and A. Qayoum, *Virulence, aggressiveness, evolution, and distribution of races of Puccinia striiformis (the cause of stripe rust of wheat) in North America, 1968-87/[Line, Roland F., and Abdul Qayoum].* 1992.
18. Chen, X. and Z. Kang, *Stripe rust*. Springer: 2017.
19. Ruiz, E. and H. Ruffner, *Immunodetection of Botrytis-specific invertase in infected grapes.* Journal of Phytopathology, 2002. **150**(2): 76-85.
20. Chang, Q., J. Liu, X. Lin, S. Hu, Y. Yang, D. Li, L. Chen, B. Huai, L. Huang, and R.T. Voegele, *A unique invertase is important for sugar absorption of an obligate biotrophic pathogen during infection.* New Phytologist, 2017. **215**(4): 1548-1561.
21. Chen, Y., H. Mao, N. Wu, J. Ma, M. Yuan, Z. Zhang, S. Yuan, and H. Zhang, *Effects of Stripe Rust Infection on the Levels of Redox Balance and Photosynthetic Capacities in Wheat.* International journal of molecular sciences, 2019. **21**(1): 268.
22. Dashek, W.V. and G.S. Miglani, *Plant cells and their organelles*,John Wiley & Sons. 2017.

23. Barthlott, W., M. Mail, B. Bhushan, and K. Koch, *Plant surfaces: structures and functions for biomimetic innovations.* Nano-Micro Letters, 2017. **9**(2): 23.
24. Yeats, T.H. and J.K. Rose, *The formation and function of plant cuticles.* Plant physiology, 2013. **163**(1): 5-20.
25. Riederer, M. and C. Müller, *Annual plant reviews, Volume 23: Biology of the plant cuticle*, Blackwell 2006.
26. Liu, R., J. Lu, M. Zhou, S. Zheng, Z. Liu, C. Zhang, M. Du, M. Wang, Y. Li, and Y. Wu, *Developing stripe rust resistant wheat (Triticum aestivum L.) lines with gene pyramiding strategy and marker-assisted selection.* Genetic Resources and Crop Evolution, 2020. **67**(2): 381-391.
27. ZENG, Q., J. ZHAO, J. WU, G. ZHAN, D. HAN, and Z. KANG, *Wheat stripe rust and integration of sustainable control strategies in China*. Front. Agric. Sci. Eng., 2021.
28. Mengesha, G.G., *Management of yellow rust (Puccinia striiformis f. sp. tritici) and stem rust (Puccinia graminis f. sp tritici) of bread wheat through host resistance and fungicide application in Southern Ethiopia.* Cogent Food & Agriculture, 2020. **6**(1): 1739493.
29. El-Orabey, W.M., M.A. Ashmawy, A.A. Shahin, and M.I. Ahmed, *Screening of CIMMYT Wheat Genotypes against Yellow Rust in Egypt.* International Journal of Phytopathology, 2020. **9**(1): 51-70.
30. Cook, N.M., S. Chng, T.L. Woodman, R. Warren, R.P. Oliver, and D.G. Saunders, *High frequency of fungicide resistance-associated mutations in the wheat yellow rust pathogen Puccinia striiformis f. sp. tritici.* Pest Management Science, 2021.**77**: 3358-3371
31. Carmona, M., F. Sautua, O. Pérez-Hérnandez, and E.M. Reis, *Role of fungicide applications on the integrated management of wheat stripe rust.* Frontiers in Plant Science, 2020. **11**: 733.
32. Tudzynski, P. and A. Sharon, *Fungal pathogenicity genes.* Applied mycology and biotechnology, 2003. **3**: 187-212.
33. Gultyaeva, E.I., E.L. Shaydayuk, K. Igor'A, A. Akhmetova, and E. Kosman, *Microsatellite analysis of Puccinia triticina from Triticum and Aegilops hosts.* Australasian Plant Pathology, 2018. **47**(2): 163-170.
34. Baldwin, I.T., *Plant volatiles.* Current Biology, 2010. **20**(9): R392-R397.
35. De Clercq, M., A. Vats, and A. Biel, *Agriculture 4.0: The future of farming technology.* Proceedings of the World Government Summit, Dubai, UAE, 2018: 11-13.

36. Ventura, E.E., J.N. Davis, and M.I. Goran, *Sugar content of popular sweetened beverages based on objective laboratory analysis: focus on fructose content.* Obesity, 2011. **19**(4): 868-874.
37. Conzuelo, F., M. Gamella, S. Campuzano, M. Ruiz, A. Reviejo, and J. Pingarron, *An integrated amperometric biosensor for the determination of lactose in milk and dairy products.* Journal of agricultural and food chemistry, 2010. **58**(12): 7141-7148.
38. (WHO), W.H.O., *Leading causes of death worldwide in 2019 (in millions)* 2020.
39. Organization, W.H., *Global health risks: mortality and burden of disease attributable to selected major risks*. World Health Organization: 2009.
40. Herman, W.H., *The global burden of diabetes: an overview.* Diabetes mellitus in developing countries and underserved communities,editted by Dagogo-Jack S., Springer. 2017: 1-5.
41. Bruen, D., C. Delaney, L. Florea, and D. Diamond, *Glucose sensing for diabetes monitoring: recent developments.* Sensors, 2017. **17**(8): 1866.
42. Heller, A. and B. Feldman, *Electrochemical glucose sensors and their applications in diabetes management.* Chemical reviews, 2008. **108**(7): 2482-2505.
43. Heller, A., *Integrated medical feedback systems for drug delivery.* AIChE journal, 2005. **51**(4): 1054-1066.
44. Kitikul, J., S. Satienperakul, A. Preechaworapun, P. Pookmanee, and T. Tangkuaram, *A simple flow amperometric electrochemical biosensor based on chitosan scaffolds and gold nanowires modified on a glassy carbon electrode for detection of glutamate in food products.* Electroanalysis, 2017. **29**(1): 264-271.
45. Ju, J., C.-M. Hsieh, Y. Tian, J. Kang, R. Chia, H. Chang, Y. Bai, C. Xu, X. Wang, and Q. Liu, *Surface Enhanced Raman Spectroscopy Based Biosensor with a Microneedle Array for Minimally Invasive In Vivo Glucose Measurements.* ACS Sensors, 2020. **5**(6): 1777-1785.
46. Bornhoeft, L.R., A. Biswas, and M.J. McShane, *Composite hydrogels with engineered microdomains for optical glucose sensing at low oxygen conditions.* Biosensors, 2017. **7**(1): 8.
47. Vafapour, Z., *Polarization-independent perfect optical metamaterial absorber as a glucose sensor in Food Industry applications.* IEEE transactions on nanobioscience, 2019. **18**(4): 622-627.
48. Shehab, M., S. Ebrahim, and M. Soliman, *Graphene quantum dots prepared from glucose as optical sensor for glucose.* Journal of Luminescence, 2017. **184**: 110-116.

49. Jernelv, I.L., K. Milenko, S.S. Fuglerud, D.R. Hjelme, R. Ellingsen, and A. Aksnes, *A review of optical methods for continuous glucose monitoring.* Applied Spectroscopy Reviews, 2019. **54**(7): 543-572.
50. Rachim, V.P. and W.-Y. Chung, *Wearable-band type visible-near infrared optical biosensor for non-invasive blood glucose monitoring.* Sensors and Actuators B: Chemical, 2019. **286**: 173-180.
51. Garzón, V., D.G. Pinacho, R.-H. Bustos, G. Garzón, and S. Bustamante, *Optical Biosensors for Therapeutic Drug Monitoring.* Biosensors, 2019. **9**(4): 132.
52. Bosch, M.E., A.J.R. Sánchez, F.S. Rojas, and C.B. Ojeda, *Recent development in optical fiber biosensors.* Sensors, 2007. **7**(6): 797-859.
53. Kausar, A.S.M.Z., A.W. Reza, T.A. Latef, M.H. Ullah, and M.E. Karim, *Optical nano antennas: state of the art, scope and challenges as a biosensor along with human exposure to nano-toxicology.* Sensors, 2015. **15**(4): 8787-8831.
54. Ahmad, O.S., T.S. Bedwell, C. Esen, A. Garcia-Cruz, and S.A. Piletsky, *Molecularly imprinted polymers in electrochemical and optical sensors.* Trends in biotechnology, 2019. **37**(3): 294-309.
55. Garcia-Cruz, A., O. Ahmad, K. Alanazi, E. Piletska, and S. Piletsky, *Generic sensor platform based on electro-responsive molecularly imprinted polymer nanoparticles (e-NanoMIPs).* Microsystems & Nanoengineering, 2020. **6**(1): 1-9.
56. Diouf, A., B. Bouchikhi, and N. El Bari, *A nonenzymatic electrochemical glucose sensor based on molecularly imprinted polymer and its application in measuring saliva glucose.* Materials Science and Engineering: C, 2019. **98**: 1196-1209.
57. Deshmukh, M.A., B.-C. Kang, and T.-J. Ha, *Non-enzymatic electrochemical glucose sensors based on polyaniline/reduced-graphene-oxide nanocomposites functionalized with silver nanoparticles.* Journal of Materials Chemistry C, 2020. **8**(15): 5112-5123.
58. Wa, Q., W. Xiong, R. Zhao, Z. He, Y. Chen, and X. Wang, *Nanoscale Ni (OH) x films on carbon cloth prepared by atomic layer deposition and electrochemical activation for glucose sensing.* ACS Applied Nano Materials, 2019. **2**(7): 4427-4434.
59. Ma, X., K.-l. Tang, M. Yang, W. Shi, and W. Zhao, *Metal–organic framework-derived yolk–shell hollow Ni/NiO@ C microspheres for bifunctional non-enzymatic glucose and hydrogen peroxide biosensors.* Journal of Materials Science, 2021. **56**(1): 442-456.
60. Huo, J., L. Lu, Z. Shen, H. Gao, and H. Liu, *Rational design of CoNi alloy and atomic Co/Ni composite as an efficient electrocatalyst.* Surface Innovations, 2020: 1-12.

61. Casella, I.G., A. Destradis, and E. Desimoni, *Colloidal gold supported onto glassy carbon substrates as an amperometric sensor for carbohydrates in flow injection and liquid chromatography.* Analyst, 1996. **121**(2): 249-254.

62. Mohammed, F.A., M.M. Khalaf, I.M. Mohamed, M. Saleh, and H.M. Abd El-Lateef, *Synthesis of mesoporous nickel ferrite nanoparticles by use of citrate framework methodology and application for electrooxidation of glucose in alkaline media.* Microchemical Journal, 2020. **153**: 104507.

63. Eryiğit, M., E. Çepni, B.K. Urhan, H.Ö. Doğan, and T.Ö. Özer, *Nonenzymatic glucose sensor based on poly (3, 4-ethylene dioxythiophene)/electroreduced graphene oxide modified gold electrode.* Synthetic Metals, 2020. **268**: 116488.

64. Gao, X., X. Du, D. Liu, H. Gao, P. Wang, and J. Yang, *Core-shell gold-nickel nanostructures as highly selective and stable nonenzymatic glucose sensor for fermentation process.* Scientific reports, 2020. **10**(1): 1-10.

65. Clark Jr, L.C. and C. Lyons, *Electrode systems for continuous monitoring in cardiovascular surgery.* Annals of the New York Academy of sciences, 1962. **102**(1): 29-45.

66. Renneberg, R., D. Pfeiffer, F. Lisdat, G. Wilson, U. Wollenberger, F. Ligler, and A.P. Turner, *Frieder Scheller and the short history of biosensors*, in *Biosensing for the 21st Century*. 2007, Springer. 1-18.

67. Bankar, S.B., M.V. Bule, R.S. Singhal, and L. Ananthanarayan, *Glucose oxidase—an overview.* Biotechnology advances, 2009. **27**(4): 489-501.

68. Güneş, M., S. Karakaya, and Y. Dilgin, *Development of an interference-minimized amperometric-FIA glucose biosensor at a pyrocatechol violet/glucose dehydrogenase-modified graphite pencil electrode.* Chemical Papers, 2020. **74**(6): 1923-1936.

69. Cohen, R., Y. Cohen, D. Mukha, and O. Yehezkeli, *Oxygen insensitive amperometric glucose biosensor based on FAD dependent glucose dehydrogenase co-entrapped with DCPIP or DCNQ in a polydopamine layer.* Electrochimica Acta, 2021. **367**: 137477.

70. Iwasa, H., A. Hiratsuka, T. Tanaka, K. Tsuji, T. Kishimoto, Y. Watanabe, Y. Hoshino, and H. Muguruma, *Xylose-insensitive direct electron transfer biosensor strip with single-walled carbon nanotubes and novel fungal flavin adenine dinucleotide glucose dehydrogenase.* IEEE Sensors Journal, 2020. **20**(21): 12522-12529.

71. Filipiak, M.S., D. Vetter, K. Thodkar, O. Gutierrez-Sanz, M. Jönsson-Niedziółka, and A. Tarasov, *Electron transfer from FAD-dependent glucose dehydrogenase to single-sheet graphene electrodes.* Electrochimica Acta, 2020. **330**: 134998.
72. Stolarczyk, K., J. Rogalski, and R. Bilewicz, *NAD (P)-dependent glucose dehydrogenase: Applications for biosensors, bioelectrodes, and biofuel cells.* Bioelectrochemistry, 2020. **135**: 107574.
73. Lisdat, F., *PQQ-GDH–Structure, function and application in bioelectrochemistry.* Bioelectrochemistry, 2020. **134**: 107496.
74. Neethirajan, S., Karunakaran, C. and Jayas, D. , *Biosensors – An Emerging Technology for the Agricultural and Food Industry.* The Canadian Society for engineering in agricultural, food and biological systems, 2005.
75. Ferri, S., K. Kojima, and K. Sode, *Review of glucose oxidases and glucose dehydrogenases: a bird's eye view of glucose sensing enzymes.* Journal of diabetes science and technology, 2011. **5**(5): 1068-1076.
76. Kettner, K., U. Krause, S. Mosler, C. Bodenstein, T.M. Kriegel, and G. Rödel, *Saccharomyces cerevisiae gene YMR291W/TDA1 mediates the in vivo phosphorylation of hexokinase isoenzyme 2 at serine-15.* FEBS letters, 2012. **586**(4): 455-458.
77. Buford, R.J., E.C. Green, and M.J. McClung. *A microwave frequency sensor for non-invasive blood-glucose measurement*. Proceeding in *IEEE Sensors Applications Symposium*. 2008, Atlanta, GA, USA. 4-7.
78. Omer, A.E., G. Shaker, S. Safavi-Naeini, H. Kokabi, G. Alquié, F. Deshours, and R.M. Shubair, *Low-cost portable microwave sensor for non-invasive monitoring of blood glucose level: novel design utilizing a four-cell CSRR hexagonal configuration.* Scientific Reports, 2020. **10**(1): 1-20.
79. Karpova, E.V., E.E. Karyakina, and A.A. Karyakin, *Wearable non-invasive monitors of diabetes and hypoxia through continuous analysis of sweat.* Talanta, 2020, ElSevier. **215**: 120922.
80. Alam, M.M., S. Saha, P. Saha, F.N. Nur, N.N. Moon, A. Karim, and S. Azam. *D-care: A non-invasive glucose measuring technique for monitoring diabetes patients*. in *Proceedings of International Joint Conference on Computational Intelligence*. Springer ,2020.
81. Updike, S. and G. Hicks, *The enzyme electrode.* Nature, 1967. **214**(5092): 986-988.

82. Guilbault, G. and G. Lubrano, *An enzyme electrode for the amperometric determination of glucose.* Analytica chimica acta, 1973. **64**(3): 439-455.

83. Chen, C., Q. Xie, D. Yang, H. Xiao, Y. Fu, Y. Tan, and S. Yao, *Recent advances in electrochemical glucose biosensors: a review.* Rsc Advances, 2013. **3**(14): 4473-4491.

84. Karyakin, A.A., O.V. Gitelmacher, and E.E. Karyakina, *Prussian blue-based first-generation biosensor. A sensitive amperometric electrode for glucose.* Analytical chemistry, 1995. **67**(14): 2419-2423.

85. Kaçar, C., B. Dalkiran, P.E. Erden, and E. Kiliç, *An amperometric hydrogen peroxide biosensor based on Co3O4 nanoparticles and multiwalled carbon nanotube modified glassy carbon electrode.* Applied surface science, 2014. **311**: 139-146.

86. Wang, J., *Electrochemical glucose biosensors.* Chemical reviews, 2008. **108**(2): 814-825.

87. Poulos, N.G., J.R. Hall, and M.C. Leopold, *Functional layer-by-layer design of xerogel-based first-generation amperometric glucose biosensors.* Langmuir, 2015. **31**(4): 1547-1555.

88. Wang, J., *Glucose biosensors: 40 years of advances and challenges.* Electroanalysis: An International Journal Devoted to Fundamental and Practical Aspects of Electroanalysis, 2001. **13**(12): 983-988.

89. Mădăraş, M.B. and R.P. Buck, *Miniaturized biosensors employing electropolymerized permselective films and their use for creatinine assays in human serum.* Analytical chemistry, 1996. **68**(21): 3832-3839.

90. Palmisano, F., C. Malitesta, D. Centonze, and P. Zambonin, *Correlation between permselectivity and chemical structure of overoxidized polypyrrole membranes used in electroproduced enzyme biosensors.* Analytical chemistry, 1995. **67**(13): 2207-2211.

91. Jeerapan, I., J.R. Sempionatto, J.-M. You, and J. Wang, *Enzymatic glucose/oxygen biofuel cells: Use of oxygen-rich cathodes for operation under severe oxygen-deficit conditions.* Biosensors and Bioelectronics, 2018. **122**: 284-289.

92. Sasso, S.V., R.J. Pierce, R. Walla, and A.M. Yacynych, *Electropolymerized 1, 2-diaminobenzene as a means to prevent interferences and fouling and to stabilize immobilized enzyme in electrochemical biosensors.* Analytical Chemistry, 1990. **62**(11): 1111-1117.

93. Malitesta, C., F. Palmisano, L. Torsi, and P.G. Zambonin, *Glucose fast-response amperometric sensor based on glucose oxidase immobilized in an electropolymerized poly (o-phenylenediamine) film.* Analytical chemistry, 1990. **62**(24): 2735-2740.

94. Zhang, Y., Y. Hu, G.S. Wilson, D. Moatti-Sirat, V. Poitout, and G. Reach, *Elimination of the acetaminophen interference in an implantable glucose sensor.* Analytical Chemistry, 1994. **66**(7): 1183-1188.

95. Emr, S.A. and A.M. Yacynych, *Use of polymer films in amperometric biosensors.* Electroanalysis, 1995. **7**(10): 913-923.

96. Wang, J., J. Liu, L. Chen, and F. Lu, *Highly selective membrane-free, mediator-free glucose biosensor.* Analytical Chemistry, 1994. **66**(21): 3600-3603.

97. Newman, J.D., S.F. White, I.E. Tothill, and A.P. Turner, *Catalytic materials, membranes, and fabrication technologies suitable for the construction of amperometric biosensors.* Analytical Chemistry, 1995. **67**(24): 4594-4599.

98. Chi, Q. and S. Dong, *Amperometric biosensors based on the immobilization of oxidases in a Prussian blue film by electrochemical codeposition.* Analytica chimica acta, 1995. **310**(3): 429-436.

99. Wang, J. and H. Wu, *Highly selective biosensing of glucose utilizing a glucose oxidase+ rhodium+ Nafion® biocatalytic-electrocatalytic-permselective surface microstructure.* Journal of Electroanalytical Chemistry, 1995. **395**(1-2): 287-291.

100. Kafi, A.K.M., S. Alim, R. Jose, and M.M. Yusoff, *Fabrication of a glucose oxidase/multiporous tin-oxide nanofiber film on Prussian blue–modified gold electrode for biosensing.* Journal of Electroanalytical Chemistry, 2019. **852**: 113550.

101. Melchels, F.P., M.A. Domingos, T.J. Klein, J. Malda, P.J. Bartolo, and D.W. Hutmacher, *Additive manufacturing of tissues and organs.* Progress in Polymer Science, 2012. **37**(8): 1079-1104.

102. Cinti, S., R. Cusenza, D. Moscone, and F. Arduini, *based synthesis of Prussian Blue Nanoparticles for the development of whole blood glucose electrochemical biosensor.* Talanta, 2018. **187**: 59-64.

103. Alhans, R., A. Singh, C. Singhal, J. Narang, S. Wadhwa, and A. Mathur, *Comparative analysis of single-walled and multi-walled carbon nanotubes for electrochemical sensing of glucose on gold printed circuit boards.* Materials Science and Engineering: C, 2018. **90**: 273-279 .

104. Tang, H., F. Yan, P. Lin, J. Xu, and H.L.W. Chan, *Highly sensitive glucose biosensors based on organic electrochemical transistors using platinum gate*

*electrodes modified with enzyme and nanomaterials.* Advanced Functional Materials, 2011. **21**(12): 2264-2272.

105. Baek, S.H., J. Roh, C.Y. Park, M.W. Kim, R. Shi, S.K. Kailasa, and T.J. Park, *Cu-nanoflower decorated gold nanoparticles-graphene oxide nanofiber as electrochemical biosensor for glucose detection.* Materials Science and Engineering: C, 2020. **107**: 110273.
106. Mei, Q., R. Fu, Y. Ding, A. Wang, D. Duan, and D. Ye, *Electrospinning of highly dispersed Ni/CoO carbon nanofiber and its application in glucose electrochemical sensor.* Journal of Electroanalytical Chemistry, 2019. **847**: 113075.
107. Reach, G. and G.S. Wilson, *Can continuous glucose monitoring be used for the treatment of diabetes.* Analytical chemistry, 1992. **64**(6): 381A-386A.
108. Sekretaryova, A.N., D.V. Vokhmyanina, T.O. Chulanova, E.E. Karyakina, and A.A. Karyakin, *Reagentless biosensor based on glucose oxidase wired by the mediator freely diffusing in enzyme containing membrane.* Analytical chemistry, 2012. **84**(3): 1220-1223.
109. Gough, D.A., J.Y. Lucisano, and P.H.S. Tse, *Two-dimensional enzyme electrode sensor for glucose.* Analytical Chemistry, 1985. **57**(12): 2351-2357.
110. Kontani, R., S. Tsujimura, and K. Kano, *Air diffusion biocathode with CueO as electrocatalyst adsorbed on carbon particle-modified electrodes.* Bioelectrochemistry, 2009. **76**(1-2): 10-13.
111. Teymourian, H., C. Moonla, F. Tehrani, E. Vargas, R. Aghavali, A. Barfidokht, T. Tangkuaram, P.P. Mercier, E. Dassau, and J. Wang, *Microneedle-based detection of ketone bodies along with glucose and lactate: Toward real-time continuous interstitial fluid monitoring of diabetic ketosis and ketoacidosis.* Analytical chemistry, 2019. **92**(2): 2291-2300.
112. Schuhmann, W., T.J. Ohara, H.L. Schmidt, and A. Heller, *Electron transfer between glucose oxidase and electrodes via redox mediators bound with flexible chains to the enzyme surface.* Journal of the American Chemical Society, 1991. **113**(4): 1394-1397.
113. Ozoemena, K.I. and T. Nyokong, *Novel amperometric glucose biosensor based on an ether-linked cobalt (II) phthalocyanine–cobalt (II) tetraphenylporphyrin pentamer as a redox mediator.* Electrochimica Acta, 2006. **51**(24): 5131-5136.
114. Ahmed, M.U., M.M. Hossain, and E. Tamiya, *Electrochemical biosensors for medical and food applications.* Electroanalysis: An International Journal Devoted to Fundamental and Practical Aspects of Electroanalysis, 2008. **20**(6): 616-626.

115. Teymourian, H., A. Barfidokht, and J. Wang, *Electrochemical glucose sensors in diabetes management: an updated review (2010–2020).* Chemical Society Reviews, 2020.

116. Suzuki, N., J. Lee, N. Loew, Y. Takahashi-Inose, J. Okuda-Shimazaki, K. Kojima, K. Mori, W. Tsugawa, and K. Sode, *Engineered glucose oxidase capable of quasi-direct electron transfer after a quick-and-easy modification with a mediator.* International journal of molecular sciences, 2020. **21**(3): 1137.

117. Lee, J., K. Hyun, and Y. Kwon, *A study on the stability and sensitivity of mediator-based enzymatic glucose sensor measured by catalyst consisting of multilayer stacked via layer-by-layer.* Journal of Industrial and Engineering Chemistry, 2021. **93**: 383-387.

118. Boussema, F., A.J. Gross, F. Hmida, B. Ayed, H. Majdoub, S. Cosnier, A. Maaref, and M. Holzinger, *Dawson-type polyoxometalate nanoclusters confined in a carbon nanotube matrix as efficient redox mediators for enzymatic glucose biofuel cell anodes and glucose biosensors.* Biosensors and Bioelectronics, 2018. **109**: 20-26.

119. Marquitan, M., T. Bobrowski, A. Ernst, P. Wilde, J. Clausmeyer, A. Ruff, and W. Schuhmann, *Miniaturized amperometric glucose sensors based on polymer/enzyme modified carbon electrodes in the sub-micrometer scale.* Journal of The Electrochemical Society, 2018. **165**(12): G3008.

120. Bobrowski, T. and W. Schuhmann, *Long-term implantable glucose biosensors.* Current Opinion in Electrochemistry, 2018. **10**: 112-119.

121. Heller, A., *Electrical connection of enzyme redox centers to electrodes.* The Journal of Physical Chemistry, 1992. **96**(9): 3579-3587.

122. Gallay, P.A., M.D. Rubianes, F.A. Gutierrez, and G.A. Rivas, *Avidin and Glucose Oxidase-non-covalently Functionalized Multi-walled Carbon Nanotubes: A New Analytical Tool for Building a Bienzymatic Glucose Biosensor.* Electroanalysis, 2019. **31**(10): 1888-1894.

123. Al-Sagur, H., S. Komathi, M.A. Khan, A.G. Gurek, and A. Hassan, *A novel glucose sensor using lutetium phthalocyanine as redox mediator in reduced graphene oxide conducting polymer multifunctional hydrogel.* Biosensors and Bioelectronics, 2017. **92**: 638-645.

124. Rafighi, P., M. Tavahodi, and B. Haghighi, *Fabrication of a third-generation glucose biosensor using graphene-polyethyleneimine-gold nanoparticles hybrid.* Sensors and Actuators B: Chemical, 2016. **232**: 454-461.

125. Mehmeti, E., D.M. Stanković, S. Chaiyo, J. Zavasnik, K. Žagar, and K. Kalcher, *Wiring of glucose oxidase with graphene nanoribbons: an electrochemical third generation glucose biosensor.* Microchimica Acta, 2017. **184**(4): 1127-1134.

126. Willner, I., V. Heleg-Shabtai, R. Blonder, E. Katz, G. Tao, A.F. Bückmann, and A. Heller, *Electrical wiring of glucose oxidase by reconstitution of FAD-modified monolayers assembled onto Au-electrodes.* Journal of the American Chemical Society, 1996. **118**(42): 10321-10322.

127. Fruk, L., C.H. Kuo, E. Torres, and C.M. Niemeyer, *Apoenzyme reconstitution as a chemical tool for structural enzymology and biotechnology.* Angewandte Chemie International Edition, 2009. **48**(9): 1550-1574.

128. Zayats, M., B. Willner, and I. Willner, *Design of amperometric biosensors and biofuel cells by the reconstitution of electrically contacted enzyme electrodes.* Electroanalysis: An International Journal Devoted to Fundamental and Practical Aspects of Electroanalysis, 2008. **20**(6): 583-601.

129. Zayats, M., E. Katz, R. Baron, and I. Willner, *Reconstitution of apo-glucose dehydrogenase on pyrroloquinoline quinone-functionalized Au nanoparticles yields an electrically contacted biocatalyst.* Journal of the American Chemical Society, 2005. **127**(35): 12400-12406.

130. Şenel, M., C. Nergiz, M. Dervisevic, and E. Çevik, *Development of amperometric glucose biosensor based on reconstitution of glucose oxidase on polymeric 3-aminophenyl boronic acid monolayer.* Electroanalysis, 2013. **25**(5): 1194-1200.

131. Degani, Y. and A. Heller, *Electrical communication between redox centers of glucose oxidase and electrodes via electrostatically and covalently bound redox polymers.* Journal of the American Chemical Society, 1989. **111**(6): 2357-2358.

132. Yehezkeli, O., S. Raichlin, R. Tel-Vered, E. Kesselman, D. Danino, and I. Willner, *Biocatalytic implant of Pt nanoclusters into glucose oxidase: A method to electrically wire the enzyme and to transform it from an oxidase to a hydrogenase.* The Journal of Physical Chemistry Letters, 2010. **1**(19): 2816-2819.

133. Zhang, H., Z. Meng, Q. Wang, and J. Zheng, *A novel glucose biosensor based on direct electrochemistry of glucose oxidase incorporated in biomediated gold nanoparticles–carbon nanotubes composite film.* Sensors and Actuators B: Chemical, 2011. **158**(1): 23-27 .

134. Tasviri, M., H.-A. Rafiee-Pour, H. Ghourchian, and M.R. Gholami, *Amine functionalized TiO2 coated on carbon nanotube as a nanomaterial for direct*

*electrochemistry of glucose oxidase and glucose biosensing.* Journal of Molecular Catalysis B: Enzymatic, 2011. **68**(2): 206-210.

135. Shan, C., H. Yang, J. Song, D. Han, A. Ivaska, and L. Niu, *Direct electrochemistry of glucose oxidase and biosensing for glucose based on graphene.* Analytical Chemistry, 2009. **81**(6): 2378-2382.

136. Jose, M.V., S. Marx, H. Murata, R.R. Koepsel, and A.J. Russell, *Direct electron transfer in a mediator-free glucose oxidase-based carbon nanotube-coated biosensor.* Carbon, 2012. **50**(11): 4010-4020.

137. Holland, J.T., C. Lau, S. Brozik, P. Atanassov, and S. Banta, *Engineering of glucose oxidase for direct electron transfer via site-specific gold nanoparticle conjugation.* Journal of the American Chemical Society, 2011. **133**(48): 19262-19265 .

138. Tasca, F., M.N. Zafar, W. Harreither, G. Nöll, R. Ludwig, and L. Gorton, *A third generation glucose biosensor based on cellobiose dehydrogenase from Corynascus thermophilus and single-walled carbon nanotubes.* Analyst, 2011. **136**(10): 2033-2036.

139. Rahman, M.M., A.J.S. Ahammad, J.-H. Jin, S.J. Ahn, and J.-J. Lee, *A Comprehensive Review of Glucose Biosensors Based on Nanostructured Metal-Oxides.* Sensors, 2010. **10**(5): 4855-4886.

140. Zhu, Z., L. Garcia-Gancedo, A.J. Flewitt, H. Xie, F. Moussy, and W.I. Milne, *A Critical Review of Glucose Biosensors Based on Carbon Nanomaterials: Carbon Nanotubes and Graphene,* Sensors, 2012. **12**(5): 5996-6022.

141. Wongkaew, N., M. Simsek, C. Griesche, and A.J. Baeumner, *Functional nanomaterials and nanostructures enhancing electrochemical biosensors and lab-on-a-chip performances: recent progress, applications, and future perspective.* Chemical reviews, 2018. **119**(1): 120-194.

142. Kumar-Krishnan, S., M.G.-F. García, E. Prokhorov, M. Estevez-González, R. Pérez, R. Esparza, and M. Meyyappan, *Synthesis of gold nanoparticles supported on functionalized nanosilica using deep eutectic solvent for an electrochemical enzymatic glucose biosensor.* Journal of Materials Chemistry B, 2017. **5**(34): 7072-7081.

143. Buk, V. and M.E. Pemble, *A highly sensitive glucose biosensor based on a micro disk array electrode design modified with carbon quantum dots and gold nanoparticles.* Electrochimica Acta, 2019. **298**: 97-105.

144. Shrestha, B.K., R. Ahmad, S. Shrestha, C.H. Park, and C.S. Kim, *Globular shaped polypyrrole doped well-dispersed functionalized multiwall carbon nanotubes/nafion composite for enzymatic glucose biosensor application.* Scientific reports, 2017. **7**(1): 1-13.

145. Li, J., Y. Liu, X. Tang, L. Xu, L. Min, Y. Xue, X. Hu, and Z. Yang, *Multiwalled carbon nanotubes coated with cobalt (II) sulfide nanoparticles for electrochemical sensing of glucose via direct electron transfer to glucose oxidase.* Microchimica Acta, 2020. **187**(1): 1-9.

146. Hao, L., S.-S. Li, J. Wang, Y. Tan, L. Bai, and A. Liu, *MnO2/multi-walled carbon nanotubes based nanocomposite with enhanced electrocatalytic activity for sensitive amperometric glucose biosensing.* Journal of Electroanalytical Chemistry, 2020. **878**: 114602.

147. Vukojević, V., S. Djurdjić, M. Ognjanović, M. Fabian, A. Samphao, K. Kalcher, and D.M. Stanković, *Enzymatic glucose biosensor based on manganese dioxide nanoparticles decorated on graphene nanoribbons.* Journal of Electroanalytical Chemistry, 2018. **823**: 610-616 .

148. Mao, Q., W. Jing, F. Zhou, S. Liu, W. Gao, Z. Wei, and Z. Jiang, *Depositing reduced graphene oxide on ZnO nanorods to improve the performance of enzymatic glucose sensors.* Materials Science in Semiconductor Processing, 2021. **121**: 105391.

149. Hossain, M.F. and G. Slaughter, *PtNPs decorated chemically derived graphene and carbon nanotubes for sensitive and selective glucose biosensing.* Journal of Electroanalytical Chemistry, 2020. **861**: 113990 .

150. Kim, I., D. Kwon, D. Lee, T.H. Lee, J.H. Lee, G. Lee, and D.S. Yoon, *A highly permselective electrochemical glucose sensor using red blood cell membrane.* Biosensors and Bioelectronics, 2018. **102**: 617-623 .

151. Zhao, F.-Q. and A.F. Keating, *Functional properties and genomics of glucose transporters.* Current genomics, 2007. **8**(2): 113-128.

152. Manolescu, A.R., K. Witkowska, A. Kinnaird, T. Cessford, and C. Cheeseman, *Facilitated hexose transporters: new perspectives on form and function.* Physiology, 2007. **22**(4): 234-240.

153. Kim, I., C. Kim, D. Lee, S.W. Lee, G. Lee, and D.S. Yoon, *A bio-inspired highly selective enzymatic glucose sensor using a red blood cell membrane.* Analyst, 2020. **145**(6): 2125-2132.

154. Yang, Y., S. Zhang, M. Kingston, G. Jones, G. Wright, and S. Spencer, *Glucose sensor with improved haemocompatibilty.* Biosensors and bioelectronics, 2000. **15**(5-6): 221-227.

155. Aydemir, N., J. Malmström, and J. Travas-Sejdic, *Conducting polymer based electrochemical biosensors.* Physical Chemistry Chemical Physics, 2016. **18**(12): 8264-8277.

156. Xu, M., Y. Song, Y. Ye, C. Gong, Y. Shen, L. Wang, and L. Wang, *A novel flexible electrochemical glucose sensor based on gold nanoparticles/polyaniline arrays/carbon cloth electrode.* Sensors and Actuators B: Chemical, 2017. **252**: 1187-1193.

157. Soylemez, S., H.Z. Kaya, Y.A. Udum, and L. Toppare, *A multipurpose conjugated polymer: Electrochromic device and biosensor construction for glucose detection.* Organic Electronics, 2019. **65**: 327-333.

158. Wang, L., M. Xu, Y. Xie, C. Qian, W. Ma, L. Wang, and Y. Song, *Ratiometric electrochemical glucose sensor based on electroactive Schiff base polymers.* Sensors and Actuators B: Chemical, 2019. **285**: 264-270.

159. Krishnan, S.K., E. Prokhorov, D. Bahena, R. Esparza, and M. Meyyappan, *Chitosan-covered Pd@ Pt core–shell nanocubes for direct electron transfer in electrochemical enzymatic glucose biosensor.* ACS omega, 2017. **2**(5): 1896-1904.

160. Csoeregi, E., D.W. Schmidtke, and A. Heller, *Design and optimization of a selective subcutaneously implantable glucose electrode based on" wired" glucose oxidase.* Analytical Chemistry, 1995. **67**(7): 1240-1244.

161. Chen, Y., S. Lu, S. Zhang, Y. Li, Z. Qu, Y. Chen, B. Lu, X. Wang, and X. Feng, *Skin-like biosensor system via electrochemical channels for noninvasive blood glucose monitoring.* Science advances, 2017. **3**(12): e1701629.

162. Arakawa, T., Y. Kuroki, H. Nitta, P. Chouhan, K. Toma, S.-i. Sawada, S. Takeuchi, T. Sekita, K. Akiyoshi, and S. Minakuchi, *Mouthguard biosensor with telemetry system for monitoring of saliva glucose: A novel cavitas sensor.* Biosensors and Bioelectronics, 2016. **84**: 106-111.

163. Orzari, L.O., R.C. de Freitas, I.A. de Araujo Andreotti, A. Gatti, and B.C. Janegitz, *A novel disposable self-adhesive inked paper device for electrochemical sensing of dopamine and serotonin neurotransmitters and biosensing of glucose.* Biosensors and Bioelectronics, 2019. **138**: 111310.

164. Nguyen, T.N.H., X. Jin, J.K. Nolan, J. Xu, K.V.H. Le, S. Lam, Y. Wang, M.A. Alam, and H. Lee, *Printable Nonenzymatic Glucose Biosensors Using Carbon Nanotube-PtNP Nanocomposites Modified with AuRu for Improved Selectivity.* ACS Biomaterials Science & Engineering, 2020. **6**(9): 5315-5325.

165. Vassilyev, Y.B., O.A. Khazova, and N.N. Nikolaeva, *Kinetics and mechanism of glucose electrooxidation on different electrode-catalysts: Part I. Adsorption and oxidation on platinum.* Journal of electroanalytical chemistry and interfacial electrochemistry, 1985. **196**(1): 105-125.

166. Vassilyev, Y.B., O.A. Khazova, and N.N. Nikolaeva, *Kinetics and mechanism of glucose electrooxidation on different electrode-catalysts: Part II. Effect of the nature of the electrode and the electrooxidation mechanism.* Journal of electroanalytical chemistry and interfacial electrochemistry, 1985. **196**(1): 127-144.

167. Toghill, K.E. and R.G. Compton, *Electrochemical non-enzymatic glucose sensors: a perspective and an evaluation.* International Journal of Electrochemical Science, 2010. **5**(9): 1246-1301.

168. Hwang, D.-W., S. Lee, M. Seo, and T.D. Chung, *Recent advances in electrochemical non-enzymatic glucose sensors–a review.* Analytica chimica acta, 2018. **1033**: 1-34.

169. Yamauchi, Y., N. Suzuki, L. Radhakrishnan, and L. Wang, *Breakthrough and future: nanoscale controls of compositions, morphologies, and mesochannel orientations toward advanced mesoporous materials.* The Chemical Record, 2009. **9**(6): 321-339.

170. Mohamed, M.G., E.C. Atayde Jr, B.M. Matsagar, J. Na, Y. Yamauchi, K.C.W. Wu, and S.-W. Kuo, *Construction hierarchically mesoporous/microporous materials based on block copolymer and covalent organic framework.* Journal of the Taiwan Institute of Chemical Engineers, 2020. **112**: 180-192

171. Ci, S., T. Huang, Z. Wen, S. Cui, S. Mao, D.A. Steeber, and J. Chen, *Nickel oxide hollow microsphere for non-enzyme glucose detection.* Biosensors and Bioelectronics, 2014. **54**: 251-257.

172. Fu, S., G. Fan, L. Yang, and F. Li, *Non-enzymatic glucose sensor based on Au nanoparticles decorated ternary Ni-Al layered double hydroxide/single-walled carbon nanotubes/graphene nanocomposite.* Electrochimica acta, 2015. **152**: 146-154.

173. Choi, T., S.H. Kim, C.W. Lee, H. Kim, S.-K. Choi, S.-H. Kim, E. Kim, J. Park, and H. Kim, *Synthesis of carbon nanotube–nickel nanocomposites using atomic layer deposition for high-performance non-enzymatic glucose sensing.* Biosensors and Bioelectronics, 2015. **63**: 325-330 .

174. Şavk, A., H. Aydın, K. Cellat, and F. Şen, *A novel high performance non-enzymatic electrochemical glucose biosensor based on activated carbon-supported Pt-Ni nanocomposite.* Journal of Molecular Liquids, 2020. **300**: 112355.

175. Burke, L.D., *Premonolayer oxidation and its role in electrocatalysis.* Electrochimica Acta, 1994. **39**(11-12): 1841-1848.

176. Norsko, J.K., *Chemisorption on metal surfaces.* Reports on Progress in Physics, 1990. **53**(10): 1253.

177. Lee, S., J. Lee, S. Park, H. Boo, H.C. Kim, and T.D. Chung, *Disposable non-enzymatic blood glucose sensing strip based on nanoporous platinum particles.* Applied Materials Today, 2018. **10**: 24-29.

178. Verma, N., *A green synthetic approach for size tunable nanoporous gold nanoparticles and its glucose sensing application.* Applied Surface Science, 2018. **462**: 753-759.

179. Wang, J., D. Zhao, and C. Xu, *Nonenzymatic electrochemical sensor for glucose based on nanoporous platinum-gold alloy.* Journal of Nanoscience and Nanotechnology, 2016. **16**(7): 7145-7150.

180. Jafarian, M., F. Forouzandeh, I. Danaee, F. Gobal, and M. Mahjani, *Electrocatalytic oxidation of glucose on Ni and NiCu alloy modified glassy carbon electrode.* Journal of Solid State Electrochemistry, 2009. **13**(8): 1171-1179.

181. Skou, E., *The electrochemical oxidation of glucose on platinum—I. The oxidation in 1 M H2SO4.* Electrochimica Acta, 1977. **22**(4): 313-318.

182. Zhao, Y., X. Li, J.M. Schechter, and Y. Yang, *Revisiting the oxidation peak in the cathodic scan of the cyclic voltammogram of alcohol oxidation on noble metal electrodes.* RSC advances, 2016. **6**(7): 5384-5390.

183. Xu, Q., L. Yin, C. Hou, X. Liu, and X. Hu, *Facile fabrication of nanoporous platinum by alloying–dealloying process and its application in glucose sensing.* Sensors and Actuators B: Chemical, 2012. **173**: 716-723.

184. Pasta, M., F. La Mantia, and Y. Cui, *Mechanism of glucose electrochemical oxidation on gold surface.* Electrochimica Acta, 2010. **55**(20): 5561-5568.

185. Hu, Y., F. He, A. Ben, and C. Chen, *Synthesis of hollow Pt–Ni–graphene nanostructures for nonenzymatic glucose detection.* Journal of Electroanalytical Chemistry, 2014. **726**: 55-61.

186. Unmüssig, T., A. Weltin, S. Urban, P. Daubinger, G.A. Urban, and J. Kieninger, *Non-enzymatic glucose sensing based on hierarchical platinum micro-/nanostructures.* Journal of Electroanalytical Chemistry, 2018. **816**: 215-222.

187. Weremfo, A., S.T.C. Fong, A. Khan, D.B. Hibbert, and C. Zhao, *Electrochemically roughened nanoporous platinum electrodes for non-enzymatic glucose sensors.* Electrochimica Acta, 2017. **231**: 20-26.

188. Hu, Y., X. Niu, H. Zhao, J. Tang, and M. Lan, *Enzyme-free amperometric detection of glucose on platinum-replaced porous copper frameworks.* Electrochimica Acta, 2015. **165**: 383-389.

189. Lin, K.-C., C.-Y. Yang, and S.-M. Chen, *Fabrication of a nonenzymatic glucose sensor based on multi-walled carbon nanotubes decorated with platinum and silver hybrid composite.* Int. J. Electrochem. Sci, 2015. **10**: 3726-3737.

190. Xiao, F., Y. Li, H. Gao, S. Ge, and H. Duan, *Growth of coral-like PtAu–MnO2 binary nanocomposites on free-standing graphene paper for flexible nonenzymatic glucose sensors.* Biosensors and Bioelectronics, 2013. **41**: 417-423.

191. Zhang, C., R. Zhang, X. Gao, C. Cheng, L. Hou, X. Li, and W. Chen, *Small naked Pt nanoparticles confined in mesoporous shell of hollow carbon spheres for high-performance nonenzymatic sensing of H2O2 and glucose.* Acs Omega, 2018. **3**(1): 96-105.

192. Chang, G., H. Shu, Q. Huang, M. Oyama, K. Ji, X. Liu, and Y. He, *Synthesis of highly dispersed Pt nanoclusters anchored graphene composites and their application for non-enzymatic glucose sensing.* Electrochimica acta, 2015. **157**: 149-157.

193. Li, C., M. Iqbal, J. Lin, X. Luo, B. Jiang, V. Malgras, K.C.W. Wu, J. Kim, and Y. Yamauchi, *Electrochemical deposition: an advanced approach for templated synthesis of nanoporous metal architectures.* Accounts of chemical research, 2018. **51**(8): 1764-1773.

194. Kim, S.H., J.B. Choi, Q.N. Nguyen, J.M. Lee, S. Park, T.D. Chung, and J.Y. Byun, *Nanoporous platinum thin films synthesized by electrochemical dealloying for nonenzymatic glucose detection.* Physical Chemistry Chemical Physics, 2013. **15**(16): 5782-5787.

195. Park, S., T.D. Chung, and H.C. Kim, *Nonenzymatic glucose detection using mesoporous platinum.* Analytical chemistry, 2003. **75**(13): 3046-3049.

196. Bai, Y., W. Yang, Y. Sun, and C. Sun, *Enzyme-free glucose sensor based on a three-dimensional gold film electrode.* Sensors and Actuators B: Chemical, 2008. **134**(2): 471-476.

197. Cherevko, S. and C.-H. Chung, *Gold nanowire array electrode for non-enzymatic voltammetric and amperometric glucose detection.* Sensors and Actuators B: Chemical, 2009. **142**(1): 216-223.

198. Sanzó, G., I. Taurino, R. Antiochia, L. Gorton, G. Favero, F. Mazzei, G. De Micheli, and S. Carrara, *Bubble electrodeposition of gold porous nanocorals for the enzymatic and non-enzymatic detection of glucose.* Bioelectrochemistry, 2016. **112**: 125-131.

199. Han, L., S. Zhang, L. Han, D.-P. Yang, C. Hou, and A. Liu, *Porous gold cluster film prepared from Au@ BSA microspheres for electrochemical nonenzymatic glucose sensor.* Electrochimica acta, 2014. **138**: 109-114.

200. Xue, Y., S. Wang, P. Shi, Y. Huang, F. Scaglione, P. Rizzi, L. Battezzati, P. Denis, and H.-J. Fecht, *Nanoporous gold chemically de-alloyed from Au-based amorphous thin film for electrochemical nonenzymatic H2O2 sensing.* Chemical Physics Letters, 2019. **723**: 22-27.

201. Scandurra, A., F. Ruffino, S. Sanzaro, and M.G. Grimaldi, *Laser and thermal dewetting of gold layer onto graphene paper for non-enzymatic electrochemical detection of glucose and fructose.* Sensors and Actuators B: Chemical, 2019. **301**: 127113.

202. Niu, X., X. Li, J. Pan, Y. He, F. Qiu, and Y. Yan, *Recent advances in non-enzymatic electrochemical glucose sensors based on non-precious transition metal materials: opportunities and challenges.* RSC advances, 2016. **6**(88): 84893-84905.

203. Marioli, J.M. and T. Kuwana, *Electrochemical characterization of carbohydrate oxidation at copper electrodes.* Electrochimica Acta, 1992. **37**(7): 1187-1197.

204. Kano, K., M. Torimura, Y. Esaka, M. Goto, and T. Ueda, *Electrocatalytic oxidation of carbohydrates at copper (II)-modified electrodes and its application to flow-through detection.* Journal of Electroanalytical Chemistry, 1994. **372**(1-2): 137-143.

205. Perušković, D.S., N.R. Stevanović, G.N. Kovačević, D.M. Stanković, A.Đ. Lolić, and R.M. Baošić, *Application of N, N'-Bis (acetylacetonato) propylenediimine Copper (II) Complex as Mediator for Glucose Biosensor.* ChemistrySelect, 2020. **5**(5): 1671-1675.

206. Niu, X., Y. Li, J. Tang, Y. Hu, H. Zhao, and M. Lan, *Electrochemical sensing interfaces with tunable porosity for nonenzymatic glucose detection: A Cu foam case.* Biosensors and Bioelectronics, 2014. **51**: 22-28.

207. Riman, D., K. Spyrou, A.E. Karantzalis, J. Hrbac, and M.I. Prodromidis, *Glucose sensing on graphite screen-printed electrode modified by sparking of copper nickel alloys.* Talanta, 2017. **165**: 466-473.

208. Chen, X., X. Tian, L. Zhao, Z. Huang, and M. Oyama, *Nonenzymatic sensing of glucose at neutral pH values using a glassy carbon electrode modified with graphene nanosheets and Pt-Pd bimetallic nanocubes.* Microchimica Acta, 2014. **181**(7-8): 783-789.

209. Chen, H., G. Fan, J. Zhao, M. Qiu, P. Sun, Y. Fu, D. Han, and G. Cui, *A portable micro glucose sensor based on copper-based nanocomposite structure.* New Journal of Chemistry, 2019. **43**(20): 7806-7813.

210. Zhang, Y., N. Li, Y. Xiang, D. Wang, P. Zhang, Y. Wang, S. Lu, R. Xu, and J. Zhao, *A flexible non-enzymatic glucose sensor based on copper nanoparticles anchored on laser-induced graphene.* Carbon, 2020. **156**: 506-513.

211. Liu, X., W. Yang, L. Chen, and J. Jia, *Three-dimensional copper foam supported CuO nanowire arrays: an efficient non-enzymatic glucose sensor.* Electrochimica Acta, 2017. **235**: 519-526.

212. Gao, X., W. Feng, Z. Zhu, Z. Wu, S. Li, S. Kan, X. Qiu, A. Guo, W. Chen, and K. Yin, *Rapid Fabrication of Superhydrophilic Micro/Nanostructured Nickel Foam Toward High-Performance Glucose Sensor.* Advanced Materials Interfaces, 2021. **8**(7): 2002133.

213. Wang, F., X. Chen, L. Chen, J. Yang, and Q. Wang, *High-performance non-enzymatic glucose sensor by hierarchical flower-like nickel (II)-based MOF/carbon nanotubes composite.* Materials Science and Engineering: C, 2019. **96**: 41-50.

214. Zhang, X., Y. Xu, and B. Ye, *An efficient electrochemical glucose sensor based on porous nickel-based metal organic framework/carbon nanotubes composite (Ni-MOF/CNTs).* Journal of Alloys and Compounds, 2018. **767**: 651-656.

215. Aoun, S.B., Z. Dursun, T. Koga, G.S. Bang, T. Sotomura, and I. Taniguchi, *Effect of metal ad-layers on Au (1 1 1) electrodes on electrocatalytic oxidation of glucose in an alkaline solution.* Journal of Electroanalytical Chemistry, 2004. **567**(2): 175-183.

216. Zhao, Y., L. Fan, B. Hong, J. Ren, M. Zhang, Q. Que, and J. Ji, *Nonenzymatic detection of glucose using three-dimensional PtNi nanoclusters electrodeposited on*

*the multiwalled carbon nanotubes.* Sensors and Actuators B: Chemical, 2016. **231**: 800-810.

217. Xiao, F., F. Zhao, D. Mei, Z. Mo, and B. Zeng, *Nonenzymatic glucose sensor based on ultrasonic-electrodeposition of bimetallic PtM (M= Ru, Pd and Au) nanoparticles on carbon nanotubes–ionic liquid composite film.* Biosensors and Bioelectronics, 2009. **24**(12): 3481-3486.

218. Li, J., P. Koinkar, Y. Fuchiwaki, and M. Yasuzawa, *A fine pointed glucose oxidase immobilized electrode for low-invasive amperometric glucose monitoring.* Biosensors and Bioelectronics, 2016. **86**: 90-94.

219. Nantaphol, S., T. Watanabe, N. Nomura, W. Siangproh, O. Chailapakul, and Y. Einaga, *Bimetallic Pt–Au nanocatalysts electrochemically deposited on boron-doped diamond electrodes for nonenzymatic glucose detection.* Biosensors and Bioelectronics, 2017. **98**: 76-82.

220. Guascito, M.R., D. Chirizzi, C. Malitesta, M. Siciliano, T. Siciliano, and A. Tepore, *Amperometric non-enzymatic bimetallic glucose sensor based on platinum tellurium microtubes modified electrode.* Electrochemistry communications, 2012. **22**: 45-48.

221. Guo, T., Y. Zhang, Y. Ouyang, G. Yu, Y. Liao, and Z. Zhang, *Facile Synthesis of Bimetallic PtxCu1-x Nanostrands and Their Application in Non-Enzymatic Glucose Sensor.* Int. J. Electrochem. Sci., 2016. **11**: 6477-6490.

222. Pandey, P.C., D. Panday, and G. Pandey, *3-Aminopropyltrimethoxysilane and organic electron donors mediated synthesis of functional amphiphilic gold nanoparticles and their bioanalytical applications.* RSC advances, 2014. **4**(105): 60563-60572.

223. MARKETSANDMARKETS. *Biosensors Market*. 2019 [accessed on16/July/2019]; Available from: https://www.marketsandmarkets.com/Market-Reports/biosensors-market-798.html.

224. Abrera, A.T., L. Sützl, and D. Haltrich, *Pyranose oxidase: a versatile sugar oxidoreductase for bioelectrochemical applications.* Bioelectrochemistry, 2020. **132**: 107409.

225. Brugger, D., I. Krondorfer, C. Shelswell, B. Huber-Dittes, D. Haltrich, and C.K. Peterbauer, *Engineering pyranose 2-oxidase for modified oxygen reactivity.* PLoS One, 2014. **9**(10): e109242.

226. Kurbanoglu, S., M.N. Zafar, F. Tasca, I. Aslam, O. Spadiut, D. Leech, D. Haltrich, and L. Gorton, *Amperometric Flow Injection Analysis of Glucose and Galactose*

*Based on Engineered Pyranose 2-Oxidases and Osmium Polymers for Biosensor Applications.* Electroanalysis, 2018. **30**(7): 1496-1504.

227. Zafar, M.Q. and H. Zhao, *4D Printing: Future Insight in Additive Manufacturing.* Metals and Materials International, 2019: 1-22.
228. Zhang, Z., K.G. Demir, and G.X. Gu, *Developments in 4D-printing: a review on current smart materials, technologies, and applications.* International Journal of Smart and Nano Materials, 2019. **10**(3): 205-224.
229. Maniruzzaman, M., *3D and 4D printing in biomedical applications: process engineering and additive manufacturing*. John Wiley & Sons., 2019.
230. Benson, J., C.M. Fung, J.S. Lloyd, D. Deganello, N.A. Smith, and K.S. Teng, *Direct patterning of gold nanoparticles using flexographic printing for biosensing applications.* Nanoscale research letters, 2015. **10**(1): 1-8.
231. Setti, L., A. Fraleoni-Morgera, B. Ballarin, A. Filippini, D. Frascaro, and C. Piana, *An amperometric glucose biosensor prototype fabricated by thermal inkjet printing.* Biosensors and Bioelectronics, 2005. **20**(10): 2019-2026.
232. Basnar, B. and I. Willner, *Dip-pen-nanolithographic patterning of metallic, semiconductor, and metal oxide nanostructures on surfaces.* Small, 2009. **5**(1): 28-44.
233. Taleat, Z., A. Khoshroo, and M. Mazloum-Ardakani, *Screen-printed electrodes for biosensing: a review (2008–2013).* Microchimica Acta, 2014. **181**(9-10): 865-891.
234. Saunders, R.E. and B. Derby, *Inkjet printing biomaterials for tissue engineering: bioprinting.* International Materials Reviews, 2014. **59**(8): 430-448.
235. Salaita, K., Y. Wang, and C.A. Mirkin, *Applications of dip-pen nanolithography.* Nature nanotechnology, 2007. **2**(3): 145-155.
236. Park, S., S. Park, R.-A. Jeong, H. Boo, J. Park, H.C. Kim, and T.D. Chung, *Nonenzymatic continuous glucose monitoring in human whole blood using electrified nanoporous Pt.* Biosensors and Bioelectronics, 2012. **31**(1): 284-291.
237. Duda, T. and L.V. Raghavan, *3D metal printing technology.* IFAC-PapersOnLine, 2016. **49**(29): 103-110.
238. Rana, J., J. Jindal, V. Beniwal, and V. Chhokar, *Utility biosensors for applications in agriculture–A Review.* Journal of American Science, 2010. **6**(9): 353-375.
239. Otero, F. and E. Magner, *Biosensors—recent advances and future challenges in electrode materials.* Sensors, 2020. **20**(12): 3561.

240. J. Oliveira, V.C., H. Castro, P. Martins, S. Lanceros-Mendez, *Polymer-based smart materials by printing technologies: Improving application and integration.* Additve manufacturing, 2018. **21**: 269-283.
241. Schäfer, H., A. Hartwig, and K. Koschek, *The nature of bonding matters: Benzoxazine based shape memory polymers.* Polymer, 2018. **135**: 285-294.
242. Zhang, F., Y. Xia, Y. Liu, and J. Leng, *Nano/microstructures of shape memory polymers: From materials to applications.* Nanoscale horizons, 2020. **5**(8): 1155-1173.
243. Lendlein, A., M. Balk, N.A. Tarazona, and O.E. Gould, *Bioperspectives for shape-memory polymers as shape programmable, active materials.* Biomacromolecules, 2019. **20**(10): 3627-3640.
244. Reece, P.L., *Smart materials and structures: new research*. 2007: Nova Publishers.
245. L. K. Rivera-Tarazona, V.D.B., H. Kim, Z. T. Campbell, T. H. Ware, *Shape-morphing living composites.* Journal of Materials Chemisty 2020. **17;6**(3), 11375.
246. Qiji Ze, X.K., Shuai Wu, Janet Wong, S. Macrae Montgomery, Rundong Zhang, Joshua M. Kovitz, Fengyuan Yang, H. Jerry Qi, Ruike Zhao, *Magnetic Shape Memory Polymers with Integrated Multifunctional Shape Manipulation.* Advanced materials, 2019. **32**(4), 1906657.
247. Alina Kirillova, L.I., *Shape-changing polymers for biomedical applications.* Journal of Materials Chemistry B, 2019. **7**(10): 1597-1624.
248. Musavir Bashir, C.F.L.and P.R., *Shape Memory Materials and their applications in Aircraft Morphing: An Introspective Study* ARPN Journal of Engineering and Applied Sciences, 2017. **12**(19): 5434-5446.
249. Dr. Rong Yang, P.D.Y.Z., *Non-Uniform Optical Inscription of Actuation Domains in a Liquid Crystal Polymer of Uniaxial Orientation: An Approach to Complex and Programmable Shape Changes.* Angewandte Chemie, 2017. **129**(45).
250. Vernon, B., *Injectable biomaterials: science and applications*. 2011: Elsevier.
251. Buschow, K.J., R.W. Cahn, M.C. Flemings, B. Ilschner, E.J. Kramer, and S. Mahajan, *Encyclopedia of materials.* Science and technology, 2001. **1**(11).
252. Lu, H., Y. Liu, J. Gou, J. Leng, and S. Du, *Synergistic effect of carbon nanofiber and carbon nanopaper on shape memory polymer composite.* Applied Physics Letters, 2010. **96**(8): 084102.

253. Hager, M.D., S. Bode, C. Weber, and U.S. Schubert, *Shape memory polymers: Past, present and future developments.* Progress in Polymer Science, 2015. **49**: 3-33.

254. Kamila, S., *Introduction, classification and applications of smart materials: an overview.* American Journal of Applied Sciences, 2013. **10**(8): 876.

255. Greninger, A.B.a.M., V.G., *Strain transformation in metastable beta copper-zinc and beta copper-tin alloys.* Trans. AIME, 1938. **128**: pp. 337-341.

256. C.M.Wayman, *Shape memory and related phenomena.* Progress in Materials Science 1992. **36**: pages 203-224.

257. Otsuka, K., Kakeshita, T., *Science and Technology of Shape-Memory Alloys: New Developments.* MRS Bulletin, 2002. **27**: 91-100.

258. J. Mohdjani, M.L., A. Subic, M.A. Gibson, *A review of shape memory alloy research, applications and opportunities.* Materials Design, 2014. **56**: 1078-1113.

259. Peng, H., Chen, J., Wang, Y. and Wen, Y., *Key Factors Achieving Large Recovery Strains in Polycrystalline Fe–Mn–Si-Based Shape Memory Alloys: A Review.* Adv. Eng. Mater., 2018. **20**(3), 1700741.

260. Swadhin Kumar Patel, B.S., Rakesh Roshan, Niroj K. Sahu, A. Behera, *A brief review of shape memory effects and fabrication processes of NiTi shape memory alloys.* Materials Today: Proceedings, 2020. **33**: Pages 5552-5556.

261. Buchler, William J., Wiley, Raymond C. 1965 Nickel-base alloys United States Buchler, William J.,Wiley, Raymond C. 3174851 (https://www.freepatentsonline.com/3174851.html)

262. Lester B Vernon, Harold M. Vernon, 1947 *Process of manufacturing articles of thermoplastic synthetic resins*, United States C08f265/06 (https://patents.google.com/patent/US2234993A/en#citedBy).

263. Jing Li, Q.D., Enhe Zhang, Julian Wang, *Applications of Shape Memory Polymers in Kinetic Buildings.* Advances in Materials Science and Engineering, 2018. **2018**: 1-13.

264. Dr., A.L.D.S.K., *Shape-Memory Polymers.* A Journal of the German Chemical Society 2002. **41**: 2034 - 2057.

265. Akabori Sadatoshi, H.Y., Nakazawa Misako, Yamada Yoko, Shindo Yoichi, Sugimura Tokuko, Sato Sadao, *The Novel Syntheses of Photoreversible Cyclobutanocrown Ethers by the Intramolecular Photoaddition of α,ω-Dicinnamoyl Polyethylene Glycol Derivatives.* Bulletin of the Chemical Society of Japan, 1987. **60**(9).

266. Hada, M., Yamaguchi, D., Ishikawa, T., *Ultrafast isomerization-induced cooperative motions to higher molecular orientation in smectic liquid-crystalline azobenzene molecules.* Nat Commun, 2019. **10,** 1-8.

267. S.J. Jeon, A.W.H., R.C. Hayward,, *Shape-morphing materials from stimuli-responsive hydrogels hybrids.* Acc Chem Res, 2017. **50**: 161-169.

268. Tong Mu, L.L., Xin Lan, Yanju Liu, Jinsong Leng, *Shape memory polymers for composites.* Composites Science and Technology, 2018. **160**, 169-198

269. Liu, C.Q., Haihu & Mather, Patrick, *Review of progress in shape-memory polymers.* J MATER CHEM, 2007. **17**, 1543-1558

270. Reginald Desroches, M.A., Jason Mccormick, Michael Delemont, *Cyclic Properties of Superelastic Shape Memory Alloy Wires and Bars*. Journal of Structural Engineering, 2004. **130:1**(38).

271. Zhao, M.Q.Z.H., *4D Printing: Future Insight in Additive Manufacturing.* Met. Mater. Int., 2020. **26**: 564–585.

272. Voit, W., Ware, T., Dasari, R.R., Smith, P., Danz, L., Simon, D., Barlow, S., Marder, S.R. and Gall, K. , *High-Strain Shape-Memory Polymers.* Adv. Funct. Mater., 2010. **20**: 162-171.

273. Agustina B. Leonardi, L.A.F., Ileana A. Zucchi, Cristina E. Hoppe, Ezequiel R. Soulé, Claudio J. Pérez, Roberto J.J. Williams,, *Shape memory epoxies based on networks with chemical and physical crosslinks.* European Polymer Journal, 2011. **47**(3): 362-369.

274. Bowman, C.N., *Smart shape changing and shape morphing polymeric materials.* Polymer, 2014. **55**(23): 5847-5848.

275. Marc Behl, M.Y.R., Andreas Lendlein, *Multifunctional Shape-Memory Polymers.* Advanced materials, 2010. **22**(31), 3388-3410.

276. Hassan, M.H., A.M. Omar, E. Daskalakis, Y. Hou, B. Huang, I. Strashnov, B.D. Grieve, and P. Bártolo, *The Potential of Polyethylene Terephthalate Glycol as Biomaterial for Bone Tissue Engineering.* Polymers, 2020. **12**(12): 3045.

277. Mehrpouya, M., H. Vahabi, S. Janbaz, A. Darafsheh, T.R. Mazur, and S. Ramakrishna, *4D printing of shape memory polylactic acid (PLA).* Polymer, 2021. **230**: 124080.

278. Ramezani, M. and M.B.B. Monroe, *Biostable Segmented Thermoplastic Polyurethane Shape Memory Polymers for Smart Biomedical Applications.* ACS Applied Polymer Materials, 2022. **4**(3): 1956-1965.

279. Hwang, T., Z. Frank, J. Neubauer, and K.J. Kim, *High-performance polyvinyl chloride gel artificial muscle actuator with graphene oxide and plasticizer.* Scientific reports, 2019. **9**(1): 1-9.

280. Mahanty, B., K. Maity, S. Sarkar, and D. Mandal, *Human skin interactive self-powered piezoelectric e-skin based on PVDF/MWCNT electrospun nanofibers for non-invasive health care monitoring.* Materials Today: Proceedings, 2020. **21**: 1964-1968.

281. Pang, X., J.a. Lv, C. Zhu, L. Qin, and Y. Yu, *Photodeformable azobenzene-containing liquid crystal polymers and soft actuators.* Advanced Materials, 2019. **31**(52): 1904224.

282. Urbina, L., A. Alonso-Varona, A. Saralegi, T. Palomares, A. Eceiza, M.Á. Corcuera, and A. Retegi, *Hybrid and biocompatible cellulose/polyurethane nanocomposites with water-activated shape memory properties.* Carbohydrate polymers, 2019. **216**: 86-96.

283. Teng, J., Z. Wang, J. Liu, and X. Sun, *Effect of dynamic vulcanization system on the thermodynamics and shape memory properties of TPI/HDPE hybrid shape memory polymers.* European Polymer Journal, 2020. **132**: 109707.

284. Sun, Y.C., M. Chu, M. Huang, O. Hegazi, and H.E. Naguib, *Hybrid electroactive shape memory polymer composites with room temperature deformability.* Macromolecular materials and engineering, 2019. **304**(10): 1900196.

285. Huang, W.M., C. Song, Y.Q. Fu, C.C. Wang, Y. Zhao, H. Purnawali, H. Lu, C. Tang, Z. Ding, and J. Zhang, *Shaping tissue with shape memory materials.* Advanced Drug Delivery Reviews, 2013. **65**(4): 515-535.

286. Wu, X., W.M. Huang, Y. Zhao, Z. Ding, C. Tang, and J. Zhang, *Mechanisms of the shape memory effect in polymeric materials.* Polymers, 2013. **5**(4): 1169-1202.

287. Leng, J., X. Lan, Y. Liu, and S. Du, *Shape-memory polymers and their composites: stimulus methods and applications.* Progress in Materials Science, 2011. **56**(7): 1077-1135.

288. Ahmed, N., A. Kausar, and B. Muhammad, *Advances in shape memory polyurethanes and composites: A review.* Polymer-Plastics Technology and Engineering, 2015. **54**(13): 1410-1423.

289. Fan, P., W. Chen, B. Zhao, J. Hu, J. Gao, G. Fang, and F. Peng, *Formulation and numerical implementation of tensile shape memory process of shape memory polymers.* Polymer, 2018. **148**: 370-381.

290. Wolfgang Wagermaier, K.K., Matthias Heuchel, Andreas Lendlein, *Characterization Methods for Shape-Memory Polymers*, in *Shape-Memory Polymers*, M.B. Andreas Lendlein, Natalia A. Tarazona, and Oliver E. C. Gould, Editor, Springer . 2009. 97-145.
291. Eujin Pei, G.H.L., and Seokwoo Nam, *Concepts and Terminologies in 4D Printing.* Appl. Sci., 2020. **10**(13), 4443.
292. Delaey, J., Dubruel, P., Van, S., *Shape-Memory Polymers for Biomedical Applications.* Advanced Functional Materials, 2020. **30**(44), 1909047
293. Xie, T., *Tunable polymer multi-shape memory effect.* Nature, 2010. **464**: 267–270.
294. Apsite, I., A. Biswas, Y. Li, and L. Ionov, *Microfabrication Using Shape-Transforming Soft Materials.* Advanced Functional Materials, 2020. **30**(26): 1908028.
295. Miao, S., H. Cui, T. Esworthy, B. Mahadik, S.j. Lee, X. Zhou, S.Y. Hann, J.P. Fisher, and L.G. Zhang, *4D Self-Morphing Culture Substrate for Modulating Cell Differentiation.* Advanced Science, 2020. **7**(6): 1902403.
296. Guan, X., Y. Dong, H. Xia, J. Yao, and Q.-Q. Ni, *Mechanical and shape memory performance of shape memory polyurethane-based aligned nanofibers.* Polymer Testing, 2020. **91**: 106778.
297. Choong, Y.Y.C., S. Maleksaeedi, H. Eng, J. Wei, and P.-C. Su, *4D printing of high performance shape memory polymer using stereolithography.* Materials & Design, 2017. **126**: 219-225.
298. Park, S., N. Baugh, H.K. Shah, D.P. Parekh, I.D. Joshipura, and M.D. Dickey, *Ultrastretchable elastic shape memory fibers with electrical conductivity.* Advanced Science, 2019. **6**(21): 1901579.
299. Chen, J.H.a.S., *A review of actively moving polymers in textile applications.* Journal of Materials Chemistry B, 2010. **20**(17): 3346-3355.
300. Jinlian Hu, Y.Z., Huahua Huang, Jing Lu, *Recent advances in shape–memory polymers: Structure, mechanism, functionality, modeling and applications.* Progress in Polymer Science, 2012. **37**(12): 1720-1763.
301. Mohadeseh Zare, M.P.P., Nader Parvin, Seeram Ramakrishna, *Thermally-induced two-way shape memory polymers: Mechanisms, structures, and applications.* Chemical Engineering Journal, 2019. **374**(15): 706-720.
302. Zhao, J., J. Li, Y. Li, and J. You, *Thermoplastic shape memory composites with enhanced recovery stress and recovery ratio based on double roles of PVAc-g-GO.* Composites Communications, 2019. **13**: 52-56.

303. Xie, F., L. Huang, J. Leng, and Y. Liu, *Thermoset shape memory polymers and their composites.* Journal of Intelligent Material Systems and Structures, 2016. **27**(18): 2433-2455.

304. Yao, Y., J. Wang, H. Lu, B. Xu, Y. Fu, Y. Liu, and J. Leng, *Thermosetting epoxy resin/thermoplastic system with combined shape memory and self-healing properties.* Smart Materials and Structures, 2015. **25**(1): 015021.

305. Bengisu, M. and M. Ferrara, *Materials that move: smart materials, intelligent design*. , Springer ,2018.

306. Matsunaga, Y.-J.K.a.Y.T., *Thermo-responsive polymers and their application as smart biomaterials.* J. Mater. Chem. B, 2017. **5**: 4307-4321.

307. Phattarin Mora, D.H.S., Prof. Chanchira Jubsilp, Prof. Sarawut Rimdusit, Dr. Katharina Koschek, *Thermosetting Shape Memory Polymers and Composites Based on Polybenzoxazine Blends, Alloys and Copolymers.* Chemistry – An Asian Journal, 2019. **14**(23), 4129-4139.

308. Kim, H., J.M. Boothby, S. Ramachandran, C.D. Lee, and T.H. Ware, *Tough, shape-changing materials: crystallized liquid crystal elastomers.* Macromolecules, 2017. **50**(11): 4267-4275.

309. Davidson, E.C., A. Kotikian, S. Li, J. Aizenberg, and J.A. Lewis, *3D printable and reconfigurable liquid crystal elastomers with light-induced shape memory via dynamic bond exchange.* Advanced Materials, 2020. **32**(1): 1905682.

310. Gohy, O.B.a.J.-F., *Photo-responsive polymers: synthesis and applications.* Polym. Chem., 2017. **8**: 52-73.

311. Florica Adriana Jerca, V.V.J. and a.I.-C. Stancu, *Development and characterization of photoresponsive polymers*, in *Polymer and Photonic Materials Towards Biomedical Breakthroughs*, H.O. Jasper Van Hoorick, Hugo Thienpont, Peter Dubruel, Sandra Van Vlierberghe, Editor. Springer, 2018. 3-48.

312. Yuan, Z., A. Muliana, and K.R. Rajagopal, *Modeling the response of light-activated shape memory polymers.* Mathematics and Mechanics of Solids, 2017. **22**(5): 1116-1143.

313. Herath, M., J. Epaarachchi, M. Islam, L. Fang, and J. Leng, *Light activated shape memory polymers and composites: A review.* European Polymer Journal, 2020. **136**: 109912.

314. Wang, Y., A. Dang, Z. Zhang, R. Yin, Y. Gao, L. Feng, and S. Yang, *Repeatable and reprogrammable shape morphing from photoresponsive gold nanorod/liquid crystal elastomers.* Advanced Materials, 2020. **32**(46): 2004270.

315. Yang, M., Z. Yuan, J. Liu, Z. Fang, L. Fang, D. Yu, and Q. Li, *Photoresponsive Actuators Built from Carbon-Based Soft Materials.* Advanced Optical Materials, 2019. **7**(16): 1900069.

316. Müller, L.A., T. Zimmermann, G. Nyström, I. Burgert, and G. Siqueira, *Mechanical properties tailoring of 3D printed photoresponsive nanocellulose composites.* Advanced functional materials, 2020. **30**(35): 2002914.

317. Yang, H., W.R. Leow, T. Wang, J. Wang, J. Yu, K. He, D. Qi, C. Wan, and X. Chen, *3D printed photoresponsive devices based on shape memory composites.* Advanced Materials, 2017. **29**(33): 1701627.

318. Wang, X., N. Jiao, S. Tung, and L. Liu, *Photoresponsive graphene composite bilayer actuator for soft robots.* ACS applied materials & interfaces, 2019. **11**(33): 30290-30299.

319. Hui Xie, K.-K.Y., Yu-Zhong Wang, *Photo-cross-linking: A powerful and versatile strategy to develop shape-memory polymers.* Progress in Polymer Science, 2019. **95**: 32-64.

320. Da Cunha, M.P., E.A. van Thoor, M.G. Debije, D.J. Broer, and A.P. Schenning, *Unravelling the photothermal and photomechanical contributions to actuation of azobenzene-doped liquid crystal polymers in air and water.* Journal of Materials Chemistry C, 2019. **7**(43): 13502-13509.

321. Burdette, H.M.D.B.a.S.C., *Photoisomerization in different classes of azobenzene.* Chem. Soc. Rev., 2012. **41**(5): 1809-1825.

322. Woolley, A.A.B.a.G.A., *Azobenzene photoswitches for biomolecules.* Chem. Soc. Rev., 2011. **40**(8): 4422-4437.

323. Martin D.Hager, S.B., Christine Weber, Ulrich S.Schubert, *Shape memory polymers: Past, present and future developments.* Progress in Polymer Science, 2015. **49-50**: 3-33.

324. Ying Hu, Z.L., Tian Lan, Wei Chen, *Photoactuators for Direct Optical-to-Mechanical Energy Conversion: From Nanocomponent Assembly to Macroscopic Deformation.* Advanced Materials, 2016. **28**(47).

325. Larisa Florea, D.D., Fernando Benito-Lopez, *Photo-Responsive Polymeric Structures Based on Spiropyran.* Macromol. Mater. Eng. 2, 2012. **297**: 1148–1159.

326. Hideko Koshima, K.T., Hidetaka Uchimoto, Motoo Shirob and Daisuke Hashizume, *Photomechanical bending of salicylideneaniline crystals†.* Chemical Communications, 2011. **47**(41): 11423-11425.

327. Kondo, M., *Photomechanical materials driven by photoisomerization or photodimerization.* Polymer Journal, 2020. **52**: 1027–1034.

328. Wenhao Shen, J.Z., Zhansong Zhou, Dinglin Zhang, *Approaches for the synthesis of o-nitrobenzyl and coumarin linkers for use in photocleavable biomaterials and bioconjugates and their biomedical applications.* Acta Biomaterialia, 2020. **115**: 75-91.

329. Dr. Taehyung Kim, D.L.Z., Prof. Dr. Rabih O. Al-Kaysi, Prof. Dr. Christopher J. Bardeen, *Organic Photomechanical Materials.* ChemPhysChem, 2014. **15**(3).

330. Guin, T., M.J. Settle, B.A. Kowalski, A.D. Auguste, R.V. Beblo, G.W. Reich, and T.J. White, *Layered liquid crystal elastomer actuators.* Nature communications, 2018. **9**(1): 1-7.

331. Carpi, F., D. De Rossi, R. Kornbluh, R.E. Pelrine, and P. Sommer-Larsen, *Dielectric elastomers as electromechanical transducers: Fundamentals, materials, devices, models and applications of an emerging electroactive polymer technology*. Elsevier ,2011.

332. Wang, J., Z. Wang, Z. Song, L. Ren, Q. Liu, and L. Ren, *Biomimetic Shape–Color Double-Responsive 4D Printing.* Advanced Materials Technologies, 2019. **4**(9): 1900293.

333. Correia, D.M., L.C. Fernandes, P.M. Martins, C. García-Astrain, C.M. Costa, J. Reguera, and S. Lanceros-Méndez, *Ionic liquid–polymer composites: a new platform for multifunctional applications.* Advanced Functional Materials, 2020. **30**(24): 1909736.

334. Kiyohara, K., T. Sugino, and K. Asaka, *Molecular mechanism of ionic electroactive polymer actuators.* Smart materials and structures, 2011. **20**(12): 124009.

335. Meng, H. and J. Hu, *A brief review of stimulus-active polymers responsive to thermal, light, magnetic, electric, and water/solvent stimuli.* Journal of Intelligent Material Systems and Structures, 2010. **21**(9): 859-885.

336. Ask, A., A. Menzel, and M. Ristinmaa, *Electrostriction in electro-viscoelastic polymers.* Mechanics of Materials, 2012. **50**: 9-21.

337. Bar-Cohen, Y. and I.A. Anderson, *Electroactive polymer (EAP) actuators—background review.* Mechanics of Soft Materials, 2019. **1**(1): 5.

338. Humberto Palza, P.A.Z., Carolina Angulo-Pineda, *Electroactive Smart Polymers for Biomedical Applications.* Materials; Polymeric Materials: Surfaces, Interfaces and Bioapplications, 2019. **12**(2).

339. Binayak Bhandari, G.-Y.L.S.-H.A., *A review on IPMC material as actuators and sensors: Fabrications, characteristics and applications.* International Journal of Precision Engineering and Manufacturing, 2012. **13**: 141-163.

340. Haifei Wang, Z.W., Jian Yang, Chen Xu, Qi Zhang, Zhengchun Peng, *Ionic Gels and Their Applications in Stretchable Electronics.* Macromolecular Rapid Communications, 2018. **39**(16).

341. Y.Bar-Cohen, *Electroactive polymers as actuators*, in *Advanced Piezoelectric Materials*, K. Uchino, Editor. Woodhead Publishing, 2010. 287-317.

342. V.F.Cardoso, C.R., S.Lanceros-Mendez, *Metamorphic biomaterials*, in *Bioinspired Materials for Medical Applications*, L.R.a.M. Mota, Editor. 2017, Woodhead Publishing. 69-99.

343. Romasanta, L.J., M.A. López-Manchado, and R. Verdejo, *Increasing the performance of dielectric elastomer actuators: A review from the materials perspective.* Progress in Polymer Science, 2015. **51**: 188-211.

344. Qiu, Y., E. Zhang, R. Plamthottam, and Q. Pei, *Dielectric elastomer artificial muscle: materials innovations and device explorations.* Accounts of chemical research, 2019. **52**(2): 316-325.

345. Yi Li, D.L., C. P. Wong, *Intrinsically Conducting Polymers (ICPs)*, in *Electrical Conductive Adhesives with Nanotechnologies* 2009, Springer. 361-424.

346. Zijie Qiu, B.A.G.H., Klaus Müllen, *Conjugated polymers – Problems and promises.* Progress in Polymer Science, 2019. **100,** 101179.

347. Sahika Inal, J.R., Andreea-Otilia Suiu, George G. Malliaras, and Iain McCulloch, *Conjugated Polymers in Bioelectronics.* Acc. Chem. Res, 2018. **51**(6): 1368–1376.

348. A. Mora, F.H., G. Lubineau, *Estimating and understanding the efficiency of nanoparticles in enhancing the conductivity of carbon nanotube/polymer composites.* Results in Physics, 2018. **10**: 81-90.

349. F. Avilés, A.M.-P., M.A. López-Manchado, R. Verdejo, A. Bachmatiuk, M.H. Rümmeli, *A comparative study on the mechanical, electrical and piezoresistive properties of polymer composites using carbon nanostructures of different topology.* European Polymer Journal, 2018. **99**: 394-402.

350. Sebastián Román, F.L., Javier Bustos and Humberto Palza, *About the relevance of waviness, agglomeration, and strain on the electrical behavior of polymer composites filled with carbon nanotubes evaluated by a Monte-Carlo simulation.* Mater. Res. Express, 2018. **5.** 015044.

351. A J Marsden, D.G.P., C Vallés, A Liscio, V Palermo, M A Bissett, R J Young and I A Kinloch, *Electrical percolation in graphene–polymer composites.* 2D Materials, 2018. **5**(3), 032003.

352. Seulki Kwon, H.W.C., Gyemin Gwon, Heesuk Kim, and Bong June Sung, *Effects of shape and flexibility of conductive fillers in nanocomposites on percolating network formation and electrical conductivity.* PHYSICAL REVIEW E 2016. **93,** 032501.

353. MuhammadNawaz, Y.S., Ismail Ercan, Michele K.Lima-Tenório, Ernandes T.Tenório-Neto, Chariya Kaewsaneha, Abdelhamid Elaissari, *Magnetic and pH-responsive magnetic nanocarriers*, in *Stimuli Responsive Polymeric Nanocarriers for Drug Delivery Applications*, A.S.H.M.a.N.Y. Abu-Thabi, Editor. 2019, Woodhead Publishing. **30**(32), 37-85.

354. Eduardo Guisasola, M.V.-R., Alejandro Baeza, *Magnetically responsive polymers for drug delivery applications*, in *Stimuli Responsive Polymeric Nanocarriers for Drug Delivery Applications*, A.S.H.M.a.N.Y. Abu-Thabit, Editor. Woodhead Publishing , 2018.

355. Kolhatkar, A.G., A.C. Jamison, D. Litvinov, R.C. Willson, and T.R. Lee, *Tuning the Magnetic Properties of Nanoparticles.* International Journal of Molecular Sciences, 2013. **14**(8): 15977-16009.

356. Yuan Siang Lui, W.T.S., Lay Poh Tan, Yunlong Wu, Yuekun Lai, Huaqiong Li, *4D printing and stimuli-responsive materials in biomedical aspects.* Acta Biomaterialia, 2019. **92**: 19-36.

357. Kandasubramanian, J.M.K.a.B., *Fundamentals and Effects of Biomimicking Stimuli-Responsive Polymers for Engineering Functions.* Ind. Eng. Chem. Res, 2019. **59**(10): 4838–4841.

358. A. Bashari, N.H.N.A.P., *Applications of stimuli responsive hydrogels: a textile engineering approach.* The Journal of The Textile Institute, 2013. **104**(11): 1145-1155.

359. G. Kocak, C.T.a.V.B., *pH-Responsive polymers* Polym. Chem., 2017. **8**(1): 144-176.

360. Wenxin Wang, H.L., Yanju Liub and Jinsong Leng, *Sodium dodecyl sulfate/epoxy composite: water-induced shape memory effect and its mechanism.* Journal of Materials Chemistry A, 2-14. **2**(15): 5441-5449.

361. Hemjyoti Kalita, M.M.N.K., *Biodegradable solvent-induced shape-memory hyperbranched polyurethane.* Journal of Polymer Research, 2012. **19,** 9982.

362. Jiyu Yang, Y.Z., Linjuan Sheng, Hongmei Chen, Lijuan Zhao, Wenhao Yu, Ke-Qing Zhao, and Ping Hu, *Water Induced Shape Memory and Healing Effects by Introducing Carboxymethyl Cellulose Sodium into Poly(vinyl alcohol).* Ind. Eng. Chem. Res, 2018. **57**(44): 15046–15053.

363. Zhang, H.D.a.J., *Solvent induced shape recovery of shape memorypolymer based on chemically cross-linked poly(vinyl alcohol).* Soft Matter, 2010. **6**(14): 3370-3376.

364. Xiaodong Qi, X.Y., Sha Deng, Tiannan Zhoua and Qiang Fu, *Water-induced shape memory effect of graphene oxide reinforced polyvinyl alcohol nanocomposites†.* Journal of Materials Chemistry A, 2014. **2**(7): 2240-2249.

365. Julie Mendez, Pratheep K. Annamalai, Stephen J. Eichhorn, Rafeadah Rusli, Stuart J. Rowan, E. Johan Foster, and Christoph Weder, *Bioinspired Mechanically Adaptive Polymer Nanocomposites with Water-Activated Shape-Memory Effect.* Macromolecules 2011. **44**(17): 6827–6835.

366. Liu, X., C. Li, J. Lv, F. Huang, Y. An, L. Shi, and R. Ma, *Glucose and H2O2 Dual-Responsive Polymeric Micelles for the Self-Regulated Release of Insulin.* ACS Applied Bio Materials, 2020. **3**(3): 1598-1606.

367. Shen, D., H. Yu, L. Wang, A. Khan, F. Haq, X. Chen, Q. Huang, and L. Teng, *Recent progress in design and preparation of glucose-responsive insulin delivery systems.* Journal of Controlled Release, 2020. **321**: 236-258.

368. Song, J., Y. Zhang, S.Y. Chan, Z. Du, Y. Yan, T. Wang, P. Li, and W. Huang, *Hydrogel-based flexible materials for diabetes diagnosis, treatment, and management.* npj Flexible Electronics, 2021. **5**(1): 26.

369. Webber, M.J. and D.G. Anderson, *Smart approaches to glucose-responsive drug delivery.* Journal of Drug targeting, 2015. **23**(7-8): 651-655.

370. Honey Priya James, R.J., Anju Alex, Anoop. K.R., *Smart polymers for the controlled delivery of drugs – a concise overview.* Acta Pharmaceutica Sinica B, 2014. **4**(2): 120-127.

371. Zhen-Qiang Dong, Y.C., Qi-Juan Yuan, Yi-Fu Wang, Jian-Hu Li, Bang-Jing Li, Sheng Zhang, *Redox- and Glucose-Induced Shape-Memory Polymers.* Macromol. Rapid Commun., 2013. **34**: 867-872.

372. Hu, J., G. Zhang, and S. Liu, *Enzyme-responsive polymeric assemblies, nanoparticles and hydrogels.* Chemical Society Reviews, 2012. **41**(18): 5933-5949.

373. Shelby L. Buffingtonm Justine E.Paula, M.M.A., Mark M. Macios, Patrick T. Mather, James H. Henderson, *Enzymatically triggered shape memory polymers.* Acta Biomaterialia, 2019. **84**: 88-97.

374. Varsha Khare, S.S., Gil-Yong Lee, Won-Shik Chu, *From 3D to 4D printing – design, material and fabrication for multi-functional multi-materials.* International Journal of Precision Engineering and Manufacturing-Green Technology, 2017. **4**(3): 291-299.

375. Zhizhou Zhang, K.G.D.G.X.G., *Developments in 4D-printing: a review on current smart materials, technologies, and applications.* International Journal of Smart and Nano Materials, 2019. **10**(3): 205-224.

376. Pisani, S., I. Genta, T. Modena, R. Dorati, M. Benazzo, and B. Conti, *Shape-memory polymers hallmarks and their biomedical applications in the form of nanofibers.* International Journal of Molecular Sciences, 2022. **23**(3): 1290.

377. Gao, H., J. Li, F. Zhang, Y. Liu, and J. Leng, *The research status and challenges of shape memory polymer-based flexible electronics.* Materials Horizons, 2019. **6**(5): 931-944.

378. Rasmussen, L., P.N. Vicars, C. Briggs, T. Cheng, E.A. Clancy, S. Carey, and B. Secino. *Synthetic Muscle electroactive polymer (EAP) shape-morphing and pressure sensing for robotic grippers*. in *Electroactive Polymer Actuators and Devices (EAPAD) XXII*. SPIE ,2020.**11375**, 7-14

379. Dilara Goksu Tamay, T.D.U., Ayse Selcen Alagoz, Deniz Yucel, Nesrin Hasirci, and Vasif Hasirci, *3D and 4D Printing of Polymers for Tissue Engineering Applications.* Front. Bioeng. Biotechnol., 2019. **7**:164.

380. M. Bodaghi A.R. Damanpack, W.H.L., *Adaptive metamaterials by functionally graded 4D printing.* Mateirals & Design, 2017. **135**: 26-36.

381. Lukas Kacˇergis, R.M.a.M.S., *Influence of fused deposition modeling process parameters on the transformation of 4D printed morphing structures.* Smart Mater. Struct., 2019. **28,** 105042.

382. Wenzheng Wu, W.Y., Zichao Wu, Peng Geng, Yulei Wang, and Ji Zhao, *Influence of Layer Thickness, Raster Angle, Deformation Temperature and Recovery Temperature*

*on the Shape-Memory Effect of 3D-Printed Polylactic Acid Samples.* materials 2017. **10**(8): 970.

383. Yu Ying Clarrisa Choong, S.M., Hengky Eng, Pei-Chen Su & Jun Wei, *Curing characteristics of shape memory polymers in 3D projection and laser stereolithography.* Virtual and Physical Prototyping, 2017. **12**(1): 77-84.

384. Jain, S., T. Fuoco, M.A. Yassin, K. Mustafa, and A. Finne-Wistrand, *Printability and critical insight into polymer properties during direct-extrusion based 3D printing of medical grade polylactide and copolyesters.* Biomacromolecules, 2019. **21**(2): 388-396.

385. Chatham, C.A., C.E. Zawaski, D.C. Bobbitt, R.B. Moore, T.E. Long, and C.B. Williams, *Semi-Crystalline Polymer Blends for Material Extrusion Additive Manufacturing Printability: A Case Study with Poly (ethylene terephthalate) and Polypropylene.* Macromolecular Materials and Engineering, 2019. **304**(5): 1800764.

386. Pereira, G.G., S. Figueiredo, A.I. Fernandes, and J.F. Pinto, *Polymer Selection for Hot-Melt Extrusion Coupled to Fused Deposition Modelling in Pharmaceutics.* Pharmaceutics, 2020. **12**(9): 795.

387. Niazy, D., A. Elsabbagh, and M.R. Ismail, *Mono–Material 4D Printing of Digital Shape–Memory Components.* Polymers, 2021. **13**(21): 3767.

388. Tao, Y., F. Kong, Z. Li, J. Zhang, X. Zhao, Q. Yin, D. Xing, and P. Li, *A review on voids of 3D printed parts by fused filament fabrication.* Journal of Materials Research and Technology, 2021. **15**: 4860-4879.

389. Alshahrani, H.A., *Review of 4D printing materials and reinforced composites: Behaviors, applications and challenges.* Journal of Science: Advanced Materials and Devices, 2021. **6**(2): 167-185.

390. Justino Netto, J.M., H.T. Idogava, L.E. Frezzatto Santos, Z.d.C. Silveira, P. Romio, and J.L. Alves, *Screw-assisted 3D printing with granulated materials: a systematic review.* The International Journal of Advanced Manufacturing Technology, 2021. **115**(9): 2711-2727.

391. Liu, F., C. Vyas, G. Poologasundarampillai, I. Pape, S. Hinduja, W. Mirihanage, and P.J. Bartolo, *Process-Driven Microstructure Control in Melt-Extrusion-Based 3D Printing for Tailorable Mechanical Properties in a Polycaprolactone Filament.* Macromolecular Materials and Engineering, 2018. **303**(8): 1800173.

392. Liu, F., C. Vyas, G. Poologasundarampillai, I. Pape, S. Hinduja, W. Mirihanage, and P. Bartolo, *Structural Evolution of PCL during Melt Extrusion 3D Printing.* Macromolecular Materials and Engineering, 2018. **303**(2): 1700494.

393. Wan, X., L. Luo, Y. Liu, and J. Leng, *Direct Ink Writing Based 4D Printing of Materials and Their Applications.* Advanced Science, 2020. **7**(16): 2001000.

394. del Barrio, J. and C. Sánchez-Somolinos, *Light to Shape the Future: From Photolithography to 4D Printing.* Advanced Optical Materials, 2019. **7**(16): 1900598.

395. Ligon, S.C., R. Liska, J. Stampfl, M. Gurr, and R. Mülhaupt, *Polymers for 3D Printing and Customized Additive Manufacturing.* Chemical Reviews, 2017. **117**(15): 10212-10290.

396. Tagliaferri, S., A. Panagiotopoulos, and C. Mattevi, *Direct ink writing of energy materials.* Materials Advances, 2021. **2**(2): 540-563.

397. Hou, Z., H. Lu, Y. Li, L. Yang, and Y. Gao, *Direct Ink Writing of Materials for Electronics-Related Applications: A Mini Review.* Frontiers in Materials, 2021. **8:** 647229.

398. Li, L., Q. Lin, M. Tang, A.J.E. Duncan, and C. Ke, *Advanced Polymer Designs for Direct-Ink-Write 3D Printing.* Chemistry – A European Journal, 2019. **25**(46): 10768-10781.

399. Yan, J., S. Huang, Y.V. Lim, T. Xu, D. Kong, X. Li, H.Y. Yang, and Y. Wang, *Direct-ink writing 3D printed energy storage devices: From material selectivity, design and optimization strategies to diverse applications.* Materials Today, 2022. **54**: 110-152.

400. Guo, Y., Y. Liu, J. Liu, J. Zhao, H. Zhang, and Z. Zhang, *Shape memory epoxy composites with high mechanical performance manufactured by multi-material direct ink writing.* Composites Part A: Applied Science and Manufacturing, 2020. **135**: 105903.

401. Wei, H., Q. Zhang, Y. Yao, L. Liu, Y. Liu, and J. Leng, *Direct-Write Fabrication of 4D Active Shape-Changing Structures Based on a Shape Memory Polymer and Its Nanocomposite.* ACS Applied Materials & Interfaces, 2017. **9**(1): 876-883.

402. Wei, H., X. Cauchy, I.O. Navas, Y. Abderrafai, K. Chizari, U. Sundararaj, Y. Liu, J. Leng, and D. Therriault, *Direct 3D Printing of Hybrid Nanofiber-Based Nanocomposites for Highly Conductive and Shape Memory Applications.* ACS Applied Materials & Interfaces, 2019. **11**(27): 24523-24532.

403. Wan, X., Y. He, Y. Liu, and J. Leng, *4D printing of multiple shape memory polymer and nanocomposites with biocompatible, programmable and selectively actuated properties.* Additive Manufacturing, 2022. **53**: 102689.

404. Zhang, W., H. Wang, H. Wang, J.Y.E. Chan, H. Liu, B. Zhang, Y.-F. Zhang, K. Agarwal, X. Yang, A.S. Ranganath, H.Y. Low, Q. Ge, and J.K.W. Yang, *Structural multi-colour invisible inks with submicron 4D printing of shape memory polymers.* Nature Communications, 2021. **12**(1): 112.

405. Yuan, C., F. Wang, and Q. Ge, *Multimaterial direct 4D printing of high stiffness structures with large bending curvature.* Extreme Mechanics Letters, 2021. **42**: 101122.

406. Jakus, A.E., A.L. Rutz, S.W. Jordan, A. Kannan, S.M. Mitchell, C. Yun, K.D. Koube, S.C. Yoo, H.E. Whiteley, C.-P. Richter, R.D. Galiano, W.K. Hsu, S.R. Stock, E.L. Hsu, and R.N. Shah, *Hyperelastic “bone”: A highly versatile, growth factor–free, osteoregenerative, scalable, and surgically friendly biomaterial.* Science Translational Medicine, 2016. **8**(358): 358ra127-358ra127.

407. Jakus, A.E., N.R. Geisendorfer, P.L. Lewis, and R.N. Shah, *3D-printing porosity: A new approach to creating elevated porosity materials and structures.* Acta Biomaterialia, 2018. **72**: 94-109.

408. Rivera-Tarazona, L.K., T. Shukla, K.A. Singh, A.K. Gaharwar, Z.T. Campbell, and T.H. Ware, *4D Printing of Engineered Living Materials.* Advanced Functional Materials, 2022. **32**(4): 2106843.

409. Zolfagharian, A., A. Kaynak, M. Bodaghi, A.Z. Kouzani, S. Gharaie, and S. Nahavandi, *Control-based 4D printing: Adaptive 4D-printed systems.* Applied Sciences, 2020. **10**(9): 3020.

410. Zolfagharian, A., A. Kaynak, and A. Kouzani, *Closed-loop 4D-printed soft robots.* Materials & Design, 2020. **188**: 108411.

411. Ji, Q., M. Chen, C. Zhao, X. Zhang, X.V. Wang, L. Wang, and L. Feng, *Feedback control for the precise shape morphing of 4D Printed Shape Memory Polymer.* IEEE Transactions on Industrial Electronics, 2020, **68**(12): 12698-12707.

412. Wang, J., Z. Wang, Z. Song, L. Ren, Q. Liu, and L. Ren, *Programming multistage shape memory and variable recovery force with 4D printing parameters.* Advanced Materials Technologies, 2019. **4**(11): 1900535.

413. Kim, N.-G., M.-W. Han, A. Iakovleva, H.-B. Park, W.-S. Chu, and S.-H. Ahn, *Hybrid composite actuator with shape retention capability for morphing flap of unmanned aerial vehicle (UAV).* Composite Structures, 2020. **243**: 112227.

414. Pieczyska, E., M. Staszczak, K. Kowalczyk-Gajewska, M. Maj, K. Golasiński, S. Golba, H. Tobushi, and S. Hayashi, *Experimental and numerical investigation of yielding phenomena in a shape memory polymer subjected to cyclic tension at various strain rates.* Polymer Testing, 2017. **60**: 333-342.

415. Hassan, M.H., C. Vyas, B. Grieve, and P. Bartolo, *Recent advances in enzymatic and non-enzymatic electrochemical glucose sensing.* Sensors, 2021. **21**(14): 4672.

416. Granado, L.M., L.G. Carr, L.L. Fernandes, D.F. Parra, J.S. Sato, A.B. Lugão, L.G. Marchini, and P. Ponce, *Permeability and mechanical properties of PCL films.* World Polymer Congress, Rio De Janeiro 2006.

417. Vernon, B., *Injectable biomaterials : science and applications*. Woodhead Publishing in materials, Oxford. 2011.

418. Needham, D., *Smart Materials for Drug Delivery: Volume 1*. Smart Materials Series, editted by C. Alvarez-Lorenzo. Royal Society of Chemistry, 2013:.393.

419. Montaudo, G., Samperi, F. and Montaudo, M., *Characterization of synthetic polymers by MALDI-MS. Progress in Polymer Science.* 2006, **31**(3): 277-357.

420. Ting Wu, H.L.H., *Discrimination of Thermoplastic Polyesters by MALDI-TOF MS and Py-GC/MS.* International Journal of Polymer Analysis and Characterization, 2014. **19**(5): 441-452.

421. Lendlein, A., *Shape-Memory Polymers.* Advances in Polymer Science, 2010.

422. Charles, L., *MALDI of synthetic polymers with labile end-groups.* Mass Spectrometry Reviews, 2013. **33**(6): 523-543.

423. Wang, Y., J. Gao, Y. Ma, and U.S. Agarwal, *Study on mechanical properties, thermal stability and crystallization behavior of PET/MMT nanocomposites.* Composites part B: engineering, 2006. **37**(6): 399-407.

424. Tayebi, L. and K. Moharamzadeh, *Biomaterials for oral and dental tissue engineering*. Woodhead Publishing ,2017.

425. Orlando, G., *Regenerative medicine applications in organ transplantation*. Academic Press , 2013.

426. Dwivedi, R. and D. Mehrotra, *3D bioprinting and craniofacial regeneration.* Journal of Oral Biology and Craniofacial Research, 2020. **10**(4): 650-659.

427. Pereira, R.F., A. Sousa, C.C. Barrias, P.J. Bártolo, and P.L. Granja, *A single-component hydrogel bioink for bioprinting of bioengineered 3D constructs for dermal tissue engineering.* Materials Horizons, 2018. **5**(6): 1100-1111.

428. Pereira, R.F. and P.J. Bártolo, *3D photo-fabrication for tissue engineering and drug delivery.* Engineering, 2015. **1**(1): 090-112.

429. Christy, P.N., S.K. Basha, V.S. Kumari, A. Bashir, M. Maaza, K. Kaviyarasu, M.V. Arasu, N.A. Al-Dhabi, and S. Ignacimuthu, *Biopolymeric nanocomposite scaffolds for bone tissue engineering applications–A review.* Journal of Drug Delivery Science and Technology, 2020. **55**: 101452.

430. Ghorbani, F., D. Li, S. Ni, Y. Zhou, and B. Yu, *3D printing of acellular scaffolds for bone defect regeneration: a review.* Materials Today Communications, 2020. **22**: 100979.

431. Dwivedi, R., S. Kumar, R. Pandey, A. Mahajan, D. Nandana, D.S. Katti, and D. Mehrotra, *Polycaprolactone as biomaterial for bone scaffolds: Review of literature.* Journal of Oral Biology and Craniofacial Research, 2019. **10**(1): 6.

432. Baptista, R. and M. Guedes, *Morphological and mechanical characterization of 3D printed PLA scaffolds with controlled porosity for trabecular bone tissue replacement.* Materials Science and Engineering: C, 2020. **118**: 111528.

433. Bártolo, P., C. Chua, H. Almeida, S. Chou, and A. Lim, *Biomanufacturing for tissue engineering: present and future trends.* Virtual and Physical Prototyping, 2009. **4**(4): 203-216.

434. Bartolo, P., J.-P. Kruth, J. Silva, G. Levy, A. Malshe, K. Rajurkar, M. Mitsuishi, J. Ciurana, and M. Leu, *Biomedical production of implants by additive electro-chemical and physical processes.* CIRP annals, 2012. **61**(2): 635-655.

435. Hench, L. and J. Jones, *Biomaterials, artificial organs and tissue engineering*. Elsevier , 2005.

436. Remes, A. and D. Williams, *Immune response in biocompatibility.* The Biomaterials: Silver Jubilee Compendium, 1992: **13**(11),79-91.

437. Bártolo, P. and B. Bidanda, *Bio-materials and prototyping applications in medicine*. Springer , 2008.

438. Zhou, M., X. Yang, S. Li, K. Kapat, K. Guo, F.H. Perera, L. Qian, P. Miranda, and Y. Che, *Bioinspired channeled, rhBMP-2-coated β-TCP scaffolds with embedded autologous vascular bundles for increased vascularization and osteogenesis of*

*prefabricated tissue-engineered bone.* Materials Science and Engineering: C, 2021. **118**: 111389.

439. Wang, C., W. Huang, Y. Zhou, L. He, Z. He, Z. Chen, X. He, S. Tian, J. Liao, and B. Lu, *3D printing of bone tissue engineering scaffolds.* Bioactive Materials, 2020. **5**(1): 82-91.

440. Tonelli, F., N. DE CÁSSIA OLIVEIRA PAIVA, R. de Medeiros, M. Pinto, F. Tonelli, and R. Resende, *Tissue Engineering: The Use of Stem Cells in Regenerative Medicine*. *Current developments in biotechnology and bioengineering: human and animal health applications.* Elsevier,2016: 315-24.

441. Ribas, R.G., V.M. Schatkoski, T.L. do Amaral Montanheiro, B.R.C. de Menezes, C. Stegemann, D.M.G. Leite, and G.P. Thim, *Current advances in bone tissue engineering concerning ceramic and bioglass scaffolds: A review.* Ceramics International, 2019. **45**(17): 21051-21061.

442. Huang, B., G. Caetano, C. Vyas, J.J. Blaker, C. Diver, and P. Bártolo, *Polymer-ceramic composite scaffolds: The effect of hydroxyapatite and β-tri-calcium phosphate.* Materials, 2018. **11**(1): 129.

443. Wang, W., J.R.P. Junior, P.R.L. Nalesso, D. Musson, J. Cornish, F. Mendonça, G.F. Caetano, and P. Bártolo, *Engineered 3D printed poly (ε-caprolactone)/graphene scaffolds for bone tissue engineering.* Materials Science and Engineering: C, 2019. **100**: 759-770.

444. Wang, W., Z. Lu, J. Li, and P. Bártolo, *Engineering the biological performance of hierarchical nanostructured poly(ε-carpolactone) scaffolds for bone tissue engineering.* CIRP Annals, 2020. **69**(1): 217-220.

445. Vyas, C., G. Ates, E. Aslan, J. Hart, B. Huang, and P. Bartolo, *Three-Dimensional Printing and Electrospinning Dual-Scale Polycaprolactone Scaffolds with Low-Density and Oriented Fibers to Promote Cell Alignment.* 3D printing and additive manufacturing, 2020. **7**(3): 105-113.

446. Liu, F., W. Wang, W. Mirihanage, S. Hinduja, and P.J. Bartolo, *A plasma-assisted bioextrusion system for tissue engineering.* CIRP Annals, 2018. **67**(1): 229-232.

447. Caetano, G.F., W. Wang, W.-H. Chiang, G. Cooper, C. Diver, J.J. Blaker, M.A. Frade, and P. Bártolo, *3D-Printed poly (ε-caprolactone)/graphene scaffolds activated with P1-latex protein for bone regeneration.* 3D Printing and Additive Manufacturing, 2018. **5**(2): 127-137.

448. Caetano, G., R. Violante, A.B. Sant´Ana, A.B. Murashima, M. Domingos, A. Gibson, P. Bártolo, and M.A. Frade, *Cellularized versus decellularized scaffolds for bone regeneration.* Materials Letters, 2016. **182**: 318-322.

449. Huang, B., C. Vyas, J.J. Byun, M. El-Newehy, Z. Huang, and P. Bártolo, *Aligned multi-walled carbon nanotubes with nanohydroxyapatite in a 3D printed polycaprolactone scaffold stimulates osteogenic differentiation.* Materials Science and Engineering: C, 2020. **108**: 110374.

450. Li, Y., T. Ma, S.-T. Yang, and D.A. Kniss, *Thermal compression and characterization of three-dimensional nonwoven PET matrices as tissue engineering scaffolds.* Biomaterials, 2001. **22**(6): 609-618.

451. Taniguchi, I., S. Yoshida, K. Hiraga, K. Miyamoto, Y. Kimura, and K. Oda, *Biodegradation of PET: Current Status and Application Aspects.* ACS Catalysis, 2019. **9**(5): 4089-4105.

452. Montaudo, G., F. Samperi, and M.S. Montaudo, *Characterization of synthetic polymers by MALDI-MS.* Progress in Polymer Science, 2006. **31**(3): 277-357.

453. Wu, T., H.L. Hu, Y.P. Du, D. Jiang, and B.H. Yu, *Discrimination of thermoplastic polyesters by MALDI-TOF MS and Py-GC/MS.* International Journal of Polymer Analysis and Characterization, 2014. **19**(5): 441-452.

454. Li, L., *MALDI-MS for polymer characterization.* MALDI MS: A Practical Guide to Instrumentation, Methods and Applications (2007): 245-297.

455. Peacock, P.M. and C.N. McEwen, *Mass spectrometry of synthetic polymers.* Analytical chemistry, 2004. **76**(12): 3417-3428.

456. Mohamed H. Hassan, A.M.O., Evangelos Daskalakis, Fengyuan Liu and Paulo Bartolo, *Preliminary studies on the suitability of PETG for 4D printing applications*, in *7th International Conference of Materials and Manufacturing Engineering (ICMMEN 2020)*, Thessaloniki, Greece 2020. *MATEC Web of Conferences*. **318**,. 01010.

457. Turner, S.R., *Development of amorphous copolyesters based on 1, 4-cyclohexanedimethanol.* Journal of Polymer Science Part A: Polymer Chemistry, 2004. **42**(23): 5847-5852.

458. Thomson, R.C., M.J. Yaszemski, J.M. Powers, and A.G. Mikos, *Fabrication of biodegradable polymer scaffolds to engineer trabecular bone.* Journal of Biomaterials Science, Polymer Edition, 1996. **7**(1): 23-38.

459. Williams, J.M., A. Adewunmi, R.M. Schek, C.L. Flanagan, P.H. Krebsbach, S.E. Feinberg, S.J. Hollister, and S. Das, *Bone tissue engineering using polycaprolactone scaffolds fabricated via selective laser sintering.* Biomaterials, 2005. **26**(23): 4817-4827.

460. Porter, B., J. Oldham, a. He, S-L, M. Zobitz, R. Payne, K. An and, B. Currier, A. Mikos and, and M. Yaszemski, *Mechanical properties of a biodegradable bone regeneration scaffold.* Journal of Biomechanical Engineering, 2000. **122**(3): 286-288.

461. Lotz, J.C., T.N. Gerhart, and W.C. Hayes, *Mechanical properties of trabecular bone from the proximal femur: a quantitative CT study.* Journal of Computer Assisted Tomography, 1990. **14**(1): 107-114.

462. Murphy, C.M., M.G. Haugh, and F.J. O'brien, *The effect of mean pore size on cell attachment, proliferation and migration in collagen–glycosaminoglycan scaffolds for bone tissue engineering.* Biomaterials, 2010. **31**(3): 461-466.

463. Lendlein, A., Y. Feng, D.W. Grijpma, and Y. Zhao, *Smart materials.* ChemPhysChem, 2018. **19**(16): 1938-1940.

464. Bashir, M., C.F. Lee, and P. Rajendran, *Shape memory materials and their applications in aircraft morphing: an introspective study.* J Eng Appl Sci, 2017. **12**: 50-56.

465. Bowman, C.N., *Smart shape changing and shape morphing polymeric materials.* Polymer, 2014. **23**(55): 5847-5848.

466. Lee, A.Y., J. An, and C.K. Chua, *Two-way 4D printing: a review on the reversibility of 3D-printed shape memory materials.* Engineering, 2017. **3**(5): 663-674.

467. Langford, T., A. Mohammed, K. Essa, A. Elshaer, and H. Hassanin, *4D printing of origami structures for minimally invasive surgeries using functional scaffold.* Applied Sciences, 2021. **11**(1): 332.

468. Chen, T., G. Jiang, G. Li, Z. Wu, and J. Zhang, *Poly (ethylene glycol-co-1, 4-cyclohexanedimethanol terephthalate) random copolymers: effect of copolymer composition and microstructure on the thermal properties and crystallization behavior.* RSC Advances, 2015. **5**(74): 60570-60580.

469. Abdullah, S.A., A. Jumahat, N.R. Abdullah, and L. Frormann, *Determination of shape fixity and shape recovery rate of carbon nanotube-filled shape memory polymer nanocomposites.* Procedia Engineering, 2012. **41**: 1641-1646.

470. Gilbert, M., *Crystallinity in poly (vinyl chloride).* Journal of Macromolecular Science, Part C: Polymer Reviews, 1994. **34**(1): 77-135.

471. Endo, K., *Synthesis and structure of poly (vinyl chloride).* Progress in Polymer science, 2002. **27**(10): 2021-2054.

472. Yamada, M., M. Kondo, R. Miyasato, Y. Naka, J.-i. Mamiya, M. Kinoshita, A. Shishido, Y. Yu, C.J. Barrett, and T. Ikeda, *Photomobile polymer materials—various three-dimensional movements.* Journal of Materials Chemistry, 2009. **19**(1): 60-62.

473. Bandara, H.D. and S.C. Burdette, *Photoisomerization in different classes of azobenzene.* Chemical Society Reviews, 2012. **41**(5): 1809-1825.

474. Henzl, J., M. Mehlhorn, H. Gawronski, K.H. Rieder, and K. Morgenstern, *Reversible cis–trans isomerization of a single azobenzene molecule.* Angewandte Chemie International Edition, 2006. **45**(4): 603-606.

475. Hartley, G.S., *The cis-form of azobenzene.* Nature, 1937. **140**(3537): 281-281.

476. Lenci, F., *CRC Handbook of Organic Photochemistry and Photobiology*. CRC Press ,2004.

477. Rau, H. and E. Lueddecke, *On the rotation-inversion controversy on photoisomerization of azobenzenes. Experimental proof of inversion.* Journal of the American Chemical Society, 1982. **104**(6): 1616-1620.

478. Dürr, H. and H. Bouas-Laurent, *Photochromism: molecules and systems*. Elsevier, 2003.

479. Turanský, R., M. Konôpka, N.L. Doltsinis, I. Štich, and D. Marx, *Switching of functionalized azobenzene suspended between gold tips by mechanochemical, photochemical, and opto-mechanical means.* Physical Chemistry Chemical Physics, 2010. **12**(42): 13922-13932.

480. Cole, K., J. Guevremont, A. Ajji, and M. Dumoulin, *Characterization of surface orientation in poly (ethylene terephthalate) by front-surface reflection infrared spectroscopy.* Applied Spectroscopy, 1994. **48**(12): 1513-1521.

481. Alexiou, V.F., G.N. Mathioudakis, K.S. Andrikopoulos, A. Soto Beobide, and G.A. Voyiatzis, *Poly (ethylene terephthalate) carbon-based nanocomposites: A crystallization and molecular orientation study.* Polymers, 2020. **12**(11): 2626.

482. Solodovnichenko, V., V. Polyboyarov, A. Zhdanok, A. Arbuzov, E. Zapevalova, Y.G. Kryazhev, and V. Likholobov, *Synthesis of carbon materials by the short-term mechanochemical activation of polyvinyl chloride.* Procedia engineering, 2016. **152**: 747-752.

483. Paszkiewicz, S., A. Szymczyk, D. Pawlikowska, I. Irska, I. Taraghi, R. Pilawka, J. Gu, X. Li, Y. Tu, and E. Piesowicz, *Synthesis and characterization of poly (ethylene*

*terephthalate-co-1, 4-cyclohexanedimethylene terephtlatate)-block-poly (tetramethylene oxide) copolymers.* RSC advances, 2017. **7**(66): 41745-41754.

484. Pandey, M., G.M. Joshi, A. Mukherjee, and P. Thomas, *Electrical properties and thermal degradation of poly (vinyl chloride)/polyvinylidene fluoride/ZnO polymer nanocomposites.* Polymer International, 2016. **65**(9): 1098-1106.

485. Swinehart, D.F., *The beer-lambert law.* Journal of chemical education, 1962. **39**(7): 333.

486. García-Amorós, J. and D. Velasco, *Recent advances towards azobenzene-based light-driven real-time information-transmitting materials.* Beilstein journal of organic chemistry, 2012. **8**(1): 1003-1017.

487. Danowski, W., T. van Leeuwen, W.R. Browne, and B.L. Feringa, *Photoresponsive porous materials.* Nanoscale Advances, 2021. **3**(1): 24-40.

488. Meng, H., X. Yu, H. Feng, Z. Xue, and N. Yang, *Superior thermal conductivity of poly (ethylene oxide) for solid-state electrolytes: A molecular dynamics study.* International Journal of Heat and Mass Transfer, 2019. **137**: 1241-1246.

489. Taniguchi, T., L. Blanc, T. Asahi, H. Koshima, and P. Lambert. *Statistical Modeling of Photo-Bending Actuation of Hybrid Silicones Mixed with Azobenzene Powder*. in *Actuators*. 2019. Multidisciplinary Digital Publishing Institute (MDPI). **8**(4), 96.

490. Santer, S., *Remote control of soft nano-objects by light using azobenzene containing surfactants.* Journal of Physics D: Applied Physics, 2017. **51**(1): 013002.

491. Hao, Y., S. Huang, Y. Guo, L. Zhou, H. Hao, C.J. Barrett, and H. Yu, *Photoinduced multi-directional deformation of azobenzene molecular crystals.* Journal of Materials Chemistry C, 2019. **7**(3): 503-508.

492. Mota, C., D. Puppi, D. Dinucci, C. Errico, P. Bártolo, and F. Chiellini, *Dual-scale polymeric constructs as scaffolds for tissue engineering.* Materials, 2011. **4**(3): 527-542.

493. Dias, J.R., A. Sousa, A. Augusto, P.J. Bártolo, and P.L. Granja, *Electrospun polycaprolactone (PCL) degradation: an in vitro and in vivo study.* Polymers, 2022. **14**(16): 3397.

494. Aslan, E., C. Vyas, J. Yupanqui Mieles, G. Humphreys, C. Diver, and P. Bartolo, *Preliminary Characterization of a Polycaprolactone-SurgihoneyRO Electrospun Mesh for Skin Tissue Engineering.* Materials, 2021. **15**(1): 89.

495. Huang, B., E. Aslan, Z. Jiang, E. Daskalakis, M. Jiao, A. Aldalbahi, C. Vyas, and P. Bártolo, *Engineered dual-scale poly (ε-caprolactone) scaffolds using 3D printing and*

*rotational electrospinning for bone tissue regeneration.* Additive Manufacturing, 2020. **36**: 101452.

496. Asma Sadat Motamedi, H.M., Fereshteh Hajiesmaeilbaigi, Shadab Bagheri-Khoulenjani & MohammadAli Shokrgozar *Effect of electrospinning parameters on morphological properties of PVDF nanofibrous scaffolds.* Progress in Biomaterials 2017. **6**: 113-123.

497. Yarin, A.L., S. Koombhongse, and D.H. Reneker, *Taylor cone and jetting from liquid droplets in electrospinning of nanofibers.* Journal of applied physics, 2001. **90**(9): 4836-4846.

498. Hunley, M.T. and T.E. Long, *Electrospinning functional nanoscale fibers: a perspective for the future.* Polymer International, 2008. **57**(3): 385-389.

499. Tang, Y., X. Lan, C. Liang, Z. Zhong, R. Xie, Y. Zhou, X. Miao, H. Wang, and W. Wang, *Honey loaded alginate/PVA nanofibrous membrane as potential bioactive wound dressing.* Carbohydrate polymers, 2019. **219**: 113-120.

500. Stojkovska, J., Z. Djurdjevic, I. Jancic, B. Bufan, M. Milenkovic, R. Jankovic, V. Miskovic-Stankovic, and B. Obradovic, *Comparative in vivo evaluation of novel formulations based on alginate and silver nanoparticles for wound treatments.* Journal of biomaterials applications, 2018. **32**(9): 1197-1211.

501. Yang, X., Y. Wang, and X. Qing, *A flexible capacitive sensor based on the electrospun PVDF nanofiber membrane with carbon nanotubes.* Sensors and Actuators A: Physical, 2019. **299**: 111579.

502. Hussain, Z., S. Ullah, J. Yan, Z. Wang, I. Ullah, Z. Ahmad, Y. Zhang, Y. Cao, L. Wang, and M. Mansoorianfar, *Electrospun tannin-rich nanofibrous solid-state membrane for wastewater environmental monitoring and remediation.* Chemosphere, 2022. **307**: 135810.

503. Luo, C., M. Nangrejo, and M. Edirisinghe, *A novel method of selecting solvents for polymer electrospinning.* Polymer, 2010. **51**(7): 1654-1662.

504. Barton, A.F., *CRC handbook of solubility parameters and other cohesion parameters*. Routledge ,2017.

505. Heseltine, P.L., J. Ahmed, and M. Edirisinghe, *Developments in pressurized gyration for the mass production of polymeric fibers.* Macromolecular Materials and Engineering, 2018. **303**(9): 1800218.

506. Luo, C., E. Stride, and M. Edirisinghe, *Mapping the influence of solubility and dielectric constant on electrospinning polycaprolactone solutions.* Macromolecules, 2012. **45**(11): 4669-4680.

507. Burke, J., *Solubility parameters: theory and application.* 1984.

508. Ciera, L., L. Beladjal, X. Almeras, T. Gheysens, L. Van Landuyt, J. Mertens, V. Nierstrasz, and L. Van Langenhove, *Morphological and material properties of polyethyleneterephthalate (PET) fibres with spores incorporated.* Fibres & Textiles in Eastern Europe, 2014. **22,4**(106): 29-36

509. Bindraban, P., H. van Keulen, A. Kuyvenhoven, R. Rabbinge, and P. Uithol, *Food security at different scales: demographic, biophysical and socio-economic considerations*, Proceedings of AB-DLO, Wageningen, Netherlands, 1999.

510. (FAO), F.a.A.O.o.t.U.N., *The future of food and agriculture Trends and challenges*. Rome, Italy.2017.

511. Vos, R. and L.G. Bellù, *Chapter 2 - Global Trends and Challenges to Food and Agriculture into the 21st Century*, in *Sustainable Food and Agriculture*, C. Campanhola and S. Pandey, Editors. Academic Press. 2019, 11-30.

512. Calicioglu, O., A. Flammini, S. Bracco, L. Bellù, and R. Sims, *The future challenges of food and agriculture: An integrated analysis of trends and solutions.* Sustainability, 2019. **11**(1): 222.

513. Serraj, R. and P. Pingali, *Agriculture & Food Systems to 2050: Global Trends, Challenges and Opportunities*. Vol. 2. World Scientific , 2018.

514. Qian, L., F. Li, H. Liu, L. Wang, B. McCarthy, and S. Jin, *Rice vs. Wheat: Does staple food consumption pattern affect food waste in Chinese university canteens?* Resources, Conservation and Recycling, 2022. **176**: 105902.

515. Agriculture, F.U.D.o. *Worldwide production of grain in 2021/22, by type*. 2022 access date: 03/03/2022]; Available from: https://www.statista.com/statistics/263977/world-grain-production-by-type/.

516. Grausgruber, H., A. Lovegrove, P. Shewry, and F. Békés, *FODMAPs in wheat*, in *Wheat quality for improving processing and human health*. Springe, 2020, r. 517-534.

517. Singh, R., A.D. Chintagunta, D.K. Agarwal, R. Kureel, and S.J. Kumar, *Varietal replacement rate: Prospects and challenges for global food security.* Global Food Security, 2020. **25**: 100324.

518. Murray, G., P. Ellison, and A. Watson, *Effects of stripe rust on the wheat plant.* Australasian Plant Pathology, 1995. **24**(4): 261-270.

519. Solh, M., K. Nazari, W. Tadesse, and C. Wellings. *The growing threat of stripe rust worldwide*. in *Borlaug Global Rust Initiative (BGRI) conference, Beijing, China*. 2012.

520. Kang, Z., *Ultrastructure of plant pathogenic fungi.* China Science and Technology Press, Beijing, China, 1996.

521. Kang, Z., L. Huang, and J. Li, *Morphology of plant pathogenic fungi under scanning electron microscope*, Beijing: China Agriculture Press 1997.

522. Chen, W., C. Wellings, X. Chen, Z. Kang, and T. Liu, *Wheat stripe (yellow) rust caused by P uccinia striiformis f. sp. tritici.* Molecular plant pathology, 2014. **15**(5): 433-446.

523. Wang, X., C. Tang, G. Zhang, Y. Li, C. Wang, B. Liu, Z. Qu, J. Zhao, Q. Han, and L. Huang, *cDNA-AFLP analysis reveals differential gene expression in compatible interaction of wheat challenged with Puccinia striiformis f. sp. tritici.* BMC genomics, 2009. **10**(1): 1-12.

524. Mendgen, K., C. Struck, R.T. Voegele, and M. Hahn, *Biotrophy and rust haustoria.* Physiological and Molecular Plant Pathology, 2000. **56**(4): 141-145.

525. French, R.C., *Stimulation of uredospore germination in wheat stem rust by terpenes and related compounds.* Botanical Gazette, 1961. **122**(3): 194-198.

526. Guo, A., W. Huang, Y. Dong, H. Ye, H. Ma, B. Liu, W. Wu, Y. Ren, C. Ruan, and Y. Geng, *Wheat yellow rust detection using UAV-based hyperspectral technology.* Remote Sensing, 2021. **13**(1): 123.

527. Bohnenkamp, D., J. Behmann, and A.-K. Mahlein, *In-field detection of yellow rust in wheat on the ground canopy and UAV scale.* Remote Sensing, 2019. **11**(21): 2495.

528. Su, J., C. Liu, M. Coombes, X. Hu, C. Wang, X. Xu, Q. Li, L. Guo, and W.-H. Chen, *Wheat yellow rust monitoring by learning from multispectral UAV aerial imagery.* Computers and electronics in agriculture, 2018. **155**: 157-166.

529. Jonathan S. West, Cedric Bravo, Roberto Oberti, Dimitri Lemaire, Dimitrios Moshou, and H.A. McCartney, *THE POTENTIAL OF OPTICAL CANOPY MEASUREMENT FOR TARGETED CONTROL OF FIELD CROP DISEASES.* Annual Review of Phytopathology, 2003. **41**(1): 593-614.

530. Wahabzada, M., A.-K. Mahlein, C. Bauckhage, U. Steiner, E.-C. Oerke, and K. Kersting, *Plant Phenotyping using Probabilistic Topic Models: Uncovering the Hyperspectral Language of Plants.* Scientific Reports, 2016. **6**(1): 22482.

531. Whetton, R.L., K.L. Hassall, T.W. Waine, and A.M. Mouazen, *Hyperspectral measurements of yellow rust and fusarium head blight in cereal crops: Part 1: Laboratory study.* Biosystems Engineering, 2018. **166**: 101-115.

532. Whetton, R.L., T.W. Waine, and A.M. Mouazen, *Hyperspectral measurements of yellow rust and fusarium head blight in cereal crops: Part 2: On-line field measurement.* Biosystems Engineering, 2018. **167**: 144-158.

533. Gupta, S. and V. Kakkar, *Development of environmental biosensors for detection, monitoring, and assessment*, in *Nanomaterials and Environmental Biotechnology*. 2020, Springer. 107-125.

534. Adetunji, C.O., W. Nwankwo, K.E. Ukhurebor, A.S. Olayinka, and A.S. Makinde, *Application of Biosensor for the Identification of Various Pathogens and Pests Mitigating Against the Agricultural Production: Recent Advances.* Biosensors in Agriculture: Recent Trends and Future Perspectives, 2021: 169-189.

535. Singh, S., V. Kumar, D.S. Dhanjal, S. Datta, R. Prasad, and J. Singh, *Biological biosensors for monitoring and diagnosis*, in *Microbial biotechnology: basic research and applications*. 2020, Springer. 317-335.

536. Su, X., L. Sutarlie, and X.J. Loh, *Sensors, biosensors, and analytical technologies for aquaculture water quality.* Research, 2020. **2020**.

537. Roy, R., S. Ray, A. Chowdhury, and R. Anand, *Tunable multiplexed whole-cell biosensors as environmental diagnostics for ppb-level detection of aromatic pollutants.* ACS sensors, 2021. **6**(5): 1933-1939.

538. Shi, H., G. Zhao, M. Liu, L. Fan, and T. Cao, *Aptamer-based colorimetric sensing of acetamiprid in soil samples: sensitivity, selectivity and mechanism.* Journal of hazardous materials, 2013. **260**: 754-761.

539. Singh, K.R., V. Nayak, J. Singh, A.K. Singh, and R.P. Singh, *Potentialities of bioinspired metal and metal oxide nanoparticles in biomedical sciences.* RSC advances, 2021. **11**(40): 24722-24746.

540. Read, N.D., L.J. Kellock, T.J. Collins, and A.M. Gundlach, *Role of topography sensing for infection-structure differentiation in cereal rust fungi.* Planta, 1997. **202**(2): 163-170.

541. Wang, J., X. Cao, X. Wang, S. Yang, and R. Wang, *Electrochemical oxidation and determination of glucose in alkaline media based on Au (111)-like nanoparticle array on indium tin oxide electrode.* Electrochimica Acta, 2014. **138**: 174-186.

542. Zhong, G.-X., W.-X. Zhang, Y.-M. Sun, Y.-Q. Wei, Y. Lei, H.-P. Peng, A.-L. Liu, Y.-Z. Chen, and X.-H. Lin, *A nonenzymatic amperometric glucose sensor based on three dimensional nanostructure gold electrode.* Sensors and Actuators B: Chemical, 2015. **212**: 72-77.

543. Burke, L., *Premonolayer oxidation and its role in electrocatalysis.* Electrochimica Acta, 1994. **39**(11-12): 1841-1848.

544. Gao, X., X. Du, D. Liu, H. Gao, P. Wang, and J. Yang, *Core-shell gold-nickel nanostructures as highly selective and stable nonenzymatic glucose sensor for fermentation process.* Scientific Reports, 2020. **10**(1): 1365.

545. Qin, L., L. He, J. Zhao, B. Zhao, Y. Yin, and Y. Yang, *Synthesis of Ni/Au multilayer nanowire arrays for ultrasensitive non-enzymatic sensing of glucose.* Sensors and Actuators B: Chemical, 2017. **240**: 779-784.

546. Huang, J.-F., *Facile preparation of an ultrathin nickel film coated nanoporous gold electrode with the unique catalytic activity to oxidation of glucose.* Chemical communications, 2009.**10** : 1270-1272.

547. Kim, H.-U., H.Y. Kim, A. Kulkarni, C. Ahn, Y. Jin, Y. Kim, K.-N. Lee, M.-H. Lee, and T. Kim, *A sensitive electrochemical sensor for in vitro detection of parathyroid hormone based on a MoS2-graphene composite.* Scientific reports, 2016. **6**(1): 1-9.

548. Manikandan, V.S., B. Sidhureddy, A.R. Thiruppathi, and A. Chen, *Sensitive electrochemical detection of caffeic acid in wine based on fluorine-doped graphene oxide.* Sensors, 2019. **19**(7): 1604.

549. Marie, M., S. Mandal, and O. Manasreh, *An electrochemical glucose sensor based on zinc oxide nanorods.* Sensors, 2015. **15**(8): 18714-18723.

550. Wang, H.-C., H. Zhou, B. Chen, P.M. Mendes, J.S. Fossey, T.D. James, and Y.-T. Long, *A bis-boronic acid modified electrode for the sensitive and selective determination of glucose concentrations.* Analyst, 2013. **138**(23): 7146-7151.

551. Rinaldi, A.L. and R. Carballo, *Impedimetric non-enzymatic glucose sensor based on nickel hydroxide thin film onto gold electrode.* Sensors and Actuators B: Chemical, 2016. **228**: 43-52.

552. Koskun, Y., A. Şavk, B. Şen, and F. Şen, *Highly sensitive glucose sensor based on monodisperse palladium nickel/activated carbon nanocomposites.* Analytica Chimica Acta, 2018. **1010**: 37-43.

553. Arikan, K., H. Burhan, E. Sahin, and F. Sen, *A sensitive, fast, selective, and reusable enzyme-free glucose sensor based on monodisperse AuNi alloy nanoparticles on activated carbon support.* Chemosphere, 2022. **291**: 132718.

554. Singh, P., K.R. Singh, R. Verma, P. Prasad, R. Verma, S.N. Das, J. Singh, and R.P. Singh, *Preparation, antibacterial activity, and electrocatalytic detection of hydrazine based on biogenic CuFeO 2/PANI nanocomposites synthesized using Aloe barbadensis miller.* New Journal of Chemistry, 2022. **46**(18): 8805-8816.

555. Singh, J., K.R. Singh, M. Kumar, R. Verma, R. Verma, P. Malik, S. Srivastava, R.P. Singh, and D. Kumar, *Melt-quenched vanadium pentoxide-stabilized chitosan nanohybrids for efficient hydrazine detection.* Materials Advances, 2021. **2**(20): 6665-6675.

556. Figueroa, M., K.E. Hammond-Kosack, and P.S. Solomon, *A review of wheat diseases—a field perspective.* Molecular plant pathology, 2018. **19**(6): 1523-1536.

557. Duplessis, S., C.A. Cuomo, Y.-C. Lin, A. Aerts, E. Tisserant, C. Veneault-Fourrey, D.L. Joly, S. Hacquard, J. Amselem, and B.L. Cantarel, *Obligate biotrophy features unraveled by the genomic analysis of rust fungi.* Proceedings of the National Academy of Sciences, 2011. **108**(22): 9166-9171.

558. Kiran, K., H.C. Rawal, H. Dubey, R. Jaswal, B. Devanna, D.K. Gupta, S.C. Bhardwaj, P. Prasad, D. Pal, and P. Chhuneja, *Draft genome of the wheat rust pathogen (Puccinia triticina) unravels genome-wide structural variations during evolution.* Genome biology and evolution, 2016. **8**(9): 2702-2721.

559. Goodwin, S.B., S. Ben M'Barek, B. Dhillon, A.H. Wittenberg, C.F. Crane, J.K. Hane, A.J. Foster, T.A. Van der Lee, J. Grimwood, and A. Aerts, *Finished genome of the fungal wheat pathogen Mycosphaerella graminicola reveals dispensome structure, chromosome plasticity, and stealth pathogenesis.* PLoS genetics, 2011. **7**(6): e1002070.

560. Hane, J.K., R.G. Lowe, P.S. Solomon, K.-C. Tan, C.L. Schoch, J.W. Spatafora, P.W. Crous, C. Kodira, B.W. Birren, and J.E. Galagan, *Dothideomycete–plant interactions illuminated by genome sequencing and EST analysis of the wheat pathogen Stagonospora nodorum.* The Plant Cell, 2007. **19**(11): 3347-3368.

561. Backes, A., G. Guerriero, E.A. Barka, and C. Jacquard, *Pyrenophora teres: taxonomy, morphology, interaction with barley, and mode of control.* Frontiers in Plant Science, 2021. **12:** 614951.

562. Korn, U., T. Müller, A. Ulrich, and M.E.H. Müller, *Impact of aggressiveness of Fusarium graminearum and F. culmorum isolates on yield parameters and mycotoxin production in wheat.* Mycotoxin research, 2011. **27**(3): 195-206.

563. Liu, R., J. Lu, S. Zheng, M. Du, C. Zhang, M. Wang, Y. Li, J. Xing, Y. Wu, and L. Zhang, *Molecular mapping of a novel lesion mimic gene (lm4) associated with enhanced resistance to stripe rust in bread wheat.* BMC Genomic Data, 2021. **22**(1): 1.

564. FAO, I., *WFP (2013): The State of Food Insecurity in the World. The Multiple Dimensions of Food Security.* Food and Agriculture Organisation, Rome, 2015.

565. Chauhan, N., J. Narang, and U. Jain, *Amperometric acetylcholinesterase biosensor for pesticides monitoring utilising iron oxide nanoparticles and poly (indole-5-carboxylic acid).* Journal of Experimental Nanoscience, 2016. **11**(2): 111-122.

566. Fang, Y. and R.P. Ramasamy, *Current and Prospective Methods for Plant Disease Detection.* Biosensors, 2015. **5**(3): 537-561.

567. Zeinhom, M.M.A., Y. Wang, L. Sheng, D. Du, L. Li, M.-J. Zhu, and Y. Lin, *Smart phone based immunosensor coupled with nanoflower signal amplification for rapid detection of Salmonella Enteritidis in milk, cheese and water.* Sensors and Actuators B: Chemical, 2018. **261**: 75-82.

568. Soubeyrand, S., J. Enjalbert, A. Sanchez, and I. Sache, *Anisotropy, in density and in distance, of the dispersal of yellow rust of wheat: experiments in large field plots and estimation.* Phytopathology, 2007. **97**(10): 1315-1324.